COPPER-BASED NANOCRYSTALS AND THEIR USE AS CATALYSTS FOR THE ELECTROCHEMICAL REDUCTION OF CARBON DIOXIDE

A Dissertation
Presented to
The Academic Faculty

by

Zhiheng Lyu

In Partial Fulfillment
of the Requirements for the Degree
of Doctor of Philosophy in the
School of Chemistry and Biochemistry

Georgia Institute of Technology
December 2020

COPPER-BASED NANOCRYSTALS AND THEIR USE AS CATALYSTS FOR THE ELECTROCHEMICAL REDUCTION OF CARBON DIOXIDE

Approved by:

Dr. Younan Xia, Advisor
Department of Biomedical Engineering
Georgia Institute of Technology

Dr. Henry S. La Pierre
School of Chemistry and Biochemistry
Georgia Institute of Technology

Dr. Z. John Zhang
School of Chemistry and Biochemistry
Georgia Institute of Technology

Dr. Zhiqun Lin
School of Materials Science and Engineering
Georgia Institute of Technology

Dr. Angus P. Wilkinson
School of Chemistry and Biochemistry
Georgia Institute of Technology

Date Approved: [October 23, 2020]

Dedicated to my parents, my friends, and all those who give me support, encouragement, advice, and love in my life.

ACKNOWLEDGEMENTS

The four-year Ph.D. life benefited me a lot in research, knowledge, and daily life, during which period I received help and support from many people. I would like to thank everyone for their invaluable assistance throughout these years. First and foremost, I would like to express my deepest gratitude to my graduate advisor Prof. Younan Xia, for his continuous support in my Ph.D. research. His expertise in nanoscience, valuable suggestions, and insightful feedbacks greatly inspired me, guided me, and encouraged me to be more professional. I am also grateful to my committee members, Prof. Z. John Zhang, Angus P. Wilkinson, Henry La Pierre, and Zhiqun Lin, who offered me useful advice and fascinating ideas regarding my research.

I would like to pay special regards to my collaborators: Prof. Minhua Shao and Dr. Shangqian Zhu for their tremendous help in electrochemical measurements; Prof. Manos Mavrikakis and Dr. Lang Xu for their efforts in simulations; Prof. Jingyue Liu and Prof. Miaofang Chi for the electron microscopy analysis. It is their help that brought my work to a higher level.

I would like to thank my friends: Dr. Xuan Yang, Dr. Ming Zhao, Dr. Shan Zhou, and Dr. Kyle D. Gilroy for their help in starting my research; Dr. Yu Zhang for her assistance in electrochemical measurements; Dr. Zach Hood, Dr. Da Huo, Ruhui Chen, Yifeng Shi, Minghao Xie, Janssen Annemieke, Zitao Chen, Zhenming Cao, and all the current and former Xia Group members for their support in my Ph.D. research; Ningxin Jiang, Tianran Deng, Minsi Li, and many others for their company in the past four years.

In the end, I would like to express my sincere gratitude to my parents and other family members for their care, their support, and their love. Your encouragements and

concerns significantly light up my life and give me confidence throughout my years of study and research.

TABLE OF CONTENTS

LIST OF TABLES

LIST OF FIGURES

LIST OF SYMBOLS AND ABBREVIATIONS

1-D	one-dimensional
3-D	three-dimensional
ac	acetate
ATR-IR	attenuated total reflection infrared
BE_{avg}	average binding energy
BF-STEM	bright-field scanning transmission electron microscopy
C_{2+}	multi-carbon
CTAB	cetyltrimethylammonium bromide
CTAC	cetyltrimethylammonium chloride
CO_2RR	CO_2 reduction reaction
CuNW	Cu nanowire
CV	cyclic voltammetry
dBE	differential binding energy
DDA	discrete dipole approximation
DEG	diethylene glycol
DFT	density functional theory
DI water	deionized water
DLS	dynamic light scattering
ECSA	electrochemically active surface area
EDX	energy dispersive X-ray
EELS	electron energy loss spectroscopy
EXAFS	extended X-Ray absorption fine structure
FAO	formic acid oxidation

fcc	face-centered cubic
FE	faradaic efficiency
FEM	finite-element method
FFT	fast Fourier transform
FID	flame ionization detector
GGA	generalized gradient approximation
HAADF-STEM	high-angle annular dark-field scanning transmission electron microscopy
HDA	hexadecylamine
HER	hydrogen evolution reaction
HRTEM	high-resolution transmission electron microscopy
ICP-MS	inductively coupled plasma mass spectrometry
IR	infrared
ITO	indium-tin-oxide
LSPR	localized surface plasmon resonance
ML	monolayer
MS	mass spectrometry
NBED	nano-beam electron diffraction
NMR	nuclear magnetic resonance
OAm	oleylamine
ODA	octadecylamine
OER	Oxygen evolution reaction
ORR	oxygen reduction reaction
PAW	projector augmented-wave
PdH	palladium hydride

PVP	poly(vinyl pyrrolidone)
RBP	right bipyramid
rGO	reduced graphene oxides
RHE	reversible hydrogen electrode
SEM	scanning electron microscope
SERS	surface-enhanced Raman scattering
SHE	standard hydrogen electrode
STEM	scanning transmission electron microscopy
TCD	thermal conductivity detector
TEM	transmission electron microscopy
TOP	trioctylphosphine
TOPO	trioctylphosphine oxide
UHV	ultra-high vacuum
UV-vis	ultraviolet-visible
WGS	water gas shift
XANES	X-ray absorption near edge structure
XPS	X-ray photoelectron spectroscopy
XRD	X-ray diffraction
ZPE	zero-point energy

SUMMARY

Benefiting from the high abundance, low price, and fascinating properties of copper (Cu), Cu and Cu-based nanocrystals have found wide-spread use in many applications. In recent years, they received increasing attention as catalysts due to their uniqueness in generating substantial amounts of hydrocarbons and oxygenates in electrochemical CO_2 reduction. Both experimental and computational studies suggest that the selectivity and activity of Cu-based catalysts are highly dependent on their surface structures, emphasizing the importance of shape-controlled synthesis of Cu nanocrystals. In this dissertation, I will introduce different strategies of synthesizing Cu nanocrystals with well-defined shapes, together with their catalytic performance in electrochemical CO_2 reduction. By leveraging the reduction potential difference, a trace amount of Pd(II) was introduced to the Cu(II) precursor to induce the formation of Pd seeds, onto which Cu atoms deposited and grew into a right bipyramidal shape enclosed by {100} facets and twin boundaries. The coordination of hexadecylamine to metal ions was also revealed, which significantly slowed down their reduction rates and contributed to the generation of multiple parallel planar defects in a seed. Switching from one-pot synthesis to seed-mediated growth, Au@Cu core-shell nanocubes with sizes below 30 nm were produced, taking advantage of the small size of 5-nm Au seeds. Due to the large lattice mismatch (12%) between Au and Cu, an island growth mode was observed for Cu, resulting in a random location of Au core inside the Cu shell. When applying Pd icosahedra with a relatively larger size (13 nm) as seeds, Pd-Cu Janus nanocrystals with different shapes and twinned structures were obtained. By varying the reduction rate of Cu(II) precursor from slow to fast, Cu atoms selectively grew from either the vertex or

the edge of an icosahedral seed, leading to the formation of penta-twinned or singly-twinned nanostructures. The presence of twin boundaries, exposure of Pd as a CO generator, and phase-segregated morphology of Pd and Cu all made Pd-Cu nanocrystals promising catalysts for electrochemical CO_2 reduction. In addition to manipulating the twin defects and composition, I also demonstrated that both C_{2+} selectivity and catalytic stability of Cu nanocrystals could be improved by introducing surface oxidation and controlling the oxidation pathway. Compared to Cu nanowires oxidized by O_2, which possessed a rough surface and non-uniform oxide layer, those oxidized by H_2O_2 showed a much smoother surface covered by oxide sheath with even thickness. The uniformity of the sheath greatly mitigated the fragmentation of nanowires, contributing to their superior stability in CO_2 reduction.

CHAPTER 1

INTRODUCTION

1.1 Copper-based Nanocrystals: Properties and Applications

As a soft, malleable, and ductile metal with high thermal and electrical conductivities, copper (Cu) is widely used in our daily life as conductors, building materials, and decorations, among others [1]. It also serves as a major constituent of various alloys, such as bronze when mixed with tin (Sn), brass when mixed with zinc (Zn), and cupronickel when mixed with nickel (Ni). Presented at a concentration of around 50 parts per million (ppm), Cu is one of the abundant metals in the Earth's crust and the high abundance also contributes to its relatively low price (6.53 USD per kilogram), especially when compared to other noble metals (Table 1.1) [2,3].

Table 1.1. Prices, standard reduction potentials, and physicochemical properties of some typical noble metals.

Metal	Price (USD per kg)[(a)]	Standard reduction potential (V_{SHE})[(b)]		Crystal lattice (abbr.)	Lattice constant (Å)[(c)]	Stacking fault energy (mJ m^{-2})[(d)]
Cu	6.53	Cu^{2+}/Cu	0.340	*fcc*	3.597	41
Pd	70361.91	Pd^{2+}/Pd	0.915	*fcc*	3.859	180
Ag	867.43	Ag^{+}/Ag	0.799	*fcc*	4.079	18
Pt	31266.60	Pt^{2+}/Pt	1.188	*fcc*	3.912	322
Au	65540.90	Au^{3+}/Au	1.52	*fcc*	4.065	33

(a) values taken from ref [2], updated on Aug 5th. (b) values taken from ref [4]. (c) values taken from ref [5]. (d) values taken from ref [6].

Compared to other noble metals such as Pt and Au, Cu is much more vulnerable to oxidation, which could be ascribed to its low reduction potential (0.34 and 0.52 V_{SHE} for Cu^{2+}/Cu and Cu^{+}/Cu pairs, respectively; SHE: standard hydrogen electrode). One famous oxidation product of Cu, patina, is a green verdigris often used as roofing of many old buildings. Different from rust formed on iron in moist air, Cu reacts slowly with the O_2 in air to generate a layer of brown/black copper oxides, which could to some extent protect the underlying metal from further corrosion [1]. The oxidation process of Cu was also investigated using *in situ* transmission electron microscopy (TEM). Instead of forming a uniform layer, oxides nucleate and grow as islands upon exposure to O_2 under atmospheric pressure, followed by their growth and coalescence into a film to passivate and protect the underlying Cu [7].

When decreasing the size down to nanoscale, Cu nanocrystals exhibit large specific surface areas and properties unique from bulk solids. By manipulating the size, shape, structure, composition, and elemental distribution, their properties can be finely tuned, satisfying various applications while exhibiting extraordinary performance. To this end, Cu-based nanocrystals have been widely used in organic transformations, biomedicine, photocatalysis, and electrocatalysis, among others [8]. For example, with Cu nanoparticles serving as the catalyst, primary, secondary, tertiary, and even phenyl Grignard reagents could be coupled to primary alkyl bromides or chlorides in high yields [9]. In another example, by modifying with Cu nanoparticles, the activity of TiO_2 was greatly improved toward photocatalytic hydrogen evolution reaction (HER). The photogenerated electrons in TiO_2 could be easily transferred to metallic Cu, and the well-separated electron-hole pairs then contributed to an enhanced photocatalytic activity

[10,11]. Currently used as an industrial catalyst, the facet-dependent activity of Cu nanocrystals was also analyzed for low-temperature water gas shift (WGS) reaction and Cu{100} facets were found to be more active than Cu{111} [12]. In recent years, Cu nanocrystals have been largely explored as catalysts in electrochemical CO_2 reduction reaction (CO_2RR) due to the uniqueness of Cu in converting CO_2 into multi-carbon (C_{2+}) products in a considerable quantity [13]. With performance highly dependent on the shape, structure, and composition, the development of effective Cu catalysts has attracted attention of researchers all over the world.

1.2 Electrochemical Reduction of CO_2: Cu-based Catalysts and the Importance of Surface Structure and Composition

As a harmful greenhouse gas, excessive emission of CO_2 has caused major environmental concern [13]. To reduce the net CO_2 emission, electrochemically reducing CO_2 to valuable fuels and feedstock is a promising approach [14]. This process can be conducted at room temperature and ambient pressure, while generating products that cannot be easily prepared through thermal reduction/hydrogenation of CO_2. During the reduction process, the chemically stable CO_2 will be firstly reduced to CO on the surface of a catalyst. The CO intermediate then undergoes further reduction, hydrogenation, and C-C coupling to generate hydrocarbons and multi-carbon products (*e.g.*, CH_4, C_2H_4, and ethanol). The adsorbed CO can also be released from the surface for the production of CO. Compared with the commonly produced small molecules (*e.g.*, CO and formate), the further reduced products such as multi-carbon oxygenates and hydrocarbons have attracted more attention due to their higher energy densities, a wider scope of application, and the corresponding higher values and larger markets [14]. As documented by many

reports, the selectivity of a catalyst toward a specific product is highly sensitive to its surface structure, in addition to other parameters such as size, composition, oxidation state, support, and electrolyte [15].

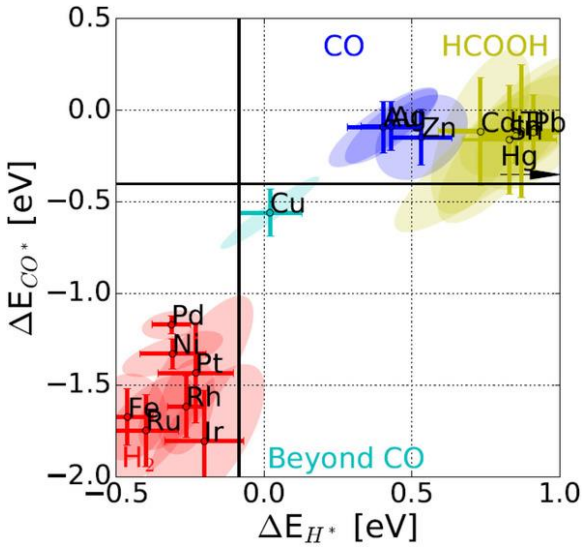

Figure 1.1. Binding energies of the intermediates ΔE_{CO*} and ΔE_{H*} for different metals. The black lines show the thermodynamics of adsorbed or none-adsorbed hydrogen (ΔG_{H*}=0, for ½ $H_2 \leftrightarrow$H*) or CO (ΔG_{CO*}=0, for CO↔CO*). The red, yellow, blue, and cyan colors represent the major product of H_2, formic acid, CO, and beyond CO*, respectively. The plot shows the ability of Cu to reduce CO_2 beyond CO while not having H_{UPD}. Reprinted with permission from ref [16] and [17]. Copyright 1989 Royal Society of Chemistry and 2017 Wiley-VCH.

Different from other metals that typically generate CO or formate as the major product, Cu stands out uniquely in producing significant amounts of oxygenates and hydrocarbons such as ethylene and ethanol (Figure 1.1). The catalysts based on Cu nanocrystals, however, tend to suffer from several drawbacks: *i*) poor selectivity as a variety of products such as CO, CH_4, formate, ethylene, ethanol, and n-propanol can all be generated; *ii*) high overpotentials as the highest selectivity toward multi-carbon

products is often achieved at a potential more negative than -1.0 V_{RHE} (RHE: reversible hydrogen electrode); and *iii*) poor stability as the original shape of the Cu nanocrystals can hardly be maintained during CO_2RR, making it difficult to keep the selectivity and activity.

Engineering the surface structure of Cu nanocrystals holds great promise in achieving purer products at a reduced overpotential. According to the results from both experimental and computational studies (Figure 1.2, a and b), the {100} and {111} facets on Cu nanocrystals favored the formation of ethylene and methane, respectively [18,19]. The formation of ethylene involved the dimerization of CO molecules to generate $C_2O_2^-$ intermediates, followed by their protonation. The square arrangement of Cu atoms on {100} facets presented an optimal geometry for the adsorption of $C_2O_2^-$ dimers while the negative charges on the adsorbed dimers could cause additional stabilization through solvation [19−23].

The size of the Cu nanocrystals also plays an important role in determining their catalytic performance. Decreasing the size would lead to an increase in the mass activity, but the change in surface structure could also impact the selectivity and, in most cases, was detrimental to CO_2RR. A dramatic increase in both activity and selectivity toward H_2 and CO was reported when the Cu nanoparticles were reduced to a size below 5 nm (Figure 1.2c) [24,25]. At the same time, the selectivity toward hydrocarbons such as methane and ethylene was substantially suppressed. Based on density functional theory (DFT) calculations, the higher proportion of low-coordination atoms (CN < 8, starting as low as CN = 5) on smaller nanoparticles imposed strong chemisorption for CO and H, limiting their movement on the Cu surface and thus their coupling for the generation of

hydrocarbons.

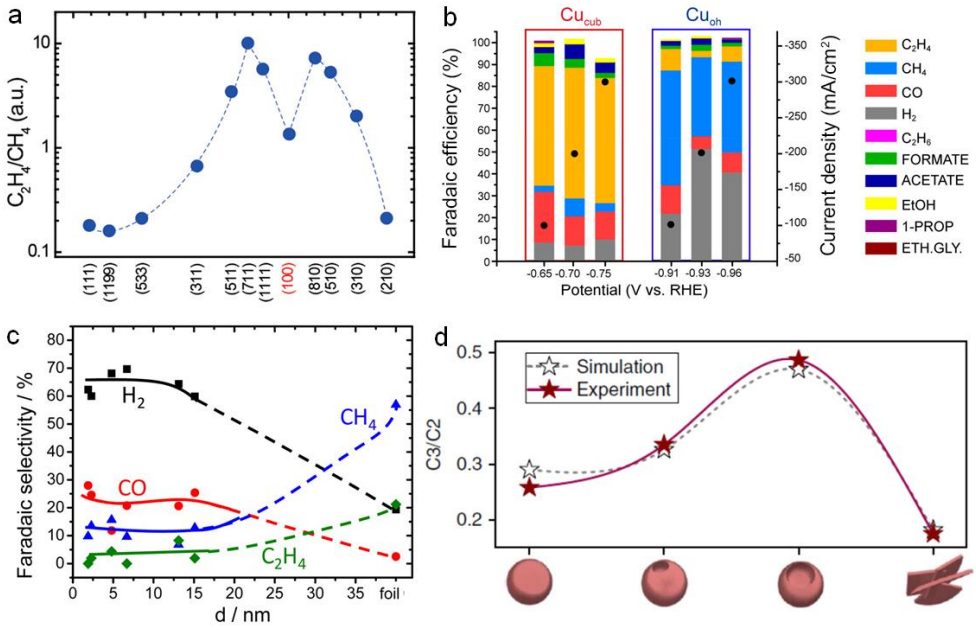

Figure 1.2. (a) Variation in the ratio of C_2H_4 to CH_4 in terms of current efficiency on different types of Cu surfaces. (b) Faradaic efficiencies (FEs) of Cu cube (250 μg/cm^2) and octahedra (50 μg/cm^2) measured in the gas-fed flow cell in 1 M KOH. Black dots represent the geometric current density in each case. (c) Faradaic selectivity of reaction products during CO_2RR on Cu nanoparticles with different sizes. The measurements were conducted in a 0.1 M $KHCO_3$ solution at -1.1 V_{RHE}. (d) The experimental and finite-element method (FEM) simulation results of the C_3/C_2 product selectivity on Cu catalysts with a morphology of solid, cavity (with two different opening levels), and fragment. (a−c) Modified with permission from ref [13], [19], and [24]. Copyright 2019, 2020, and 2014 American Chemical Society, respectively. (d) Reprinted with permission from ref [27]. Copyright 2018 Nature Publishing Group.

Planar defects, including twin boundaries and stacking faults, can also enhance the selectivity toward C_{2+} products by affecting the adsorption of CO intermediate. As reported for Cu star decahedra, the presence of twin boundaries and tensile strain, together with the stacking faults induced by a stress release mechanism, led to an upshift

in the *d*-band center of the surface atoms and thus an increase in the binding energy between the catalyst and CO molecules [26]. The higher coverage density of CO on the Cu surface greatly promoted C-C coupling and improved the selectivity toward C_{2+} products. Similar mechanism also applies to high-index facets, which are generated by introducing a certain number of steps into the surface of a nanocrystal and are rich of under-coordinated sites with a relatively strong adsorption of CO molecules [18,28]. In addition to defects, the introduction of cavities was demonstrated to further enhance the reduction of CO to C_3 products. Compared to both solid and fragmented structures, the cavity on Cu nanoparticles could help restrict the outflow of C_2 species, leading to a locally high concentration of C_2 intermediates and thus a heightened C_3 production rate (Figure 1.2d).

Different from the intrinsic twin defects that could be maintained after long-term electrolysis [26], the steps and kinks on the Cu surface could hardly be stabilized and their contribution to the enhancement of C_{2+} production was questionable. For example, a decrease in the FE of ethylene from 57% to below 40% was observed for Cu dendrites after 150 min of electrolysis, and this was mainly assigned to the structural degradation [29]. After long-term electrolysis, the needle shape of the dendrites was hardly retained and the high-index facets containing low-coordinated sites were also lost, leading to a decrease in the production of C_{2+} species. More attention and efforts are still needed for the stabilization of Cu nanocrystals enclosed by active high-index facets [29−32].

Apart from surface reconstruction, it is also challenging to prevent the fragmentation and sintering of Cu nanocrystals. As revealed in a recent report, when Cu cubes of different sizes were used as catalysts, Cu clusters were observed around the

catalysts, together with the sintering of the cubes [33]. Based on DFT calculations, {111}, {110}, and high-index facets were more effective in stabilizing H and CO intermediates under negative potentials. To this end, pinholes were generated on the surface of cubes, and clusters appeared around the cubes. Interestingly, when lower overpotentials (*e.g.*, -0.7 and -0.3 V_{RHE}) were applied, the cubic shape was essentially preserved and no aggregation of the nanocrystals was observed either, indicating the importance of decreasing the overpotential of CO_2RR for Cu-based catalysts [33]. Besides lowering the overpotential, other methods such as covering the nanocrystals with graphene or surface oxides [34] and *in situ* generation of nanocrystals with well-defined facets [35] are also promising in improving the stability of Cu nanocrystals.

Aside from pure Cu, a second metal can also be introduced to tailor both activity and selectivity of the catalyst. The modification of the interatomic distance of surface atoms and the variation in surface strain may shift the center of the *d*-band, altering the binding strength of the intermediates [39]. Tandem catalysis may also be realized in Cu-based bimetallic catalysts, with a CO-producing metal such as Au or Ag being favorable [40]. It is expected that the excess amount of CO generated on the second metal would migrate to the Cu site, increasing the CO coverage density on Cu surface and facilitating the C-C coupling. In this case, the geometric distribution of elements plays a significant role. Compared with alloy and intermetallic CuPd catalysts, the phase-separated Cu-Pd particles exhibited the highest selectivity toward C_{2+} products due to the presence of neighboring Cu atoms, which had the favorable molecular distance and small steric hindrance for the dimerization of CO intermediates (Figure 1.3a) [36].

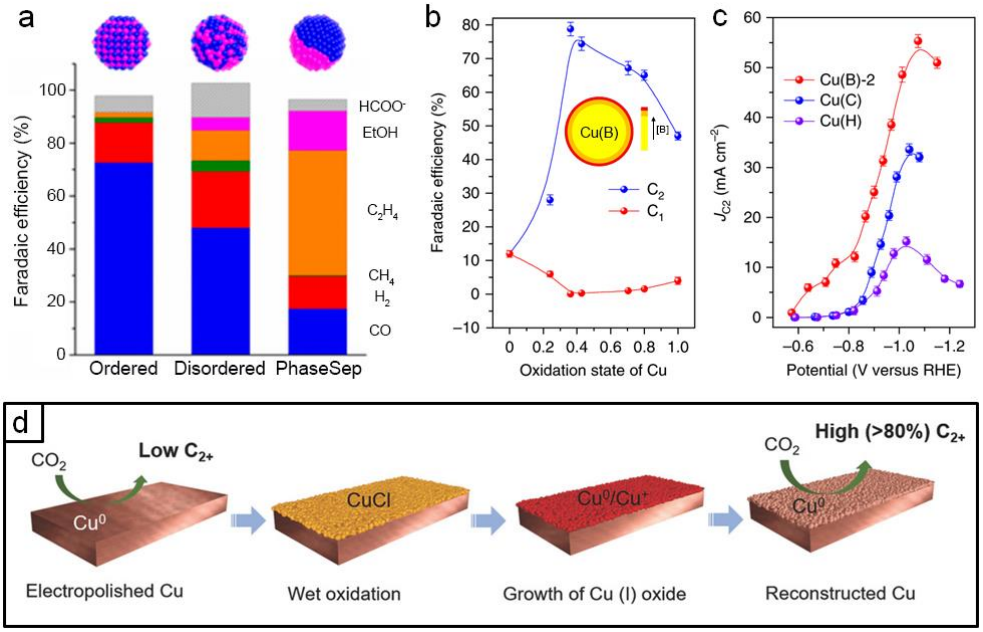

Figure 1.3. (a) FE of bimetallic CuPd catalysts with different mixing patterns: ordered (intermetallic), disordered (alloy), and phase-separated. (b) FE of Cu(B) catalysts in different Cu oxidation states. All samples were tested at -1.1 V_{RHE} in 0.1 M $KHCO_3$. (c) Partial current density toward C_{2+} products at different potentials on Cu(B)-2, oxidized Cu (Cu(C)), and pristine Cu (Cu(H)). (d) Schematic illustration of the surface reconstruction process by oxidation and subsequent reduction of Cu. (a) Reprinted with permission from ref [36]. Copyright 2017 American Chemical Society. (b) Modified with permission from ref [37]. Copyright 2018 Nature Publishing Group. (c) Reprinted with permission from ref [38]. Copyright 2018 Wiley-VCH.

The doping of non-metal elements, usually with a higher electronegativity than Cu such as B, N, and S, can also help augment the C_{2+} yield by tuning the electronic structure and oxidation state of surface Cu [37,41–43]. Additionally, the existence of these elements enables the prolonged presence of Cu(I) over time, allowing for the stable C_{2+} production with negligible decay during CO_2RR. In one example, by doping with varying amounts of B, the oxidation state of Cu could be tuned from 0 to +1, with the one at +0.35 (labeled as Cu(B)-2) showing the highest C_{2+} selectivity approaching 80%, together with a large current density (55 mA cm^{-2}) toward C_2 products (Figure 1.3, b and

c) [37].

Recently, Cu catalysts derived from copper oxides have attracted extensive attention and debates in their ability to boost C_{2+} selectivity. Due to the smaller lattice constant of Cu than its oxides, when applied with negative potentials, the reduction of copper oxides will cause size shrinkage and thus the formation of a rougher surface containing more high-index facets, defects, and grain boundaries (Figure 1.3d) [38]. These features, as well as the potential elevation in the oxidation state of Cu, all contribute to a lower onset potential and higher selectivity toward C_{2+} products. As an example, the reduction and subsequent fragmentation of Cu_2O nanoparticles during CO_2RR led to the formation of a large density of grain boundaries, resulting in a high ethylene selectivity approaching 60% at -1.1 V_{RHE} in 0.1 M aqueous $KHCO_3$ [44].

It should be emphasized that the potential presence of residue oxygen during electrolysis is still under debate. Intuitively, one would expect the copper oxides to be all reduced to Cu(0) under a potential as negative as -1.0 V_{RHE}. Such an idea has also been verified by various *in situ* techniques [44–47]. However, it was challenged in recent years and several reports demonstrated the presence of remaining oxygen species based on both *ex situ* and *in situ* methods [48–52]. Noted that the *ex situ* experiments were all conducted under the protection of Ar or in the vacuum, with an effort to prevent Cu from being oxidized during transfer process. In the meantime, it was also reported that the Cu nanocrystals would be easily re-oxidized to Cu_2O at open circuit voltage even in the electrolyte without exposing to air, making the origin of the as-detected residue oxygen more elusive [44,45]. More reliable *in situ* characterizations are still needed to further prove the presence/absence of remaining oxygen. With regard to the oxygen, there are

also debates on its contribution to the augment of C_{2+} selectivity. It is typically argued that subsurface oxygen can enhance the CO binding strength by withdrawing electron density from surface Cu atoms [53]. However, comparing the oxide- and non-oxide-derived three-dimensional (3-D) Cu electrodes, a similar product distribution was observed, indicating that the surface reconstruction might play a more important role than the oxidation state in determining the CO_2RR performance [13,51].

To conclude, Cu and Cu-based catalysts have shown great promise in CO_2RR and their remarkable performance is highly dependent on the facets, sizes, structures, and compositions, emphasizing the critical importance of rational design and shape-controlled synthesis of Cu nanocrystals.

1.3 Shape-controlled Synthesis of Cu Nanocrystals: Challenges and Opportunities

1.3.1 Colloidal Synthesis of Metal Nanocrystals

In a typical colloidal synthesis of metal nanocrystals, a precursor compound is either decomposed or reduced to generate zero-valent atoms—the basic building blocks of the nanostructures. The atoms then undergo homogeneous nucleation (or self-nucleation) to generate nuclei, followed by growth to evolve into seeds and then nanocrystals. This process is expected to follow the LaMer model established in the 1950s to account for the chemical synthesis of sulfur hydrosols (Figure 1.4a) [54]. During this process, the type of seeds will determine the twin structure of the nanocrystal, and the initial reduction rate of the precursor can serve as a quantitative knob for manipulating the twin structure of the seed. Using Pd as an example, it was established that the twin structure changed from stacking-fault-lined to multiply-twinned and then

single-crystal as the initial reduction rate was increased from 10^{-8} to 10^{-6} and then 10^{-4} M s^{-1} [55]. Though more efforts are required to explore the generality of this correlation, it offers a quantitative relationship between the initial reduction rate and the twin structure of the seeds, as well as an effective approach to controlling the twin structure and thus the shape taken by the metal nanocrystal.

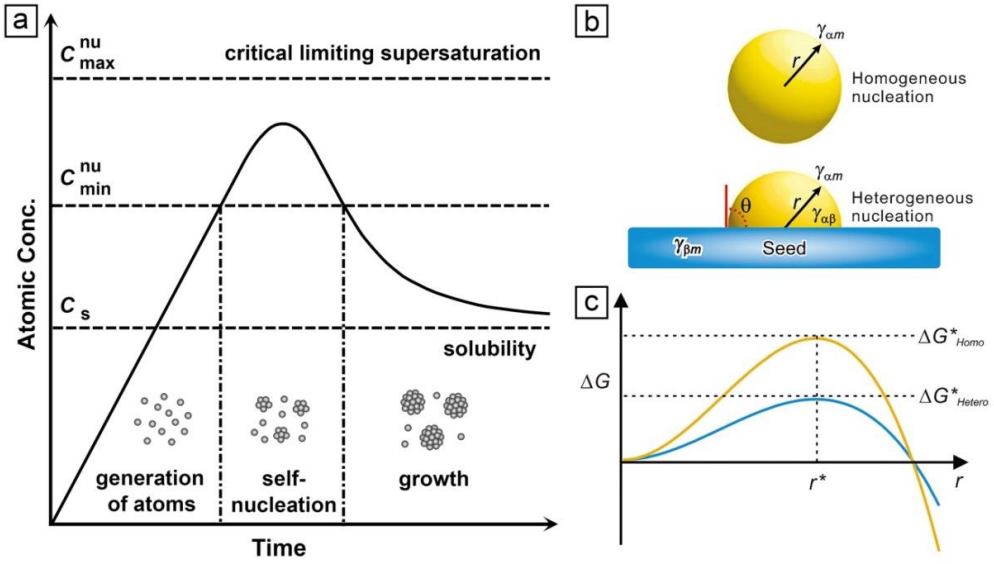

Figure 1.4. (a) Plot of the concentration of atoms as a function of time, illustrating the processes of atom generation, self-nucleation, and growth. (b) Illustration of two different nucleation modes: (top) homogeneous nucleation in the reaction solution and (bottom) heterogeneous nucleation on the surface of a seed. (c) Plot showing the change in Gibbs free energy as a function of particle size for homogeneous (yellow line) and heterogeneous nucleation (blue line). (a) Modified with permission from ref [54]. Copyright 1950 American Chemical Society. (b, c) Reprinted with permission from ref [56]. Copyright 2017 Wiley-VCH.

Preformed seeds with well-defined structures and facets can also be introduced into a synthesis to serve as primary sites for nucleation and growth (Figure 1.4b) [56]. In this case, the newly formed atoms can nucleate on the surface of the introduced seeds at a

concentration well below the minimum level of supersaturation in a process referred to as heterogeneous nucleation. If the incoming atoms and those on the seeds have the same chemical identity, the newly formed atoms will be deposited on the seeds through an epitaxial process and take a crystal structure identical to that of the seed. When two metals with a large lattice mismatch are involved, island growth mode will be preferred, usually resulting in the generation of planar defects. Relative to homogeneous nucleation, a much smaller driving force (*i.e.*, with the requirement of a lower concentration of atoms or a lower reaction temperature) is needed for heterogeneous nucleation (Figure 1.4c), making seed-mediated growth favorable and easier to occur in most cases.

The formation of nanocrystals with well-defined shapes is mainly controlled by both thermodynamics and kinetics [57]. Processes such as oxidative etching and galvanic replacement may also be used to alter the shape, twin structure, and composition of final products [57,58]. The thermodynamically-controlled product exhibits a global minimum in total free energy, at which point the sum of the surface and volume free energies, as well as internal defect, and strain energies, are collectively minimized. When surrounded by vacuum, the equilibrium shape of a nanocrystal can be derived from the Wulff construction, where the specific energy of a given facet should be in direct proportion to the distance from the center to the facet [59,60]. One way to obtain nanocrystals with shapes different from the Wulff polyhedron is the introduction of a capping agent [61]. Capping agents are ionic species, small molecules, or macromolecules that can selectively bind to different types of facets on a nanostructure to alter the surface free energies and therefore their proportions in the final product. The facets preferentially stabilized by the capping agent will exhibit a lower surface free energy, leading to the

formation of nanocrystals with a shape that maximizes the surface area of the capped facet. From a kinetic perspective, the capping agent chemisorbed on a facet will serve as a physical barrier to hinder or even prohibit the deposition of atoms on this facet, eventually leading to the formation of a shape with that particular facet preferentially exposed.

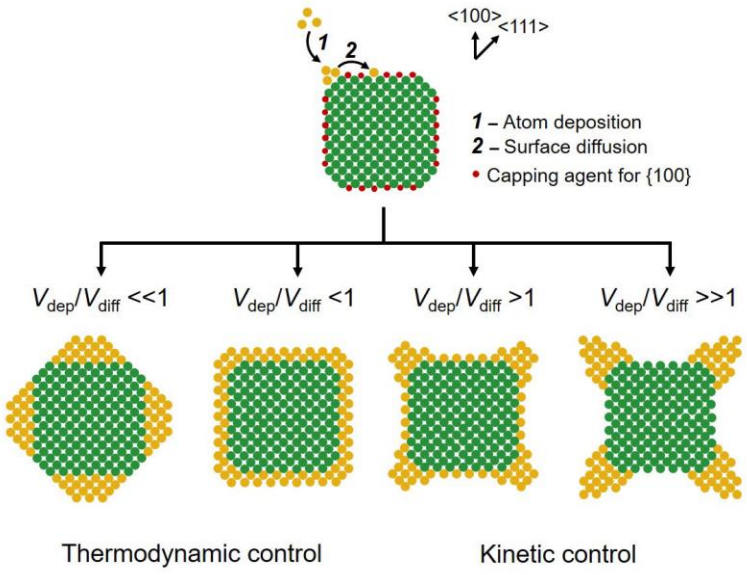

Figure 1.5. Schematic illustration showing the shape evolution of a cubic seed under different experimental conditions. Reprinted with permission from ref [62]. Copyright 2020 American Chemical Society.

Although thermodynamics provides useful information with regard to the most favored structure, in most cases, the nanocrystals would rather settle into locally-stable positions, a propensity determined by the interplay of thermodynamics and kinetics [57]. To this end, the exact shape or morphology taken by the nanocrystal will be largely determined by the relative ratio of the rates corresponding to atom deposition (V_{dep}) and

surface diffusion (V_{diff}) (Figure 1.5) [63]. When a greater V_{diff} relative to V_{dep} is involved, the newly formed atoms tend to hit then diffuse across the surface of a seed, giving rise to the formation of nanocrystals featuring the Wulff shape. In contrast, as the ratio of V_{diff} and V_{dep} is decreased, the atoms under kinetic control suggest a site-selected growth, producing nanocrystals with an increased concavity such as concave cubes and octapods. Both rates can be manipulated by changing the experimental conditions, including variations of reagent concentration and reaction temperature, the choice of reductant or precursor, the introduction of capping agents, and the type of coordination ligand for the metal ion.

1.3.2 Shape-controlled Synthesis of Cu Nanocrystals

Due to the low standard reduction potential of Cu (0.34 and 0. 52 V_{SHE} for Cu^{2+}/Cu and Cu^{+}/Cu pairs) and its vulnerability to oxidation, it is of great difficulty to synthesize Cu nanocrystals, let alone controlling their shapes. Typically, the syntheses of Cu nanocrystals are mostly conducted in an O_2-free environment, and the addition of proper capping agents is of great significance in controlling their shapes. Among all the reports on the shape-controlled synthesis of Cu nanocrystals, nanowires make up the majority of them. Others include cube, octahedron, bipyramid, rod, plate, sheet, and some novel shapes such as nanostars and tadpole-like nanowires [62]. Some typical examples are shown in Figure 1.6.

To generate Cu nanocrystals with a single-crystal structure, such as cube and octahedron, high temperature and Cu(I) precursor are usually used in order to achieve a fast reduction rate [25,64–68]. For example, by heating CuCl in oleylamine (OAm) at a temperature above 300 ^{o}C, together with the presence of trioctylphosphine (TOP) and

octadecylamine (ODA) or trioctylphosphine oxide (TOPO), Cu nanocubes or octahedra were obtained in high purity (Figure 1.6, a and b) [64,66]. In addition to high temperature, Cu nanocubes can also be produced under the mediation of oxidative etching, with a typical example involving the reduction of $CuCl_2$ with glucose in the presence of hexadecylamine (HDA) at a temperature as low as 100 °C [69]. When oxygen was present, twinned seeds with high surface energy were removed, leaving behind single-crystal seeds that further grew into nanocubes. A modified protocol was reported afterwards by adding Pd cubic seeds into the reaction solution. Pd@Cu core-shell nanocubes with uniform shape and tunable sizes were obtained and the experiments could be easily reproduced [70].

Regarding Cu bipyramids bearing one or multiple planar defects, there are very few reports on them although they were often observed as byproducts in the synthesis of other types of Cu nanocrystals [72,73]. The challenge of producing high-purity Cu bipyramids mainly lies in the susceptibility of twinned seeds to oxidative etching, and the difficulty in controlling the reduction rate of the precursor. To overcome this problem, a trace amount of Pd was introduced to generate seeds lined with multiple planar defects, intended for the subsequent deposition of Cu and their growth into a right bipyramidal shape [74]. More details will be discussed in Chapter 2. Multiply-twinned Cu nanocrystals can be produced without the assistance of other metal precursors. In one example, Cu decahedra with a star-like shape were synthesized by reducing $Cu(acac)_2$ with ascorbic acid in the presence of OAm (Figure 1.6, e and f) [26]. To arrest the twinned structure, a slow growth rate was achieved by leveraging a weak reducing agent and a relatively low reaction temperature (130 ^{o}C).

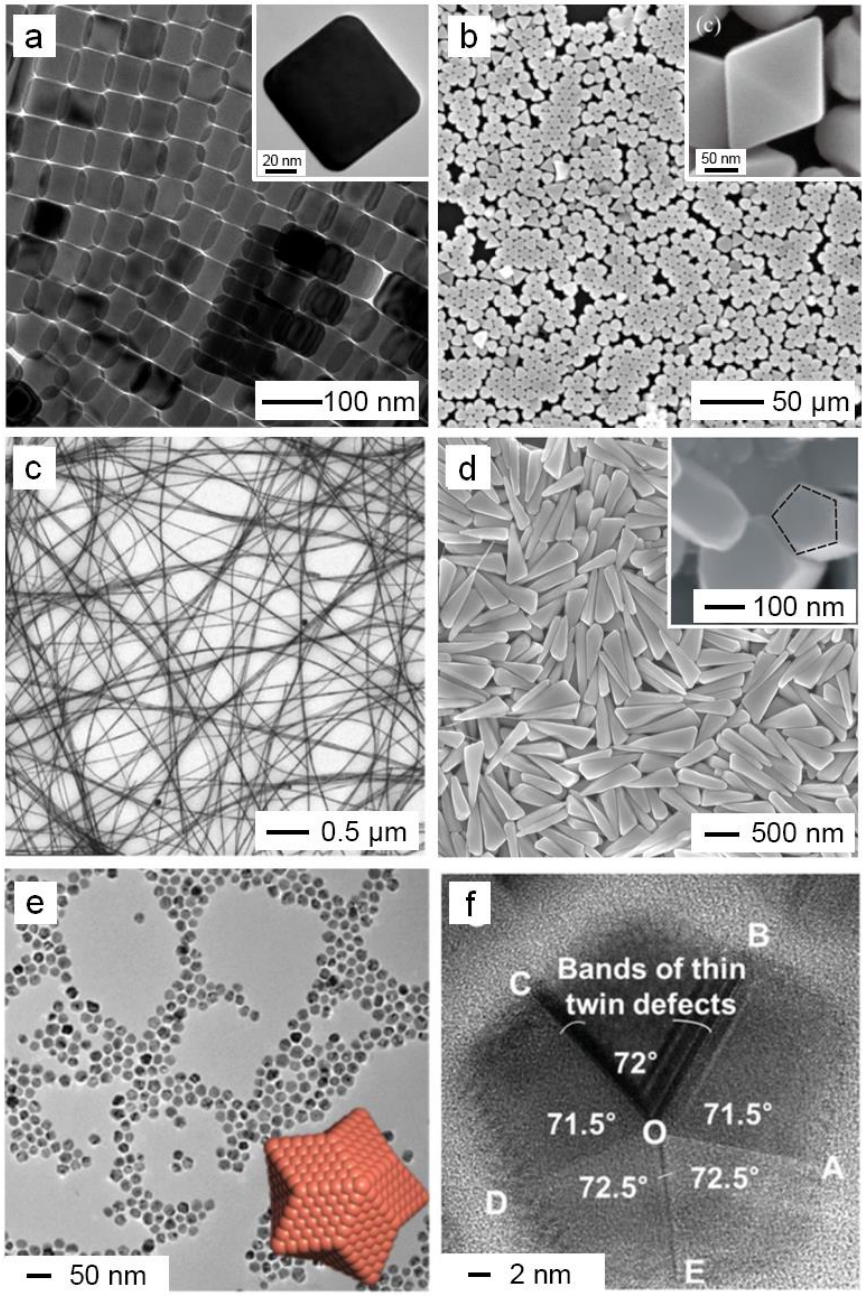

Figure 1.6. (a) TEM image of Cu nanocubes with the inset showing an enlarged view of a single cube. (b) Scanning electron microscope (SEM) image of Cu octahedra with the inset showing an enlarged view of a single octahedron. (c) TEM image of CuNWs. (d) SEM image of tadpole-like Cu nanocrystals with inset showing their pentagonal cross section. (e) TEM image and atomic model of Cu star decahedra. (f) High-resolution TEM (HRTEM) image showing the five-fold symmetry and twinned structure of the Cu star decahedron. (a, b) Reprinted with permission from ref [64] and [66]. Copyright 2014 and 2015 American Chemical Society. (c–f) Reprinted with permission from ref [71], [69], and [26]. Copyright 2017, 2011, and 2018 Wiley-VCH.

Penta-twinned nanowire is one of the most commonly observed morphologies among Cu nanocrystals, not only as the targeted product but also as impurities in most syntheses. In general, a relatively low reduction rate of the Cu(II) precursor and the introduction of capping agent(s) capable of blocking {100} facets are required for the synthesis of CuNWs. By using HDA as a capping agent and glucose as a reducing agent, CuNWs with high purity and an average diameter down to 15 nm could be produced (Figure 1.6c) [66]. Removal of O_2 was regarded as an important factor in producing the ultrathin nanowires as it protected the formation of a large number of penta-twinned seeds in the initial stage and prevented the ends of nanowires from being oxidized and blocked by oxygen. When the temperature was reduced while the concentration of glucose was doubled, tadpole-like CuNWs with a penta-twinned structure were obtained, whose generation could be contributed to the decrease in reduction rate for the Cu(II) precursor in the initial and later stages (Figure 1.6d) [67].

The presence of HDA played an important role in the evolution of CuNWs, which used to be regarded as a capping agent for Cu{100} facets. However, this assumption was challenged in recent years. Single-crystal electrochemical measurements, together with DFT calculations, revealed that the preferential disruption of HDA layer on {111} facets by Cl^- ions was the major reason responsible for the selective passivation of {100} facets [75]. More experimental evidence is still required to further prove the roles played by HDA and halide ions in the synthesis of Cu nanocrystals enclosed by {100} facets.

Seed-mediated growth was also explored for the synthesis of CuNWs with ethylenediamine (EDA) serving as a "capping agent" [76–78]. Large polycrystalline Cu nanoparticles were generated first, from which nanowires were grown. Instead of

selectively capping Cu {100} facets, EDA promoted the growth of wires by keeping Cu{111} facets free from oxidation. With {100} facets covered by oxides, the newly formed Cu atoms would prefer to deposit onto {111} facets at two ends, enabling the elongation of nanowires. CuNWs could also be synthesized at high temperatures using OAm as a solvent, which served as a coordination ligand for Cu(I) or Cu(II) ions and a capping agent for Cu{100} facets at the same time [79,80]. Uniquely, benzoin, which is commonly used as a photoinitiator in polymerization, can also be used as a reductant in the synthesis of CuNWs [81]. Under inert atmosphere and heating, benzoin decomposed into radicals that could donate electrons to Cu(II) ions. The reactivity of the radicals could be further tuned through the modification of the aromatic rings with electron donating/withdrawing groups.

Characterized by the presence of parallel stacking faults, Cu nanoplates are typically synthesized at a slow reduction rate for the Cu(II) precursor achieved through the addition of I_2 [82] or the leverage of a low reaction temperature [83]. Other methods such as the use of a $Cu(AOT)_2$/NaAOT/water/isooctane reverse micellar system [84] or poly(vinyl pyrrolidone) (PVP) as a Cu {111} capping agent [85] were also reported.

1.4 Scope of This Work

The aim of this dissertation is to introduce various strategies for synthesizing Cu-based nanocrystals with well-defined shapes, together with a systematic evaluation of their performance in electrochemical CO_2RR. By utilizing seeds with different structures, Cu nanocrystals with unconventional shapes and tunable sizes can be produced. I then characterize their structures and analyze their optical properties, in addition to elucidation of the reaction mechanisms. I further look into the roles played by surface structure and

composition in determining the catalytic performance of Cu nanocrystals in CO_2RR, and how these factors can be manipulated to improve the catalyst's activity, selectivity, and stability toward C_{2+} products.

In CHAPTER 2, I demonstrate a rationally designed route to the facile synthesis of Cu right bipyramids (RBPs) with tunable sizes in the presence of a trace amount of Pd. According to the standard reduction potential (0.91 and 0.34 V_{SHE} for Pd^{2+}/Pd and Cu^{2+}/Cu pairs, respectively), Pd(II) precursor would be reduced first, generating seeds for the subsequent deposition of Cu atoms. The amount of Pd in the final product was so low that it has no effect on the surface and bulk properties, thus the nanocrystals could be considered as nearly monometallic Cu RBPs. Owing to coordination with HDA, the reduction kinetics of Pd(II) and Cu(II) precursors were greatly slowed down, leading to the formation of twinned seeds and surface reduction, respectively. From HRTEM, multiple planar defects were observed in a single RBP, illustrating the unique structure of the product different from traditional, singly-twinned RBPs. Due to their anisotropic shape, two localized surface plasmon resonance (LSPR) peaks were observed for Cu RBPs, and the peak positions were red-shifted as the edge length was increased.

In CHAPTER 3, I develop a seed-mediated approach to the synthesis of Au@Cu core-shell nanocubes with small sizes and high uniformity. The use of 5-nm Au spheres as seeds was critical to the production of Cu nanocubes with edge length as short as 20–30 nm. The large lattice mismatch (12%) between Cu and Au led to the island growth of Cu on the Au spheres, resulting in the random distribution of Au core in the Cu cube. The lower energy barrier of heterogeneous nucleation contributed to an accelerated reduction of Cu(II) ions in the presence of Au seeds relative to the case of no seeds, suggesting an

effective and simpler way of synthesizing Cu nanocrystals with well-controlled shapes. The as-synthesized core-shell nanocubes exhibited a strong LSPR peak in the visible region, and the resonance was found to be independent of the Au core position.

In CHAPTER 4, I apply the concept of site-selected growth to the synthesis of Pd-Cu Janus nanocrystals with different shapes and twinned structures. By leveraging Pd icosahedra as seeds, Cu atoms could be initially deposited onto either a vertex or an edge of the seed, leading to the formation of penta-twinned or singly-twinned structures with a shape of pentagonal bipyramid, decahedron, or truncated bitetrahedron. The growth was mainly controlled by the reduction rate of the Cu(II) precursor, with slow reduction preferring the nucleation from vertex while fast reduction preferring the edge. The introduction of Pd as a CO generator, the phase segregation of Pd and Cu, and the presence of twin boundaries on Cu surface all make the Pd-Cu Janus nanocrystals effective catalysts toward electrochemical CO_2RR. DFT calculations and Pourbaix phase diagram were also performed to unveil the reaction mechanism underlying the high C_{2+} selectivity of the Pd-Cu catalysts.

In CHAPTER 5, I demonstrate that the introduction of surface oxides and control of the oxidation process are of great importance in improving both C_{2+} selectivity and stability of Cu nanocrystals in CO_2RR. CuNWs oxidized by the O_2 from air and aqueous H_2O_2 were evaluated, and both of them showed high FEs toward ethylene and suppressed hydrogen production. The increased surface roughness after reduction of the oxides, the one-dimensional (1-D) morphology, and the penta-twinned structure intrinsic to the nanowires synergistically contributed to the high yields of C_{2+} species. A comparison of the two types of CuNWs also indicated that a relatively thick and uniform oxide sheath

could help improve the stability of the nanowires by mitigating their fragmentation during electrolysis.

1.5 Notes to Chapter 1

Part of this Chapter is adapted from the review articles "One-Dimensional Metal Nanostructures: From Colloidal Syntheses to Applications" and "Noble-Metal Nanocrystals with Controlled Shapes for Catalytic and Electrocatalytic Applications" co-authored by me and published in *Chemical Reviews* [62,86].

1.6 References

[1] https://en.wikipedia.org/wiki/Copper

[2] https://markets.businessinsider.com/commodities/realtime-list

[3] https://www.usgs.gov/centers/nmic/copper-statistics-and-information

[4] Bard, A. J.; Parsons, R.; Jordan, J. *Standard Potentials in Aqueous Solution*, Marcel Dekker, New York, **1985**.

[5] Davey, W. P. *Phys. Rev.* **1925**, *25*, 753–761.

[6] Kibey, S.; Liu, J. B.; Johnson, D. D.; Sehitoglu, H. *Acta Mater.* **2007**, *55*, 6843–6851.

[7] Yang, J. C.; Kolasa, B.; Gibson, J. M.; Yeadon, M. *Appl. Phys. Lett.* **1998**, *73*, 2841–2843.

[8] Gawande, M. B.; Goswami, A.; Felpin, F. X.; Asefa, T.; Huang, X.; Silva, R.; Zou, X.; Zboril, R.; Varma, R. S. *Chem. Rev.* **2016**, *116*, 3722–3811.

[9] Kim, J. H.; Chung, Y. K. *Chem. Commun.* **2013**, *49*, 11101–11103.

[10] Ran, J.; Zhang, J.; Yu, J.; Jaroniec, M.; Qiao, S. Z. *Chem. Soc. Rev.* **2014**, *43*, 7787–7812.

[11] Tian, H.; Zhang, X. L.; Scott, J.; Ng, C.; Amal, R. *J. Mater. Chem. A* **2014**, *2*, 6432–6438.

[12] Zhang, Z.; Wang, S. S.; Song, R.; Cao, T.; Luo, L.; Chen, X.; Gao, Y.; Lu, J.; Li, W. X.; Huang, W. *Nat. Commun.* **2017**, *8*, 488.

[13] Nitopi, S.; Bertheussen, E.; Scott, S. B.; Liu, X.; Engstfeld, A. K.; Horch, S.; Seger, B.; Stephens, I. E. L.; Chan, K.; Hahn, C.; Nørskov, J. K.; Jaramillo, T. F.; Chorkendorff, I. *Chem. Rev.* **2019**, *119*, 7610–7672.

[14] Gao, D.; Arán-Ais, R. M.; Jeon, H. S.; Roldan Cuenya, B. *Nat. Catal.* **2019**, *2*, 198–210.

[15] Arán-Ais, R. M.; Gao, D.; Roldan Cuenya, B. *Acc. Chem. Res.* **2018**, *51*, 2906–2917.

[16] Hori, Y.; Murata, A.; Takahashi, R. *J. Chem. Soc. Faraday Trans. 1 Phys. Chem. Condens. Phases* **1989**, *85*, 2309–2326.

[17] Bagger, A.; Ju, W.; Varela, A. S.; Strasser, P.; Rossmeisl, J. *ChemPhysChem* **2017**, *18*, 3266–3273.

[18] Hori, Y.; Takahashi, I.; Koga, O.; Hoshi, N. *J. Mol. Catal. A Chem.* **2003**, *199*, 39–47.

[19] De Gregorio, G. L.; Burdyny, T.; Loiudice, A.; Iyengar, P.; Smith, W. A.; Buonsanti, R. *ACS Catal.* **2020**, *10*, 4854–4862.

[20] Calle-Vallejo, F.; Koper, M. T. M. *Angew. Chem. Int. Ed.* **2013**, *52*, 7282–7285.

[21] Montoya, J. H.; Shi, C.; Chan, K.; Nørskov, J. K. *J. Phys. Chem. Lett.* **2015**, *6*, 2032–2037.

[22] Suen, N. T.; Kong, Z. R.; Hsu, C. S.; Chen, H. C.; Tung, C. W.; Lu, Y. R.; Dong, C. L.; Shen, C. C.; Chung, J. C.; Chen, H. M. *ACS Catal.* **2019**, *9*, 5217–5222.

[23] Luo, W.; Nie, X.; Janik, M. J.; Asthagiri, A. *ACS Catal.* **2016**, *6*, 219–229.

[24] Reske, R.; Mistry, H.; Behafarid, F.; Roldan Cuenya, B.; Strasser, P. *J. Am. Chem. Soc.* **2014**, *136*, 6978–6986.

[25] Loiudice, A.; Lobaccaro, P.; Kamali, E. A.; Thao, T.; Huang, B. H.; Ager, J. W.;

Buonsanti, R. *Angew. Chem. Int. Ed.* **2016**, *55*, 5789–5792.

[26] Choi, C.; Cheng, T.; Flores Espinosa, M.; Fei, H.; Duan, X.; Goddard, W. A.; Huang, Y. *Adv. Mater.* **2019**, *31*, 1–7.

[27] Zhuang, T. T.; Pang, Y.; Liang, Z. Q.; Wang, Z.; Li, Y.; Tan, C. S.; Li, J.; Dinh, C. T.; De Luna, P.; Hsieh, P. L.; Burdyny, T.; Li, H. H.; Liu, M.; Wang, Y.; Li, F.; Proppe, A.; Johnston, A.; Nam, D. H.; Wu, Z. Y.; Zheng, Y. R.; Ip, A. H.; Tan, H.; Chen, L. J.; Yu, S. H.; Kelley, S. O.; Sinton, D.; Sargent, E. H. *Nat. Catal.* **2018**, *1*, 946–951.

[28] Jeon, H. S.; Kunze, S.; Scholten, F.; Roldan Cuenya, B. *ACS Catal.* **2018**, *8*, 531–535.

[29] Reller, C.; Krause, R.; Volkova, E.; Schmid, B.; Neubauer, S.; Rucki, A.; Schuster, M.; Schmid, G. *Adv. Energy Mater.* **2017**, *7*, 1–8.

[30] Scholten, F.; Sinev, I.; Bernal, M.; Cuenya, B. R. *ACS Catal.* **2019**, 5496–5502.

[31] Cheng, T.; Xiao, H.; Goddard, W. A. *J. Am. Chem. Soc.* **2017**, *139*, 11642–11645.

[32] Jiang, K.; Huang, Y.; Zeng, G.; Toma, F. M.; Goddard, W. A.; Bell, A. T. *ACS Energy Lett.* **2020**, *5*, 1206–1214.

[33] Huang, J.; Hörmann, N.; Oveisi, E.; Loiudice, A.; De Gregorio, G. L.; Andreussi, O.; Marzari, N.; Buonsanti, R. *Nat. Commun.* **2018**, *9*, 1–9.

[34] Li, Y.; Cui, F.; Ross, M. B.; Kim, D.; Sun, Y.; Yang, P. *Nano Lett.* **2017**, *17*, 1312–1317.

[35] Kim, D.; Kley, C. S.; Li, Y.; Yang, P. *Proc. Natl. Acad. Sci. U. S. A.* **2017**, *114*, 10560–10565.

[36] Ma, S.; Sadakiyo, M.; Heim, M.; Luo, R.; Haasch, R. T.; Gold, J. I.; Yamauchi, M.; Kenis, P. J. A. *J. Am. Chem. Soc.* **2017**, *139*, 47–50.

[37] Zhou, Y.; Che, F.; Liu, M.; Zou, C.; Liang, Z.; De Luna, P.; Yuan, H.; Li, J.; Wang, Z.; Xie, H.; Li, H.; Chen, P.; Bladt, E.; Quintero-Bermudez, R.; Sham, T. K.; Bals, S.; Hofkens, J.; Sinton, D.; Chen, G.; Sargent, E. H. *Nat. Chem.* **2018**, *10*, 974–980.

[38] Kibria, M. G.; Dinh, C. T.; Seifitokaldani, A.; De Luna, P.; Burdyny, T.; Quintero-Bermudez, R.; Ross, M. B.; Bushuyev, O. S.; García de Arquer, F. P.; Yang, P.;

Sinton, D.; Sargent, E. H. *Adv. Mater.* **2018**, *30*, 1–7.

[39] Reske, R.; Duca, M.; Oezaslan, M.; Schouten, K. J. P.; Koper, M. T. M.; Strasser, P. *J. Phys. Chem. Lett.* **2013**, *4*, 2410–2413.

[40] Huang, J.; Mensi, M.; Oveisi, E.; Mantella, V.; Buonsanti, R. *J. Am. Chem. Soc.* **2019**, *141*, 2490–2499.

[41] Liang, Z. Q.; Zhuang, T. T.; Seifitokaldani, A.; Li, J.; Huang, C. W.; Tan, C. S.; Li, Y.; De Luna, P.; Dinh, C. T.; Hu, Y.; Xiao, Q.; Hsieh, P. L.; Wang, Y.; Li, F.; Quintero-Bermudez, R.; Zhou, Y.; Chen, P.; Pang, Y.; Lo, S. C.; Chen, L. J.; Tan, H.; Xu, Z.; Zhao, S.; Sinton, D.; Sargent, E. H. *Nat. Commun.* **2018**, *9*, 3828.

[42] Zhuang, T.; Liang, Z.; Seifitokaldani, A.; Li, Y.; Luna, P. De; Burdyny, T.; Che, F.; Meng, F.; Min, Y.; Quintero-bermudez, R.; Dinh, C. T.; Pang, Y.; Zhong, M.; Zhang, B.; Li, J.; Chen, P.; Zheng, X.; Liang, H.; Ge, W.; Ye, B.; Sinton, D.; Yu, S.; Sargent, E. H. *Nat. Catal.* **2018**, *1*, 421–428.

[43] Yin, Z.; Yu, C.; Zhao, Z.; Guo, X.; Shen, M.; Li, N.; Muzzio, M.; Li, J.; Liu, H.; Lin, H.; Yin, J.; Lu, G.; Su, D.; Sun, S. *Nano Lett.* **2019**, *19*, 8658–8663.

[44] Jung, H.; Lee, S. Y.; Lee, C. W.; Cho, M. K.; Won, D. H.; Kim, C.; Oh, H. S.; Min, B. K.; Hwang, Y. J. *J. Am. Chem. Soc.* **2019**, *141*, 4624–4633.

[45] Ren, D.; Deng, Y.; Handoko, A. D.; Chen, C. S.; Malkhandi, S.; Yeo, B. S. *ACS Catal.* **2015**, *5*, 2814–2821.

[46] Mandal, L.; Yang, K. R.; Motapothula, M. R.; Ren, D.; Lobaccaro, P.; Patra, A.; Sherburne, M.; Batista, V. S.; Yeo, B. S.; Ager, J. W.; Martin, J.; Venkatesan, T. *ACS Appl. Mater. Interfaces* **2018**, *10*, 8574–8584.

[47] Eilert, A.; Roberts, F. S.; Friebel, D.; Nilsson, A. *J. Phys. Chem. Lett.* **2016**, *7*, 1466–1470.

[48] Kim, J.; Choi, W.; Park, J. W.; Kim, C.; Kim, M.; Song, H. *J. Am. Chem. Soc.* **2019**, *141*, 6986–6994.

[49] Gao, D.; Zegkinoglou, I.; Divins, N. J.; Scholten, F.; Sinev, I.; Grosse, P.; Roldan Cuenya, B. *ACS Nano* **2017**, *11*, 4825–4831.

[50] Cavalca, F.; Ferragut, R.; Aghion, S.; Eilert, A.; Diaz-Morales, O.; Liu, C.; Koh, A. L.; Hansen, T. W.; Pettersson, L. G. M.; Nilsson, A. *J. Phys. Chem. C* **2017**, *121*, 25003–25009.

[51] Zhao, Y.; Chang, X.; Malkani, A. S.; Yang, X.; Thompson, L.; Jiao, F.; Xu, B. *J. Am. Chem. Soc.* **2020**, *142*, 9735–9743.

[52] Mistry, H.; Varela, A. S.; Bonifacio, C. S.; Zegkinoglou, I.; Sinev, I.; Choi, Y. W.; Kisslinger, K.; Stach, E. A.; Yang, J. C.; Strasser, P.; Cuenya, B. R. *Nat. Commun.* **2016**, *7*, 12123.

[53] Liu, C.; Lourenço, M. P.; Hedström, S.; Cavalca, F.; Diaz-Morales, O.; Duarte, H. A.; Nilsson, A.; Pettersson, L. G. M. *J. Phys. Chem. C* **2017**, *121*, 25010–25017.

[54] Lamer, V. K.; Dinegar, R. H. *J. Am. Chem. Soc.* **1950**, *72*, 4847–4854.

[55] Wang, Y.; Peng, H. C.; Liu, J.; Huang, C. Z.; Xia, Y. *Nano Lett.* **2015**, *15*, 1445–1450.

[56] Xia, Y.; Gilroy, K. D.; Peng, H. C.; Xia, X. *Angew. Chem. Int. Ed.* **2017**, *56*, 60–95.

[57] Xia, Y.; Xia, X.; Peng, H. C. *J. Am. Chem. Soc.* **2015**, *137*, 7947–7966.

[58] Xia, X.; Wang, Y.; Ruditskiy, A.; Xia, Y. *Adv. Mater.* **2013**, *25*, 6313–6333.

[59] Wulff, G. *Z Krist.* **1901**, *34*, 449–530.

[60] Barmparis, G. D.; Lodziana, Z.; Lopez, N.; Remediakis, I. N. *Beilstein J. Nanotechnol.* **2015**, *6*, 361–368.

[61] Yang, T. H.; Shi, Y.; Janssen, A.; Xia, Y. *Angew. Chem. Int. Ed.* **2019**, DOI 10.1002/anie.201911135.

[62] Shi, Y.; Lyu, Z.; Zhao, M.; Chen, R.; Nguyen, Q.; Xia, Y. *Chem. Rev.* **2020**, DOI 10.1021/acs.chemrev.0c00454.

[63] Xia, X.; Xie, S.; Liu, M.; Peng, H. C.; Lu, N.; Wang, J.; Kim, M. J.; Xia, Y. *Proc. Natl. Acad. Sci. U. S. A.* **2013**, *110*, 6669–6673.

[64] Yang, H. J.; He, S. Y.; Chen, H. L.; Tuan, H. Y. *Chem. Mater.* **2014**, *26*, 1785–1793.

[65] Guo, H.; Chen, Y.; Cortie, M. B.; Liu, X.; Xie, Q.; Wang, X.; Peng, D. L. *J. Phys. Chem. C* **2014**, *118*, 9801–9808.

[66] Lu, S. C.; Hsiao, M. C.; Yorulmaz, M.; Wang, L. Y.; Yang, P. Y.; Link, S.; Chang, W. S.; Tuan, H. Y. *Chem. Mater.* **2015**, *27*, 8187–8188.

[67] Suen, N. T.; Kong, Z. R.; Hsu, C. S.; Chen, H. C.; Tung, C. W.; Lu, Y. R.; Dong, C. L.; Shen, C. C.; Chung, J. C.; Chen, H. M. *ACS Catal.* **2019**, *9*, 5217–5222.

[68] Strach, M.; Mantella, V.; Pankhurst, J. R.; Iyengar, P.; Loiudice, A.; Das, S.; Corminboeuf, C.; Van Beek, W.; Buonsanti, R. *J. Am. Chem. Soc.* **2019**, *141*, 16312–16322.

[69] Jin, M.; He, G.; Zhang, H.; Zeng, J.; Xie, Z.; Xia, Y. *Angew. Chem. Int. Ed.* **2011**, *50*, 10560–10564.

[70] Jin, M.; Zhang, H.; Wang, J.; Zhong, X.; Lu, N.; Li, Z.; Xie, Z.; Kim, M. J.; Xia, Y. *ACS Nano* **2012**, *6*, 2566–2573.

[71] Luo, M.; Zhou, M.; Da Silva, R. R.; Tao, J.; Figueroa-Cosme, L.; Gilroy, K. D.; Peng, H. C.; He, Z.; Xia, Y. *ChemNanoMat* **2017**, *3*, 190–195.

[72] Thoka, S.; Madasu, M.; Hsia, C. F.; Liu, S. Y.; Huang, M. H. *Chem.: Asian J.* **2017**, *12*, 2318–2322.

[73] Lyu, Z.; Xie, M.; Aldama, E.; Zhao, M.; Qiu, J.; Zhou, S.; Xia, Y. *ACS Appl. Nano Mater.* **2019**, *2*, 1533–1540.

[74] Lyu, Z.; Xie, M.; Gilroy, K. D.; Hood, Z. D.; Zhao, M.; Zhou, S.; Liu, J.; Xia, Y. *Chem. Mater.* **2018**, *30*, 6469–6477.

[75] Kim, M. J.; Alvarez, S.; Chen, Z.; Fichthorn, K. A.; Wiley, B. J. *J. Am. Chem. Soc.* **2018**, *140*, 14740–14746.

[76] Rathmell, A. R.; Bergin, S. M.; Hua, Y. L.; Li, Z. Y.; Wiley, B. J. *Adv. Mater.* **2010**, *22*, 3558–3563.

[77] Ye, S.; Rathmell, A. R.; Stewart, I. E.; Ha, Y. C.; Wilson, A. R.; Chen, Z.; Wiley, B. J. *Chem. Commun.* **2014**, *50*, 2562–2564.

[78] Kim, M. J.; Flowers, P. F.; Stewart, I. E.; Ye, S.; Baek, S.; Kim, J. J.; Wiley, B. J. *J. Am. Chem. Soc.* **2017**, *139*, 277–284.

[79] Cui, F.; Yu, Y.; Dou, L.; Sun, J.; Yang, Q.; Schildknecht, C.; Schierle-Arndt, K.; Yang, P. *Nano Lett.* **2015**, *15*, 7610–7615.

[80] Ye, E.; Zhang, S. Y.; Liu, S.; Han, M. Y. *Chem. Eur. J.* **2011**, *17*, 3074–3077.

[81] Cui, F.; Dou, L.; Yang, Q.; Yu, Y.; Niu, Z.; Sun, Y.; Liu, H.; Dehestani, A.; Schierle-Arndt, K.; Yang, P. *J. Am. Chem. Soc.* **2017**, *139*, 3027–3032.

[82] Lee, J. W.; Han, J.; Lee, D. S.; Bae, S.; Lee, S. H.; Lee, S. K.; Moon, B. J.; Choi, C. J.; Wang, G.; Kim, T. W. *Small* **2018**, *14*, 1–7.

[83] Pastoriza-Santos, I.; Sánchez-Iglesias, A.; Rodríguez-González, B.; Liz-Marzán, L. M. *Small* **2009**, *5*, 440–443.

[84] Salzemann, C.; Urban, J.; Lisiecki, I.; Pileni, M. P. *Adv. Funct. Mater.* **2005**, *15*, 1277–1284.

[85] Sun, Y.; Xu, L.; Yin, Z.; Song, X. *J. Mater. Chem. A* **2013**, *1*, 12361–12370.

[86] Huo, D.; Kim, M. J.; Lyu, Z.; Shi, Y.; Wiley, B. J.; Xia, Y. *Chem. Rev.* **2019**, *119*, 8972–9073.

CHAPTER 2

A RATIONALLY DESIGNED ROUTE TO THE ONE-POT SYNTHESIS OF RIGHT BIPYRAMIDAL NANOCRYSTALS OF COPPER

2.1 Introduction

For noble-metal nanocrystals, the notion of shape control has received considerable attention due to the direct impact of this parameter on various properties of nanocrystals and thereby their performance in an array of applications ranging from catalysis [1] to electronics [2], photonics [3] and biomedicine [4]. Among the different shapes of nanocrystals, those lined with planar defects have emerged as a focus of recent inquiries, with notable examples including RBPs [5], decahedra [6], icosahedra [7], and thin prisms or plates [8,9]. In addition to their important role in controlling the shape evolution of nanocrystals by breaking the symmetry of crystal lattice, it has been established that the presence of planar defects often leads to nanocrystals with greatly enhanced catalytic activities due to the favorable strain field associated with a planar defect on the surface [10]. When compared with single-crystal counterparts enclosed by the same {111} facets, for example, PtNi alloy icosahedral nanocrystals showed a 50% increase in specific activity towards the oxygen reduction reaction (ORR) [11]. The same trend has also been reported for other systems, including Pt and Pd@Pt core-shell icosahedral nanocrystals in terms of ORR activity [7,12].

Nanoscale RBPs are of great interest for both fundamental studies and catalytic applications. As reported for Ag, Pd, and Pt [5,13–15], an RBP is covered by six right

isosceles triangular {100} facets and bisected by a planar defect perpendicular to the <111> direction. Compared to a cube with the same edge length (see Figure 2.1 for the definition), the surface-to-volume ratio of an RBP is 33% greater. The relatively high surface-to-volume ratio, together with the single type of facet and the defect zones on the surface, makes RBPs attractive for use as a catalytic material. In a prior study, the specific activity of Pd nanoscale RBPs towards the formic acid oxidation (FAO) reaction was found to be 50% greater than that of Pd cubes even though they are both enclosed by {100} facets [5]. Furthermore, the two oppositely-positioned, right-angle corners on an RBP are favorable for surface-enhanced Raman scattering (SERS) and related applications. Simulations suggested that the electric field enhancement can be greatly improved on RBPs, relative to spheres, owing to the presence of sharp corners [16].

Despite their interesting properties and intriguing applications, it remains a grand challenge to rationally produce RBPs in high yields. According to our recent work on Pd nanocrystals, the type and number of planar defects contained in seeds are closely related to the initial reduction rate of the metal precursor [17]. To produce the seeds lined with parallel planar defects for RBPs, the initial reduction rate has to be tuned down to a level below that for the formation of multiply-twinned seeds with a decahedral or icosahedral shape. On the other hand, compared with their single-crystal counterparts, metal nanocrystals with planar defects are prone to oxidative etching in the presence of oxygen, making it hard to generate RBPs, as well as other types of twinned nanocrystals, under ambient conditions [18]. The difficulty in achieving the optimal reduction kinetics and the vulnerability of planar defects towards oxidative etching greatly limit the development of synthetic protocols for RBPs. As a result, there are significantly more

reports on the synthesis of metal nanocrystals with a single-crystal structure (*e.g.*, cubes, cuboctahedra, and octahedra) when compared with those containing planar defects.

Copper nanocrystals have gained a lot of interest in recent years because of the high natural abundance (60 parts per million by weight in the earth's crust) and low cost ($0.18 per oz.) of this element, as well as their outstanding performance in applications related to catalysis [19,20], electronics [21], and plasmonics [22]. There are a number of reports on the solution-phase synthesis of Cu nanocrystals, including nanowires [23,24] and nanorods [25,26] with one-dimensional morphology, as well as those in the shapes of disk [27], sheet [28], prism [29], cube [30–32], and octahedron [33]. To our knowledge, however, there is still no report dedicated to the synthesis of Cu RBPs although this morphology was sometimes observed as the byproduct of a synthesis in a relatively low yield. If Cu RBPs can be prepared in high purity, together with controllable edge lengths (see Figure 2.1 for the definition) down to 20 nm, they will offer interesting system for the electrocatalytic reactions considering the presence of both {100} facets and planar defects on the surface [34].

Herein, I report a rationally designed, one-pot method for the facile synthesis of Cu RBPs under argon protection with the assistance of a trace amount of Pd(II) precursor. Since Pd RBPs have been produced with purity approaching 100%, I argue that Pd can potentially serve as a seeding material for the formation of Cu RBPs. I choose to pursue a one-pot protocol, rather than seed-mediated growth, in an effort to facilitate future scaling up for large-volume production. Considering the higher reduction potential of Pd(II)/Pd (0.91 V_{SHE}) relative to that of Cu(II)/Cu (0.34 V_{SHE}), it is anticipated that the Pd(II) precursor should be preferentially reduced in the initial stage of a synthesis for the

formation of Pd seeds containing planar defects, followed by the deposition of Cu atoms. At a relatively mild temperature of 100 °C, I am able to leverage the coordination effect of HDA to slow down the reduction kinetics of Pd(II) for the formation of parallel planar defects in the Pd seeds. Since only a trace amount of Pd(II) is introduced into the reaction solution, the effect of Pd on the composition and optical properties of the resultant RBPs can be largely neglected. By simply varying the concentration of Pd(II) relative to that of Cu(II), the edge length of the RBPs can be tuned in the range of 30–70 nm. When the reaction solution is saturated with air instead of argon, Cu nanoscale cubes will be generated due to the vulnerability of planar defect towards oxidative etching.

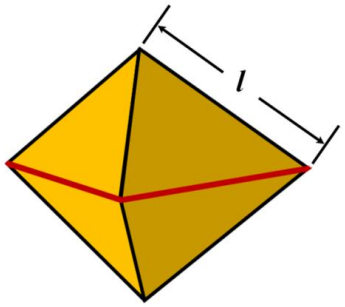

Figure 2.1. Definition of the edge length (*l*) of an RBP.

2.2 Results and Discussion

Synthesis of Cu RBPs. Figure 2.2a shows a typical TEM image of the as-prepared Cu RBPs with an average edge length of 56 ± 6 nm and purity over 80%. A close examination indicates three major projected profiles for the RBPs: irregular

tetragon, triangle, and rhombus [5]. Figure 2.2b shows TEM images and the corresponding models of individual RBPs in the three common orientations, which are correlated to those particles labeled in Figure 2.2a.

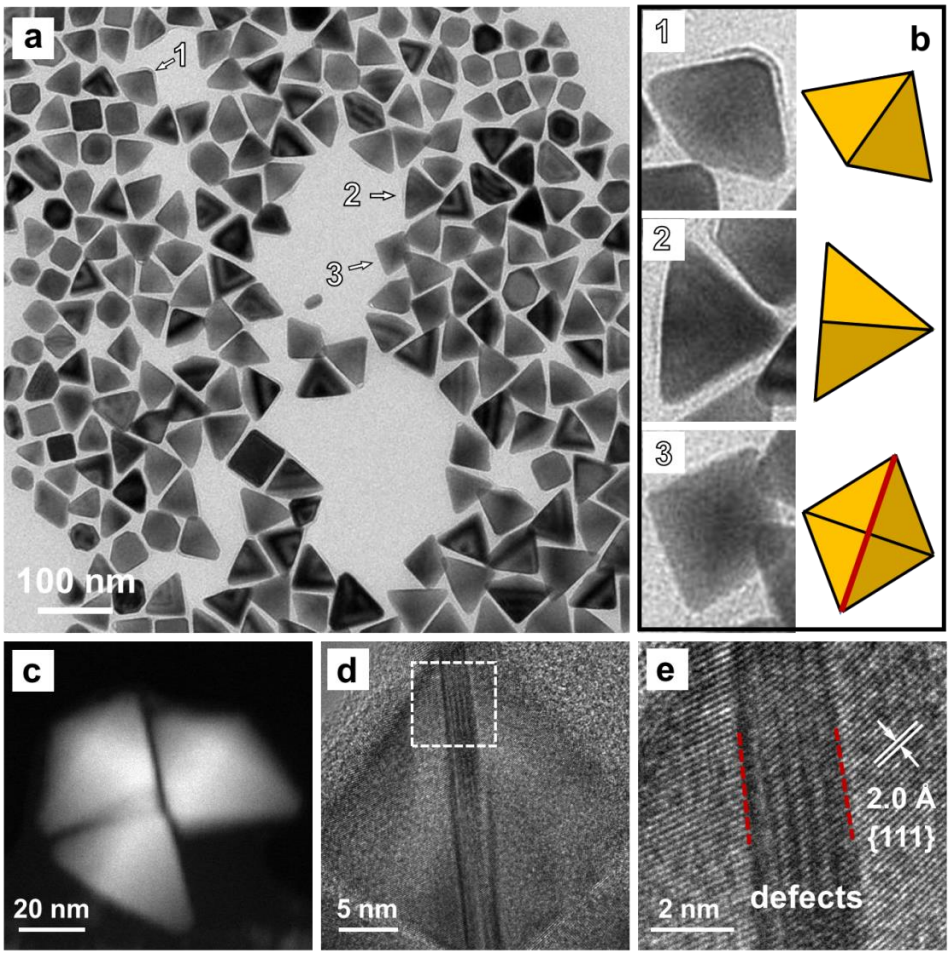

Figure 2.2. (a) TEM image of a typical sample of Cu RBPs prepared using the standard protocol. (b) TEM images and models of Cu RBPs in three common orientations that correspond to the RBPs marked with the same numbers in panel (a). The yellow color denotes the {100} facets on the nanocrystals, while the red lines represent the planar defects. (c) HAADF-STEM and (d) HRTEM images of an individual Cu RBP nanocrystal. (e) HRTEM image taken from the region marked by a box in (d).

Similar to what was observed in Pd and Ag RBPs, each Cu RBP has six right isosceles triangular (100) side faces and an equilateral, triangular base [5,14]. As demonstrated in Figure 2.2c, the RBPs can be easily and clearly resolved using high-angle annular dark-field scanning transmission electron microscopy (HAADF-STEM). As indicated by the high-resolution TEM images in Figure 2.2, d and e, the RBP is bisected by a set of parallel planar defects perpendicular to the <111> direction [14]. Figure 2.3 shows X-ray diffraction (XRD) pattern and X-ray photoelectron spectroscopy (XPS) data of the Cu RBPs. It should be mentioned that I only introduced a trace amount of Na_2PdCl_4 (1:200 relative to Cu) into the reaction solution so the proportion of Pd in the final products can be largely neglected. No peak for Pd was observed in the XRD pattern and XPS spectrum, in addition to the absence of Pd under energy dispersive X-ray (EDX) mapping, indicating that the nanocrystals were mainly composed of Cu and could be considered as Cu RBPs instead of Pd-Cu bimetallic structures.

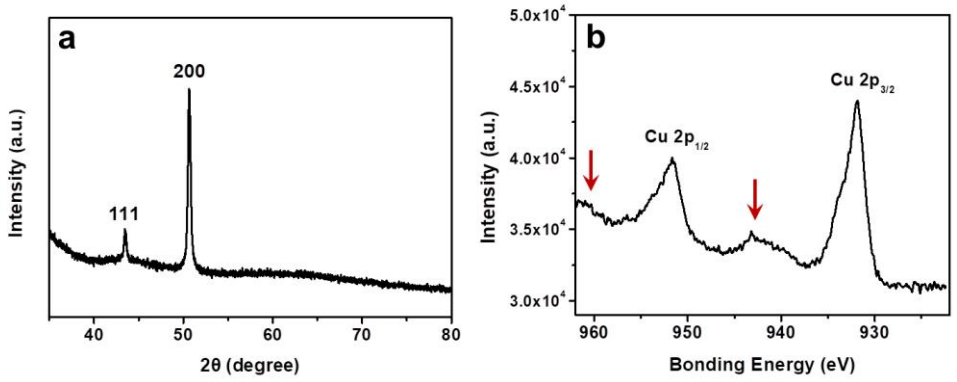

Figure 2.3. (a) Powder XRD pattern and (b) XPS spectrum of Cu RBPs prepared using the standard protocol. The weak satellite peaks at around 943 and 962 eV, which are marked by arrows, can be ascribed to the thin layers of CuO formed on the surface of the RBPs.

The weak satellite peaks marked by arrows in the XPS spectrum could be attributed to the thin layers of CuO typically formed on the surface of Cu nanocrystals [35]. The as-prepared Cu RBPs could be stored in ethanol for more than one week with little oxidation on the surface. However, if the samples were stored in water without removing the air, the particles would be oxidized quickly and voids were observed at corner sites even just after one day.

To gain a better understanding of the growth mechanism, a set of experiments were conducted using the standard protocol except for the variation in reaction time, and the products were analyzed using TEM. At the early stage of a synthesis (t=0.5 h, Figure 2.4a), small RBPs together with some cubic nanocrystals with edge lengths between 20 and 30 nm were observed. I was able to identify the defects in most of the RBPs in this stage, as illustrated in the inset at the upper-right corner. There are also a small portion of tiny spheres of about 8 nm in size, as marked by circles in Figure 2.4a. Energy-dispersive X-ray mapping indicates that these spheres are mainly composed of Cu, with essentially no signals for Pd. When the reaction was prolonged to t=1 h (Figure 2.4b), the spherical particles disappeared due to the involvement of Ostwald ripening, in which the particles smaller in size were dissolved and the Cu atoms were re-deposited onto the RBPs for their growth into larger sizes, together with sharpening of their corners. When the reaction time was prolonged to 3 and 6 h (Figure 2.4, c and d), respectively, the edge length was increased to roughly 45 and 56 nm. Further extension of reaction time did not result in any obvious changes to either size or shape. These results indicate that larger Cu RBPs were grown from smaller ones without altering the planar defect structure. As

shown in the sample in Figure 2.4d, RBPs of similar quality and sizes could be obtained when the standard protocol was repeated, demonstrating its good reproducibility.

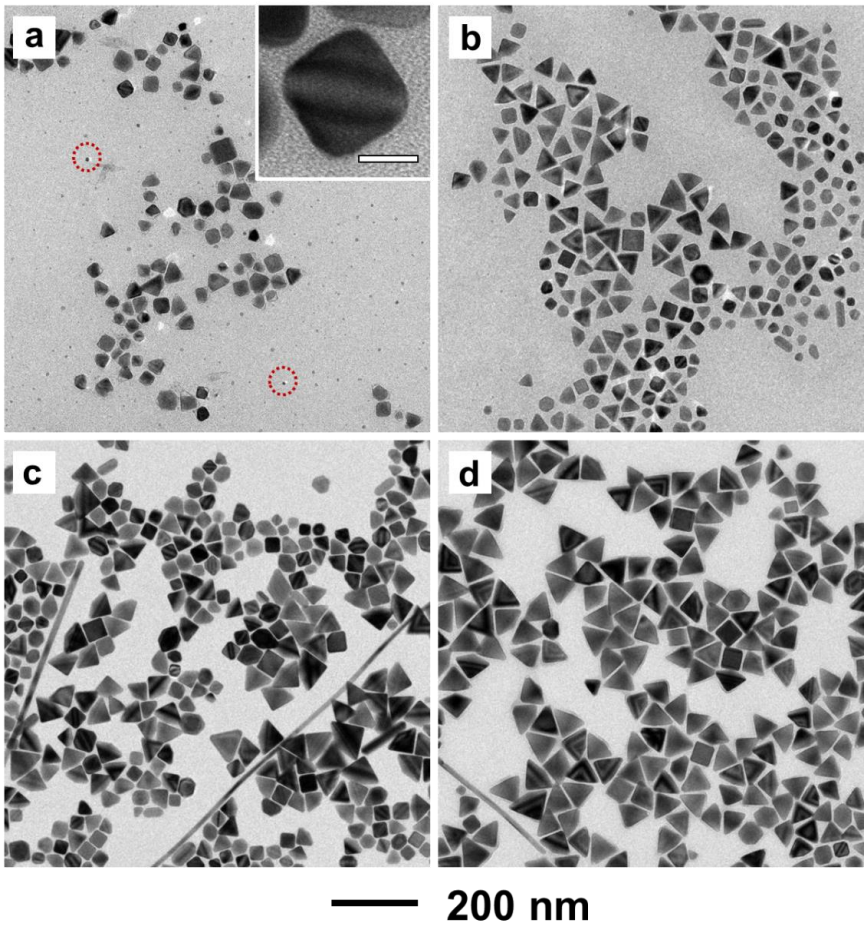

Figure 2.4 TEM images of Cu nanocrystals prepared using the standard protocol except for the variation in reaction time: (a) 0.5, (b) 1, (c) 3, and (d) 6 h, respectively. The scale bar in the inset of (a) is 15 nm. Small Cu nanospheres indicated by the red circles in (a) disappeared after 0.5 h due to the involvement of Ostwald ripening.

To validate the critical role of Pd as a seeding material, I conducted a set of experiments by varying the amount of Pd(II) precursor added into the reaction solution of a standard synthesis.

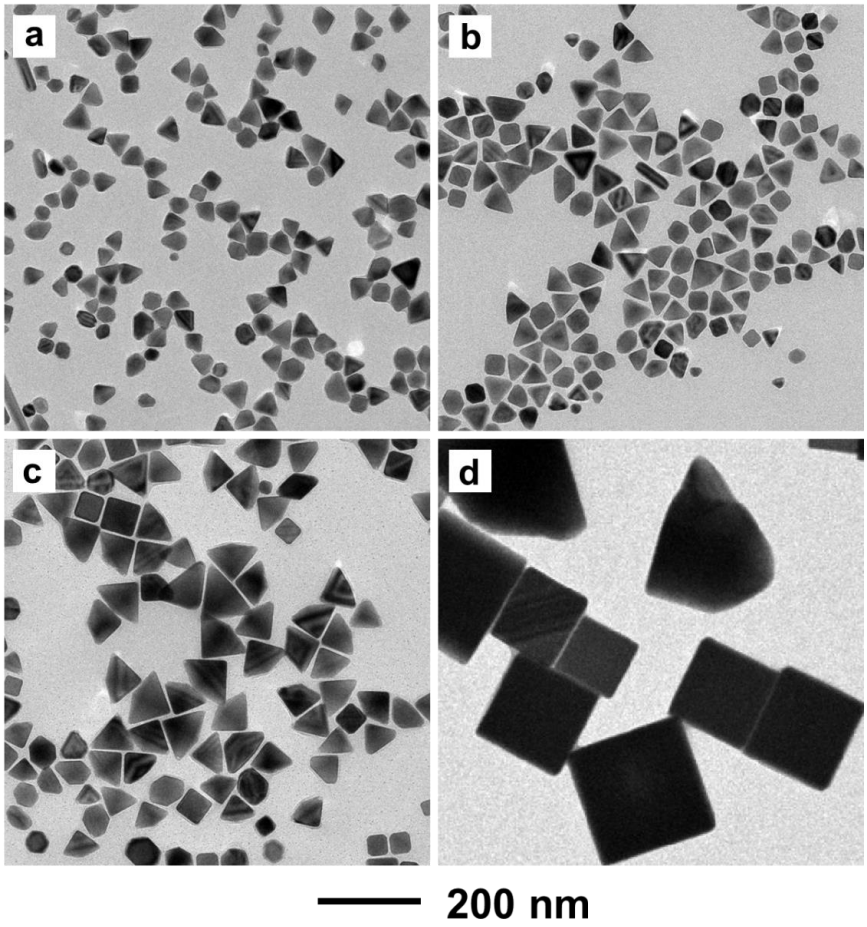

Figure 2.5. TEM images of Cu nanocrystals prepared using the standard protocol except for the variation in the amount of Na_2PdCl_4: (a) 0.36, (b) 0.18, (c) 0.06, and (d) 0 mg, respectively. The average edge lengths of the Cu RBPs were: (a) 38 ± 4, (b) 45 ± 6, and (c) 67 ± 10 nm, respectively.

When the amount of Pd(II) precursor was increased from 0.09 to 0.36 and 0.18 mg, respectively, Cu RBPs with average edge lengths of 38 and 45 nm were obtained (Figure 2.5, a and b). If 0.06 mg of Na_2PdCl_4 was used instead, Cu RBPs with an edge length around 67 nm were formed (Figure 2.5c). Some small particles with a spherical profile could be regarded as RBPs with truncation at corners. These results suggest the involvement of Pd-based seeds because the number of seeds in the reaction system should increase with increasing concentration of Pd(II) precursor and thus inversely

affect the size of the final products if the Cu atoms were supposed to be evenly divided and deposited onto the initially formed Pd seeds. When the total number of Cu atoms was fixed, a larger number of seeds would produce smaller particles and *vice versa*. When I carried out a synthesis using the standard protocol but in the absence of Pd(II) precursor, the final products were relatively large Cu nanocrystals with an edge length approaching 200 nm (Figure 2.5d). These results not only validated the involvement of Pd seeds in the growth of Cu RBPs but also confirmed that the addition of Pd(II) facilitated the nucleation process for the formation of Cu RBPs in high purity. Using this protocol, one can control the size of the Cu RBPs by simply adding different amounts of Pd(II) precursor into the reaction solution.

As indicated by the HRTEM image in Figure 2.2d, multiple parallel planar defects could be identified in the Cu RBP. This result suggests that the Cu RBPs were not grown from singly-twinned Pd seeds, but rather from seeds lined with multiple planar defects (twin planes and/or stacking faults) parallel to each other. To prove this assumption, I took HRTEM image from the Pd seed obtained using the standard protocol but in the absence of Cu(II) precursor. As shown in Figure 2.6, more than one planar defect could indeed be resolved in the Pd seed. A similar defect structure was also reported for the formation of Ag RBPs [15,36]. Taken together, it can be concluded that the RBPs were produced through continuous deposition of Cu atoms onto the Pd seeds formed in the initial stage of a synthesis, with the bipyramidal structure dictated by the parallel planar defects in the seeds. It should be pointed out that a prior study of Ag RBPs demonstrated that odd-numbered twin planes would lead to the formation of RBPs whereas even-numbered twin planes would generate twinned cubes [36]. Different from the Ag RBPs,

the Cu RBPs took a relatively larger size and covered by a CuO skin on the surface, making it quite difficult to count the number of the twin planes by recording atomic-resolution images of the twin boundaries.

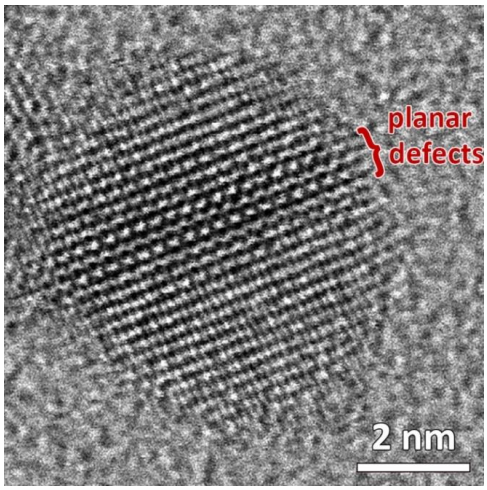

Figure 2.6. HRTEM image of a single Pd seed prepared using the standard protocol but in the absence of Cu(II) precursor.

To better understand the nucleation mechanism, I took UV-vis spectra from aqueous Na_2PdCl_4 solution in the absence and presence of HDA (Figure 2.7a). While the aqueous solution displayed a strong peak at 424 nm, the peak disappeared after the introduction of HDA, indicating the coordination of HDA to Pd(II) ions for the formation of Pd(II)-HDA complexes. Because of the hydrophobic, long alkyl tail, the complexes further assembled into vesicles, with the Pd(II) ions serving as the hydrophilic heads that interact more favorably with water. The vesicles led to the formation of a cloudy, opaque solution, as confirmed by the strong scattering of light over the visible region by the reaction mixture.

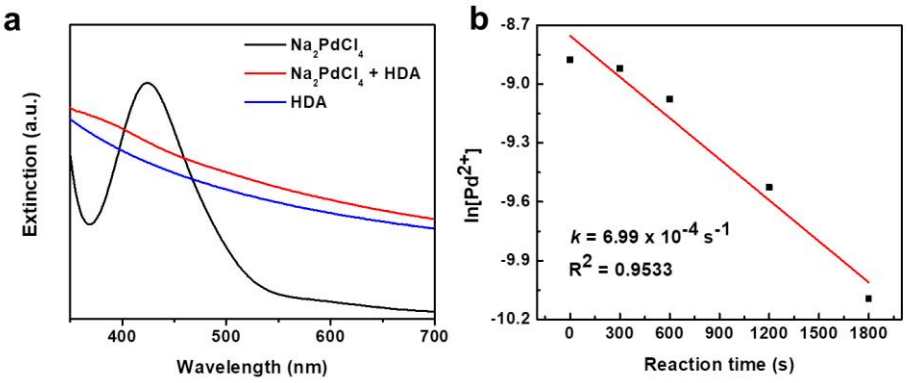

Figure 2.7. (a) Ultraviolet-visible (UV-vis) extinction spectra of Na_2PdCl_4 in the absence/presence of HDA, with reference to pure HDA, in an aqueous solution. (b) A plot showing the concentration of remaining Pd(II) as a function of reaction time in the synthesis of 38-nm Cu RBPs. The rate constant (k) was 7.0×10^{-4} s^{-1}.

To avoid the possible influence arising from the insolubility of HDA in water, I also measured the UV-vis spectra of Na_2PdCl_4 in the absence/presence of HDA, with reference to pure HDA, using ethanol as the solvent (Figure 2.8a). Since HDA is soluble in ethanol, almost no signature from HDA was found in the spectrum. The peak associated with Na_2PdCl_4 still disappeared and strong scattering was observed after the introduction of HDA, suggesting the formation of Pd(II)-HDA complexes. Similar results were also observed for the case of Cu(II) precursor and HDA. The peak of $CuCl_2$ at 800 nm disappeared after the addition of HDA (Figure 2.8b), indicating the formation of Cu(II)-HDA complexes. The existence of vesicles was further confirmed by DLS measurement (Table 2.1). The sizes of the vesicles generated from the Pd(II)-HDA and Cu(II)-HDA complexes were measured to be 1078.0 and 639.5 nm, respectively. Their high zeta potentials, 95.3 and 75.6 mV for the Pd(II)-HDA and Cu(II)-HDA vesicles, respectively, made them highly stable in aqueous media.

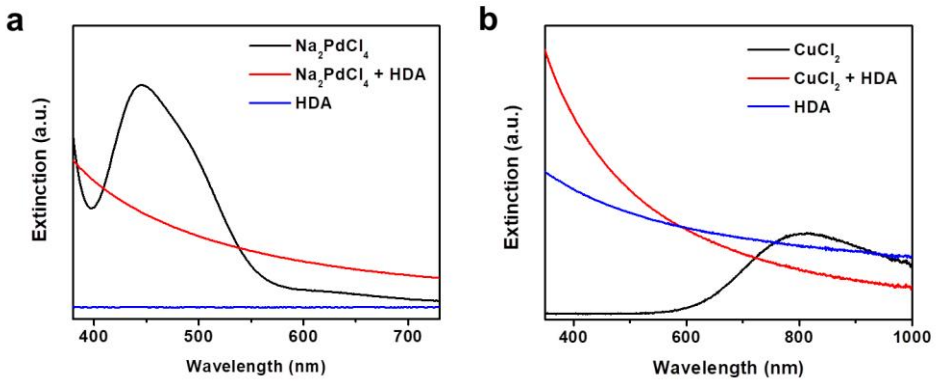

Figure 2.8. UV-vis spectra of (a) Na_2PdCl_4 in the absence/presence of HDA, with reference to pure HDA, using ethanol as the solvent; and (b) $CuCl_2$ in the absence/presence of HDA using water as the solvent.

Table 2.1. Dynamic light scattering (DLS) data of the Pd(II)-HDA and Cu(II)-HDA complexes in aqueous solutions.

Sample	Z-average diameter (nm)	Polydispersity index (PDI)	Zeta potential (mV)
Pd(II)-HDA complex	1078.0	0.539	95.3
Cu(II)-HDA complex	639.5	0.417	75.6
reaction solution containing Pd(II)-HDA and Cu(II)-HDA complexes	452.5	0.286	75.6

The coordination with amine groups drove down the reduction potentials of metal precursors (the standard reduction potentials of $Pd(NH_3)_4^{2+}$/Pd and $Cu(NH_3)_2^{2+}$/Cu are 0.0 and -0.1 V, respectively), leading to a decrease in the reduction rate [37,38]. According to our previous work on Pd nanocrystals, the formation of seeds lined with parallel planar

defects required an initial reduction rate down to a level below 10^{-7} M·s^{-1} for the Pd(II) precursor [17]. Based on the inductively coupled plasma mass spectrometry (ICP-MS) results (Figure 2.7b), the initial reduction rate of Pd(II) in the presence of HDA was indeed as low as 9.8×10^{-8} M·s^{-1}, which favored the formation of parallel planar defects, in agreement with the argument that the Cu RBPs were grown from platelet-like Pd seeds. Taken together, it can be concluded that the coordination to HDA slowed down the reduction rate of Pd(II) so Pd seeds with multiple parallel planar defects were generated for the growth of Cu RBPs (Figure 2.9).

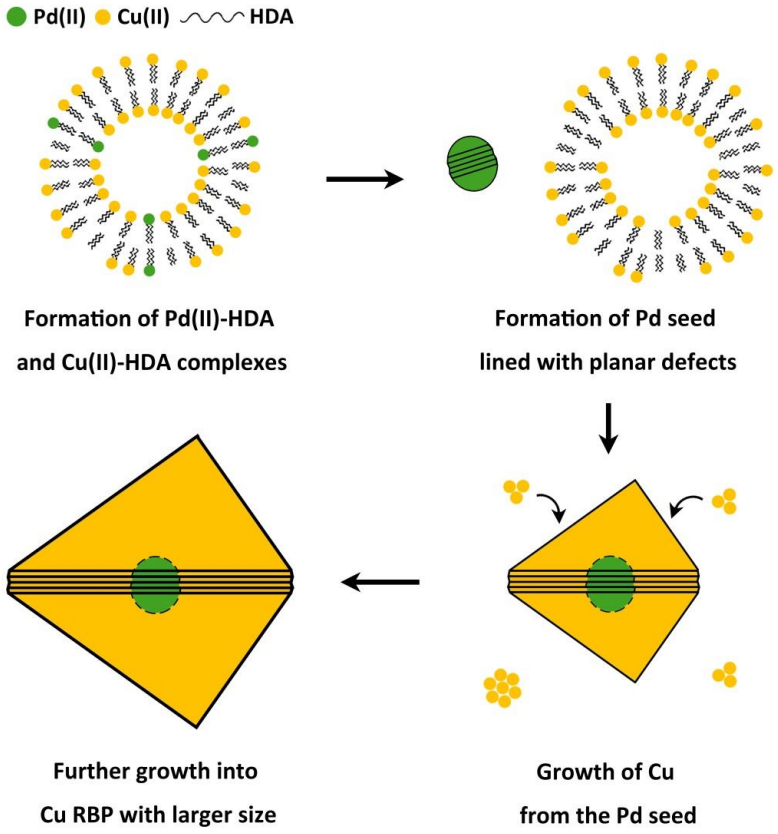

Figure 2.9. Schematic illustration showing the formation of Cu RBPs with the assistance of a trace amount of Pd(II) precursor. Lined with planar defects, Pd seeds were first generated from Pd(II)-HDA complexes, followed by the growth of Cu on them through direct deposition or Ostwald ripening process.

The prevention of oxidative etching also plays an important role in the formation of Cu RBPs. By simply changing the ratio of dissolved oxygen, nanocrystals with different structures can be obtained. As shown in Figure 2.10a, when argon or nitrogen was blown over the solution surface to remove oxygen, I obtained Cu RBPs as the final product. When the reaction was conducted in air, the product was mainly composed of Cu nanocubes with an average edge length of 60 nm (Figure 2.10b). As indicated in our previous work, twin-structured seeds with high energy defects are more vulnerable to oxidative etching, while single-crystal seeds could survive and grow into cubes [18]. It should be mentioned that when the reaction was conducted using the standard protocol but saturated with oxygen, no Cu nanocrystals were obtained owing to the slow reduction rate of Cu(II) influenced by dissolved oxygen [39].

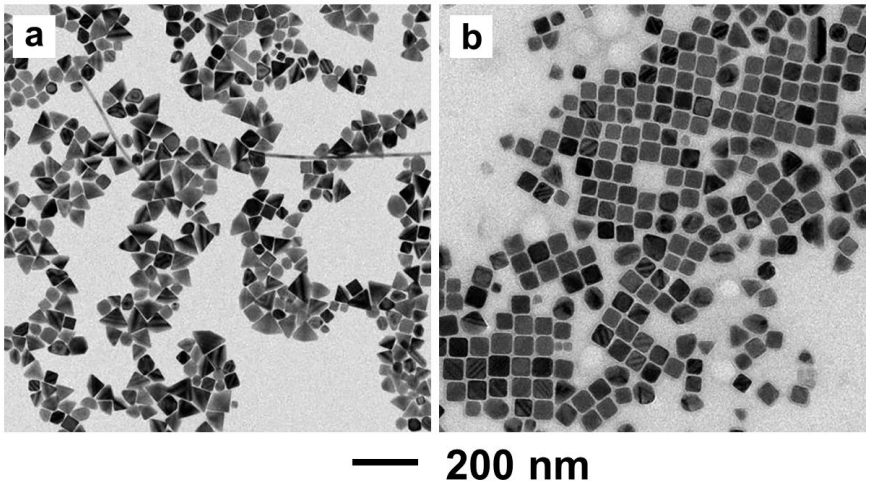

Figure 2.10. TEM images of Cu nanocrystals prepared using the standard protocol except under (a) nitrogen and (b) air atmospheres, respectively.

The shape and structure of Cu nanocrystals also depended on the amount of Cu(II) precursor added in the solution. As shown in Figure 2.11a, when 8 mg of $CuCl_2$ was used, the amount of Cu was insufficient for the complete growth of RBPs and I obtained highly truncated nanocrystals as the final product. When the amount of Cu(II) precursor was increased to 12 mg, an obvious increase in the proportions of nanowires and spheres was observed, indicating the presence of self-nucleation (Figure 2.11b). However, the average edge length of RBPs was around 58 nm, which did not show obvious difference from the sample synthesized using the standard protocol. Taken together, it can be concluded that, when the total amount of Pd seeds was fixed, varying the amount of Cu(II) precursor could not change the size of nanocrystals directly.

In general, capping agent is necessary for the formation of nanocrystals enclosed by high energy facets. In our previous work, it was demonstrated that HDA not only served as an effective capping agent for Cu {100} facets, but also helped prevent oxidative etching [26]. According to DFT simulations, the amine group of HDA strongly binds to the surface of Cu nanocrystals, and the long and hydrophobic alkyl tails of HDA can repel water molecules and help protect Cu from oxygen [40]. When the amount of HDA was reduced from 90 to 45 mg, with all the other conditions kept the same, nanocubes were observed as the product (which accounted for 58%) because of the enhanced oxidative etching (Figure 2.11c). When 120 mg of HDA was used for the synthesis, the proportion of irregular-shaped twinned nanocrystals increased to 38% while the percentage of RBPs decreased to 57% (Figure 2.11d). These results further confirm that HDA works as both a capping agent and a protective layer that prevents Cu nanocrystals from oxidative etching.

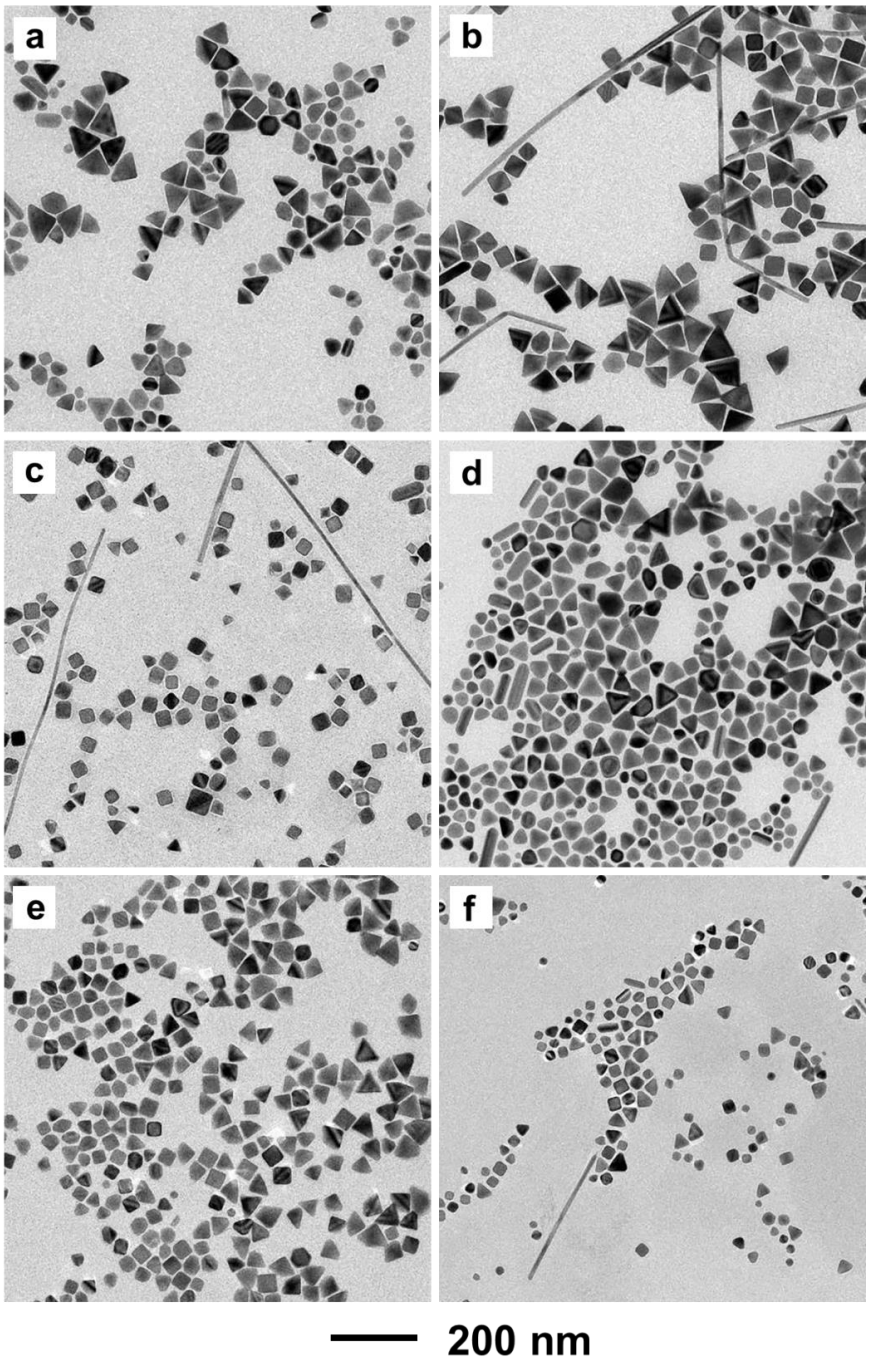

Figure 2.11. TEM images of Cu nanocrystals prepared using the standard protocol except for the variations in the amount of $CuCl_2$: (a) 8 and (b) 12 mg; the amount of HDA: (c) 45 and (d) 120 mg; and the amount of glucose: (e) 50 and (f) 250 mg, respectively.

Chloride ions also played an important role in the synthesis of Cu RBPs. The

influence of halide ions on the formation of Cu nanocrystals can be summarized as the following: *i*) complexation with metal ions to affect the reduction kinetics of the metal precursors, *ii*) serving as a capping agent to direct the growth of nanocrystals by selectively binding to certain facets of metal nanocrystals, and *iii*) forming halide/oxygen oxidative pair in the presence of oxygen, which can act as an etchant and thus influence the shape and structure of the nanocrystals.

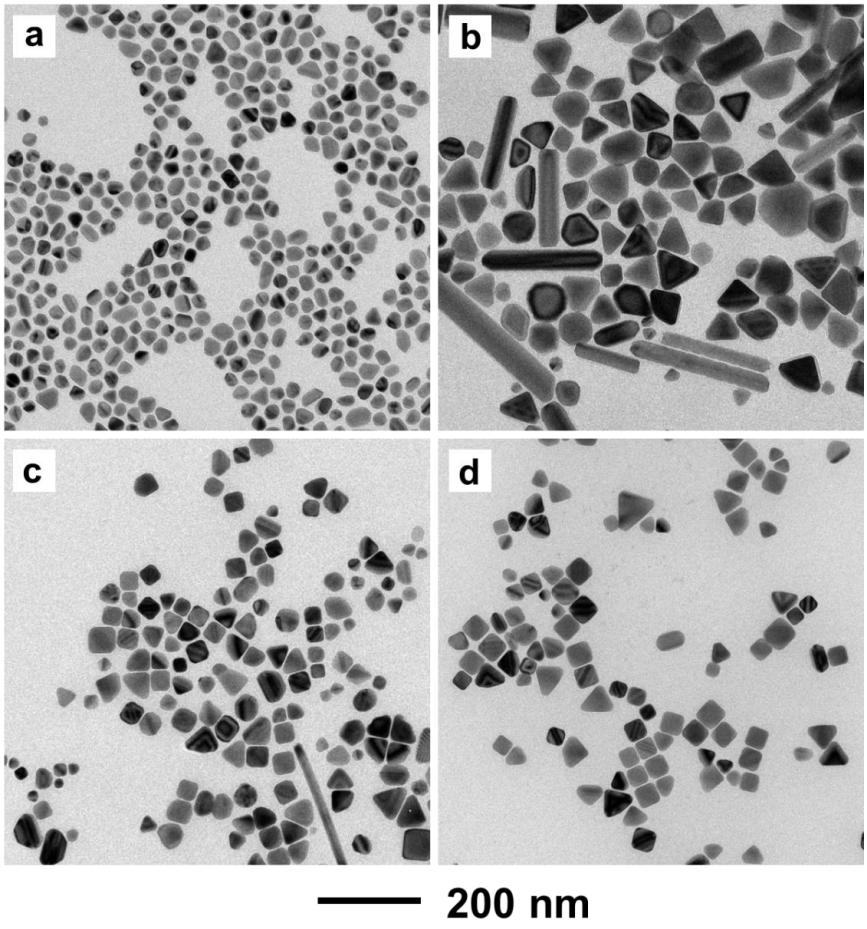

Figure 2.12. TEM images of Cu nanocrystals prepared using the standard protocol except for the variation of Cu(II) precursor: (a) 14.3 mg $Cu(NO_3)_2$, (b) 14.3 mg $Cu(NO_3)_2$ + 7.2 mg NaCl, (c) 14.3 mg $Cu(NO_3)_2$ + 12.7 mg NaBr, and (d) 10.5 mg $CuCl_2$ + 12.7 mg NaBr.

When $Cu(NO_3)_2$, instead of $CuCl_2$, was used as precursor, Cu nanocrystals with irregular shapes and decreased sizes were obtained (Figure 2.12a). Some nanocubes and RBPs were still found in the products. With an additional amount of NaCl introduced, as shown in Figure 2.12b, RBPs and nanorods with increased sizes were obtained. These results indicate that Cl^- ions could not only serve as a capping agent for the Cu(100) facets, but also coordinate to Pd(II) and Cu(II) ions and help slow down the reduction rate of metal precursors [26]. The decrease in reduction rate for the precursors led to the formation of fewer seeds, and thus larger nanocrystals in the products. When NaBr, instead of NaCl, was added into the reaction solution containing $Cu(NO_3)_2$, nanocubes were observed as the main product and this can be attributed to the presence of oxidative etching (Figure 2.12c). Because I only purged the solution with argon for 5 min, there was still little oxygen left behind. A combination of the remaining oxygen and Br^- ions, which was more corrosive than the Cl^-/oxygen pair, was able to remove the twinned seeds through oxidative etching, leading to the formation of nanocubes [41]. A control experiment was also conducted by introducing a small amount of NaBr into the reaction solution containing $CuCl_2$, and the proportion of nanocubes was found to increase while that of RBPs decreased (Figure 2.12d).

Glucose serves as the major reducing agent in this reaction system. By varying the amount of glucose, the reaction kinetics can be directly manipulated, leading to variation in size and structure of the final products. As illustrated in Figure 2.11e, nanocrystals with an average edge length of 35 nm were generated when the amount of glucose was doubled to 50 mg. A further increase in the amount of glucose to 250 mg resulted in a decrease in the size of the nanocrystals to 28 nm (Figure 2.11f). In both cases, a higher

percentage of single crystals was observed compared to the Cu RBPs synthesized using the standard protocol. Higher concentration of glucose led to an acceleration in the reduction of Pd(II) precursor, thus resulting in an increase in both the amount and ratio of single-crystal seeds in the beginning of the reaction.

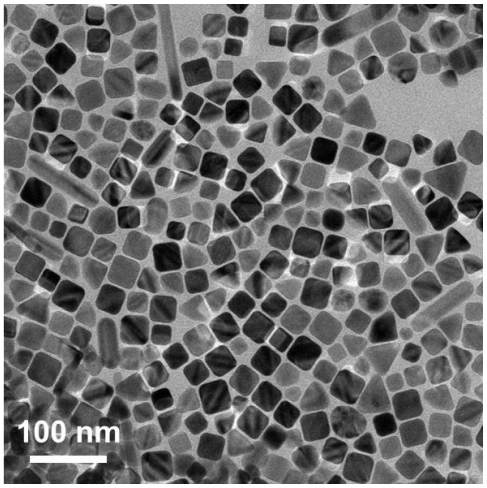

Figure 2.13. TEM image of Cu nanocrystals prepared using the standard protocol except for the use of ascorbic acid instead of glucose as the reducing agent.

Ascorbic acid and citric acid were also used as reducing agents, and the results were shown in Figure 2.13. When ascorbic acid was used, the product was mainly composed of nanocubes instead of RBPs, This result can be attributed to the stronger reducing power of ascorbic acid, which led to an increase in the initial reduction rate of Pd(II) precursors and thus the formation of single-crystal seeds [17]. When citric acid was used as reducing agent, no solid product was obtained due to its relatively weak reducing power. Taken together, it can be concluded that the introduction of glucose can

not only reduce Cu(II) ions to Cu atoms, but also adjust the initial reduction rate to the suitable range for the formation of seeds with planar defects.

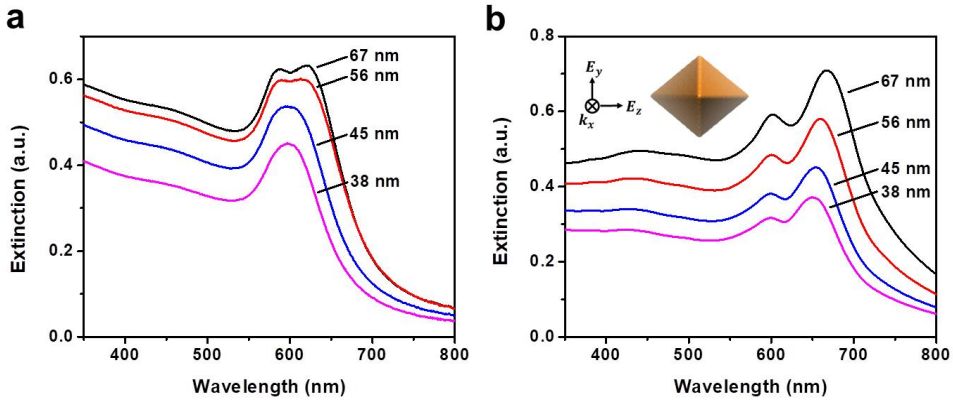

Figure 2.14. (a) UV-vis extinction spectra corresponding to the Cu RBPs with different sizes shown in Figure 1,3. Prior to the spectral measurement, the as-obtained colloidal suspensions were diluted by 32.5 times with deionized (DI) water. (b) DDA simulations showing the extinction spectra for Cu RBPs with different sizes.

Optical Properties of the Cu RBPs. Figure 2.14a shows the UV-vis extinction spectra recorded from aqueous suspensions of the Cu RBPs with different edge lengths. The RBPs exhibited extinction peaks in the visible region. I observed a broad peak around 597 nm for the RBPs of 38 and 45 nm in edge length. When the edge length was increased to 56 and 67 nm, two well-separated peaks were resolved at 586 and 621 nm. Different from spherical or icosahedral nanocrystals, which are highly symmetric, the optical properties of RBPs are supposed to strongly depend on its geometric anisotropy. To investigate their optical properties theoretically, my collaborator performed simulations for Cu RBPs with increasing sizes using the discrete dipole approximation (DDA) method (Figure 2.14b). We took the edge lengths measured from TEM images.

The spectra simulated for RBPs of all four different edge lengths showed two separate peaks, corresponding to two LSPR modes. The peak at 600 nm can be attributed to the dipolar oscillation perpendicular to the equilateral triangular base (transverse dipolar resonance), and the peak at 667 nm arises from the orthogonal dipolar oscillation parallel to the triangular base (longitudinal dipolar resonance) [16]. The slight red shift can be attributed to the increase in particle size.

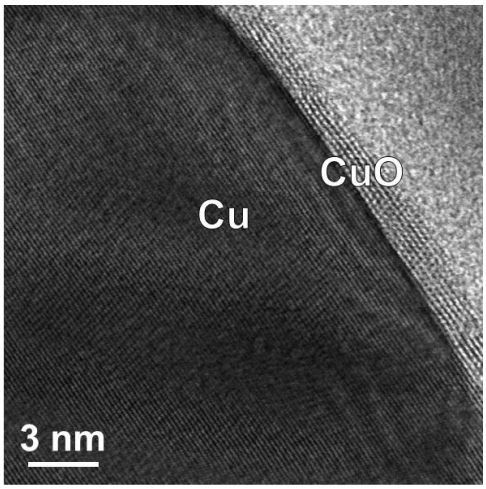

Figure 2.15. Atomic resolution phase contrast STEM image showing a thin layer of CuO on Cu(100) facet. The lattice spacing of the outer and inner layers is 0.237 and 0.178 nm, matching that of the (200) planes of CuO and Cu, respectively.

Compared to the simulation, the peaks observed in the experimental spectra are blue-shifted and several reasons may contribute to the difference. As indicated by the XPS spectrum and STEM image (Figure 2.3b and Figure 2.15, respectively), the Cu RBPs were covered by an oxide skin composed of CuO with a thickness of around 1.5 nm, which may lead to a red shift to the LSPR peaks [42]. Furthermore, the additional oxide layer technically makes the size of the Cu RBP smaller if the oxide skin is ignored,

and this should cause a blue shift to the peak position. The spectrum simulated for a 67-nm Cu RBP covered by a 1.5-nm CuO skin showed two peaks at 613 nm and 675 nm, indicating the dominance of red-shift caused by the oxide layer when compared with the blue shift caused by the decrease in size (Figure 2.16a). In addition to the oxide skin, we also introduced corner truncation to the RBP in our simulation. The resultant blue shift to the LSPR peak position also contributed to the differences between simulation and experimental results [15]. The spectrum simulated for a Cu RBP with 5-nm truncation at all corners is shown in Figure 2.16b. For a 67-nm truncated RBP, we observed two peaks at 590 nm and 658 nm. The peaks were blue-shifted by about 10 nm relative to those of a RBP without truncation, and this trend is consistent with a previous report on Ag RBPs in that truncation also led to a blue shift to the LSPR peak position [16].

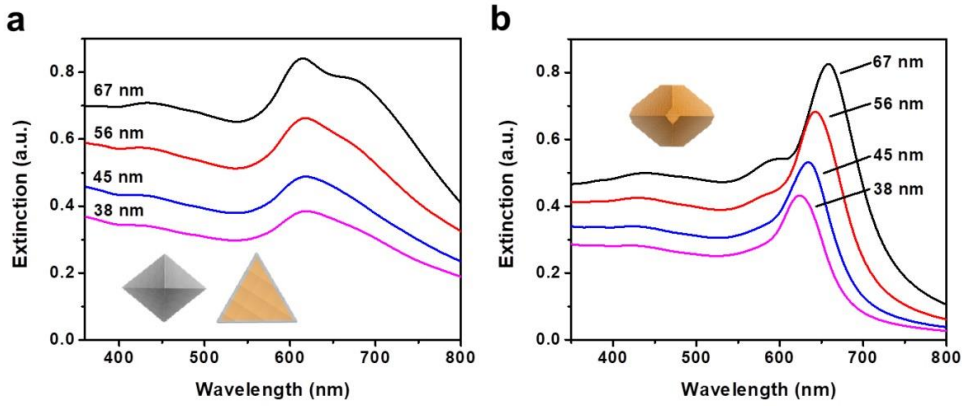

Figure 2.16. DDA simulations showing the extinction spectra of Cu RBPs in different sizes with (a) 1.5-nm CuO layer on the surface and (b) 5-nm truncation at all corners, respectively.

As the size of the truncated RBPs was decreased to 38 and 45 nm, respectively, the peaks corresponding to transverse and longitudinal dipolar resonance begin to overlap

and only one peak was observed, in agreement with a previously reported simulation for Cu spherical nanoparticles [30]. The truncation made the 38-nm Cu RBP appear pseudo-spherical, so the impact of structural anisotropy was reduced. Simulations were also conducted on Cu RBPs with 5-nm truncation at all corners and covered by a 1.5-nm CuO skin, as shown in Figure 2.17. Two peaks positioned at 606 nm and 701 nm were observed for the 67-nm RBP, both red-shifted when compared to the simulated peaks for those without truncation or oxide layer. This result suggests a great influence for the oxide layer, whose red shift exceeded the blue shifts caused by both corner truncation and decrease in size.

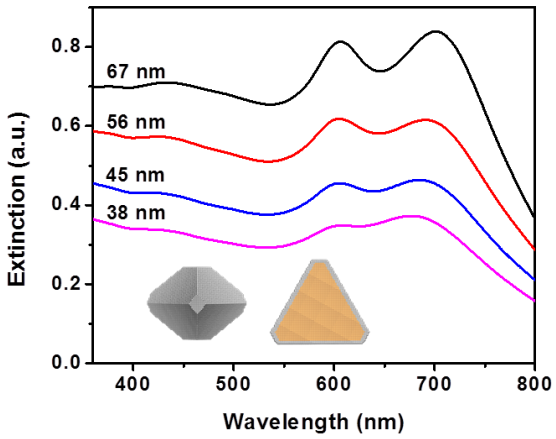

Figure 2.17. DDA simulations showing the extinction spectra of Cu RBPs in different sizes with 5-nm truncation at all corners and covered by 1.5-nm CuO layer.

However, the peaks in our simulated spectra were still positioned at longer wavelengths than those observed experimentally, and this discrepancy could be attributed to the impurities in the products, such as small cubic or spherical nanocrystals that would cause blue shifts to the peak position. In addition, we mainly focused on simulations with

the incident photon propagating along one particular direction relative to the RBP. Due to the shape anisotropy of RBP, simulations along different directions of propagation may vary from each other, and this could also contribute to the difference between the simulated and experimental results.

2.3 Conclusion

In summary, I have demonstrated a rationally designed, one-pot method for the facile synthesis of Cu RBPs with the assistance of Pd. The coordination of HDA slowed down the reduction rate of Pd(II) and led to the formation of Pd seeds lined with multiple parallel planar defects, followed by the growth of Cu on them. By simply varying the amount of Pd(II) precursor introduced, the edge length of the RBPs can be tuned in a range of 38−67 nm. The prevention of oxidative etching also played an important role in the formation of Cu RBPs. When the reaction solution was saturated with air instead of argon, seeds with defects were removed through oxidative etching and nanocubes were obtained as the main product. The as-synthesized Cu RBPs showed absorbance at around 600 nm and two separate peaks were observed due to the anisotropy of bipyramids. Compared to the simulated spectra, blue shift of peaks was observed in experimental results, which can be attributed to the corner truncation and impurities in the product. The one-pot method of synthesizing Cu RBPs based on the difference between reduction potentials opens up opportunities for a broad range of nanocrystal synthesis. It is worth noting that despite the high price of Pd ($2204.1 per oz. at the moment), our Cu RBPs are still more cost-effective than nanocrystals composed of other noble metals, such as Ag RBPs, due to the small amount of Pd involved (1:200 in molar ratio compared to Cu). Although the material cost of our Cu RBPs is $16.8 per oz. (with that of Pd accounting

for more than 90%), it is only about half of the material cost for Ag RBPs ($28.35 per oz.). By reducing the size of Pd seeds, the material cost of the resultant Cu RBPs could be further reduced. Considering their unique shape and structure, we believe that Cu RBPs with tunable sizes will find widespread use in various applications such as catalysis and SERS detection.

2.4 Experimental Section

Chemicals and Materials. Copper(II) chloride dihydrate ($CuCl_2 \cdot 2H_2O$, 99.0%), copper(II) nitrate hemi(pentahydrate) (98%), sodium tetrachloropalladate(II) (Na_2PdCl_4, 98%), hexadecylamine (HDA, 98%), D-(+)-glucose ($C_6H_{12}O_6$, 99.5%), sodium chloride (>99%), sodium bromide (>99%), ammonium hydroxide solution (28% NH_3 in H_2O, purified by double-distillation) were all obtained from Sigma-Aldrich. Ethanol (200 proof) was obtained from Pharmco Products. All chemicals were used as received without further purification. I used DI water with resistivity of 18.2 MΩ·cm throughout all the experiments.

Synthesis of Cu RBPs. In a standard protocol for the synthesis of Cu RBPs, an aqueous solution (5 mL) containing HDA (90 mg), glucose (25 mg), $CuCl_2 \cdot 2H_2O$ (10.5 mg), and Na_2PdCl_4 (0.091 mg) was magnetically stirred at room temperature overnight. Before the reaction started, argon was blown over the solution surface for 5 min. The vial was then tightly capped, transferred into an oil bath (held at 100 ^oC) and heated for 6 h under magnetic stirring. The product was collected by centrifugation at 13,300 ×g and washed twice with water, twice with ethanol to remove excess HDA, and finally re-dispersed in ethanol for further characterization.

Characterization. TEM images were taken using a Hitachi HT7700 microscope by drop-casting the nanoparticle suspension onto carbon-coated Cu grids and drying under ambient conditions. High-resolution TEM images were captured on an aberration-corrected FEI Titan S 80-300 STEM/TEM microscope equipped with a Gatan OneView camera at an acceleration voltage of 300 kV. STEM images were collected on a JEOL JEM 2200FS STEM/TEM microscope (Heidelberg, Germany) at an acceleration voltage of 200 kV equipped with a CEOS probe corrector to provide nominal resolution of ~0.07 nm. A portion of the aberration-corrected STEM images were obtained on a JEM-ARM200F with a guaranteed spatial resolution of 0.08 nm. UV-vis extinction spectra were recorded on a Cary 60 spectrometer (Agilent Technologies, Santa Clara, CA). EDX analyses were performed using an HT2700 aberration-corrected STEM (Hitachi) operated at 200 kV. The Cu contents in the solid products and the concentrations of remaining Pd(II) were determined using an ICP-MS (NexION 300Q, Perkin-Elmer). To determine the concentrations of Pd(II) remaining in the solution, 0.5 mL of the reaction solution was added into a mixture of 2 mL of ammonium hydroxide and 7.5 mL of ethanol. The mixture was incubated at room temperature for 1 h to enable the formation of $Pd(NH_3)_4^{2+}$ and the dissolution of HDA in ethanol. After centrifugation, 0.5 mL of the supernatant was taken out and diluted by 20 times for ICP-MS measurement. XRD pattern was recorded using an X'Pert PRO Alpha-1 diffractometer (PANalytical, Almelo, Netherlands) with a 1.8 kW ceramic copper tube source. XPS data were recorded using a Thermo K-Alpha spectrometer with an Al Kα source (hν = 1486.6 eV). DLS and zeta potential measurements were determined using a Zetasizer Nano ZS (Malvern Instruments, Worcestershire, UK).

Discrete Dipole Approximation Calculations. All optical spectra were simulated using DDScat 7.3.0 software [43,44]. For Cu and Cu@CuO RBPs without truncation, a continuum of dipoles (N = 72934) with a right-bipyramidal shape was created using Large-scale Atomic/Molecular Massively Parallel Simulator (LAMMPS) software [45] and visualized using Visual molecular dynamics (VMD) software [46]. For comparison, Cu and Cu@CuO RBPs with 5 nm truncation at all corners were also created by reduced the number of dipoles. The shape file was then uploaded into the software using the FROM-FILE function. The dielectric constant of Cu was taken from the work of Johnson and Christy (downloaded from refractiveindex.info [47]), and the dielectric constant of CuO was taken from the work of Drobny and Pulfrey [48]. Since all the spectra were measured in an aqueous solution, the dielectric constant of the medium was taken to be $\varepsilon_m = n^2 = 1.78$. The *k*-vector and *E*-fields of the incident photon with respect to the orientation of the RBP are shown in the inset of Figure 2.18. Additional details regarding how the shape was constructed can be found in the Table 2.2.

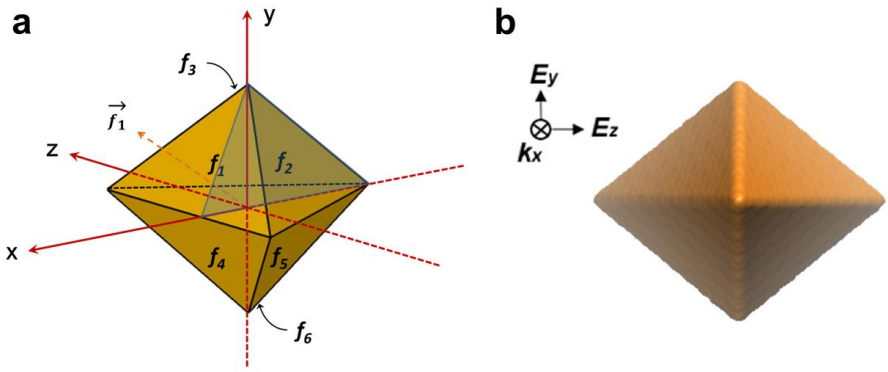

Figure 2.18. (a) Schematic drawing showing the six faces of Cu RBPs. (b) The *k*-vector and *E*-fields of the incident photon with respect to the orientation of an individual RBP used for the DDA calculation.

Table 2.2. Unit vectors for the six faces of Cu RBPs.

Face	Unit Vector
f_1	(0.82, 0.58, 0)
f_2	(-0.41, 0.58, 0.71)
f_3	(-0.41, 0.58, -0.71)
f_4	(0.82, -0.58, 0)
f_5	(-0.41, -0.58, 0.71)
f_6	(-0.41, -0.58, -0.71)

2.5 Notes to Chapter 2

Part of this Chapter is adapted from the paper "A Rationally Designed Route to the One-Pot Synthesis of Right Bipyramidal Nanocrystals of Copper" published in *Chemistry of Materials* [49].

2.6 References

[1] Fan, Z.; Zhang, H. *Chem. Soc. Rev.* **2016**, *45*, 63–82.

[2] Jeong, S.; Woo, K.; Kim, D.; Lim, S.; Kim, J. S.; Shin, H.; Xia, Y.; Moon, J. *Adv. Funct. Mater.* **2008**, *18*, 679–686.

[3] Camden, J. P.; Dieringer, J. A.; Zhao, J.; Van Duyne, R. P. *Acc. Chem. Res.* **2008**, *41*, 1653–1661.

[4] Jain, P. K.; Lee, K. S.; El-Sayed, I. H.; El-Sayed, M. A. *J. Phys. Chem. B* **2006**, *110*, 7238–7248.

[5] Xia, X.; Choi, S. Il; Herron, J. A.; Lu, N.; Scaranto, J.; Peng, H. C.; Wang, J.; Mavrikakis, M.; Kim, M. J.; Xia, Y. *J. Am. Chem. Soc.* **2013**, *135*, 15706–15709.

[6] Huang, H.; Wang, Y.; Ruditskiy, A.; Peng, H. C.; Zhao, X.; Zhang, L.; Liu, J.; Ye, Z.; Xia, Y. *ACS Nano* **2014**, *8*, 7041–7050.

[7] Zhou, W.; Wu, J.; Yang, H. *Nano Lett.* **2013**, *13*, 2870–2874.

[8] Zhang, J.; Langille, M. R.; Mirkin, C. A. *J. Am. Chem. Soc.* **2010**, *132*, 12502–12510.

[9] Figueroa-Cosme, L.; Hood, Z. D.; Gilroy, K. D.; Xia, Y. *J. Mater. Chem. C* **2018**, *6*, 4677–4682.

[10] Elechiguerra, J. L.; Reyes-Gasga, J.; Yacaman, M. J. *J. Mater. Chem.* **2006**, *16*, 3906–3919.

[11] Wu, J.; Qi, L.; You, H.; Gross, A.; Li, J.; Yang, H. *J. Am. Chem. Soc.* **2012**, *134*, 11880–11883.

[12] Wang, X.; Choi, S. Il; Roling, L. T.; Luo, M.; Ma, C.; Zhang, L.; Chi, M.; Liu, J.; Xie, Z.; Herron, J. A.; Mavrikakis, M.; Xia, Y. *Nat. Commun.* **2015**, *6*, 1–8.

[13] Ruan, L.; Chiu, C. Y.; Li, Y.; Huang, Y. *Nano Lett.* **2011**, *11*, 3040–3046.

[14] Wiley, B. J.; Xiong, Y.; Li, Z. Y.; Yin, Y.; Xia, Y. *Nano Lett.* **2006**, *6*, 765–768.

[15] Zhang, J.; Li, S.; Wu, J.; Schatz, G. C.; Mirkin, C. A. *Angew. Chemie* **2009**, *121*, 7927–7931.

[16] Ringe, E.; Zhang, J.; Langille, M. R.; Mirkin, C. A.; Marks, L. D.; Van Duyne, R. P. *Nanotechnology* **2012**, *23*, 444005.

[17] Wang, Y.; Peng, H. C.; Liu, J.; Huang, C. Z.; Xia, Y. *Nano Lett.* **2015**, *15*, 1445–1450.

[18] Xiong, Y.; Chen, J.; Wiley, B.; Xia, Y.; Aloni, S.; Yin, Y. *J. Am. Chem. Soc.* **2005**, *127*, 7332–7333.

[19] Zhang, Z.; Wang, S. S.; Song, R.; Cao, T.; Luo, L.; Chen, X.; Gao, Y.; Lu, J.; Li, W. X.; Huang, W. *Nat. Commun.* **2017**, *8*, 1–10.

[20] Kim, D.; Kley, C. S.; Li, Y.; Yang, P. *Proc. Natl. Acad. Sci. U. S. A.* **2017**, *114*, 10560–10565.

[21] Cui, F.; Yu, Y.; Dou, L.; Sun, J.; Yang, Q.; Schildknecht, C.; Schierle-Arndt, K.; Yang, P. *Nano Lett.* **2015**, *15*, 7610–7615.

[22] Pereira, A. J.; Gomes, J. P.; Lenz, G. F.; Schneider, R.; Chaker, J. A.; De Souza, P. E. N.; Felix, J. F. *J. Phys. Chem. C* **2016**, *120*, 12265–12272.

[23] Rathmell, A. R.; Bergin, S. M.; Hua, Y. L.; Li, Z. Y.; Wiley, B. J. *Adv. Mater.* **2010**, *22*, 3558–3563.

[24] Jin, M.; He, G.; Zhang, H.; Zeng, J.; Xie, Z.; Xia, Y. *Angew. Chem. Int. Ed.* **2011**, *50*, 10560–10564.

[25] Wang, Z.; Chen, Z.; Zhang, H.; Zhang, Z.; Wu, H.; Jin, M.; Wu, C.; Yang, D.; Yin, Y. *ACS Nano* **2015**, *9*, 3307–3313.

[26] Luo, M.; Ruditskiy, A.; Peng, H. C.; Tao, J.; Figueroa-Cosme, L.; He, Z.; Xia, Y. *Adv. Funct. Mater.* **2016**, *26*, 1209–1216.

[27] Salzemann, C.; Urban, J.; Lisiecki, I.; Pileni, M. P. *Adv. Funct. Mater.* **2005**, *15*, 1277–1284.

[28] Dai, L.; Qin, Q.; Wang, P.; Zhao, X.; Hu, C.; Liu, P.; Qin, R.; Chen, M.; Ou, D.; Xu, C.; Mo, S.; Wu, B.; Fu, G.; Zhang, P.; Zheng, N. *Sci. Adv.* **2017**, *3*, 1–10.

[29] Jeon, H. S.; Kunze, S.; Scholten, F.; Roldan Cuenya, B. *ACS Catal.* **2018**, *8*, 531–535.

[30] Guo, H.; Chen, Y.; Cortie, M. B.; Liu, X.; Xie, Q.; Wang, X.; Peng, D. L. *J. Phys. Chem. C* **2014**, *118*, 9801–9808.

[31] Jin, M.; Zhang, H.; Wang, J.; Zhong, X.; Lu, N.; Li, Z.; Xie, Z.; Kim, M. J.; Xia, Y. *ACS Nano* **2012**, *6*, 2566–2573.

[32] Hsia, C. F.; Madasu, M.; Huang, M. H. *Chem. Mater.* **2016**, *28*, 3073–3079.

[33] Lu, S. C.; Hsiao, M. C.; Yorulmaz, M.; Wang, L. Y.; Yang, P. Y.; Link, S.; Chang, W. S.; Tuan, H. Y. *Chem. Mater.* **2015**, *27*, 8187–8188.

[34] Luo, W.; Nie, X.; Janik, M. J.; Asthagiri, A. *ACS Catal.* **2016**, *6*, 219–229.

[35] Biesinger, M. C.; Lau, L. W. M.; Gerson, A. R.; Smart, R. S. C. *Appl. Surf. Sci.* **2010**, *257*, 887–898.

[36] McEachran, M.; Kitaev, V. *Chem. Commun.* **2008**, 5737–5739.

[37] Meng, M.; Fang, Z.; Zhang, C.; Su, H.; He, R.; Zhang, R.; Li, H.; Li, Z. Y.; Wu, X.; Ma, C.; Zeng, J. *Nano Lett.* **2016**, *16*, 3036–3041.

[38] Bard, A. J.; Parsons, R.; Jordan, J. *Standard Potentials in Aqueous Solution*, Marcel Dekker, New York, **1985**.

[39] Zheng, Y.; Zeng, J.; Ruditskiy, A.; Liu, M.; Xia, Y. *Chem. Mater.* **2014**, *26*, 22–33.

[40] Liu, S. H.; Fichthorn, K. A. *J. Phys. Chem. C* **2017**, *121*, 22531–22541.

[41] Zhou, S.; Mesina, D. S.; Organt, M. A.; Yang, T. H.; Yang, X.; Huo, D.; Zhao, M.; Xia, Y. *J. Mater. Chem. C* **2018**, *6*, 1384–1392.

[42] Cure, J.; Glaria, A.; Collière, V.; Fazzini, P. F.; Mlayah, A.; Chaudret, B.; Fau, P. *J. Phys. Chem. C* **2017**, *121*, 5253–5260.

[43] Johnson, P. B.; Christy, R. W. *Phys. Rev. B* **1972**, *6*, 4370–4379.

[44] Draine, B. T.; Flatau, P. J. *J. Opt. Soc. Am. A* **1994**, *11*, 1491.

[45] Plimpton, S. *J. Comput. Phys.* **1995**, *117*, 1–19.

[46] Humphrey, W.; Dalke, A.; Schulten, K. *J. Mol. Graph.* **1996**, *14*, 33–38.

[47] Polyanskiy, M. N. "Refractive index database," can be found under https://refractiveindex.info., **n.d.**

[48] Drobny, V. F.; Pulfrey, L. *Thin Solid Films* **1979**, *61*, 89–98.

[49] Lyu, Z.; Xie, M.; Gilroy, K. D.; Hood, Z. D.; Zhao, M.; Zhou, S.; Liu, J.; Xia, Y. *Chem. Mater.* **2018**, *30*, 6469–6477.

CHAPTER 3

GOLD@COPPER CORE–SHELL NANOCUBES WITH CONTROLLABLE SIZES IN THE RANGE OF 20–30 NM FOR APPLICATIONS IN CATALYSIS AND PLASMONICS

3.1 Introduction

Nanocrystals made of Cu, a highly abundant and low-cost element, have received great interest in recent years owing to their outstanding performance in applications related to catalysis [1–3], electronics [4,5], and plasmonics [6–8]. As an example, transparent conductors based on CuNWs are strong candidates for replacing indium-tin-oxide (ITO) films thanks to the intrinsically high conductivity and low price of Cu [9]. It was also demonstrated that Cu could serve as an electrocatalyst to generate substantial amounts of hydrocarbons in the electrochemical reduction of CO_2 [10]. In an effort to improve both the activity and selectivity of Cu-based catalysts, recent studies have focused on Cu nanocrystals enclosed by different types of facets. Specifically, it was reported that Cu nanocrystals covered by {100} facets were more selective toward the formation of multi-carbon products relative to those covered by {111} facets for the CO_2 reduction reaction [11]. A recent study also suggested that Cu nanocubes were more catalytically active than dodecahedral and octahedral counterparts for the low-temperature WGS reaction [2]. As the simplest structure enclosed by {100} facets, Cu nanocrystals in a cubic shape are expected to play an important role in these catalytic applications. In addition, Cu is one of the few noble metals whose nanocrystals are expected to display LSPR peaks in the visible region [12].

There are several reports on the colloidal synthesis of Cu nanocubes, but most of them are plagued by large size (typically, larger than 50 nm), poor purity, and/or hazardous experimental conditions [1,12–18]. Our group reported a facile synthesis of Cu nanocubes with controllable sizes ranging from 50−200 nm using HDA as a capping agent and glucose as a reducing agent [13]. However, the relatively low surface-to-volume ratio due to the large size make them less desirable for catalysis. Guo *et al.* reported the synthesis of Cu nanocubes with an average size of 24 ± 1.5 nm using organic solvents (Figure 3.1a) [12]. In their work, oleylamine served as both the solvent and reducing agent and TOPO was supposed to serve as a capping agent. Although small Cu nanocubes were obtained, the reaction was conducted at a temperature as high as 210 °C. Roberts *et al.* reported a synthesis of Cu nanocubes with the smallest size approaching 30 nm through electropolishing (Figure 3.1b) [1]. However, the size uniformity of the products was relatively poor, with the largest size reaching 100 nm. In generating Cu nanocubes with high purity and uniformity, seed-mediated growth has also been leveraged in addition to the conventional one-pot method that involves homogeneous nucleation and growth. Our group reported a protocol for the synthesis of Pd@Cu core-shell nanocubes with tunable sizes between 50−100 nm using 18-nm Pd cubes as the seeds [19]. It was demonstrated that the epitaxial growth of Cu shell on the Pd seeds could still be realized regardless of the large (7.1%) lattice mismatch between Cu and Pd. Later, Hsia *et al.* reported the synthesis of Au@Cu core-shell nanocubes using Au octahedra with opposite corner distance of 35 nm as the seeds and the size of the core-shell nanocubes could be controlled in a range of 49–136 nm by adding different amounts of Au seeds [20]. However, due to the large size of the seeds, Cu nanocubes smaller than

30 nm have not been produced. Inspired by their work, it was argued that the introduction of seeds smaller in size should lead to the generation of Cu nanocubes with size down to 20 nm, offering a promising catalyst for the electrocatalytic reduction of CO_2 due to the presence of a single type of {100} facets on the surface.

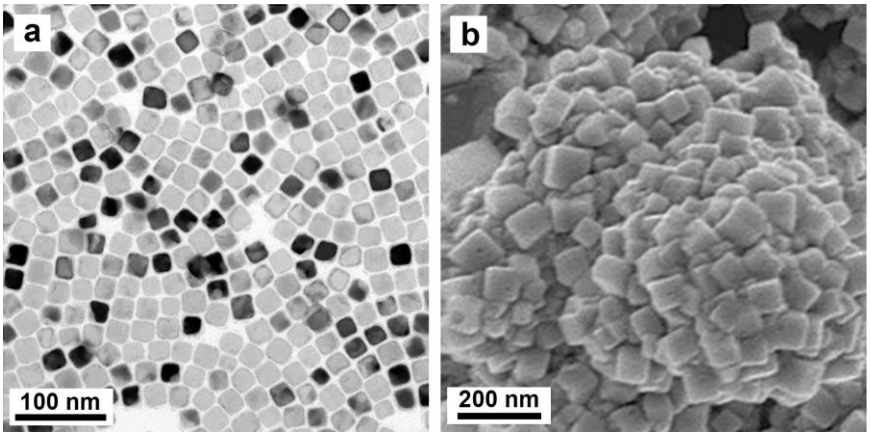

Figure 3.1. (a) TEM image of Cu nanocubes with an average size of 24 ± 1.5 nm. In a typical protocol, CuBr and TOPO were dissolved in oleylamine and the reaction solution was heated at 210 °C for 1 h. (b) SEM image of Cu nanocubes with sizes in a range of 30-100 nm synthesized from electropolishing. (a) Reprinted with permission from ref [12]. Copyright 2014 American Chemical Society. (b) Reprinted with permission from ref [1]. Copyright 2016 Wiley-VCH.

In this work, I demonstrated the use of seed-mediated growth for the production of uniform Au@Cu core-shell nanocubes by employing 5-nm Au spheres as the seeds (Figure 3.2). The Au seeds were randomly distributed inside the core-shell nanocubes, which can be attributed to the localized epitaxial growth of Cu shell due to the large (12%) lattice mismatch between Au and Cu. By varying the reaction time and/or the amount of Au seeds, Au@Cu nanocubes with size controllable in the range of 20–30 nm could be readily produced. I also found that the concentration of Cu(II) precursor had a

major impact on the structure and morphology of the resultant nanocrystals. When decreasing the concentration of the Cu(II) precursor below a critical value, Cu nanoplates with Au spheres encased were obtained.

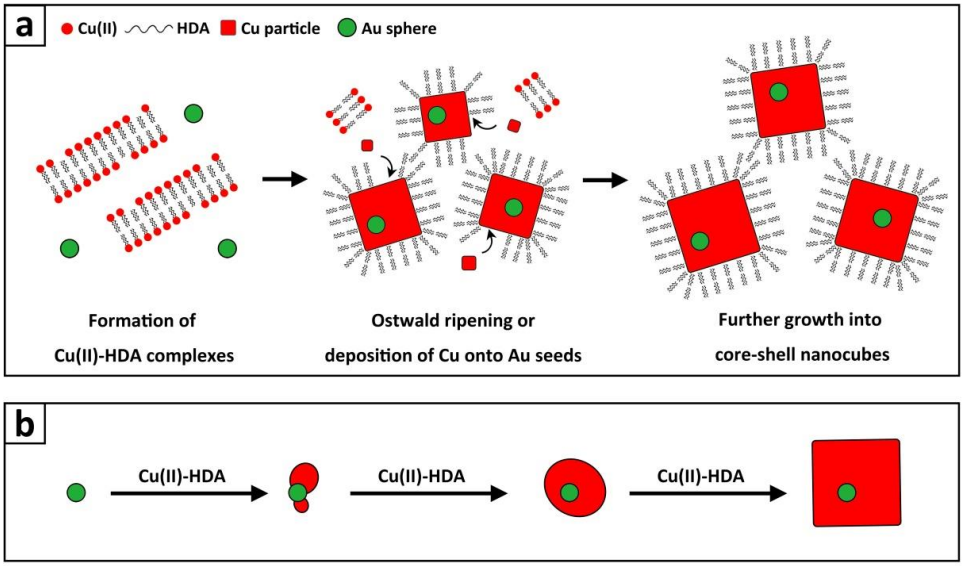

Figure 3.2. Schematic illustrations of (a) the mechanism responsible for the growth of Au@Cu core-shell nanocubes and (b) a plausible pathway for the evolution of a Au sphere into a Au@Cu nanocube. The Cu atoms nucleate and grow into different islands on the Au seed in the initial stage of a synthesis. The islands then merge to completely cover the seed when a sufficient amount of Cu(II) precursor is reduced, and the nanocrystal finally evolves into a cubic shape due to the surface capping effect of HDA and Cl^-. The red and green colors represent Cu and Au elements, respectively.

3.2 Results and Discussion

I leveraged the control provided by seed-mediated growth to prepare Au@Cu core-shell nanocubes (Figure 3.2). In this scheme, the HDA is presented as a bilayer structure according to the results of a nuclear magnetic resonance (NMR) study [21]. It should be mentioned that when Au seeds were not added, large, tadpole-like Cu particles

with dimensions as large as 1 μm were obtained, together with some nanocubes and nanowires, which were formed through self-nucleation. In the presence of Au seeds, I obtained Au@Cu core-shell nanocrystals with a cubic shape through the overgrowth of Cu on the Au seeds in the presence of glucose as a reducing agent, as well as HDA and Cl^- as the capping agents toward Cu(100) surface.

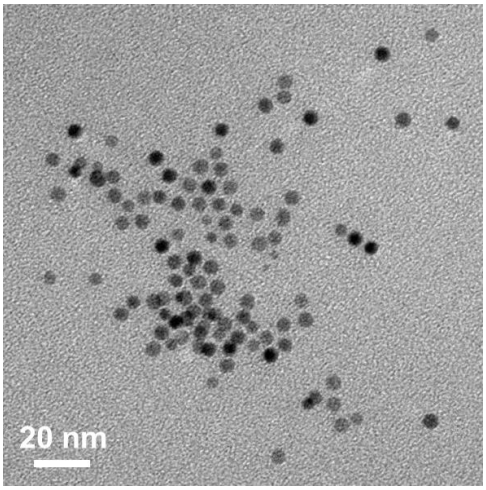

Figure 3.3. A typical TEM image of the 5-nm Au spheres that served as seeds for the growth of Cu nanocubes.

The Au spherical seeds were, in turn, synthesized in two steps: *i*) formation of Au clusters by reducing $HAuCl_4$ with $NaBH_4$ in the presence of cetyltrimethylammonium bromide (CTAB), and *ii*) growth of the clusters into 5-nm Au spheres by adding the clusters into a solution containing $HAuCl_4$, AA, and cetyltrimethylammonium chloride (CTAC). A typical TEM image of the Au seeds with a spherical shape and a uniform diameter of 4.7 ± 0.5 nm was shown in Figure 3.3. Based on our prior work, the as-synthesized Au spheres should have a single-crystal structure, making them well-suited

for the growth of Cu cubes characterized by a single-crystal structure [22]. The seed-mediated growth was typically conducted at 100 °C. When a lower temperature (*e.g.*, 70–80 °C) was used, it would be difficult to reduce the Cu(II) precursor to Cu(0) atoms. However, if the temperature was too high (*e.g.*, 110–120 °C), self-nucleation would occur, leading to the formation of Cu nanocrystals with no Au seeds included.

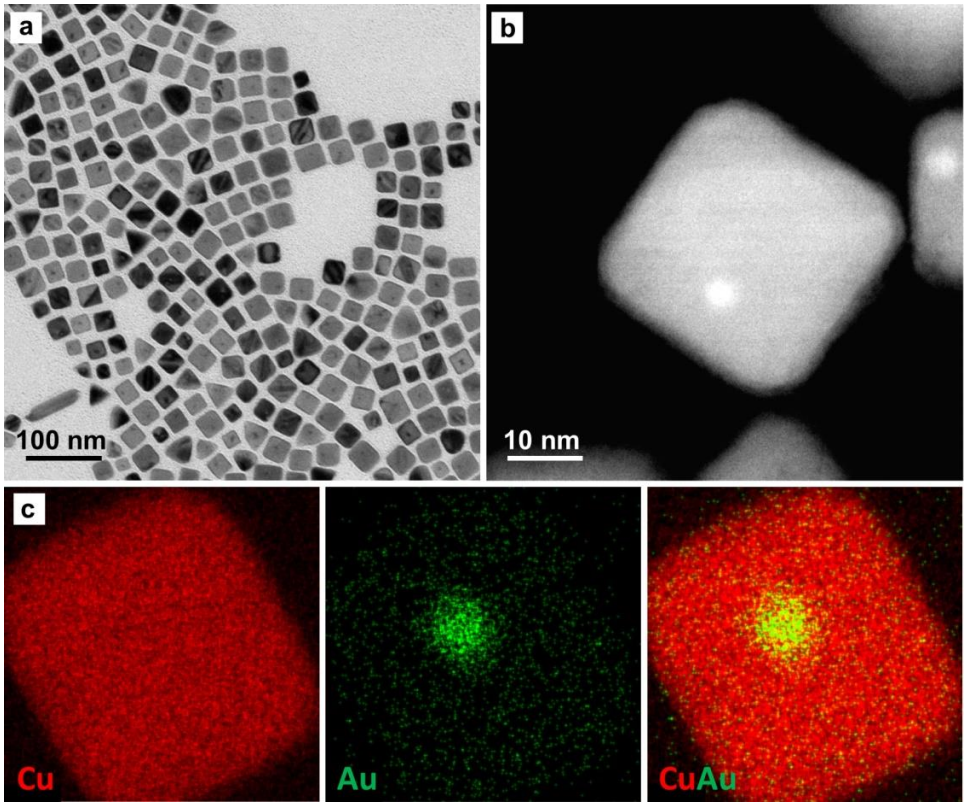

Figure 3.4. (a) TEM image of the Au@Cu core-shell nanocubes obtained using 5-nm Au spherical seeds. (b) HAADF-STEM image and (c) EDX mapping of a single core-shell nanocube. The red and green colors correspond to Cu and Au, respectively.

Figure 3.4a shows a typical TEM image of the as-synthesized Au@Cu nanocubes with an average edge length of 27.1 ± 3.0 nm and purity over 85%. Due to the different

atomic number and thus attenuation of electrons, a clear difference in contrast can be observed between the Au core and the Cu shell. The image also confirms that every cube contained one Au sphere, which was randomly distributed in the cube. I further used HAADF-STEM to resolve the Au seed due to the larger atomic number of Au relative to Cu (Figure 3.4b). No twin defect or stacking fault was observed in the core-shell nanocubes, indicating a single-crystal structure. The distributions of Au and Cu in the nanocube were also resolved by EDX mapping and a large difference in composition between the core (Au, green) and the shell (Cu, red) was clearly observed (Figure 3.4c).

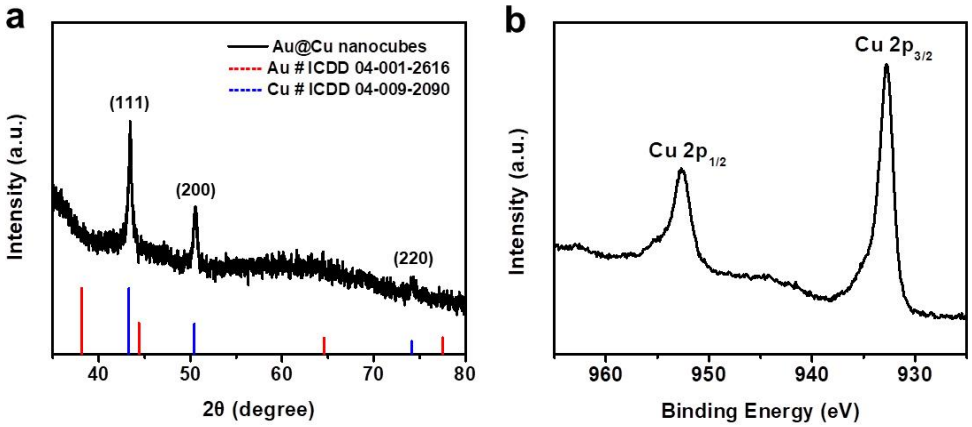

Figure 3.5. (a) Powder XRD pattern and (b) XPS spectrum of the Au@Cu nanocubes prepared using the standard protocol. Because the Au@Cu nanocubes were small in size, they tended to be randomly oriented when deposited on the substrate and, in this case, the (100) planes were not well aligned with the X-ray beam. Thus, in the XRD pattern, the (200) diffraction peak was weaker than the (111) diffraction peak.

Figure 3.5 shows the XRD pattern and XPS spectrum of the Au@Cu core-shell nanocubes, suggesting that they were mainly made of elemental Cu. In the XRD pattern, the three peaks positioned at $2\theta = 43.3°$, $50.5°$, and $74.2°$ could be indexed to the

diffractions from (111), (200), and (220) planes of *fcc* Cu [13]. In the XPS spectrum, the Cu 2p peaks were observed at 932.7 and 952.6 eV [23]. Because of its low molar concentration (2300 times lower than Cu), almost no signal from Au was detected by both XRD and XPS. The two satellite peaks at 944.2 and 963.0 eV in the XPS spectrum indicated the existence of a thin layer of CuO on the surface of the nanocubes (Figure 3.5b). Oxidation of Cu to CuO is a commonly observed phenomenon when the sample is handled under ambient conditions [23,24]. The thickness of the CuO layer was, however, too thin to be resolved by HRTEM even after the Au@Cu core-shell nanocubes had been stored in ethanol for one week. When the core-shell nanocubes were stored in water without the elimination of oxygen, voids could be observed at the corners just after one day, indicating quick oxidation of the nanocubes.

In an effort to understand the growth mechanism of the core-shell nanocubes, I conducted a set of syntheses using the standard protocol except for the variation in reaction time and then analyzed the products using TEM. At t = 5 min, the solid products showed Au spheres with or without partial coverage by Cu, together with a number of small pseudo-spherical particles with sizes between 3 and 4 nm. These particles could be attributed to Cu nanocrystals formed through self- nucleation (Figure 3.6a), as their sizes were even smaller than the original Au seeds. When the reaction time was extended to 10 min, I observed many rectangular structures with edge length in the range of 300 nm to 3 μm and small Cu nanocrystals embedded in them (Figure 3.6, b and c). Similar structures were also observed in the products obtained at t = 5 min. But different from the product obtained at t = 5 min, I also found many 20-nm cubic Au@Cu nanocrystals located near the edge of these structures at t = 10 min (Figure 3.6, b and d). The black dots in Figure

3.6b correspond to core-shell nanocubes, as confirmed by the TEM image recorded at a higher magnification (Figure 3.6d).

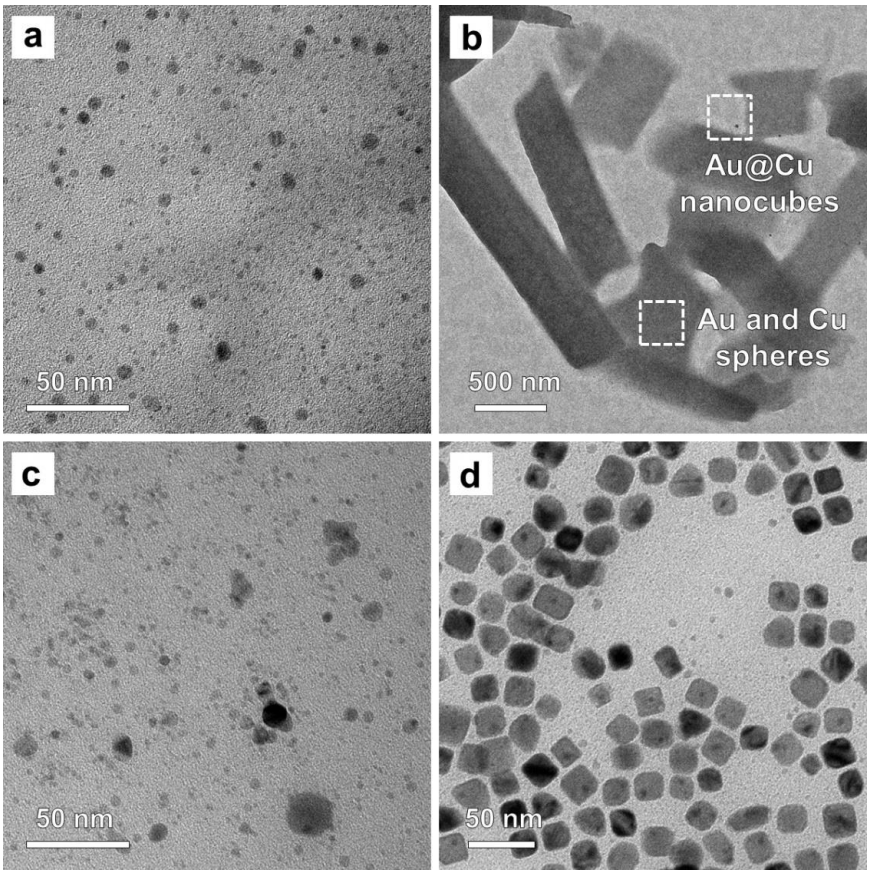

Figure 3.6. TEM images of the solid products obtained at different stages of a standard synthesis: (a) 5 and (b–d) 10 min, respectively. The large rectangular structures in (b) can be assigned to the lamellar sheets of Cu(II)-HDA complexes. It should be pointed out that (c) and (d) were taken from the same sample, but not from the exact regions marked by the two boxes in (b) due to the difficulty in achieving spatial registration.

The SEM images in Figure 3.7 further confirmed the 2D morphology of the rectangular structures while the particles marked by red circles, with sizes around 20 nm, can be ascribed to Au@Cu nanocubes. It has been demonstrated in our prior work that Cu(II) ions were first coordinated with HDA to form Cu(II)-HDA complexes, which then

served as the actual Cu(II) precursor [24]. Based on the observations mentioned above, it can be assumed that the rectangular structures were comprised of lamellar sheets of Cu(II)-HDA complexes. Upon reduction by glucose, some of the resultant Cu atoms could be deposited onto the Au seeds in close proximity to the sheet-like structures, while those atoms far from the Au seeds tended to self-nucleate for the formation of small Cu particles.

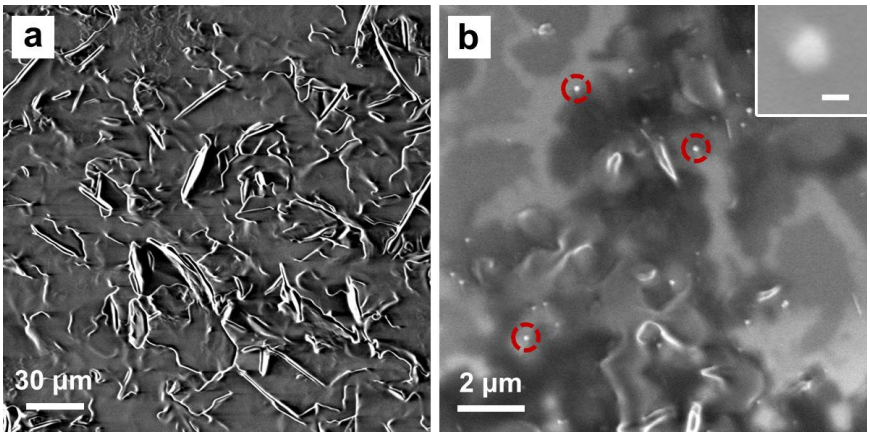

Figure 3.7. SEM images (at two different magnifications) of the solid product obtained at t = 10 min into a standard synthesis. The lamellar sheets are mainly composed of Cu(II)-HDA complexes. The particles circled in red correspond to the Au@Cu nanocrystals. The inset shows a magnified SEM image of the Au@Cu nanocrystal (scale bar: 20 nm).

In Figure 3.6d, I noticed that the majority of the Au seeds were located on or near the surface of the resultant Au@Cu nanocubes, with only a few of them being positioned in the center, indicating a non-uniform nucleation and growth pattern on the surface of a Au spherical seed. At t = 15 min (Figure 3.8a), most of the Au seeds were completely covered by Cu shells and nanocubes with an average size of 21.2 nm were obtained.

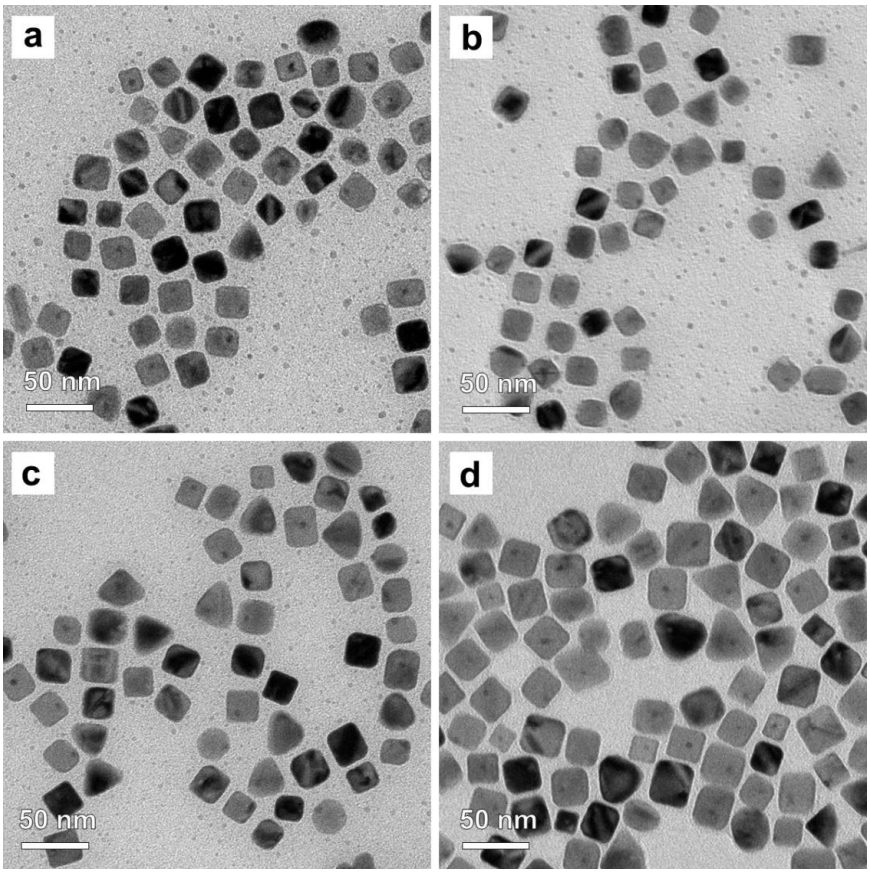

Figure 3.8. TEM images of the Au@Cu core-shell nanocubes prepared using the standard protocol except for the variation in reaction time: (a) 15, (b) 20, (c) 30, and (d) 90 min, respectively.

When the reaction time was extended to 20 and 30 min, as shown in Figure 3.8, b and c, the nanocubes grew into larger sizes of 21.4 and 22.8 nm, respectively. It was also observed that the small Cu particles gradually disappeared after 30 min, which could be attributed to the involvement of Ostwald ripening [24]. When extending the reaction time to 90 min, no obvious change was observed on the nanocubes in either size or shape as compared with the product obtained at t = 60 min (Figure 3.8d). Taken together, it can be concluded that Cu atoms were partially deposited onto the Au seeds in the initial stage of a synthesis (Figure 3.2b), which was different from the conformal, uniform growth of Ag

on Au spherical seeds [25].

A possible explanation is that the large (12%) lattice mismatch between Au and Cu favors a non-uniform deposition of Cu atoms on the surface of a Au seed [26]. The initially deposited Cu atoms could coexist in the form of islands instead of conformal layers, and the Cu nucleated and grew on Au seeds at different time points eventually led to the difference in shell thickness, and thus the random distributions for the Au seeds [19]. The Au seeds cannot be completely covered by Cu shell until a sufficient amount of Cu(II) precursor had been reduced. After the Cu shell had reached a certain thickness and surface strain had been mitigated, a cubic nanocrystal was evolved with the help of HDA and Cl^- ions [27]. Note that the localized epitaxial growth mechanism described in Figure 3.2b is similar to what was observed in the formation of Pd@Cu core-shell nanocubes when Pd cubes were used as seeds [19].

I compared the conversions of Cu(II) ions in the presence and absence of Au seeds to achieve a qualitative understanding of the reduction of Cu(II) precursor. From the plots shown in Figure 3.9, it can be clearly observed that the conversion of Cu(II) precursor in the presence of Au seeds was much higher than the case without seeds. According to our recent work [28,29], the reduction of a metal precursor may take two different pathways: solution *versus* surface reduction. Typically, solution reduction is much slower than surface reduction due to the lower activation energy barrier enabled by the seed [30]. When there is no preformed seed in the reaction solution, the Cu(II) precursor could only take the solution-reduction pathway to generate Cu nuclei, which could grow into seeds and then particles with increasing size. When Au seeds were introduced into the reaction solution, the Cu(II) precursor is anticipated to undertake

reduction on the surface of the added seeds, greatly accelerating the reduction kinetics and thus the conversion.

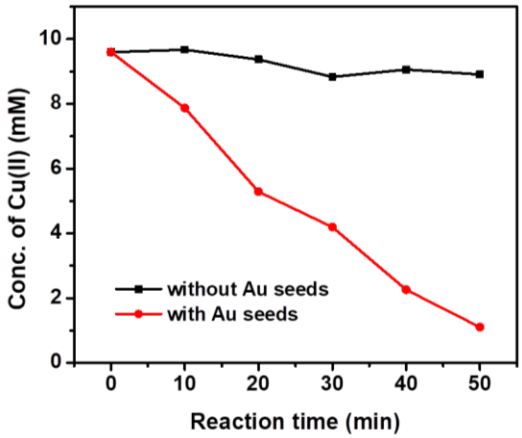

Figure 3.9. The concentration of the Cu(II) precursor remaining in the solution as a function of reaction time in the absence or presence of the 5-nm Au seeds.

Figure 3.10a shows the UV-vis extinction spectra of the Au@Cu nanocubes obtained at different stages of a synthesis and dispersed in aqueous solutions. The core-shell nanocubes exhibited an extinction peak at 581 nm, which was in agreement with the data reported for the Cu nanocubes with a similar size [12]. The intensity of the peak increased as the reaction time was extended, indicating that more Cu atoms were derived from the Cu(II) precursor. However, no red shift in peak position, which was typical of size increase for nanocrystals, was observed as the extinction peaks remained at 581 nm throughout the synthesis. This phenomenon could be attributed to the small size of the nanocubes, as well as the relatively insignificant increase in particle size as the synthesis was prolonged [31]. According to Mie theory, the LSPR peak position of a noble-metal nanocrystal will not show appreciable size dependence when its size is below 50 nm.

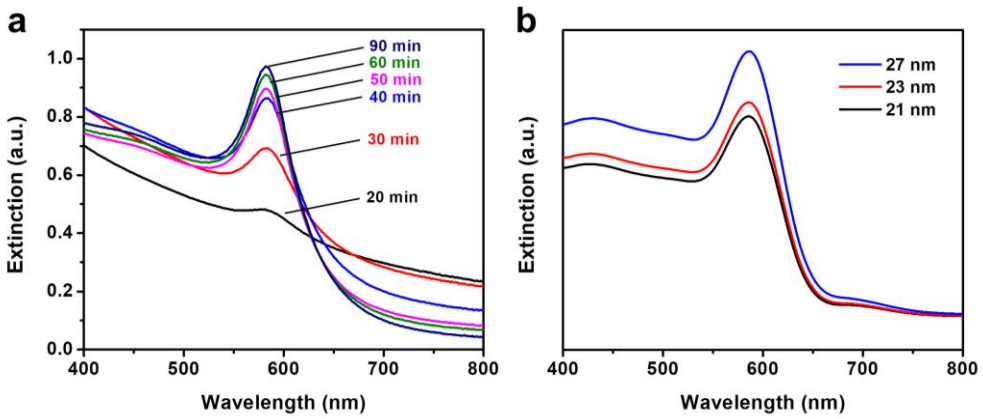

Figure 3.10. (a) UV-vis extinction spectra of the Au@Cu nanocubes prepared using the standard protocol by terminating the reaction at different time points. Prior to the spectral measurement, the as-obtained colloidal suspension was diluted by 20 times with water. (b) Extinction spectra calculated using the DDA method for a Au@Cu nanocube with an edge length of 27 nm and a 5-nm Au sphere located near the edge.

As shown in Figure 3.10b, my collaborator also simulated the extinction spectra of Au@Cu nanocubes with edge lengths ranging from 21−27 nm using the DDA method. There was almost no shift for the peak position, which was in agreement with the experimental observation. In addition to the peak position, we found that the baseline of the extinction spectra in Figure 3.10a was lowered as the reaction time was extended, and this could be attributed to the removal of HDA from the system. While some of the HDA molecules could bind to the surface of the Cu nanocrystals for the generation of a protective layer, most of them were washed away from the system prior to UV-vis measurement, leading to reduction in scattering for the colloidal suspension.

To further look into the optical properties of the Au@Cu nanocubes, we calculated the absorption and scattering cross sections using the DDA method. We used a model based on a Au@Cu core-shell nanocube with an edge length of 27 nm, together with a 5-nm Au sphere located near one of the edges. As shown in Figure 3.11, a peak

located at 586 nm was observed in the simulated spectrum. The slight blue shift of the peaks in the experimental result relative to the simulated one could be ascribed to the corner truncation of the as-prepared Au@Cu nanocubes [32]. The extinction, absorption, and scattering cross sections (abbreviated as C_{ext}, C_{abs}, and C_{sca}) were calculated to be 20.5 x 10^{-16}, 20.0 x 10^{-16}, and 0.5 x 10^{-16} m^2, respectively. The C_{abs} was about 40 times greater than C_{sca} and accounted for 97.6% of C_{ext}, indicating the domination of absorption in the intensity of extinction. This result was also consistent with previous works that, for metal particles with small sizes (*e.g.* around 20 nm), the intensity of extinction was dominated by absorption while scattering made nearly no contributions [33,34].

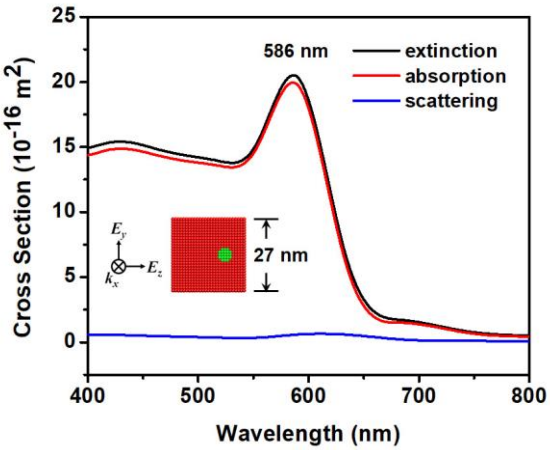

Figure 3.11. Extinction spectra calculated using the DDA method for the Au@Cu nanocubes with different edge lengths.

My collaborator also simulated the extinction spectra of pure Cu nanocubes and Au@Cu core-shell nanocubes with the Au seeds distributed at different locations in the Cu cubes. As shown in Figure 3.12, the extinction peaks of all the spectra were located at the same position (586 nm), in agreement with the spectrum recorded experimentally.

This result indicates that the Au seed actually had essentially no influence on the extinction spectra of the Au@Cu core-shell nanocubes, and this could be attributed to the relatively thick Cu shell surrounding the Au seed.

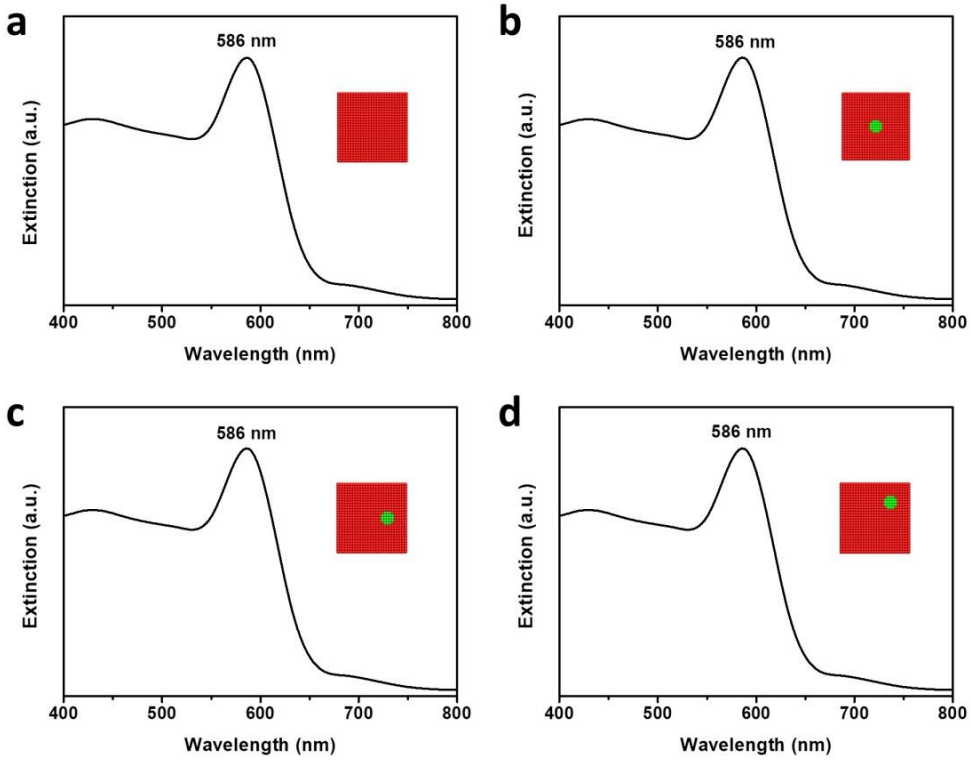

Figure 3.12. Comparison of the simulated extinction spectra for: (A) Cu cubes; (B) Au@Cu nanocubes with the Au seed located at the center; (C) Au@Cu nanocubes with the Au seed located near one of the edges; (D) Au@Cu nanocubes with the Au seed located at one of the corners. The Cu cube and Au seed are 27 nm in edge length and 5 nm in diameter, respectively.

As reported for the UV-vis spectra of Au@Ag core-shell nanocubes containing 11-nm Au spheres, the intensity of the peak from the Au spheres gradually disappeared as the Ag shell became thicker [25]. Eventually, only the peak of the Ag cubes appeared when the Ag shell reached 3.1 nm in thickness. In the present case, the diameter of the Au

sphere was 5 nm while the edge length of the Cu cubes was as large as 27 nm. The thick Cu shell attenuated all the incident light, making it impossible for the light to excite the electrons in the Au core. As a result, no peak was observed for the Au core and its spatial distribution in the nanocube had no impact on the extinction spectrum of the core-shell nanocubes.

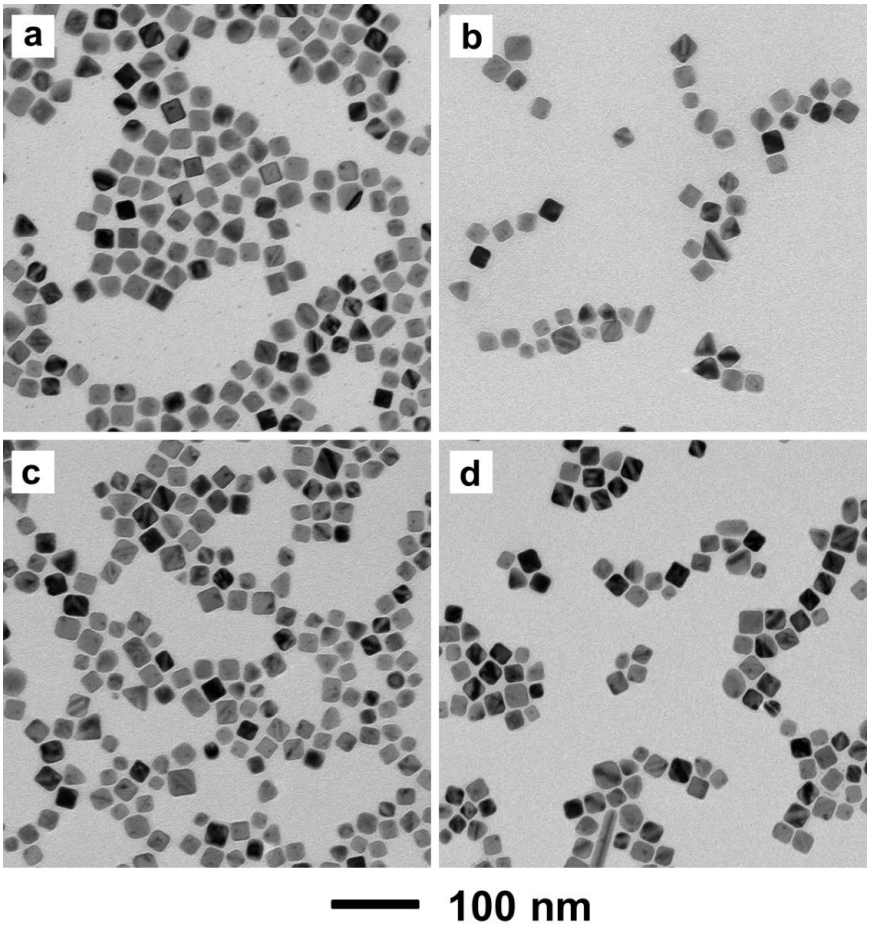

Figure 3.13. TEM images of the Au@Cu core-shell nanocubes prepared using the standard protocol except for the use of Au seed suspension (0.0262 mg·mL^{-1}) in different volumes: (a) 0.4, (b) 0.6, (c) 0.8, and (d) 1.0 mL. The average edge lengths of the resultant Au@Cu nanocubes were: (a) 23.0, (b) 21.8, (c) 21.0, and (d) 20.7 nm, respectively.

By simply varying the amount of Au seeds introduced into the reaction solution, the size of the Au@Cu core-shell nanocubes could be easily controlled. When 0.4 mL, instead of 0.2 mL, of Au seed suspension at a concentration of 0.0262 mg mL^{-1} was used, the size of the nanocubes decreased from 27.1 nm to 23.0 nm (Figure 3.13a). A further increase in the amount of Au seed suspension to 0.6, 0.8, and 1.0 mL led to the production of core-shell nanocubes with edge length of 21.8, 21.0, and 20.7 nm, respectively, and TEM images of these samples are provided in Figure 3.13, b–d. However, if all the Cu(II) precursor was supposed to be reduced to Cu atoms and deposited on the Au seeds, the edge lengths of the as-obtained nanocubes would be 21.4, 18.7, 17.1, and 15.9 nm, respectively, for the use of 0.4, 0.6, 0.8, and 1.0 mL of the Au seed suspension. Apparently, all the calculated values were smaller than the experimental results. I also measured the concentration of Cu(II) in the supernatant by ICP-MS when different amounts of Au seeds were used. Nearly the same concentration of 9.9 mM was obtained, indicating that the conversion of Cu(II) was not greatly influenced by the amount of the Au seeds. A possible explanation to the slight decrease in size for the Au@Cu nanocubes is that some of the products with small sizes were not collected when the centrifugation speed was too low.

At a fixed total amount of Cu precursor, if assuming that the newly reduced Cu atoms were evenly shared by all the seeds, increasing the number of Au seeds would lead to a decrease in size for the products. In reality, however, the Cu atoms tended to be deposited onto different Au seeds unequally, resulting in the formation of core-shell nanocubes with different sizes. While some of the Au seeds were covered by thick Cu shell, the others may only be partially covered or even unreacted. I found that small

Au@Cu nanocrystals with size in a range of 12–18 nm were observed when we increased the speed of centrifugation from 13,300 to 30,130 ×g, and these small cubes were previously not collected and taken into consideration when we calculated the average size of Au@Cu nanocubes synthesized from different amounts of Au seeds (Figure 3.14). Thus, when a larger amount of Au seeds was introduced, the proportion of small particles increased and the exclusion of them during calculation led to an increase in the average size of the nanocubes.

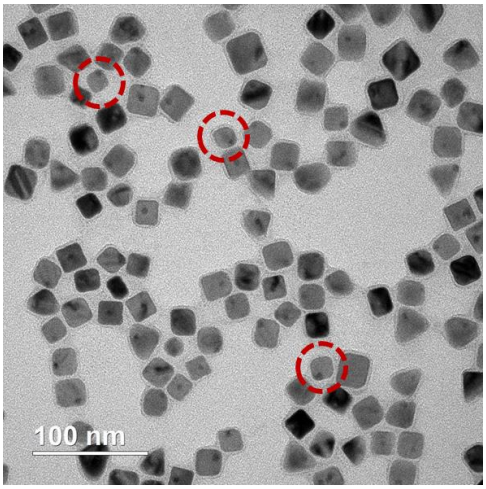

Figure 3.14. TEM image of the Au@Cu nanocubes obtained using the standard protocol and 1.0 mL of Au seed suspension (0.0262 mg/mL). The sample was collected at a speed of 30,130 ×g. Some nanocrystals with small sizes ranging from 12−18 nm are marked with red circles.

The structure and morphology of the Au@Cu nanocrystals were also influenced by the concentration of the Cu(II) precursor. When 1.05 mg of $CuCl_2$ was used, which was ten times lower than that used in the standard protocol, Au@Cu nanoplates, together with small nanocrystals in irregular shapes, were obtained (Figure 3.15a). The Au cores

can be clearly observed in the nanoplates to be surrounded by Cu, indicating that the Cu plate was grown from the Au sphere. The large lattice mismatch induced crystal twinning and the slow reduction rate of Cu(II) precursor caused by its low concentration resulted in the formation of Cu nanoplates [26]. When the reduction rate was slow and the supply of Cu atoms was limited, planar defects (including twin plane and stacking fault) were generated. Under this circumstance, nanoplates would be favored as the strain energy caused by planar defects could be mitigated by covering the surface with {111} facets, which had the lowest surface energy [35].

When the amount of $CuCl_2$ was slightly increased to 2.1 mg, as shown in Figure 3.15b, small Au@Cu nanocrystals with a tendency to grow into nanocubes were formed, together with some large particles with irregular shapes. The uniformity of the products in this stage was relatively low, with the smallest size approaching 21 nm and the largest approaching 44 nm, indicating that Cu atoms were not evenly deposited on the Au seeds. The uniformity was improved when we increased the amount of Cu(II) precursor to 5.25 mg and nanocubes, which accounted for more than 80% of the product, with an average size of 26.2 nm were obtained (Figure 3.15c). Further increase in the amount of Cu(II) precursor to 13.1 mg led to the formation of Cu nanorods, as shown in Figure 3.15d. While Au seeds could be observed in a few rods, more than 50% of the nanorods were only made of Cu and could be regarded as a product arising from self-nucleation. Taken together, it can be concluded that the concentration of Cu(II) precursor had a major impact on the structure and morphology of Au@Cu core-shell nanocrystals. A low concentration of Cu(II) precursor correspondingly led to slow reduction for the Cu(II), and nanoplates would be obtained considering the crystal twinning induced by large

lattice mismatch between Au and Cu. When a certain amount of Au seeds was used, a higher concentration of Cu(II) precursor would give rise to self-nucleation and Cu nanorods containing no Au cores were obtained.

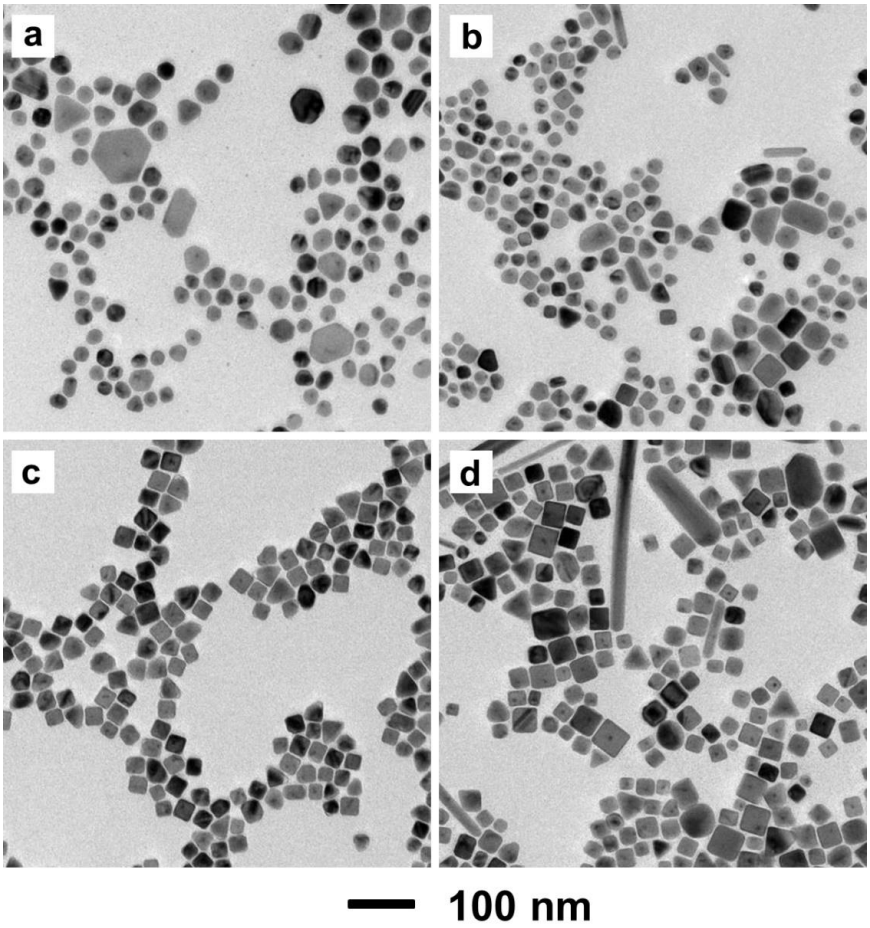

Figure 3.15. TEM images of the Au@Cu core-shell nanocrystals prepared using the standard protocol except for the use of $CuCl_2$ in different amounts: (a) 1.05, (b) 2.1, (c) 5.25, and (d) 13.1 mg, respectively.

3.3 Conclusion

I have demonstrated the synthesis of Au@Cu core-shell nanocubes in high purity

through a seed-mediated approach. The as-obtained nanocube had a randomly distributed Au core, which can be attributed to the large lattice mismatch between Au and Cu and thereby localized epitaxial overgrowth of Cu shell. By varying the reaction time and/or the amount of Au seeds, Au@Cu nanocubes with edge lengths tunable in the range of 20–30 nm could be readily obtained. When decreasing the concentration of Cu(II) precursor to a certain level, Au@Cu nanoplates rather than nanocubes were obtained. The Au@Cu core-shell nanocubes exhibited a strong extinction peak at 581 nm. Based on the DDA simulation results, the cross section of absorption was 40 times greater than that of scattering due to the small size of the nanocubes. The seed-mediated growth offers a simple, convenient, and robust route to the synthesis of Cu nanocrystals with well-defined shapes. However, it should be pointed out that it is still difficult to generate Au@Cu cubes smaller than 20 nm from 5-nm Au spherical seeds due to *i*) the uneven growth of Cu on a Au seed as a result of large lattice mismatch and *ii*) the lack of a capping agent capable of binding more strongly to {100} facets than HDA so the growth of these facets cannot be completely suppressed. Using an essentially similar protocol, I believe that relatively small Cu nanocubes can also be grown from Pt or Rh nanocrystals less than 5 nm in size. Considering the small, tunable size and the dominance of {100} facets on the surface, it is anticipated that the Au@Cu core-shell nanocubes will find use in a variety of applications, including plasmonics and catalysis.

3.4 Experimental Section

Chemicals and Materials. Gold(III) chloride trihydrate ($HAuCl_4 \cdot 3H_2O$, ≥99.9%), copper(II) chloride dihydrate ($CuCl_2 \cdot 2H_2O$, ≥99.0%), sodium borohydride ($NaBH_4$, 99%), hexadecylamine (HDA, 98%), $_D$-(+)-glucose ($C_6H_{12}O_6$, 99.5%, GC), $_L$-

ascorbic acid (AA, >99%), cetyltrimethylammonium bromide (CTAB, ≥99%), and cetyltrimethylammonium chloride solution (CTAC, 25 wt. % in H_2O) were all obtained from Sigma-Aldrich. Ethanol (200 proof) was purchased from Pharmco Products. Deionized water, which had a resistivity of 18.2 MΩ·cm at room temperature, was used in all experiments.

Synthesis of 5-nm Au Spheres. The Au spherical seeds were prepared in two steps [22]. Firstly, Au clusters were produced by adding $NaBH_4$ solution (0.6 mL, 10 mM) into a 10-mL aqueous solution containing $HAuCl_4$ (0.25 mM) and CTAB (100 mM). The solution turned brownish immediately. After shaking for 5 min, the container was transferred into a water bath set at 37 °C and undisturbed for 3 h to ensure complete decomposition of $NaBH_4$. For the synthesis of 5-nm Au spheres, 1 mL of the as-prepared Au clusters was added into a pre-mixed aqueous solution containing $HAuCl_4$ (2 mL, 0.5 mM), CTAC (2 mL, 200 mM), and AA (1.5 mL, 100 mM). The container was shaken at a speed of 300 rpm for 30 min before the Au spheres were collected by centrifugation.

Synthesis of Au@Cu Nanocubes. For a standard protocol, I added the 5-nm Au spheres (0.2 mL, 0.0262 $mg \cdot mL^{-1}$) into 5 mL of aqueous solution that contained HDA (45 mg), glucose (50 mg), and $CuCl_2 \cdot 2H_2O$ (10.5 mg) and was hosted in a 20-mL glass vial. After magnetically stirring at room temperature for about 12 h, we obtained a light blue, cloudy solution. Argon was then blown over its surface for 5 min before the vial was tightly capped and transferred into an oil bath (with temperature preset to 100 °C). After 1 h, the solid products were collected by centrifugation at 13,300 ×g, sequentially washed with water and ethanol to remove excess HDA, and finally re-dispersed in ethanol.

Characterization. TEM images were taken using a Hitachi HT7700 microscope.

Prior to imaging, the nanoparticle suspension was drop-casted onto a carbon-coated Cu grid and dried under ambient conditions. HAADF-STEM and EDX analysis was performed using a Hitachi HT2700 aberration-corrected STEM at 200 kV. SEM images were obtained on a Hitachi SU8230 scanning electron microscope at an accelerating voltage of 5 kV. UV-vis extinction spectra were measured on a Cary 60 spectrometer (Agilent Technologies, Santa Clara, CA). ICP-MS (NexION 300Q, Perkin-Elmer) was used to determine the concentration of Cu(II) ions in the supernatant. X'Pert PRO Alpha-1 diffractometer (PANalytical, Almelo, Netherlands) with a 1.8 kW ceramic copper tube source was used to record the XRD pattern. Thermo K-Alpha spectrometer with an Al Kα source (hν = 1486.6 eV) was used to record the XPS spectra.

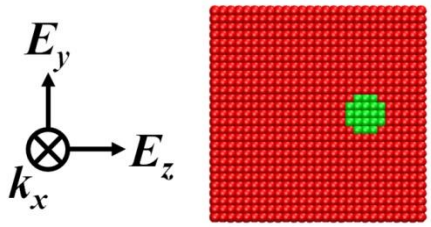

Figure 3.16. The *k*-vector and *E*-field of the incident light with respect to the orientation of an individual nanocube used for the DDA calculation.

Discrete Dipole Approximation Calculations. The simulations were carried out using the software package DDSCAT 7.3 [36,37]. For Au@Cu cubes, a continuum of dipoles (N = 19683) with a cubic shape was created using Largescale Atomic/Molecular Massively Parallel Simulator (LAMMPS) software [38] and visualized using Visual molecular dynamics (VMD) software [39]. The model was created by generating a cube, subtracting a sphere located at a specific position inside the cube, and then generating a

new sphere at the same position, which resulted in the formation of core-shell cubes with cores located at different positions. In all cases, the propagation (k-vector) and electric field (E-field) of the incident light with respect to the orientation of the nanocube are shown in Figure 3.16. The dielectric constants of pure Au and Cu were downloaded from refractiveindex.info [40]. Because all the experimental UV-vis spectra were measured using aqueous dispersions, we used the dielectric constant of water ($\varepsilon_m = n^2 = 1.78$) for the medium in all the simulations.

3.5 Notes to Chapter 3

Part of this Chapter is adapted from "Au@Cu Core−Shell Nanocubes with Controllable Sizes in the Range of 20−30 nm for Applications in Catalysis and Plasmonics" published in *ACS Applied Nano Materials* [41].

3.6 References

[1] Roberts, F. S.; Kuhl, K. P.; Nilsson, A. *ChemCatChem* **2016**, *8*, 1119–1124.

[2] Zhang, Z.; Wang, S. S.; Song, R.; Cao, T.; Luo, L.; Chen, X.; Gao, Y.; Lu, J.; Li, W. X.; Huang, W. *Nat. Commun.* **2017**, *8*, 1–10.

[3] Jeon, H. S.; Kunze, S.; Scholten, F.; Roldan Cuenya, B. *ACS Catal.* **2018**, *8*, 531–535.

[4] Rathmell, A. R.; Bergin, S. M.; Hua, Y. L.; Li, Z. Y.; Wiley, B. J. *Adv. Mater.* **2010**, *22*, 3558–3563.

[5] Lee, J. W.; Han, J.; Lee, D. S.; Bae, S.; Lee, S. H.; Lee, S. K.; Moon, B. J.; Choi, C. J.; Wang, G.; Kim, T. W. *Small* **2018**, *14*, 1–7.

[6] Zhang, P.; Sui, Y.; Wang, C.; Wang, Y.; Cui, G.; Wang, C.; Liu, B.; Zou, B. *Nanoscale* **2014**, *6*, 5343–5350.

[7] Pereira, A. J.; Gomes, J. P.; Lenz, G. F.; Schneider, R.; Chaker, J. A.; De Souza, P. E. N.; Felix, J. F. *J. Phys. Chem. C* **2016**, *120*, 12265–12272.

[8] Hsia, C. F.; Chang, C. H.; Huang, M. H. *Part. Part. Syst. Charact.* **2018**, *35*, 1800112.

[9] Cui, F.; Yu, Y.; Dou, L.; Sun, J.; Yang, Q.; Schildknecht, C.; Schierle-Arndt, K.; Yang, P. *Nano Lett.* **2015**, *15*, 7610–7615.

[10] Loiudice, A.; Lobaccaro, P.; Kamali, E. A.; Thao, T.; Huang, B. H.; Ager, J. W.; Buonsanti, R. *Angew. Chem. Int. Ed.* **2016**, *55*, 5789–5792.

[11] Luo, W.; Nie, X.; Janik, M. J.; Asthagiri, A. *ACS Catal.* **2016**, *6*, 219–229.

[12] Guo, H.; Chen, Y.; Cortie, M. B.; Liu, X.; Xie, Q.; Wang, X.; Peng, D. L. *J. Phys. Chem. C* **2014**, *118*, 9801–9808.

[13] Jin, M.; He, G.; Zhang, H.; Zeng, J.; Xie, Z.; Xia, Y. *Angew. Chem. Int. Ed.* **2011**, *50*, 10560–10564.

[14] Gao, D.; Zegkinoglou, I.; Divins, N. J.; Scholten, F.; Sinev, I.; Grosse, P.; Roldan Cuenya, B. *ACS Nano* **2017**, *11*, 4825–4831.

[15] Guo, H.; Chen, Y.; Ping, H.; Jin, J.; Peng, D. L. *Nanoscale* **2013**, *5*, 2394–2402.

[16] Yang, H. J.; He, S. Y.; Chen, H. L.; Tuan, H. Y. *Chem. Mater.* **2014**, *26*, 1785–1793.

[17] Thoka, S.; Madasu, M.; Hsia, C. F.; Liu, S. Y.; Huang, M. H. *Chem. - An Asian J.* **2017**, *12*, 2318–2322.

[18] Rej, S.; Madasu, M.; Tan, C. S.; Hsia, C. F.; Huang, M. H. *Chem. Sci.* **2018**, *9*, 2517–2524.

[19] Jin, M.; Zhang, H.; Wang, J.; Zhong, X.; Lu, N.; Li, Z.; Xie, Z.; Kim, M. J.; Xia, Y. *ACS Nano* **2012**, *6*, 2566–2573.

[20] Hsia, C. F.; Madasu, M.; Huang, M. H. *Chem. Mater.* **2016**, *28*, 3073–3079.

[21] Glaria, A.; Cure, J.; Piettre, K.; Coppel, Y.; Turrin, C. O.; Chaudret, B.; Fau, P. *Chem. - A Eur. J.* **2015**, *21*, 1169–1178.

[22] Zheng, Y.; Zhong, X.; Li, Z.; Xia, Y. *Part. Part. Syst. Charact.* **2014**, *31*, 266–273.

[23] Biesinger, M. C.; Lau, L. W. M.; Gerson, A. R.; Smart, R. S. C. *Appl. Surf. Sci.* **2010**, *257*, 887–898.

[24] Lyu, Z.; Xie, M.; Gilroy, K. D.; Hood, Z. D.; Zhao, M.; Zhou, S.; Liu, J.; Xia, Y. *Chem. Mater.* **2018**, *30*, 6469–6477.

[25] Ma, Y.; Li, W.; Cho, E. C.; Li, Z.; Yu, T.; Zeng, J.; Xie, Z.; Xia, Y. *ACS Nano* **2010**, *4*, 6725–6734.

[26] Wang, Z.; Chen, Z.; Zhang, H.; Zhang, Z.; Wu, H.; Jin, M.; Wu, C.; Yang, D.; Yin, Y. *ACS Nano* **2015**, *9*, 3307–3313.

[27] Kim, M. J.; Alvarez, S.; Chen, Z.; Fichthorn, K. A.; Wiley, B. J. *J. Am. Chem. Soc.* **2018**, *140*, 14740–14746.

[28] Yang, T. H.; Peng, H. C.; Zhou, S.; Lee, C. T.; Bao, S.; Lee, Y. H.; Wu, J. M.; Xia, Y. *Nano Lett.* **2017**, *17*, 334–340.

[29] Yang, T. H.; Zhou, S.; Gilroy, K. D.; Figueroa-Cosme, L.; Lee, Y. H.; Wu, J. M.; Xia, Y. *Proc. Natl. Acad. Sci. U. S. A.* **2017**, *114*, 13619–13624.

[30] Xia, Y.; Gilroy, K. D.; Peng, H. C.; Xia, X. *Angew. Chem. Int. Ed.* **2017**, *56*, 60–95.

[31] Link, S.; El-Sayed, M. A. *J. Phys. Chem. B* **1999**, *103*, 4212–4217.

[32] Zhang, J.; Li, S.; Wu, J.; Schatz, G. C.; Mirkin, C. A. *Angew. Chemie* **2009**, *121*, 7927–7931.

[33] Jain, P. K.; Lee, K. S.; El-Sayed, I. H.; El-Sayed, M. A. *J. Phys. Chem. B* **2006**, *110*, 7238–7248.

[34] Yang, X.; Yang, M.; Pang, B.; Vara, M.; Xia, Y. *Chem. Rev.* **2015**, *115*, 10410–10488.

[35] Xiong, Y.; Siekkinen, A. R.; Wang, J.; Yin, Y.; Kim, M. J.; Xia, Y. *J. Mater. Chem.* **2007**, *17*, 2600–2602.

[36] Draine, B. T.; Flatau, P. J. *J. Opt. Soc. Am. A* **1994**, *11*, 1491.

[37] Drain, B. T.; Piotr, F. J. *User Guide for the Discrete Dipole Approximation Code DDSCAT 7.3*, **2013**.

[38] Plimpton, S. *J. Comput. Phys.* **1995**, *117*, 1–19.

[39] Humphrey, W.; Dalke, A.; Schulten, K. *J. Mol. Graph.* **1996**, *14*, 33–38.

[40] Johnson, P. B.; Christy, R. W. *Phys. Rev. B* **1972**, *6*, 4370–4379.

[41] Lyu, Z.; Xie, M.; Aldama, E.; Zhao, M.; Qiu, J.; Zhou, S.; Xia, Y. *ACS Appl. Nano Mater.* **2019**, *2*, 1533–1540.

CHAPTER 4

KINETICALLY-CONTROLLED SYNTHESIS OF PALLADIUM-COPPER JANUS NANOCRYSTALS WITH ENRICHED SURFACE STRUCTURES AND ENHANCED CATALYTIC ACTIVITIES TOWARD CARBON DIOXIDE REDUCTION

4.1 Introduction

Bimetallic nanocrystals have received ever increasing interest for their enriched properties and enhanced applications relative to the monometallic system [1]. The involvement of two metals, for example, allows one to enhance the catalytic activity of nanocrystals toward various reactions by leveraging the geometric and ligand effects. Among the different configurations, those with a Janus or side-by-side structure are particularly attractive because both of the metals are presented on the surface. In recent years, seed-mediated and site-selected growth has emerged as one of the most effective routes to the synthesis of bimetallic nanocrystals with a Janus structure [2,3]. The success in synthesis has led to the development of catalysts with augmented performance. For example, Au nanorods bearing Pt tips at the ends showed a greatly enhanced activity toward the photocatalytic HER relative to the Au-Pt bimetallic nanocrystals with a core-shell structure [4]. By spatially confining Pt to the two ends of a Au nanorod, hot electrons could be effectively generated *via* the excitation of surface plasmons in the Au component and then transferred to the Pt tips for reducing H^+ to H_2.

While seed-mediated synthesis can be easily and conveniently implemented, it is nontrivial to achieve site-selected growth. In many cases, the lack of an internal or external driving force makes it rather difficult to ensure that the incoming atoms only nucleate and grow from one of the multiple equivalent sites on a seed [2]. From the point of thermodynamics, it is not favorable to generate the high-index facets and large surface areas typically associated with the products of site-selected growth [5]. In addition, surface diffusion tends to move the deposited atoms to other regions on the surface of a seed, ruining the pattern of site-selected growth [6]. A number of strategies have been developed to address these issues, including manipulation of the reduction kinetics of the precursor [7,8], partial passivation of the surface of a seed through the use of a capping agent [9,10], introduction of oxidative etching [11], and leverage of lattice mismatch between the two metals [12].

Copper (Cu) and Cu-based nanocrystals have received considerable interest in recent years owing to their outstanding performance in catalysis, as well as the excellent electric conductivity, high abundance in the Earth's crust, and low price of Cu [13]. They have been extensively explored as catalysts toward the electrochemical reduction of CO_2, and Cu is one of the few metals capable of generating appreciable amounts of hydrocarbons, in particular, C_{2+} species such as ethylene and ethanol with high values and large markets [14,15]. However, current Cu-based catalysts are plagued by problems such as high overpotential, low selectivity, and poor stability. Some of these issues can be addressed by maneuvering the composition, shape, and twin structure of the Cu-based catalysts. For example, it was reported that the presence of planar defects on the surface could strengthen the binding of CO and thereby increase the CO coverage density to

promote C-C coupling [16]. Such a modification has led to a high selectivity (52.4%) toward ethylene at -1.0 V_{RHE} in 0.1 M $KHCO_3$ electrolyte. On the other hand, introducing Pd or Ag into Cu in the form of segregated, nanoscale domains was able to improve the selectivity toward ethylene relative to a catalyst based on Cu nanoparticles, demonstrating the important role of both the composition and spatial distribution in determining the performance of a Cu-based catalyst [17,18].

Considering the benefits from planar defects and a segregated, bimetallic composition, I sought to develop a class of effective catalysts toward CO_2 reduction by controlling the growth of Cu from Pd icosahedral seeds. The multiple twin defects intrinsic to an icosahedron would be able to direct the deposition of Cu atoms for the generation of twin boundaries on the surface of the resultant Cu nanocrystal [19]. The large lattice mismatch (7.1%) between Pd and Cu would favor both site-selected nucleation and island growth, enabling the production of a Pd-Cu nanocrystal featuring a Janus structure [20]. It was envisioned that catalysts with such a favorable combination of twin boundaries and segregated composition would exhibit significantly improved activity, selectivity, and onset potential for the formation of C_{2+} products during the electrochemical reduction of CO_2 [21].

Here I report that Pd-Cu Janus nanocrystals with different shapes for the Cu component can be obtained by varying the experimental conditions used for seed-mediated growth involving Pd icosahedra. Specifically, by increasing the concentration of the precursor, the nucleation and growth of Cu could be shifted from a vertex to an edge of the icosahedral seed for the formation of nanocrystals in the shape of pentagonal bipyramid, decahedron, or truncated bitetrahedron. The concentration of HDA, a

stabilizer and a coordination ligand, also played an important role in the seed-mediated synthesis. An increase in HDA concentration favored the formation of pentagonal bipyramids and decahedra, whereas truncated bitetrahedra were obtained at a reduced concentration. The as-synthesized Pd-Cu nanocrystals were evaluated as catalysts toward the electrochemical reduction of CO_2. An onset potential as low as -0.7 V_{RHE}, together with a high selectivity approaching 51.0% at -1.0 V_{RHE}, was achieved for the production of C_{2+} species in a 0.5 M $KHCO_3$ electrolyte. The performance was greatly improved relative to other catalysts based on Cu (Table 4.1) [22–25].

Table 4.1. Comparison of Pd-Cu Janus nanocrystals in this work with other Cu-based catalysts reported in literature, with 0.5 M $KHCO_3$ serving as the electrolyte for all the measurements listed below.

Catalyst	E vs. RHE	Onset potential for C_{2+}	Faradaic efficiency (%)				Ref
			H_2	CH_4	C_2H_4	C_{2+}	
Pd-Cu pentagonal bipyramids	-1.0	-0.7	28.5	4.8	31.3	50.3	This work
Pd-Cu decahedra	-1.0	-0.7	25.9	6.2	34.0	51.0	This work
Pd-Cu truncated bitetrahedra	-1.0	-0.7	35.7	10.2	25.4	38.5	This work
Cu octahedra	-1.0	-0.85	N/A	15	7.5	N/A	[23]
Cu cubes	-1.05	-0.8	N/A	25	21	N/A	[23]
polydopamine-coated Cu nanowires	-0.93	-0.7	10	29	17	N/A	[24]
Pd-decorated Cu	-0.96	-0.85	30	46	5	N/A	[25]
Branched CuO	-1.0	<-0.7	53	5	36	~36	[22]
Cubic Cu_2O	-0.9	<-0.7	75	2	25	~25	[22]

Furthermore, my collaborators performed DFT calculations and constructed Pourbaix phase diagrams to investigate the role of Pd, either in its metallic or hydride form, in the bimetallic catalysts. It was demonstrated that a CO coverage exceeding 6/9 monolayer (ML) on Pd(111) or 5/9 ML on the PdH surface was required for CO spillover from Pd to Cu, both clearly achievable under the experimental conditions of the present study. Upon migration to the Cu sites, the CO could undergo C-C coupling for the generation of C_{2+} products. Additionally, we also explored the catalytic role of twin boundaries on Cu surface by comparing the binding energies of common CO_2 reduction intermediates on the twin boundary with those on the Cu(111) terrace.

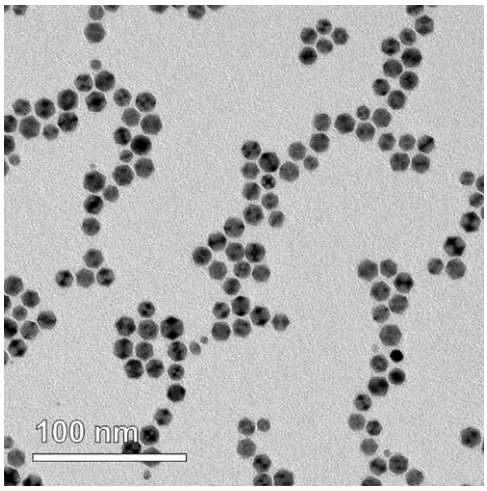

Figure 4.1. TEM image of the Pd icosahedra that served as seeds for the growth of Cu.

4.2 Results and Discussion

Pd-Cu Janus Nanocrystals with Three Different Shapes. As a highly symmetric object, the surface of an icosahedron is covered by 12 equivalent penta-twinned apexes as

the vertices, 30 equivalent twin boundaries as the edges, and 20 equivalent {111} facets as the side faces [26,27]. Figure 4.1 shows a typical TEM image of the as-prepared Pd icosahedral seeds, which had an average size of 12.7 ± 1.3 nm (see Figure 4.2 for the definition of size).

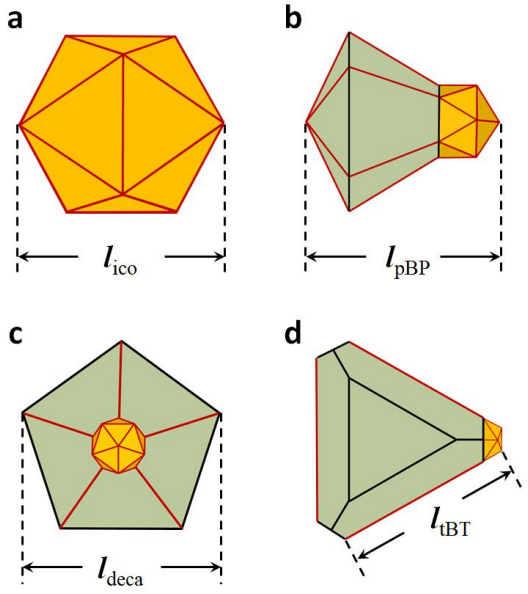

Figure 4.2. Definitions of the size or edge length of (a) an icosahedron (l_{ico}), (b) a pentagonal bipyramid (l_{pBP}), (c) a decahedron (l_{deca}), and (d) a truncated bitetrahedron (l_{tBT}).

As shown in Figure 4.3, with them serving as the seeds, I was able to obtain Pd-Cu Janus nanocrystals featuring three distinctive shapes for the Cu component by simply increasing the amount of the Cu(II) precursor involved in the synthesis. Specifically, at a fixed amount of 45 mg for HDA, I obtained Cu nanocrystals in the shapes of pentagonal bipyramid, decahedron, and truncated bitetrahedron, respectively, when 1.05, 5.25, and 10.5 mg of $CuCl_2$ were involved.

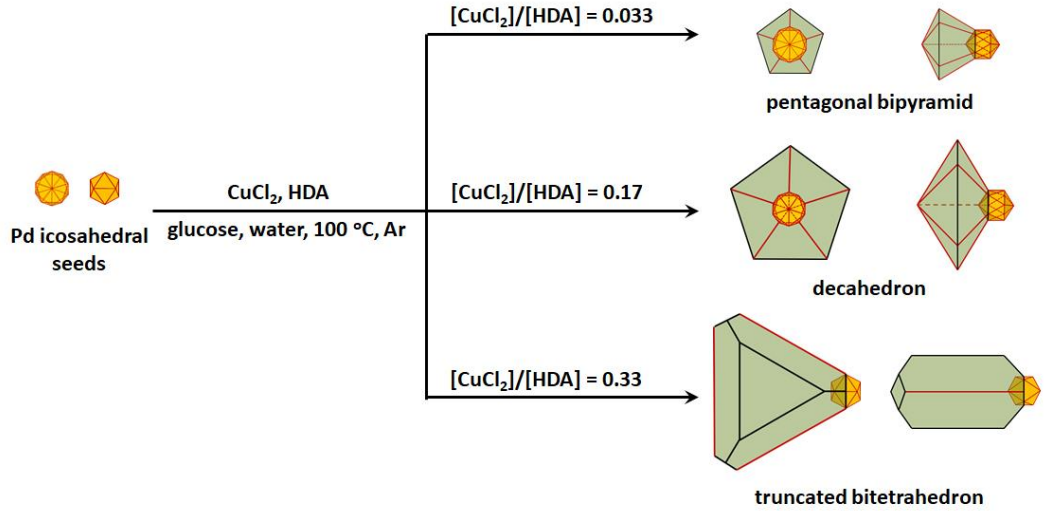

Figure 4.3. Summary of the experimental conditions corresponding to the formation of Pd-Cu Janus nanocrystals with three distinctive shapes for the Cu component: pentagonal bipyramid, decahedron, and truncated bitetrahedron. The Pd and Cu components are shown in yellow and green colors, respectively. The red lines indicate the twin boundaries on the nanocrystal.

Structural characterizations of the Pd-Cu nanocrystals with different shapes are summarized in Figure 4.4. Analyses of about 180 particles for each shape on the TEM images gave purity of 72% for the pentagonal bipyramids with an average size of 26.1 ± 2.5 nm, 79% for the decahedra with an average size of 39.3 ± 2.7 nm, and 84% for the truncated bitetrahedra with an average size of 48.2 ± 3.5 nm. The definition of size for each type of nanocrystal can be found in Figure 4.2, b–d. For the pentagonal bipyramid (Figure 4.4b), I was able to identify the borderline between Pd and Cu under bright-field (BF) STEM imaging, which confirmed a Janus structure for the overall nanocrystal. I also resolved the twin boundaries in the Cu portion, as highlighted by the red dashed lines.

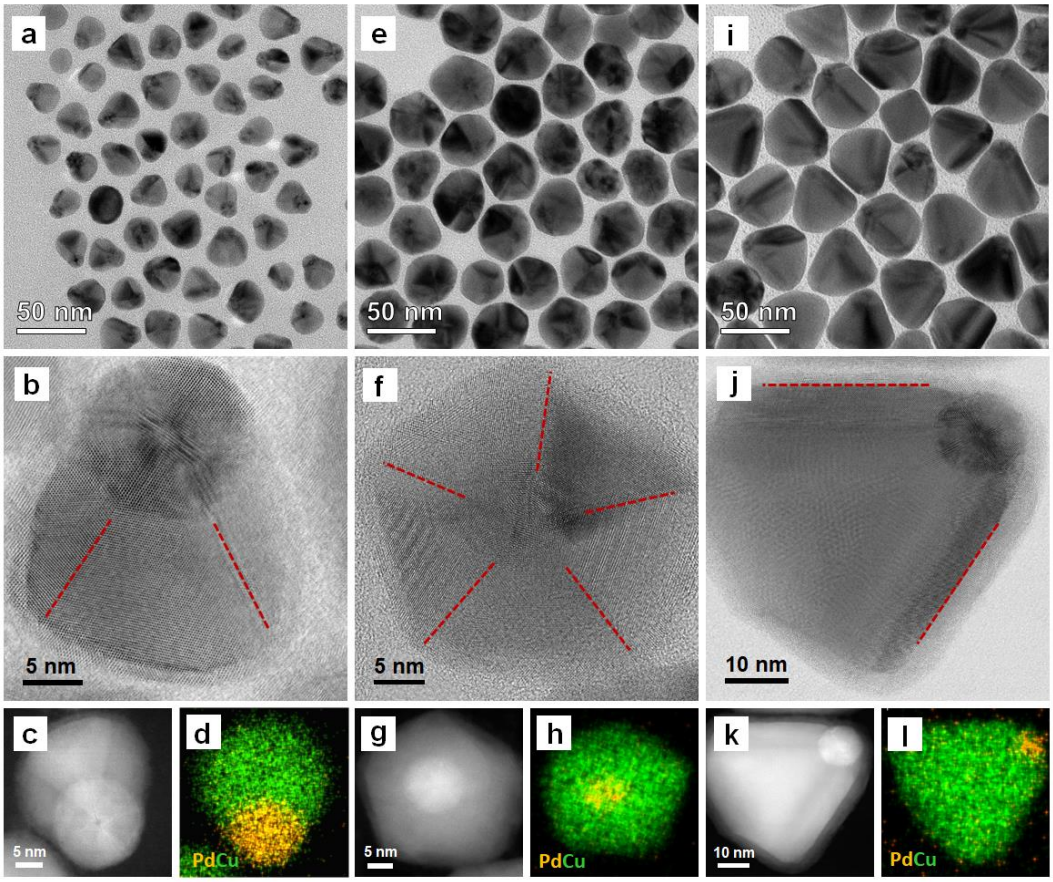

Figure 4.4. Characterizations of the Pd-Cu Janus nanocrystals prepared using the standard protocols: (a) TEM, (b) BF-, (c) DF-STEM, and (d) EDX mapping images of the pentagonal bipyramids; (e) TEM, (f) BF-, (g) DF-STEM, and (h) EDX mapping images of the decahedra; (i) TEM, (j) BF-, (k) DF-STEM, and (l) EDX mapping images of the truncated bitetrahedra. The yellow and green colors in (d), (h), and (l) correspond to Pd and Cu, respectively. The red dashed lines indicate the twin boundaries.

A horizontal projection of this penta-twinned nanocrystal is shown in Figure 4.5, revealing its pentagonal base and twin boundaries. Taken together, it can be concluded that the Cu portion had a pentagonal-bipyramidal shape and a penta-twinned structure. Different from the conventional bipyramids where the two pyramidal portions are related by reflectional symmetry, one side of the as-prepared Cu bipyramid was elongated while the other side could be hardly seen. In a sense, this new bipyramid had an asymmetric

shape similar to that of a light bulb [28]. The segregation in composition was further supported by the dark-field (DF) STEM image and EDX mapping data shown in Figure 4.4, c and d, where the signals for Pd and Cu were spatially separated from each other.

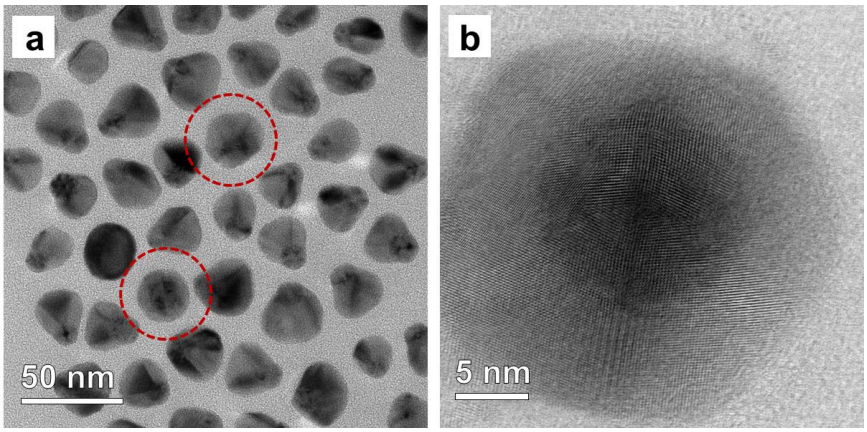

Figure 4.5. (a) TEM image of the Pd-Cu pentagonal bipyramids prepared using the standard protocol. The nanocrystals in horizontal projection were marked by red circles. (b) BF-STEM image showing the horizontal projection of a Pd-Cu pentagonal bipyramid.

Figure 4.4f shows a BF-STEM image of the decahedron, in which the five twin boundaries in Cu could be clearly resolved around the Pd seed. Interestingly, the locations of these twin defects were aligned with those in the original Pd icosahedral seed, suggesting that the twin boundaries intersecting the vertex of Pd icosahedron induced the formation of twin defects in Cu. The flat shape, pentagon projection, and penta-twinned structure all pointed toward a decahedral shape for the nanocrystal. According to the DF-STEM image in Figure 4.6, the Pd seed was located at one of the two axial vertices of the Cu decahedron instead of the center, suggesting that Cu was only grown from one side of the Pd seed. The Janus structure of the decahedra is similar to that of the pentagonal bipyramid.

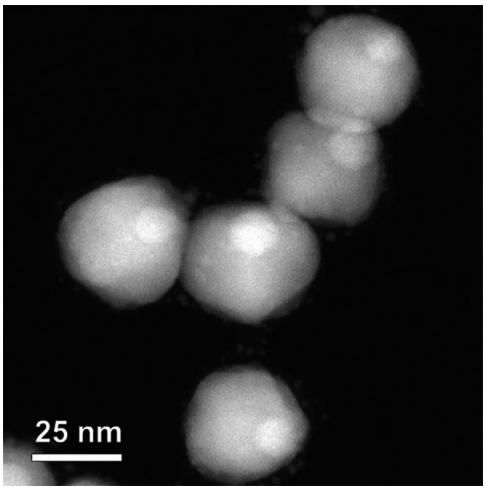

Figure 4.6. DF-STEM image showing the position of the Pd icosahedral seed in each Pd-Cu decahedron.

As for the truncated bitetrahedron shown in Figure 4.4j, the Pd seed was positioned at one of the three vertices on the equatorial plane. From the side view of a truncated bitetrahedron (Figure 4.7a), the twin boundary is next to the center of a projected hexagon while passing through the Pd seed, illustrating the singly twinned structure of the nanocrystal. Severe truncation was also observed at two corners along the axis perpendicular to the triangular base. In the [011] direction, the angle of the corner next to the Pd seed was measured to be 55°, indicating that the bipyramid was consisted of two truncated tetrahedra placed together by sharing one base [29,30]. A close examination of the flat triangular plane reveals that it was terminated in {111} facets, further confirming the truncated-bitetrahedral shape (Figure 4.7, b–d). Figure 4.4, h and l, shows EDX mapping of the decahedron and truncated bitetrahedron, confirming the spatial separation between the distributions of Pd and Cu.

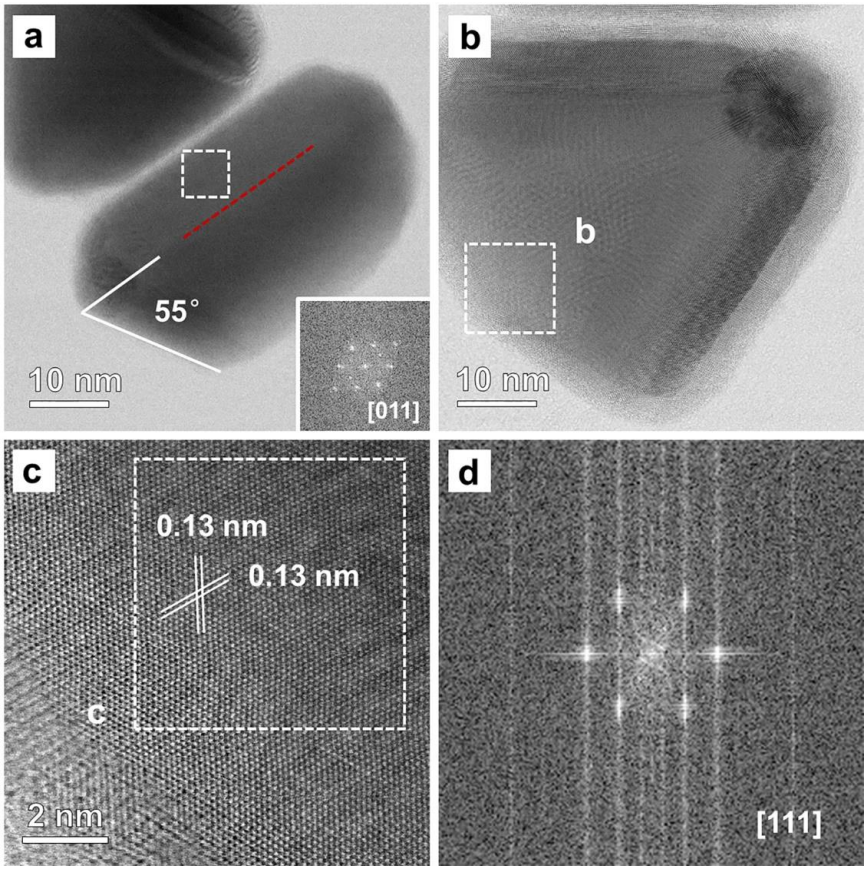

Figure 4.7. (a) BF-STEM image of a truncated bitetrahedron viewed along <011> zone axis. The angle between side face and triangular base was measured to be 55°. The twin boundary is marked by a red dashed line. (b) BF-STEM image of the truncated bitetrahedron shown in Figure 4.4j; (c) BF-STEM image taken from the region marked by a box in (b); (d) Fast Fourier transform (FFT) pattern of the region marked in (c).

Figure 4.8 shows the XRD patterns and XPS spectra of the Pd-Cu nanocrystals. For the pentagonal bipyramids (Figure 4.8a), the product containing the highest proportion of Pd, the three peaks positioned at 43.4°, 50.5°, and 74.3° can be attributed to the diffraction from Cu(111), (200), and (220) planes while the weak peak located at 40° can be assigned to the Pd(111) plane. The separation between the peaks of Cu and Pd further confirmed that these two elements were not mixed together to form an alloy [17]. Different from the case of pentagonal bipyramids, no signal was observed for Pd in the

XRD patterns of decahedra and truncated bitetrahedra due to its low content (Figure 4.8, c and e) while the peaks for Cu were obvious.

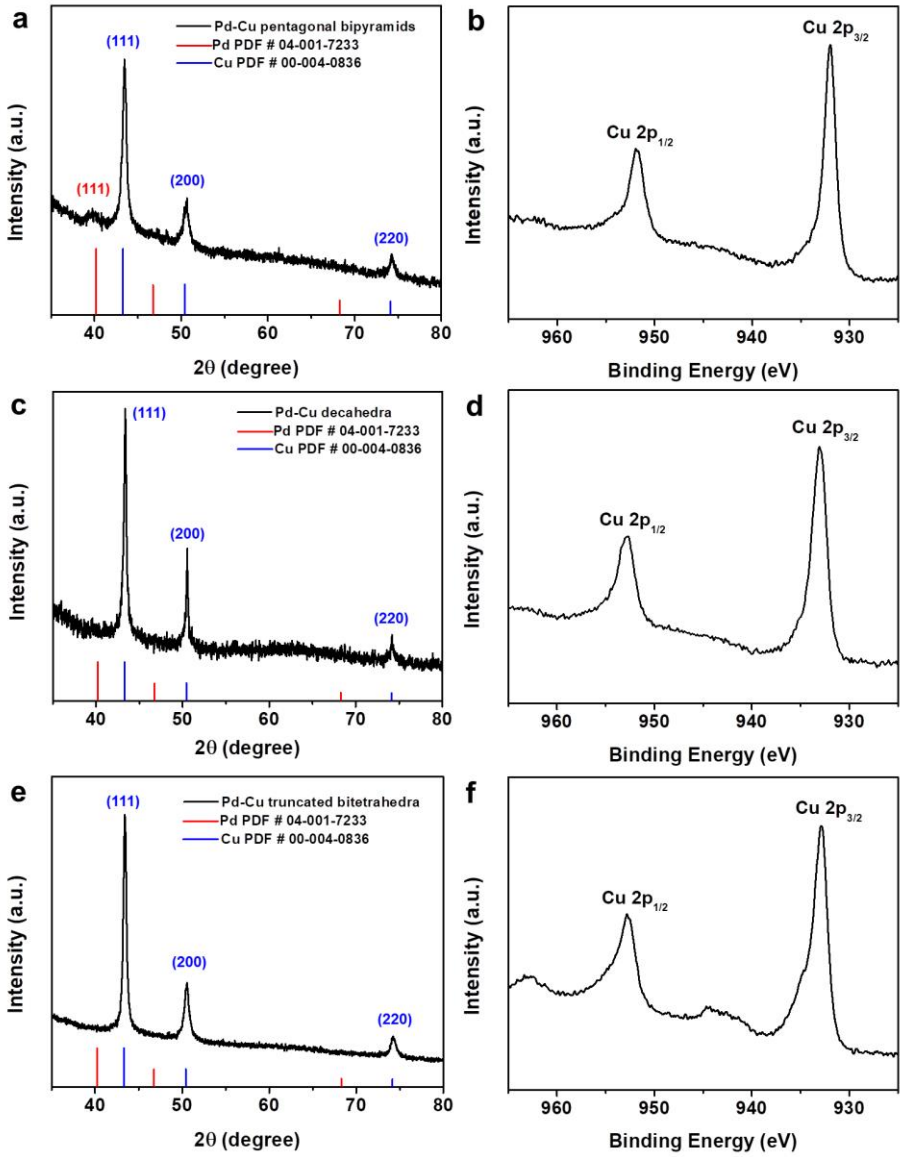

Figure 4.8. Powder XRD patterns and XPS spectra recorded from Pd-Cu nanocrystals in the shape of (a, b) pentagonal bipyramid, (c, d) decahedron, and (e, f) truncated bitetrahedron, respectively.

In the XPS spectra of all the three samples, the Cu 2p peaks were observed at

952.0 and 932.0 eV. In Figure 4.8f, two weak satellite peaks were found at 962.5 and 944.5 eV, which could be attributed to the Cu oxide layer on the surface of the truncated bitetrahedra, a phenomenon commonly observed for Cu-based nanocrystals [31,32].

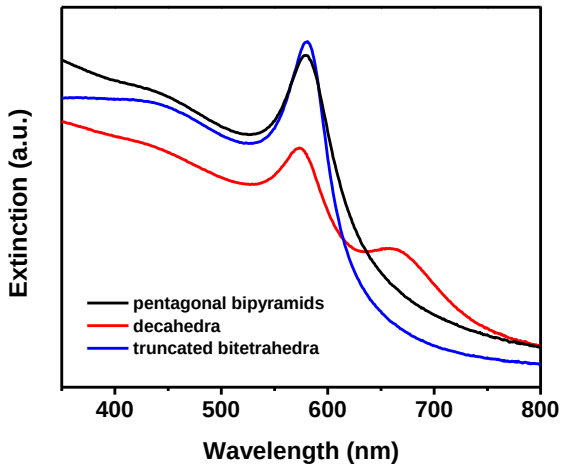

Figure 4.9. UV-vis extinction spectra of the Pd-Cu nanocrystals with different shapes.

Figure 4.9 shows the UV-vis spectra recorded from aqueous suspensions of the Pd-Cu nanocrystals. All of them exhibited extinction peaks in the visible region owing to the LSPR associated with Cu. The spectrum of the decahedra featured two resolvable peaks, corresponding to the transverse and longitudinal modes arising from the anisotropy of the decahedral shape [33]. Different from the decahedra, only one peak was observed for both the pentagonal bipyramids and truncated bitetrahedra. The former can be attributed to their pseudo-spherical shape, while the latter might be caused by the high aspect ratio and thus relatively low intensity of the transverse dipole resonance [32,34–36].

Elucidation of the Growth Mechanism. To gain mechanistic insights into the

formation of Pd-Cu nanocrystals with three different shapes, I analyzed the products obtained at different stages of each standard synthesis using TEM. Figure 4.10 shows the shape evolution in the synthesis of Pd-Cu pentagonal bipyramids. Specifically, Cu atoms were generated and initially deposited on one side of the Pd icosahedral seed to take an elliptical shape at t = 30 min (Figure 4.10a). Due to the large lattice mismatch (7.1%) between Pd and Cu, the Cu atoms preferred to grow from the already deposited Cu instead of the Pd surface, leading to the formation of one Cu bud on the Pd seed [20].

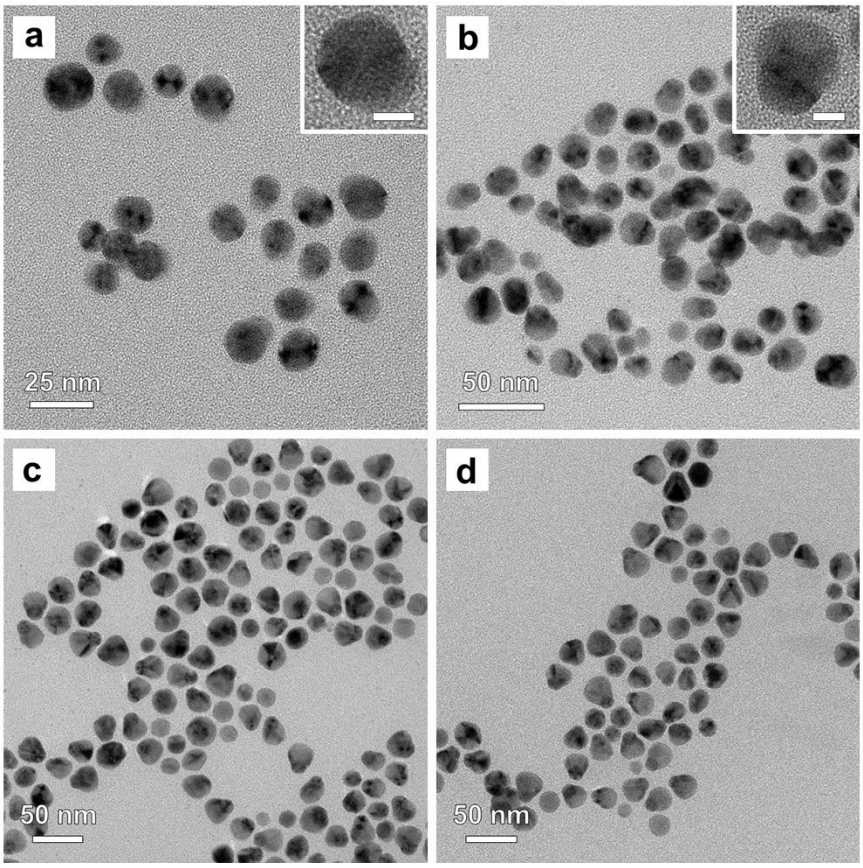

Figure 4.10. TEM images of the Pd-Cu pentagonal bipyramids prepared using the standard protocol except for the variation in reaction time: (a) 30, (b) 60, (c) 90, and (d) 120 min, respectively. The scale bars in the inset of (a) and (b) are 8 nm.

At t = 60 min (Figure 4.10b), more Cu atoms were generated and the Janus structure of the nanocrystals became more obvious. For some of the nanocrystals obtained at this stage, the twin defects could be clearly resolved during TEM imaging. After another 30 min, the majority of the nanocrystals grew into the pentagonal-bipyramidal shape, and further extension of the reaction time to 120 min did not cause additional changes to the shape and size of the nanocrystals (Figure 4.10, c and d). I also observed some Cu nanocrystals containing no Pd seeds in the products, which could be attributed to homogeneous rather than heterogeneous nucleation [37]. Since the nanocrystals made of pure Cu and the Pd-Cu nanocrystals were more or less similar in terms of size, both of them could prevail in the products owing to the suppression of Ostwald ripening [38]. From the penta-twinned structure of the bipyramid, it can be concluded that the Cu atoms initially nucleated from one of the vertices of an icosahedral seed, followed by gradual growth into an elongated, pentagonal bipyramid.

Similar to the case of pentagonal bipyramids, the Cu atoms were also selectively deposited on one side of the Pd seed during the synthesis of Pd-Cu decahedra, with Figure 4.11a showing a TEM image of the sample obtained at t = 10 min. There were also some hollow nanocrystals bearing voids next to the surface, and their formation could be attributed to the oxidation of Cu by the Kirkendall effect when washing the sample with water. The faster outward diffusion of Cu compared to the inward diffusion of oxygen led to the generation of voids next to the surface. This phenomenon was commonly observed during the storage of Cu particles [39], and similar hollow structures were also found in the early stage of truncated bitetrahedra (Figure 4.12a). At t = 20 min (Figure 4.11b), more Cu atoms were generated to increase the dimension of the Cu portion, together with

the appearance of twin boundaries. Interestingly, the shape of the nanocrystals at this stage was quite similar to that of the pentagonal bipyramids, indicating that the pentagonal bipyramid might be an intermediate involved in the formation of a decahedron.

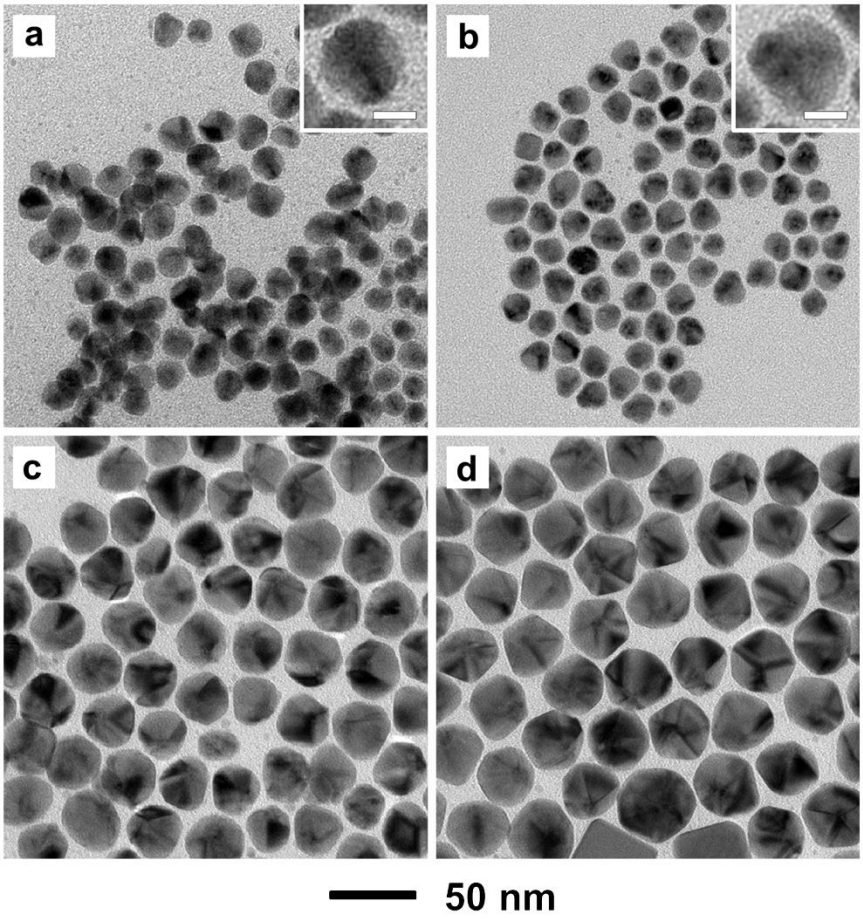

Figure 4.11. TEM images of the Pd-Cu decahedra prepared using the standard protocol except for the variation in reaction time: (a) 10, (b) 20, (c) 60, and (d) 120 min, respectively. The scale bars in the insets of (a) and (b) are 10 nm.

When extending the time to t = 60 min, the nanocrystals were found to grow laterally and their decahedral shape became obvious (Figure 4.11c). Finally, most of the

nanocrystals evolved into a decahedral shape at t = 120 min (Figure 4.11d). Taken together, it can be concluded that the Cu atoms also selectively nucleated from one of the vertices of an icosahedral seed at the beginning of a synthesis for the formation of pentagonal bipyramids. In the presence of an adequate supply of Cu atoms, they finally evolved into decahedra.

For the synthesis of Pd-Cu truncated bitetrahedra, the growth took a pathway different from what was described for the other two shapes mentioned above. As shown in Figure 4.12a, I observed intermediates with a rod-like shape in the initial stage (t = 30 min) of a synthesis. The Pd icosahedral seed could be found at one of the two ends of the rod, with a single twin boundary passing through it. There were also small, pseudo-spherical Cu particles in the sample, and they disappeared after another 30-min into the synthesis due to Ostwald ripening (Figure 4.12b). With the supply of more Cu atoms, the rods evolved into a singly-twinned, bitetrahedral structure with truncation at axial corners. When the reaction time was extended to 90 and 120 min, respectively, the average edge length of the truncated bitetrahedra increased to 45.6 and 46.1 nm, together with a slight increase in sharpness for the corners at the equilateral plane (Figure 4.12, c and d). In addition to the Pd-Cu truncated bitetrahedra, I observed some Pd-Cu decahedra and pure Cu particles in a cubic or irregular shape in the product, which could be attributed to the growth of a small proportion of Cu atoms from vertices or the presence of homogeneous nucleation. Based on the TEM images and the singly-twinned structure, it can be concluded that Cu was initially deposited onto one edge, instead of one vertex, of the Pd icosahedral seed, followed by growth into a truncated bitetrahedron as the reaction proceeded.

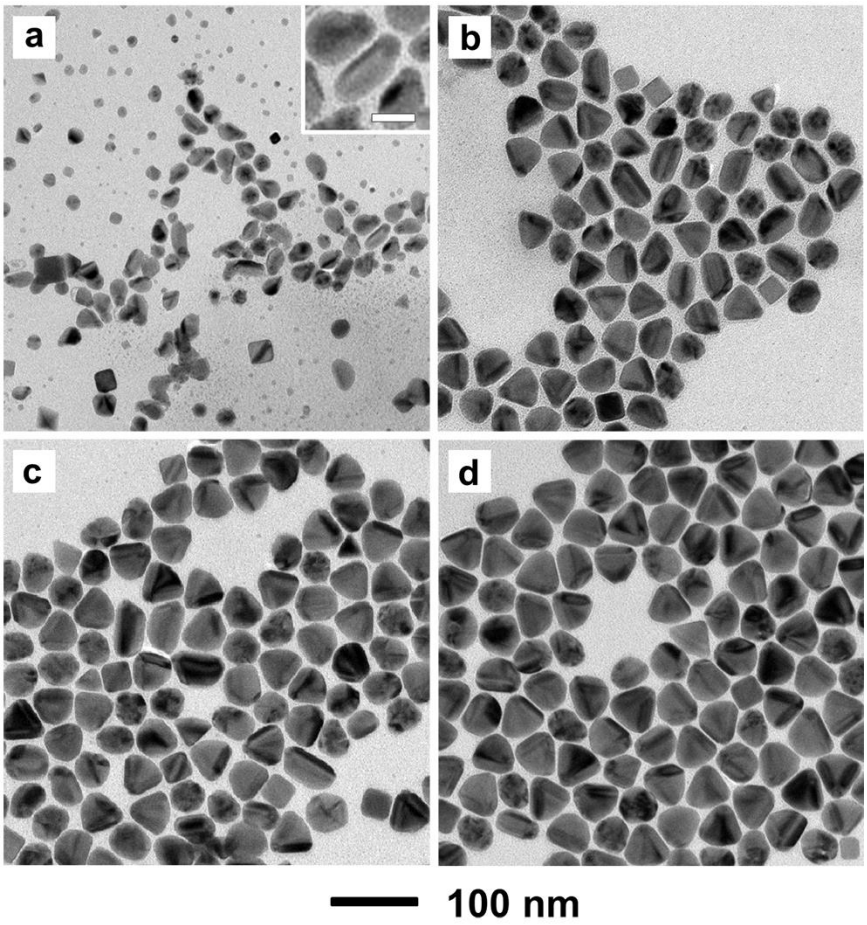

Figure 4.12. TEM images of the Pd-Cu truncated bitetrahedra prepared using the standard protocol except for the variation in reaction time: (a) 30, (b) 60, (c) 90, and (d) 120 min, respectively. The scale bars in the inset of (a) is 20 nm.

The Role of the Cu(II) Precursor. For the syntheses of Pd-Cu Janus nanocrystals with different shapes, the only variance is the amount of the Cu(II) precursor involved. When a small amount of $CuCl_2$ was used, the newly formed Cu atoms tended to nucleate and grow from one of the vertices of an icosahedral seed due to the low coordination number and high surface strain at this site [40]. The as-obtained Cu nanocrystals would take a penta-twinned structure because of the influence from the five twin planes intersecting at the vertex of the icosahedral seed. Upon increasing the amount of $CuCl_2$,

the increased supply of Cu atoms would drive them to either diffuse to or directly nucleate from the edge [19]. As a result of the twin boundary at the edge, the deposited Cu took a singly-twinned structure.

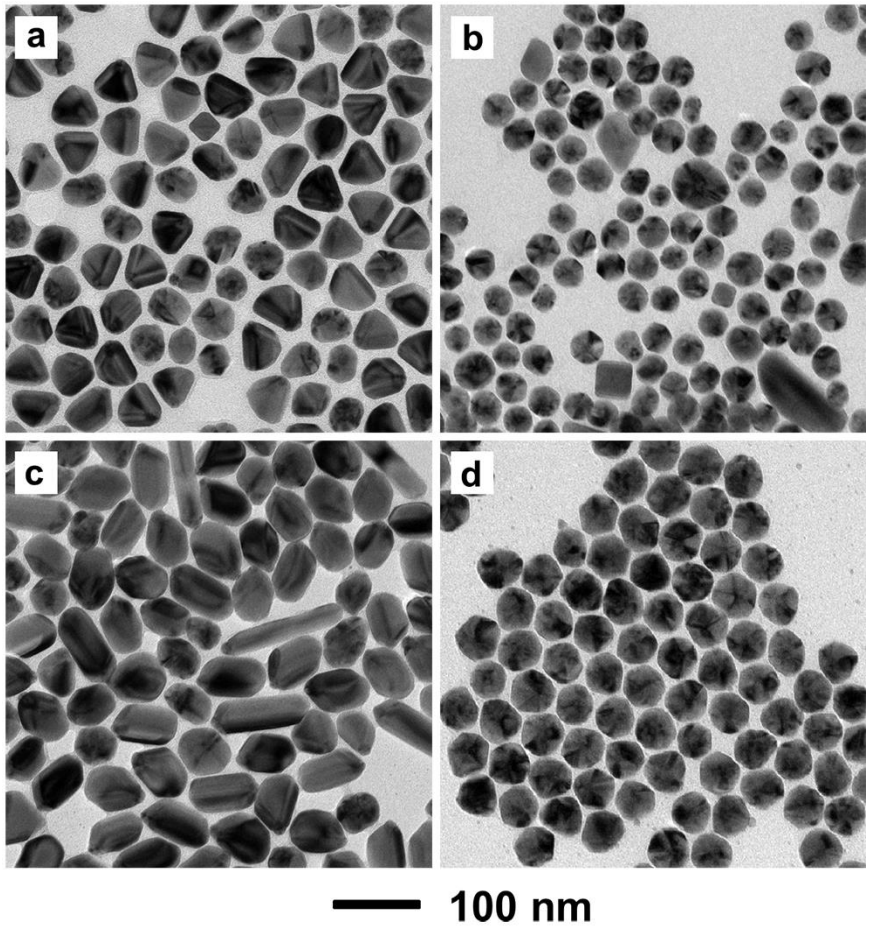

Figure 4.13. (a, b) TEM images of the Pd-Cu nanocrystals prepared using the standard protocol for decahedra except for the variation in the amount of HDA from 45 mg to (a) 22.5 and (b) 90 mg; (c, d) TEM images of the Pd-Cu nanocrystals prepared using the standard protocol for truncated bitetrahedra except for the variation in the amount of HDA from 45 mg to (c) 35 and (d) 90 mg.

The Role of HDA. When the concentration of the Cu(II) precursor was fixed, varying the concentration of HDA also resulted in the formation of Cu nanocrystals with

distinctive shapes. With reference to the standard protocol for the synthesis of Pd-Cu decahedra, the product was dominated by truncated bitetrahedra when 22.5 mg instead of 45 mg of HDA was used, as shown in Figure 4.13a. A small fraction of Pd-Cu decahedra and pseudo-spherical Cu nanocrystals was also observed as the byproducts. When increasing the amount of HDA to 90 mg, Pd-Cu decahedral nanocrystals were again obtained, together with a few large, irregular-shaped Cu nanoparticles or Pd-Cu nanorods with Pd seed located at one end (Figure 4.13b). Relative to the standard protocol for the synthesis of Pd-Cu truncated bitetrahedra, if 35 mg instead of 45 mg of HDA was used, the majority of the product was still singly-twinned bitetrahedra, together with a small portion of Pd-Cu nanorods (Figure 4.13c). When 90 mg of HDA was used, which was twice as much as the amount of HDA used in the standard protocol, Pd-Cu decahedra in high purity were obtained, together with an average size of 46.8 nm (Figure 4.13d). These observations indicate that the concentration of HDA had a major impact on the shape evolution of the nanocrystals.

To make the trends more obvious, I did a set of experiments by varying the amounts of $CuCl_2$ and HDA, and the corresponding TEM images are shown in Figure 4.14, with their dominant products summarized in Table 4.2. It is worth mentioning that, when 22.5 mg of HDA and 10.5 mg of $CuCl_2$ were used, no Cu nanocrystals were obtained. The main reason might be the lack of an adequate amount of HDA to protect the relatively large number of Cu atoms on the surface from being oxidized [41].

Fixing the concentration of the Cu(II) precursor, I observed the switching from truncated bitetrahedra to decahedra and pentagonal bipyramids as the amount of HDA

was increased, opposite to the trend observed for the Cu(II) precursor. To address this issue, I first looked into the role played by HDA in the synthesis of Cu nanocrystals.

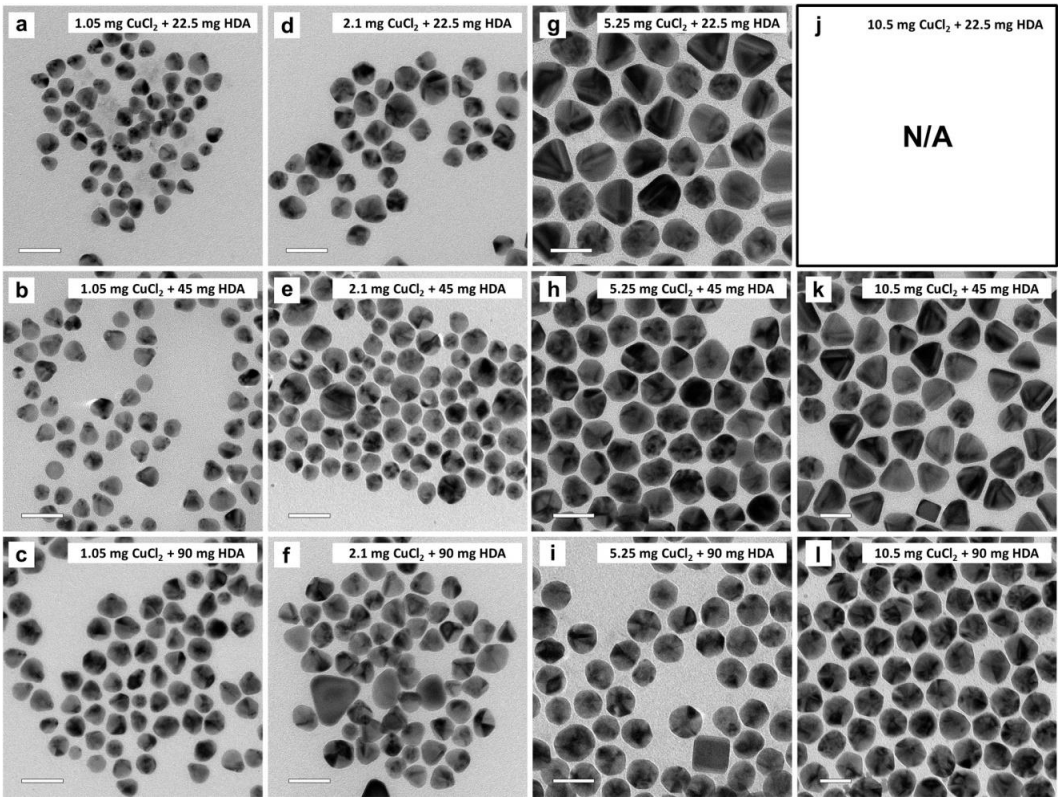

Figure 4.14. TEM images of the Pd-Cu nanocrystals shown in Table 4.2. The scale bars are 50 nm. (N/A represents no product obtained.)

Typically, the influence of HDA can be understood from two different angles. Firstly, HDA can coordinate to Cu(II) ions to generate Cu(II)-HDA complexes, slowing down the reduction of the Cu(II) precursor. As a reference, after coordinating with NH_3, the standard reduction potential of $Cu(NH_3)_4^{2+}$/Cu pair is reduced from 0.34 to 0 V_{SHE}, making it more difficult to reduce the Cu(II) ions [42,43]. Secondly, HDA can serve as a capping agent and a colloidal stabilizer for Cu nanocrystals, preventing the Cu atoms

from being oxidized by the oxygen from air [41]. In our previous work on the synthesis of Pd@Cu core-shell nanocubes, a double layer of HDA was found to cover the Cu nanocrystals and it was believed to improve the chemical stability of the nanocubes [20].

Table 4.2. The dominant shapes of Pd-Cu nanocrystals prepared using different amounts of $CuCl_2$ and HDA (pentagonal bipyramid and truncated bitetrahedron are abbreviated as pBP and tBT, respectively; N/A represents no product obtained).

$CuCl_2$ (mg) / **HDA (mg)**	**1.05**	**2.1**	**5.25**	**10.5**
22.5	pBP	decahedron	tBT	N/A
45	pBP	pBP	decahedron	tBT
90	pBP	pBP	decahedron	decahedron

Although HDA used to be considered as a selective capping agent for the Cu {100} facets, it should be mentioned that this assumption was recently challenged by several reports [44–46]. In one report, it was demonstrated that the HDA-Cu(0) interaction would be weakened when increasing the HDA packing density on the surface of Cu nanocrystals, which was attributed to a rapid exchange between the bound HDA on Cu and free HDA in solution [45]. In another report, based on the DFT calculation, the authors pointed out that the difference between the binding energies of HDA to Cu(100) and (111) surfaces was too small (0.12 eV) to enable HDA to selectively block Cu(100) surface [44,46]. In this case, I believe that the shape evolution of Cu nanocrystals was mainly dictated by the Pd icosahedral seeds. As a result, products mostly covered by

{111} facets were produced regardless of the facet-selective capping effect from HDA.

Considering all the influential factors, I proposed that the coordination to Cu(II) ions and thus the lowering in reduction potential was the major reason why penta-twinned structures were preferred at a high concentration of HDA. In the standard protocol for the synthesis of Pd-Cu truncated bitetrahedra, the molar concentration of HDA (37.3 mM) was only three times that of $CuCl_2$ (12.3 mM), comparing to 6 times for decahedra and 30 times for pentagonal bipyramids. With more HDA for coordination to Cu(II) ions, the reduction potential of Cu(II) precursor was further lowered along with a decrease in the amount of Cu atoms generated in the initial stage of the reaction [43]. In this case, the Cu atoms preferentially nucleated from one of the vertices of the icosahedral seed, similar to the case where the concentration of the Cu(II) precursor was reduced. It was also reported that HDA could bind to the surface of Pd nanoparticles [47]. Thus, increasing the concentration of HDA would increase its packing density on Pd seed and thus increase the steric hindrance for the surface diffusion of Cu atoms. Once the Cu atoms had been deposited on a vertex, their diffusion to adjacent edges and side faces would be largely blocked, resulting in the prevalence of penta-twinned Cu nanocrystals.

The Role of Glucose. In general, the reduction kinetics of the Cu(II) precursor depends on the concentrations of not only the coordination ligand and precursor but also the reductant. To look into the explicit role of glucose in the formation of Cu nanocrystals, I did another set of experiments by fixing the amount of HDA at 45 mg while varying the concentrations of the Cu(II) precursor and glucose (Figure 4.15 and Table 4.3). Surprisingly, increasing the concentration of glucose did not bring any change to the shape of the resultant nanocrystals. To be specific, when 1.05, 5.25, and 10.5 mg of

$CuCl_2$ were used, the dominant shapes of the Pd-Cu nanocrystals were pentagonal bipyramid, decahedron, and truncate bitetrahedron, regardless of the amount of glucose added as long as it was controlled in the range of 13.9–111.0 mM.

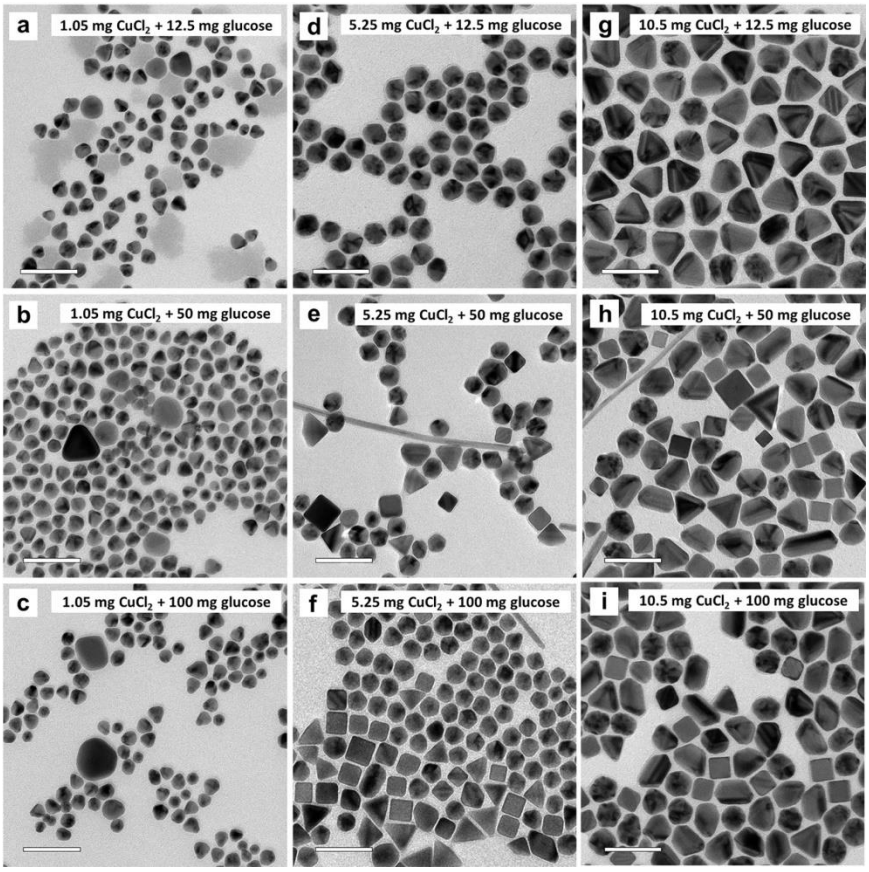

Figure 4.15. TEM images of the Pd-Cu nanocrystals shown in Table 4.3. The scale bars are 100 nm.

As the concentration of glucose was increased, I also observed an increase in proportion for the impurities, including cubes and RBP purely made of Cu. Along with the acceleration in reduction for the Cu(II) precursor, the increase in homogeneous nucleation and thus the consumption of Cu atoms reduced the amount of Cu actually

deposited on the Pd seeds, resulting in the formation of almost identical Pd-Cu products even though the concentration of reductant was increased.

Table 4.3. The dominant shapes of Pd-Cu nanocrystals prepared using different amounts of $CuCl_2$ and glucose (pentagonal bipyramid and truncated bitetrahedron are abbreviated as pBP and tBT, respectively).

$CuCl_2$ (mg) / **glucose (mg)**	**1.05**	**5.25**	**10.5**
12.5	pBP	decahedron	tBT
50	pBP	decahedron	tBT
100	pBP	decahedron	tBT

The Role of Chloride. I also investigated the effect of Cl^- ions on the shape-controlled synthesis of Pd-Cu Janus nanocrystals. As shown in Figure 4.16, the Cu atoms were deposited as irregularly-shaped, polycrystalline shells around the Pd seeds when the precursor was switched from $CuCl_2$ to $Cu(ac)_2$ (ac: acetate). In this case, the fast reduction of the precursor led to the rapid deposition of Cu atoms onto the entire surface of each Pd seed. When NaCl was added into the reaction solution, however, Pd-Cu nanocrystals with well-defined shapes were obtained again, indicating the important role played by Cl^- ions in the formation of Cu nanocrystals. Similar to HDA, Cl^- ions can coordinate to Cu(II) ions and thus slow down their reduction rate [32], enabling the selective nucleation and growth of Cu from one site on the Pd seed for the generation of a Janus nanocrystal with a well-defined shape [3].

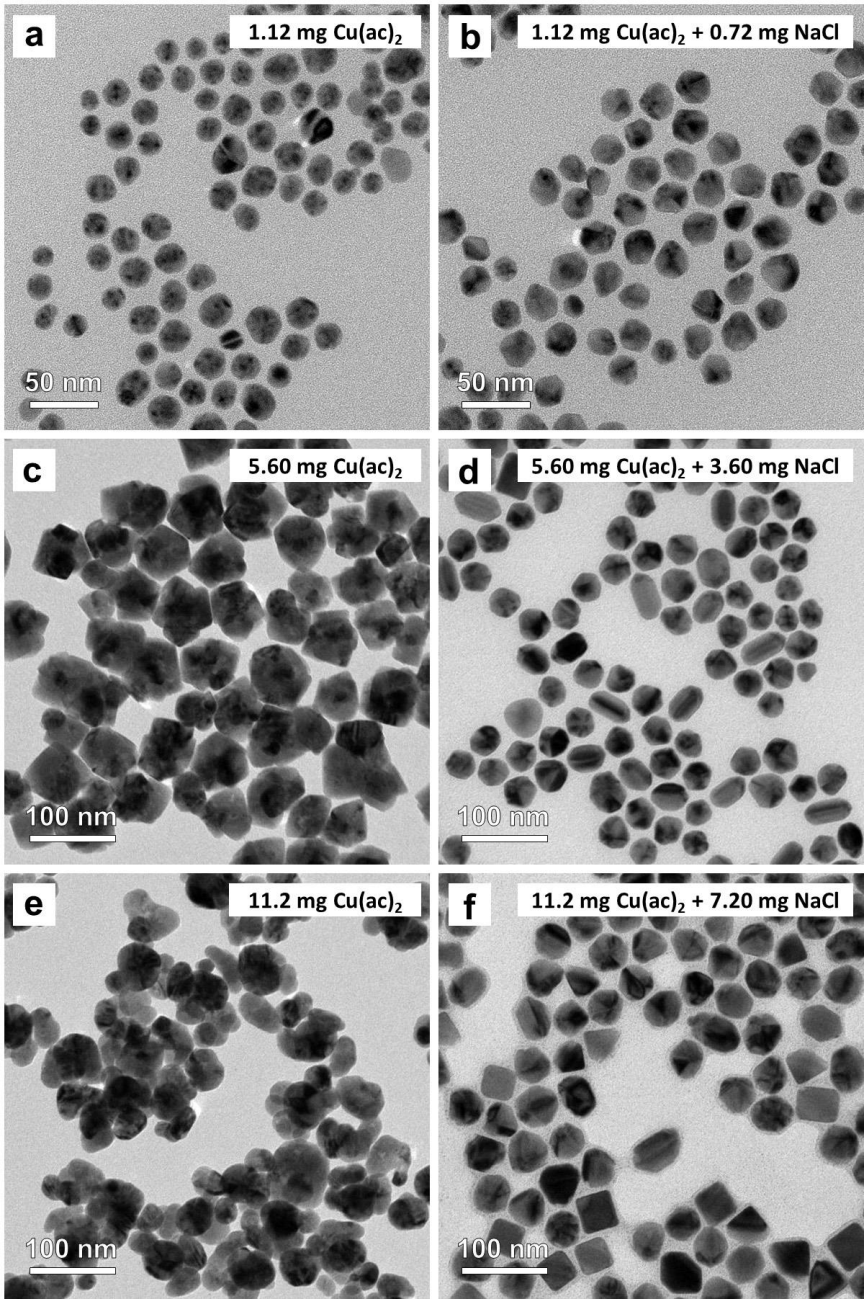

Figure 4.16. TEM images of the Pd-Cu nanocrystals prepared using the standard protocols for (a, b) pentagonal bipyramids, (c, d) decahedra, and (e, f) truncated bitetrahedra, respectively, except for the use of different Cu(II) precursors: (a, c, e) $Cu(ac)_2$, and (b, d, f) $Cu(ac)_2$ plus NaCl.

Control of Size. Although the size of the Pd-Cu nanocrystals could not be tightly controlled by simply varying the amount of the Cu(II) precursor, it could be tuned by altering the amount of the Pd icosahedral seeds. In the case of Pd-Cu decahedra, when the

amount of the Pd seeds was increased by 50 and 100%, the size of the as-obtained nanocrystals decreased from 39.3 to 32.7 and 31.7 nm (Figure 4.17, a and b). When more seeds were used with a fixed amount of the Cu(II) precursor, fewer Cu atoms were deposited on each Pd seed, leading to a smaller size for the decahedra. Similarly, the edge length of the Pd-Cu truncated bitetrahedra decreased from 48.2 to 46.4 and 41.3 nm when the amount of the Pd seeds was increased by 50 and 100% (Figure 4.17, c and d). It should be mentioned that the purity of the truncated bitetrahedra also slightly dropped, with the observation of an increased proportion of polycrystalline particles.

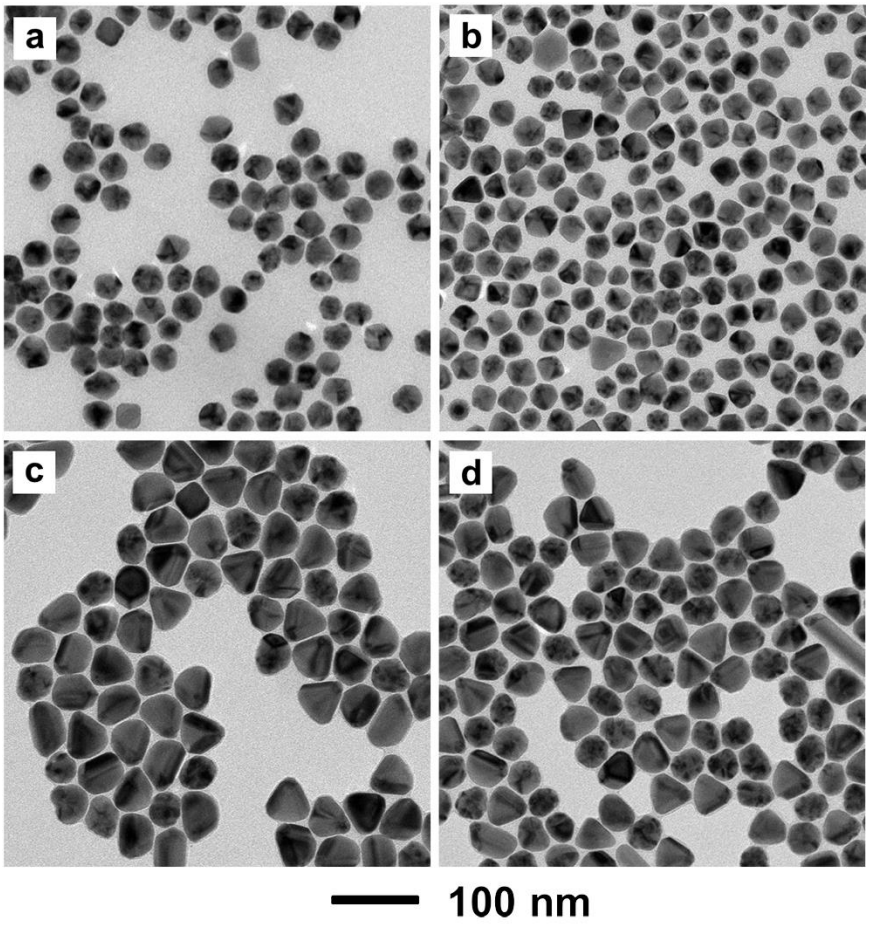

Figure 4.17. TEM images of (a, b) Pd-Cu decahedra and (c, d) truncated bitetrahedra prepared using the standard protocol except for the use of different volumes of the Pd icosahedral seed suspension (1.1 mg·mL^{-1}): (a, c) 75 and (b, d) 100 μL, respectively.

Taken together, the size of both decahedra and truncated bitetrahedra can be controlled to a certain extent by varying the amount of the Pd seeds, but the use of a large amount of seeds might lead to decrease in purity for the target products.

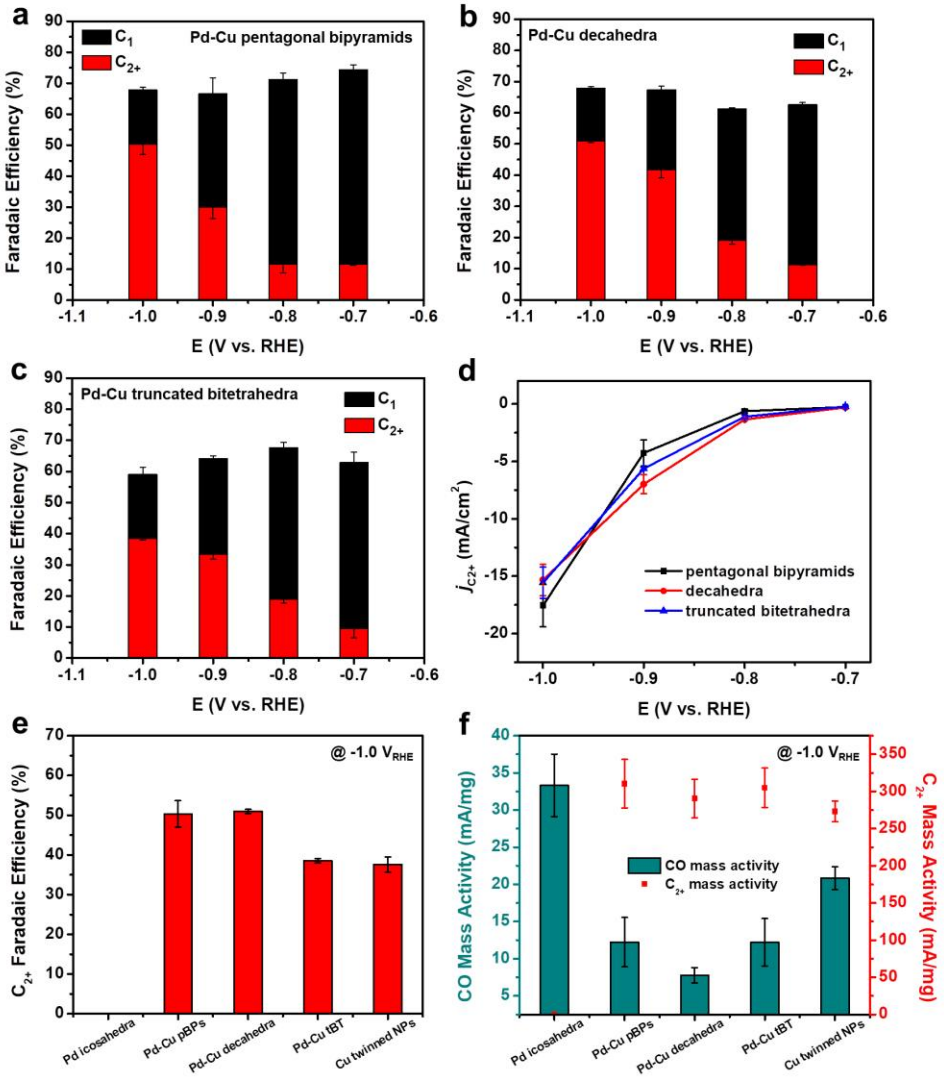

Figure 4.18. Products for the electrochemical reduction of CO_2 in the presence of catalysts based on the different types of Pd-Cu nanocrystals: (a–c) FEs of (a) pentagonal bipyramids, (b) decahedra, (c) truncated bitetrahedra, and (d) partial current density toward C_{2+} products normalized to the geometric area of the electrode. (e) The FEs of C_{2+} products and (f) the mass activities toward the production of CO and C_{2+} species at -1.0 V_{RHE} with Pd-Cu Janus nanocrystals, Pd icosahedra, and Cu twinned nanoparticles serving as the catalysts. In (e) and (f), the pentagonal bipyramids, truncated bitetrahedra, and nanoparticles are abbreviated as pBPs, tBT, and NPs, respectively.

Catalytic Activity toward the Electrochemical Reduction of CO_2. Considering the bimetallic composition and Janus structure of the Pd-Cu nanocrystals, my collaborators evaluated them as catalysts for the electrochemical reduction of CO_2 and we paid special attention to their selectivity toward C_{2+} products. The results are summarized in Figure 4.18, a–d, with the details provided in Table 4.4–4.6. At -0.7 V_{RHE} in a 0.5 M $KHCO_3$ electrolyte, we observed the generation of C_{2+} products, including ethylene and ethanol, for all the three catalysts at 11.6, 11.2, and 9.4% for the pentagonal bipyramids, decahedra, and truncated bitetrahedra, respectively. The onset potential was relatively low compared to other types of Cu-based catalysts reported in literature (Table 4.1) [22–25]. As the potential was further decreased, an increase in the selectivity toward C_{2+} products was observed. Specifically, at -1.0 V_{RHE}, the faradaic efficiencies (FEs) of C_{2+} species reached 50.3, 51.0, and 38.5% for the pentagonal bipyramids, decahedra, and truncated bitetrahedra, respectively, demonstrating superior performance relative to other Cu catalysts in 0.5 M $KHCO_3$ electrolyte (Table 4.1).

Table 4.4. Details of the selectivity and geometric current density in CO_2 reduction using the Pd-Cu pentagonal bipyramids as the catalyst.

E (V vs RHE)	H_2 (%)	CO (%)	CH_4 (%)	C_2H_4 (%)	Formate (%)	Acetate (%)	Ethanol (%)	1-Propanol (%)	Total (%)	*j* (mA•cm^{-2})
-0.7	29.9 ± 0.3	27.8 ± 0.9	0 ± 0	3.7 ± 0	7.9 ± 0.3	0 ± 0	34.8 ± 0.7	0 ± 0	104.1 ± 1.0	-2.1 ± 0.1
-0.8	27.2 ± 1.1	25.0 ± 2.2	0 ± 0	5.4 ± 1.2	4.4 ± 0.1	1.1 ± 2.0	34.7 ± 0.2	0.6 ± 0.5	98.5 ± 1.8	-5.4 ± 0.2
-0.9	27.7 ± 2.4	10.0 ± 1.6	0.3 ± 0.3	17.8 ± 3.9	6.6 ± 0.5	4.9 ± 0.4	26.4 ± 3.7	0.7 ± 0.2	94.4 ± 5.0	-14.2 ± 2.5
-1.0	28.5 ± 3.9	2.0 ± 0.5	4.8 ± 2.1	31.3 ± 0.9	12.6 ± 1.3	5.6 ± 0.9	10.9 ± 2.4	0.9 ± 0.1	96.5 ± 0.2	-34.9 ± 1.4

Table 4.5. Details of the selectivity and geometric current density in CO_2 reduction using the Pd-Cu decahedra as the catalyst.

E (V vs RHE)	H_2 (%)	CO (%)	CH_4 (%)	C_2H_4 (%)	Formate (%)	Acetate (%)	Ethanol (%)	1-Propanol (%)	Total (%)	*j* (mA•cm^{-2})
-0.7	37.7 ± 1.2	22.3 ± 0.6	0 ± 0	5.4 ± 0.1	5.8 ± 0	0 ± 0	29.2 ± 0.1	0 ± 0	100.4 ± 0.4	-2.7 ± 0
-0.8	32.9 ± 0.3	15.0 ± 0.5	0 ± 0	11.4 ± 0.5	4.4 ± 0.6	2.8 ± 0.2	27.1 ± 0.1	0.5 ± 0.1	94.1 ± 1.4	-7.0 ± 0
-0.9	27.4 ± 0.2	4.5 ± 0.2	0.8 ± 0	27.1 ± 0.8	7.8 ± 1.2	6.2 ± 0.6	20.3 ± 1.4	0.6 ± 0	94.8 ± 4.0	-16.7 ± 1.0
-1.0	25.9 ± 2.5	1.4 ± 0.1	6.2 ± 1.0	34.0 ± 0.5	11.6 ± 0.3	4.8 ± 0.4	9.4 ± 1.0	0.6 ± 0.1	95 ± 1.2	-30.1 ± 2.3

Table 4.6. Details of the selectivity and geometric current density in CO_2 reduction using the Pd-Cu truncated bitetrahedra as the catalyst.

E (V vs RHE)	H_2 (%)	CO (%)	CH_4 (%)	C_2H_4 (%)	Formate (%)	Acetate (%)	Ethanol (%)	1-Propanol (%)	Total (%)	*j* (mA•cm^{-2})
-0.7	30.4 ± 5.5	22.6 ± 1.5	0 ± 0	4.1 ± 0.5	5.4 ± 2.5	0 ± 0	30.8 ± 1.8	0 ± 0	93.2 ± 11.8	-2.3 ± 0
-0.8	30.3 ± 0.2	17.6 ± 0.4	0 ± 0	10.1 ± 0.7	5.3 ± 0.4	3.5 ± 0.2	31.1 ± 1.4	0 ± 0	98.0 ± 0.7	-5.9 ± 0.4
-0.9	29.8 ± 0.8	7.2 ± 0.2	1.5 ± 0.1	20.2 ± 0	7.8 ± 1.6	4.9 ± 0.1	22.0 ± 1.3	0.5 ± 0.1	93.9 ± 1.7	-16.9 ± 1.2
-1.0	35.7 ± 1.5	1.5 ± 0.2	10.2 ± 2.2	25.4 ± 1.4	9.1 ± 0.6	3.6 ± 0.2	8.8 ± 0.1	0.4 ± 0.1	94.8 ± 3.3	-40.4 ± 4.1

The three Janus catalysts showed similar activities toward C_{2+} products, with the geometric current densities approaching 17.6, 15.3, and 15.6 mA/cm^2 for the pentagonal bipyramids, decahedra, and truncated bitetrahedra, respectively (Figure 4.18d). Their mass activities are also close to each other (Figure 4.19, 310.5, 290.6, and 305.1 mA/mg, respectively).

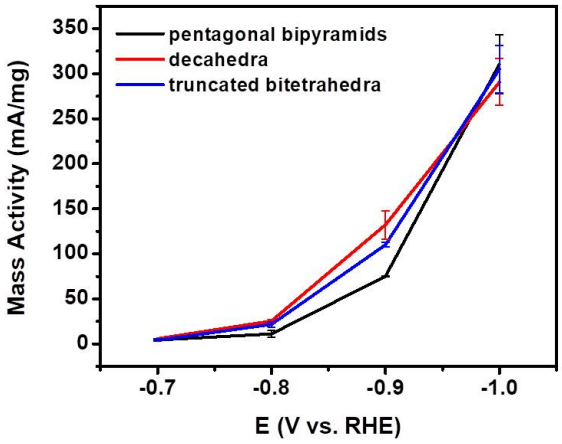

Figure 4.19. Mass activity toward C_{2+} products when different types of Pd-Cu nanocrystals were used as catalysts. The results are based on the overall mass of Pd and Cu.

The high C_{2+} selectivity of the Pd-Cu Janus nanocrystals could be largely attributed to the separation between Pd and Cu, the involvement of Pd surface in the catalysis, and the twin boundaries on Cu surface. Since Pd can actively generate CO during the electrochemical reduction of CO_2 in the potential range of -0.7 to -1.0 V_{RHE}, the excess amount of CO on Pd surface is expected to migrate to the adjacent Cu surface and then undergo C-C coupling for the formation of C_{2+} products [17,18,48,49].

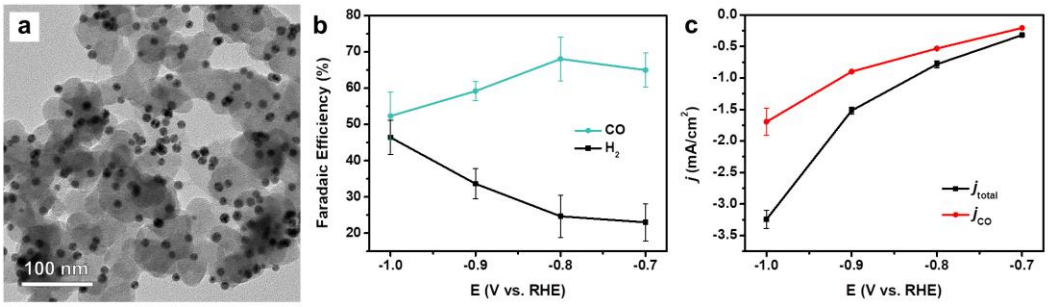

Figure 4.20. (a) TEM image of the Pd icosahedra supported on carbon. (b) FEs toward CO and H_2 and (c) geometric current density of the Pd icosahedra under different potentials in a 0.5 M $KHCO_3$ electrolyte.

To support this argument, my collaborators also measured the catalytic performance of Pd icosahedra (Figure 4.20) and Cu twinned nanoparticles (Figure 4.21), both supported on carbon, in the electrochemical reduction of CO_2. As shown in Figure 4.18, e and f, all the three Pd-Cu Janus nanocrystals exhibited greater C_{2+} selectivity and activities at -1.0 V_{RHE} compared to pure Pd (0% for C_{2+} FE) and Cu references (37.6% for C_{2+} FE and 273.1 mA/mg for mass activity), suggesting the importance of Pd in promoting the production of C_{2+} species.

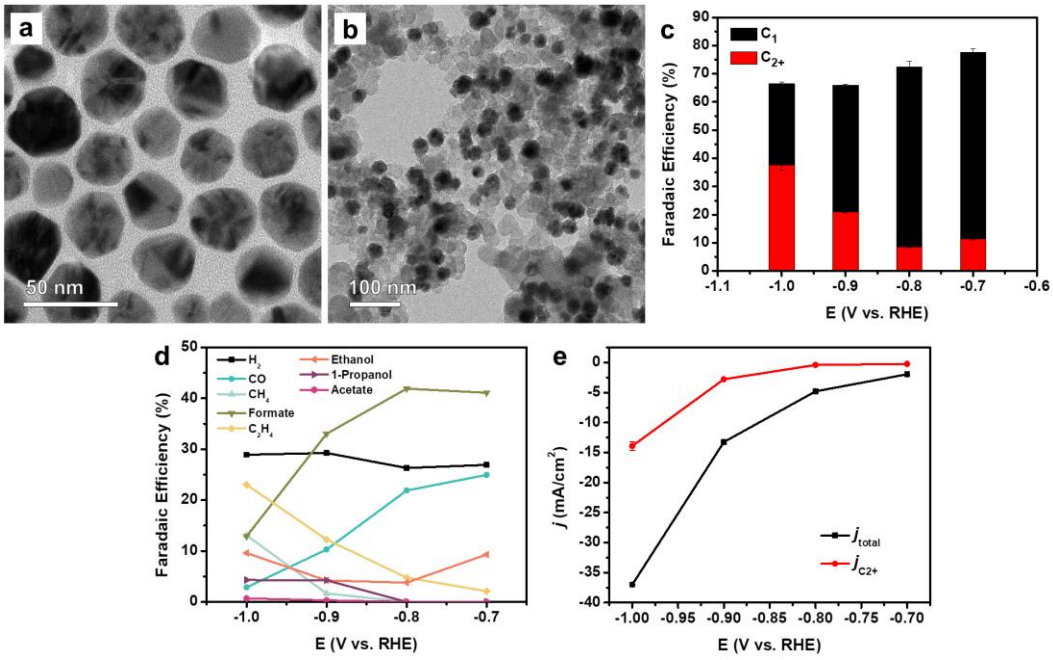

Figure 4.21. (a, b) TEM image of Cu twinned nanoparticles: (a) before, and (b) after deposition on carbon. (c, d) FEs and (e) geometric current density of the Cu twinned nanoparticles under different potentials in a 0.5 M $KHCO_3$ electrolyte.

With regard to the CO production rate (Figure 4.18f), the highest mass activity was achieved by Pd icosahedra (33.3 mA/mg), which was much greater than either those

of the Janus nanocrystals (12.2, 7.8, and 12.2 mA/mg for pentagonal bipyramids, decahedra, and truncated bitetrahedra, respectively) or that of Cu nanoparticles (20.8 mA/mg), indicating the involvement of CO spillover from Pd to Cu. These results suggest that the large amount of CO generated on the Pd surface migrated to the neighboring Cu surface, leading to an increased CO coverage density on Cu for enhanced C-C coupling and augmented C_{2+} production. Furthermore, the as-prepared Pd-Cu nanocrystals were all characterized by a twin structure. The presence of planar defects might also attract the C_1 intermediates and contribute to the production of C_{2+} species [21]. It was previously reported that the existence of twin defects and stacking faults could enhance the adsorption of CO on the surface of Cu nanocrystals, leading to a higher CO coverage density for the promotion of C-C coupling [16].

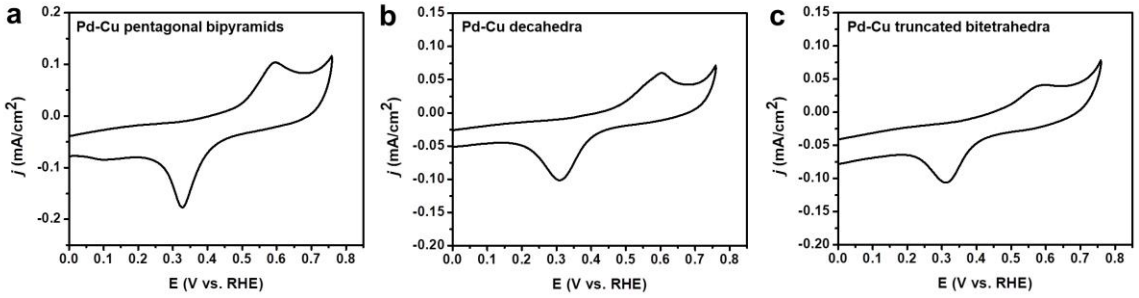

Figure 4.22. Cyclic voltammetries (CVs) recorded for the Pd-Cu Janus nanocrystals at 25 mV/s in 0.1 M KOH: (a) pentagonal bipyramids, (b) decahedra, and (c) truncated bitetrahedra, respectively.

When normalized to the electrochemically active surface area (ECSA, Figure 4.22 and Table 4.7), the truncated bitetrahedra gave a much higher current density (76.4 mA/cm^2) than those of pentagonal bipyramids (32.8 mA/cm^2) and decahedra (41.5

mA/cm^2), although they exhibited a lower C_{2+} selectivity. This trend can be ascribed to the detrimental impact of twin defects and under-coordinated atoms if they are presented at a very high density on the Cu surface. Though these defects can enhance the adsorption of CO intermediates and facilitate the C-C coupling, too many low-coordinated sites might result in strong binding of intermediates and even products, slowing down their desorption from the catalyst surface and thus lowering the activity [50].

Table 4.7. ECSAs and ECSA-normalized current densities at -1.0 V_{RHE} of the three different types of Pd-Cu Janus nanocrystals.

Sample	**ECSA (cm^2)**	**Mass-normalized ECSA (cm^2/mg)[a]**	**ECSA-normalized C_{2+} current density (mA•cm^{-2})**
Pd-Cu pentagonal bipyramids	0.42	10.5	32.8
Pd-Cu decahedra	0.29	7.25	41.5
Pd-Cu truncated bitetrahedra	0.16	4.0	76.4

[a] The ECSAs were normalized to the mass of Cu.

Besides, it is worth noting that, in the present study, the difference in ECSA for the three Pd-Cu catalysts had nearly no influence on their selectivity. Taking the Pd-Cu pentagonal bipyramids as an example, negligible changes were observed when decreasing the loading amount of Cu from 40 to 20 μg (Table 4.8), indicating the reliability in comparing the selectivity among the three different Pd-Cu catalysts.

Table 4.8. The selectivity and geometric current density in CO_2 reduction when 20 μg of the Pd-Cu pentagonal bipyramids were used as the catalyst.

E (V vs RHE)	H_2 (%)	CO (%)	CH_4 (%)	C_2H_4 (%)	Formate (%)	Acetate (%)	Ethanol (%)	1-Propanol (%)	Total (%)	*j* (mA•cm^{-2})
-0.9	26.9	12.7	0.8	17.8	27.2	0.5	5.2	4.5	95.6	-9.4
-1.0	23.0	3.3	8.7	30.1	13.3	1.0	11.2	4.5	95.0	-20.0

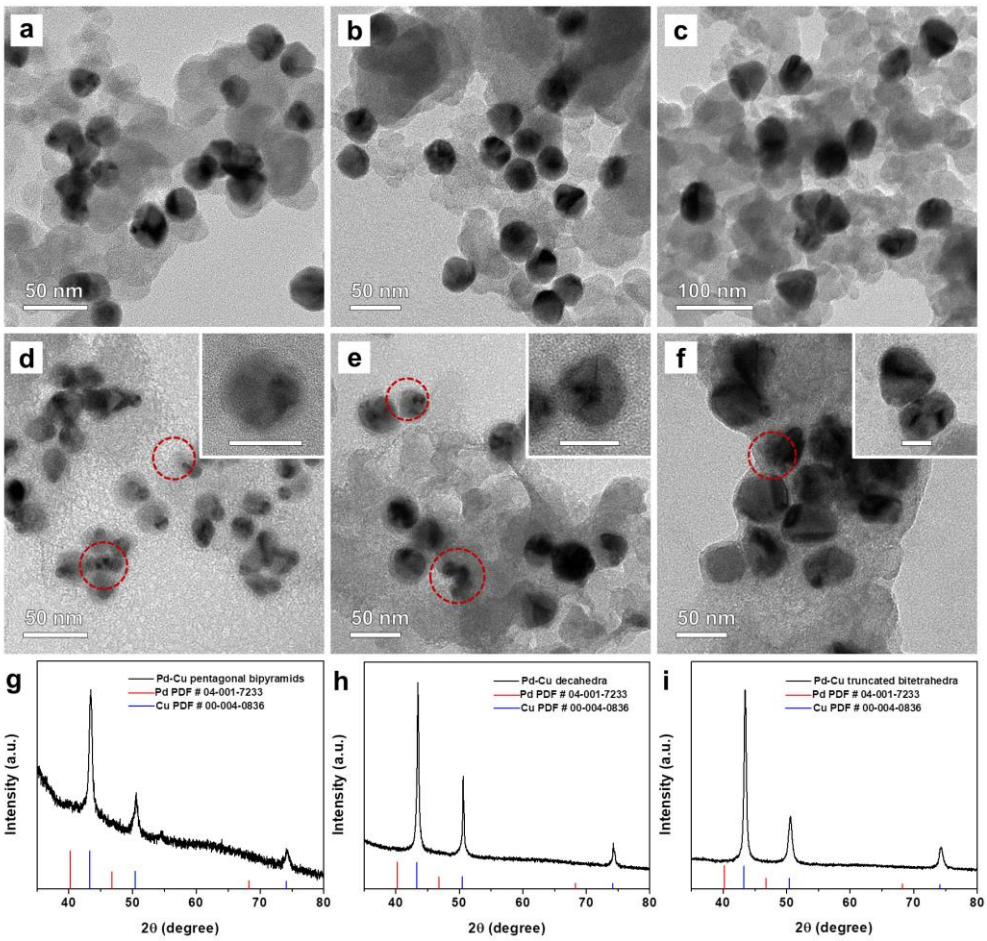

Figure 4.23. (a–c) TEM images of the Pd-Cu nanocrystals supported on carbon before electrolysis: (a) pentagonal bipyramids, (b) decahedra, and (c) truncated bitetrahedra. (d–f) TEM images and (g–i) XRD patterns of the Pd-Cu nanocrystals after 1 h of electrolysis at -1.0 V_{RHE}: (d, g) pentagonal bipyramids, (e, h) decahedra, and (f, i) truncated bitetrahedra. The scale bars in the insets of (d–f) are 30 nm. The places where dissolution of Cu or formation of small Cu nanoparticles occurred are marked by red circles.

I further evaluated the shape and compositional stability of the Pd-Cu Janus nanocrystals during CO_2 reduction. As shown in Figure 4.23, a–f, after 1 h of electrolysis at -1.0 V_{RHE}, the twin defects and well-defined facets of the nanocrystals were largely preserved. I also found some dissolution of Cu from the edges and corners, together with the formation of small Cu particles around the Pd-Cu nanocrystals, as marked by circles in Figure 4.23, d–f. Similar phenomena were also reported for Cu nanocubes [51], which can be ascribed to the adsorption of H and CO on Cu nanoparticles and the induced shape degradation under negative potentials. In Figure 4.23, d–f, the Pd and Cu portions of the nanocrystals could be easily distinguished by their contrasts and I could clearly resolve the boundaries between them, suggesting the maintenance of separation between Pd and Cu during electrolysis. This conclusion was further supported by the XRD data (Figure 4.23, g–i). The missing of shift to the Cu peaks indicated the absence of Pd-Cu alloying or interphase mixing between Pd and Cu.

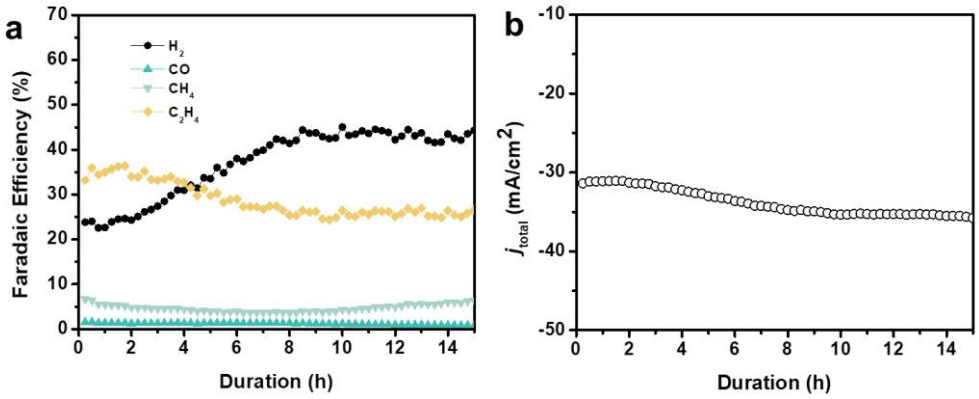

Figure 4.24. Stability test of the Pd-Cu decahedra at -1.0 V_{RHE} for 15 h: (a) FEs of gaseous products and (b) current density normalized to the geometric area.

Taking Pd-Cu decahedra, which exhibited the highest C_{2+} selectivity, as an example, my collaborators and I evaluated their long-term stability toward the electrochemical CO_2 reduction. After 15 h of electrolysis at -1.0 V_{RHE}, a decrease of 19.9% was observed for the FE toward ethylene, together with an increase of 14.0% for the total current density (Figure 4.24). Combining with the TEM images after 3 and 5 h of electrolysis (Figure 4.25), where fragmentation and sintering of the nanocrystals were observed, it could be inferred that the shape deformation contributed most significantly to the degradation in C_{2+} selectivity. Further endeavors should be devoted to improving the stability of Janus nanocrystals by maintaining their shapes and structures during long-term electrolysis.

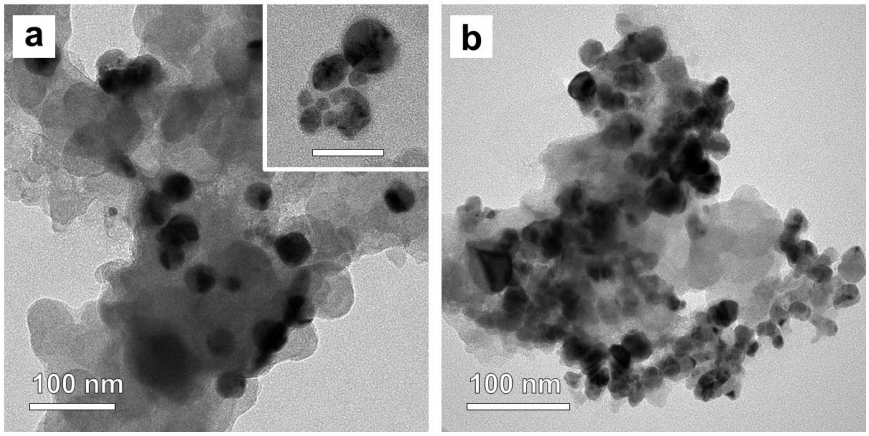

Figure 4.25. TEM images of the Pd-Cu decahedra after (a) 3 and (b) 5 h of electrolysis at -1.0 V_{RHE}, respectively. The scale bar in the inset of (a) is 50 nm.

Detection of *CO Intermediates Using Infrared (IR) Absorption Spectroscopy in an Attenuated Total Reflection (ATR) Mode. My collaborators also conducted *in situ* ATR-IR measurements on the Pd-Cu decahedra and Cu twinned

nanoparticles, with the latter serving as a reference, during CO_2 reduction. The results are presented in Figure 4.26. It should be pointed out that no IR band related to the *CO adsorbed on Pd could be detected on the Pd-Cu decahedra due to the extremely low (<7%) coverage of Pd on the surface of a Janus nanocrystal. For both the Pd-Cu decahedra and Cu twinned nanoparticles, they observed an IR band at around 1800 cm^{-1}. According to the literature [52,53], this band could be assigned to the bridge- or multiple-adsorbed *CO on Cu surface. As the applied potential became more negative, the redshift of the band could be attributed to a combination of the Stark tuning effect (redshift) and the increase in *CO coverage (blueshift) [54].

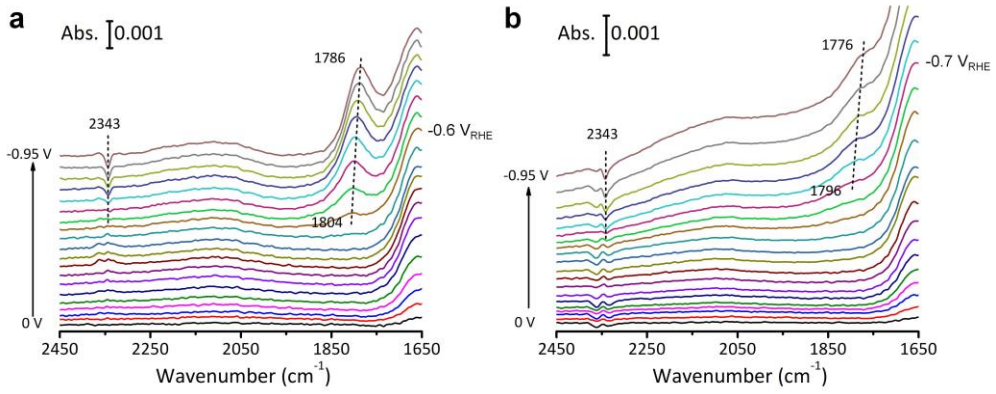

Figure 4.26. Real-time ATR-IR spectra recorded at potentials varying from 0 to -0.95 V_{RHE} on the (a) Pd-Cu decahedra and (b) Cu twinned nanoparticles in the CO_2-saturated 0.5 M $KHCO_3$ solution. The peak at 2343 cm^{-1} can be assigned to the CO_2 in the aqueous solution, and the band located at around 1800 cm^{-1} can be assigned to the bridge- or multiple-adsorbed *CO on Cu surface.

During the cathodic sweep, the *CO band started to appear on the Pd-Cu decahedra at a potential around -0.6 V_{RHE}, which was 100 mV more positive than that on Cu twinned nanoparticles. This observation indicated that *CO was more easily formed

on the Janus catalyst, offering a piece of evidence to support our argument about the role of Pd in promoting the formation of CO, which could then migrate to the Cu surface. Compared to the Cu twinned particles, the *CO band was much stronger on the Pd-Cu decahedra, which might be related to the higher *CO coverage on the surface of the Janus catalyst. However, it is impossible to quantitatively compare the band intensities between two individually prepared electrodes due to the variations in experimental conditions.

Theoretical Study of CO Spillover from Pd to Cu. To demonstrate that CO can form on the Pd surface and then migrate to the Cu surface for subsequent C-C coupling, my collaborators performed a series of DFT-based calculations on Pd(111) and Cu(111), the two extended facets exposed on the Pd-Cu Janus nanocrystals. They first investigated the conditions under which CO spillover from Pd(111) to Cu(111) would occur. To this end, they calculated the binding energies and structures of CO adsorbed on Pd(111) and Cu(111) at various CO coverages up to 1 ML, with an increment of 1/9 ML. The average and differential binding energies (abbreviated as BE_{avg} and dBE, respectively) of CO are graphically shown in Figure 4.27, a and b, as a function of CO coverage. A general trend can be observed that both the BE_{avg} and dBE values remain relatively unchanged at low CO coverages, and rapidly become less negative at higher CO coverages. This trend indicates that the CO-CO lateral interactions are generally repulsive, resulting in destabilization of CO adsorption at higher CO coverages. As shown in Figure 4.27b, the differential binding energies of CO on Pd(111) and Cu(111) are positive (*i.e.*, adsorption of additional CO is energetically unfavorable) when the CO coverage reaches 8/9 ML and 6/9 ML, respectively. Therefore, the CO saturation coverages at 0 K and under vacuum are approximately 7/9 ML on Pd(111) and 5/9 ML on Cu(111), which are in

good agreement with the experimentally measured CO saturation coverages of 0.75 ML and 0.52 ML on Pd(111) and Cu(111), respectively, under ultra-high vacuum (UHV) condition [55,56].

From Figure 4.27b, it can also be observed that CO binds more strongly to Pd(111) than to Cu(111). The differential binding energy of CO on Pd(111) remains more negative than -0.98 eV (the binding energy of CO on clean Cu(111) at 1/9 ML coverage; indicated by the red dashed line in Figure 4.27b) until the CO coverage on Pd(111) increases up to 6/9 ML. These results can be interpreted as follows: initially, when the Pd-Cu nanocrystal surface is empty, CO is mostly generated from and also prefers to bind to the Pd surface due to the stronger binding strength. The CO coverage on Pd(111) starts to build up while the Cu(111) surface remains to be largely free of CO [16,49]. Even with the increasing coverage, additional CO molecules still prefer binding to the Pd surface until the CO coverage on Pd(111) reaches 6/9 ML. Since then, the binding energy of an additional CO molecule (*i.e.*, the differential binding energy at 7/9 ML CO coverage) becomes -0.33 eV, which is 0.65 eV more positive than the binding energy of CO on clean Cu(111). As a result, the additional CO molecules generated on the 6/9 ML CO-covered Pd(111) surface would have a thermochemical driving force to migrate to the Cu(111) surface. My collaborators thus conclude that CO spillover from Pd(111) to Cu(111) becomes thermodynamically favorable when the CO coverage on Pd(111) exceeds 6/9 ML. To sustain that reactive pattern, one would need to keep the CO coverage on Cu(111) below 4/9 ML. They argue that the rate of the reaction for consuming CO on Cu(111) facets of the Janus nanocrystals is sufficient to keep up with

the migration of CO from Pd, so that the CO coverage on Cu(111) can be kept at that critical level or below.

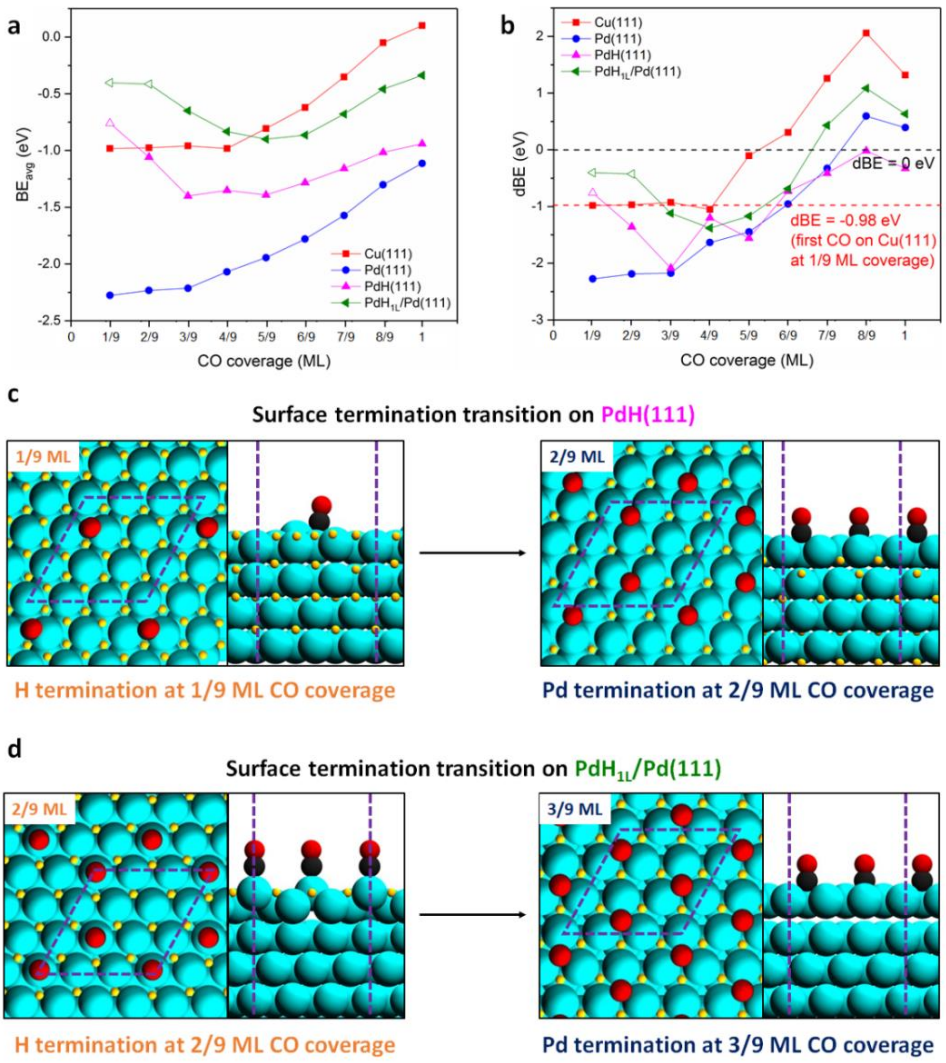

Figure 4.27. Calculated (a) average and (b) differential binding energies of CO on Cu(111) (red), Pd(111) (blue), PdH(111) (pink), and PdH_{1L}/Pd(111) (green) as a function of CO coverage. Black dashed line in (b) indicates a dBE value of 0 eV (thermal-neutral adsorption). Red dashed line in (b) indicates a dBE value of -0.98 eV (BE of CO on a clean Cu(111) surface at 1/9 ML coverage). For PdH(111) and PdH_{1L}/Pd(111), open symbol indicates that H termination is preferred; solid symbol indicates that Pd termination is preferred. (c) Illustration of transition from H termination to Pd termination on PdH(111) when CO coverage increases from 1/9 to 2/9 ML. (d) Illustration of transition from H termination to Pd termination on PdH_{1L}/Pd(111) when CO coverage increases from 2/9 to 3/9 ML. In (c) and (d), top and side views are shown side by side in each pair of images. Color code: cyan – Pd; yellow – H; black – C; red – O. Dashed lines denote the (3 × 3) surface unit cell.

My collaborators also explored the impact of potential palladium hydride (PdH) formation on the proposed CO spillover mechanism. Past experimental studies suggested that PdH could be formed on metallic Pd catalysts under the electrochemical conditions relevant to CO_2 reduction due to the competing HER [57–59]. Although we do not have direct evidence in our experiments, the possibility of PdH formation on the Pd portion of the Pd-Cu Janus nanocrystals during the measurements could not be eliminated. To this end, my collaborators considered an extensive list of possible surface/bulk PdH models, including: (1) the PdH(111) surface with its optimized lattice constant, (2) pseudomorphic PdH overlayers on a Pd(111) substrate (denoted PdH_{xL}/Pd(111); x = 1–3 denotes the number of Pd-H bilayers) as models for thin-layer surface hydride, whereby the optimized lattice constant of pure Pd is used, and (3) a compressed PdH(111) slab at the bulk lattice constant of metallic Pd (compressed by approximately 5%; denoted PdH_{comp}(111)). The last one serves as a model for the limiting case of a surface hydride grown on Pd(111), when the PdH layer thickness is sufficiently large so that the PdH surface barely experiences the electronic effect from the Pd(111) substrate, and yet the lattice confinement is preserved. In the absence of any adsorbate, all these surfaces prefer a H-terminated geometry. On each PdH slab model, they evaluated the binding structures and energies for CO at surface coverages from 1/9 to 1 ML. The calculated BE_{avg} and dBE values on PdH(111) and PdH_{1L}/Pd(111) are graphically shown in Figure 4.27, a and b, as a function of the CO surface coverage.

On all the PdH slab models, similar nonmonotonic trends were observed for the dBE of CO as a function of CO coverage (examples of PdH(111) and PdH_{1L}/Pd(111) are shown in Figure 4.27b). At 1/9 ML coverage, CO binds more weakly to all the PdH

surfaces than both Cu(111) and Pd(111); *e.g.*, the BEs of CO at 1/9 ML coverage are -0.76 eV and -0.40 eV on PdH(111) and PdH_{1L}/Pd(111), respectively, compared to -0.98 eV on Cu(111) and -2.28 eV on Pd(111). As the CO coverage increases to 3/9 ML, its dBE value rapidly becomes more negative on all the PdH slab models my collaborators studied. Importantly, their calculations suggest that the weak and increasing binding strength of CO at low coverage on the PdH surfaces is attributed to a CO-induced transition from the H termination to Pd termination of the PdH surfaces, as illustrated in Figure 4.27, c and d. The strong Pd-CO interaction draws Pd atoms to the surface, further stabilizing the subsequent CO binding. On PdH(111), this transition occurs when the CO coverage increases from 1/9 to 2/9 ML (Figure 4.27c). On all the PdH_{xL}/Pd(111) (x = 1–3) surfaces, the Pd-terminated surface becomes energetically preferred when CO coverage increases from 2/9 to 3/9 ML. Interestingly, a CO coverage of 1/9 ML is sufficient to cause the H-to-Pd surface termination transition on the PdH_{comp}(111) surface.

Once the transition is accomplished, the Pd termination remains to be preferred at higher CO coverages, and the PdH surfaces can thus be viewed as a Pd(111) over PdH substrates. The presence of a Pd-terminated surface has also been evidenced in a previous study by Gao *et al* [58]. They demonstrated that a β-PdH_x@Pd phase (*i.e.*, metallic Pd shell outside a PdH core) was formed during the electrochemical reduction of CO_2 at applied potentials more negative than -0.5 V_{RHE}, when CO started to dominate the surface. At CO coverages of 3/9–5/9 ML, the dBE of CO reaches its most negative value on every PdH model slab my collaborators studied. Within this surface coverage range, CO adsorption on any CO-covered PdH surface is thermodynamically preferred over its adsorption on clean Cu(111) (BE = -0.98 eV; red dashed line in Figure 4.27b).

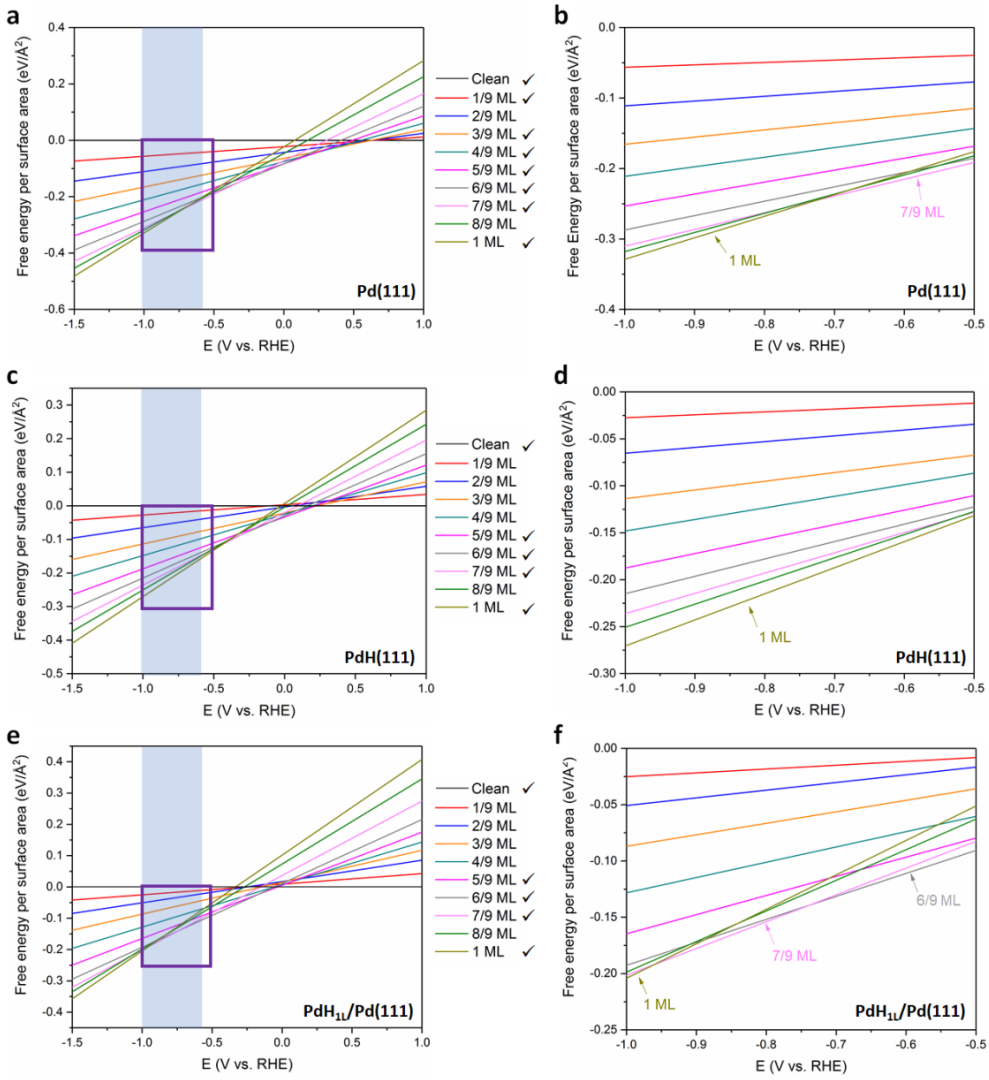

Figure 4.28. Calculated Pourbaix phase diagram for (a, b) CO on Pd(111), (c, d) CO on PdH(111), and (e, f) CO on PdH_{1L}/Pd(111) at room temperature under the electrochemical conditions for CO_2 reduction. The free energy per surface area for each CO coverage up to 1 ML is plotted as a function of the applied potential. At each potential, the most stable surface coverage is the one with the lowest free energy value. In the legend, those coverages marked with tick marks appear as the most stable phases under certain potentials; the remaining phases are not expected to be observable. The range of applied potential evaluated experimentally in this work (-0.7 to -1.0 V_{RHE}) is denoted by the shaded area on (a), (c), and (e). Enlarged views of the boxed area in (a), (c), and (e) are shown in (b), (d), and (f), respectively.

Above 5/9 ML CO coverage on PdH, the effect of lateral CO-CO repulsion becomes more potent, and the adsorption of additional CO molecules is significantly destabilized. On PdH(111), when the CO coverage increases from 5/9 ML to 6/9 ML, the dBE of CO changes from -1.56 eV (0.58 eV more negative than BE_{CO} on clean Cu(111)) to -0.73 eV (0.25 eV more positive than BE_{CO} on clean Cu(111)). Therefore, similar to the previously discussed case of CO spillover from 6/9 ML CO-covered Pd(111) to Cu(111), there exists a thermochemical driving force for additional CO molecules produced on the 5/9 ML CO-covered PdH(111) surface to migrate to Cu(111). Despite the variance in dBE values, the same 5/9 ML threshold CO coverage for CO spillover to Cu(111) is observed on all the other PdH slab models (Table 4.9). My collaborators conclude that, as long as a CO coverage of above 5/9 ML can be reached, PdH surfaces can also serve as a source of CO for its spillover to the adjacent Cu(111) surface of the Janus nanocrystals.

Table 4.9. Phase-diagram-predicted CO coverage under electrochemical CO_2 reduction conditions (room temperature, -0.7 to -1.0 V_{RHE}) on Pd(111) and PdH surfaces and comparison with the CO coverage required for CO spillover to Cu(111).

Surface	**Predicted CO coverage under CO_2 reduction conditions (ML)**	**CO coverage required for CO spillover to Cu(111) (ML)**
Pd(111)	7/9 or 1	6/9
PdH(111)	1	5/9
PdH_{1L}/Pd(111)	6/9, 7/9, or 1	5/9
PdH_{2L}/Pd(111)	7/9 or 1	5/9
PdH_{3L}/Pd(111)	7/9 or 1	5/9
PdH_{comp}(111)	6/9, 7/9, or 1	5/9

Next, they sought to address the following question: is the required CO coverages for CO spillover to Cu(111) (6/9 ML or above for Pd(111), 5/9 ML or above for PdH surfaces) achievable under the electrochemical conditions for CO_2 reduction? To tackle this question, they constructed theoretical Pourbaix phase diagrams using the DFT results from the CO coverage study on Pd(111) and PdH slab models. The procedures for the Pourbaix phase diagram construction were adapted from the work by Zeng and co-workers [60] and are detailed in the experimental section. As examples, the Pourbaix phase diagrams for CO adsorption on Pd(111), PdH(111), and PdH_{1L}/Pd(111) are shown in Figure 4.28. These phase diagrams allow my collaborators to predict the most stable CO coverage on Pd(111), including hydride phases, under any given applied potential. In general, the CO coverage gradually increases as the applied potential becomes more negative. Based on Pourbaix phase diagrams, the predicted CO coverages under the experimental conditions of interest in this work (-0.7 to -1.0 V_{RHE}) are identified and summarized in Table 4.9. On Pd(111), the predicted CO coverage under these applied potentials is either 7/9 ML or 1 ML (Figure 4.28b), which is clearly above the 6/9 ML threshold for CO spillover from Pd(111) to Cu(111). On all the PdH surfaces, the predicted CO coverages under the CO_2 reduction conditions are at least 6/9 ML, which are also greater than the 5/9 ML threshold established above for CO spillover from PdH surfaces to Cu(111). Therefore, my collaborators conclude that, under the electrochemical conditions for CO_2 reduction, a sufficiently high CO coverage can be attained on the Pd surface on our Pd-Cu Janus nanocrystals, regardless of its nature being metallic Pd, bulk hydride, or surface hydride, to enable the continuous migration of CO to Cu(111).

Adsorption of CO_2 Reduction Intermediates on Cu Twin Boundaries *vs.* Terrace. To further explore the role of under-coordinated sites at the Cu twin boundaries (Cu_{TB}) in the nanocrystals, my collaborators performed DFT calculations and compared the binding strength of common CO_2 reduction intermediates on Cu_{TB} with those on terrace Cu(111) sites. Seven strongly bound intermediates, namely, H, CO, OH, CH, CHO, COH, and CH_3O, were considered in this study. The preferred binding sites and the respective binding energies of these seven species on Cu_{TB} and Cu(111) are summarized in Table 4.10. For all the seven CO_2 reduction intermediates, they observed stronger binding on Cu_{TB} compared to Cu(111). It is worth noting that for CO and H, the binding energy difference between Cu_{TB} and Cu(111) is minimal (0.02 eV). For the other five species, the adsorption on Cu_{TB} is notably stronger, with binding energy differences ranging from 0.06 eV (for COH) to 0.23 eV (for OH). At room temperature, a difference of 0.06 eV in binding energy corresponds to one order of magnitude difference in the adsorption equilibrium constant. Therefore, under the reaction conditions, one would expect much higher coverages of OH, CH, and CH_xO_y species on Cu_{TB} than on Cu(111).

The higher surface coverage on the twin boundaries may lead to two possible scenarios for the following CO_2 reduction: (1) The under-coordinated sites on the twin boundaries are highly covered but remain active. In this case, the subsequent adsorption of C_1 intermediates on the twin boundaries become destabilized due to the high coverage, resulting in a reduced barrier for the C-C coupling and facilitating the formation of C_{2+} products. Examples of such coverage effects have been demonstrated previously in DFT studies for formic acid decomposition and Fischer-Tropsch synthesis [61,62]. (2) The

adsorption on the twin boundaries becomes so strong that the desorption of intermediates and even products is restricted, suppressing the activity of the catalysts.

Table 4.10. Comparison of energetically preferred structures of CO_2 reduction intermediates and their respective binding energies on Cu twin boundaries and on Cu(111) at the dilute limit (one adsorbate per unit cell).

Species	Cu twin boundary		Cu(111)	
	BE (eV)	Site[a,b]	BE (eV)	Site[a]
H	-2.60	*hcp* (TB) 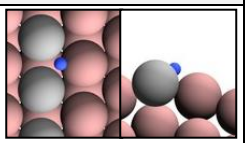	-2.58	*fcc* 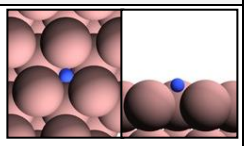
CO	-1.06	*fcc* (TB) 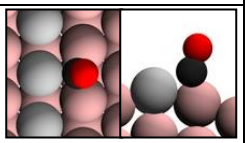	-1.04	*fcc* 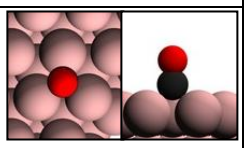
CH	-5.26	*fcc* (TB) 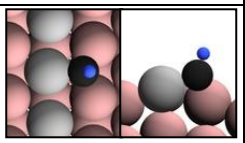	-5.12	*fcc* 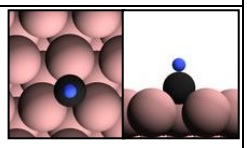
OH	-3.32	bridge (TB) 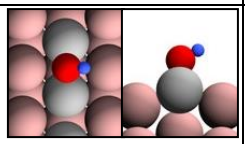	-3.10	*fcc* 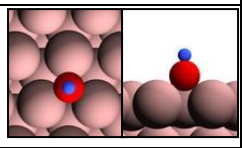
CHO	-1.71	tbt[c] (TB) 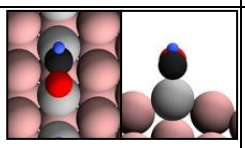	-1.56	tbt[c] 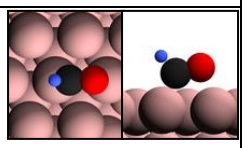
COH	-3.13	*fcc* (TB) 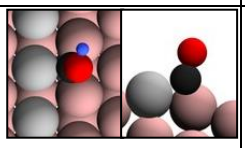	-3.06	*fcc* 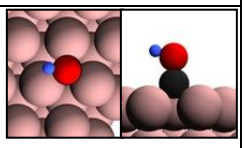
CH_3O	-2.70	*hcp* (TB) 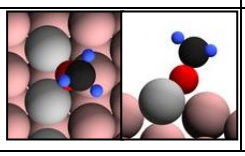	-2.52	*fcc* 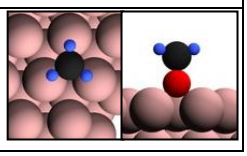

[a] Insets show the top and side views of the preferred binding structures side by side. Color code: grey – twin boundary Cu atom; pink – other Cu atom; blue – H; black – C; red – O.
[b] '(TB)' denotes a site which is either right on top of or adjacent to the twin boundary.
[c] 'tbt' denotes a binding structure across two adjacent top sites connected by a bridge site.

According to the experimental observations, the Pd-Cu truncated bitetrahedra with the largest size and lowest density of under-coordinated atoms on surface exhibited the highest current density (normalized to ECSA) toward the production of C_{2+} species, when compared to the pentagonal bipyramids and decahedra. This result suggested the detrimental role of under-coordinated atoms toward catalytic activity when they are presented in a very high proportion. A more explicit study of the twin-boundary effect would require the evaluation of the reaction kinetics for the C-C coupling steps as well as the diffusion of reaction intermediates from the twin boundary to the terrace, which is beyond the scope of this work.

4.3 Conclusion

In summary, I have demonstrated a facile, seed-mediated synthesis of Pd-Cu nanocrystals with a twinned, Janus structure while taking different shapes. Due to the large lattice mismatch between Cu and Pd, the Cu atoms prefer to nucleate and grow from one site on a Pd icosahedral seed for the generation of Pd-Cu nanocrystals with a Janus structure. By simply controlling the concentrations of the Cu(II) precursor and HDA, the deposition of Cu atoms could be selectively confined to either a vertex or an edge of the Pd icosahedral seed, leading to the formation of nanocrystals in the shapes of pentagonal bipyramid, decahedron, and truncated bitetrahedron, respectively. Specifically, decreasing the reduction rate of the Cu(II) precursor would result in the growth of Cu from the vertex for the generation of a penta-twinned nanocrystal, while a faster reduction would favor the growth from the edge for the formation of a singly-twinned product.

When applied as catalysts for the electrochemical reduction of CO_2 in a 0.5 M $KHCO_3$ electrolyte, an onset potential as low as -0.7 V_{RHE} was observed for the formation of C_{2+} products, together with high C_{2+} selectivity approaching 51.0% at -1.0 V_{RHE} for the Pd-Cu decahedra. The high yields of C_{2+} species could be attributed to the presence of Pd on the surface and the twin boundaries on Cu. The former feature facilitated the generation of CO, followed by its spillover to the Cu surface, while the latter enhanced the adsorption of CO. During the *in situ* ATR-IR measurements, the appearance of CO on Cu surface was observed at a lower overpotential on the Pd-Cu decahedra than a reference based on pure Cu, suggesting the important role of Pd in promoting the formation of CO. Based on DFT calculations and Pourbaix phase diagrams, CO spillover from Pd(111) to Cu(111) is thermodynamically favored if the CO coverage on Pd(111) exceeds 6/9 ML. On the (111) facets of bulk/surface PdH, CO spillover to Cu(111) only requires a CO coverage above 5/9 ML. Under the experimental conditions of the present study, the CO coverage can reach 7/9 ML or 1 ML on Pd(111), and at least 6/9 ML on PdH surface, suggesting that CO can readily form on the Pd or PdH surface and subsequently migrate to the Cu surface for participation in the coupling reactions. This work not only sheds light on the site-selected growth of bimetallic nanocrystals with novel shapes and structures but also allows for the rational development of bimetallic catalysts toward the CO_2 reduction reaction.

4.4 Experimental Section

Chemicals and Materials. Sodium tetrachloropalladate(II) (Na_2PdCl_4, 98%), copper(II) chloride dihydrate ($CuCl_2 \cdot 2H_2O$, 99.0%), copper(II) acetate ($Cu(ac)_2$, 98%), hexadecylamine (HDA, 98%), D-(+)-glucose ($C_6H_{12}O_6$, 99.5%), poly(vinyl pyrrolidone)

(PVP, molecular weight ≈ 55,000), sodium chloride (NaCl, >99%), diethylene glycol (DEG, lot no. BCBS2365V), potassium hydrogen carbonate ($KHCO_3$, 99.7%), 5% Nafion solution, and phenol were all obtained from Sigma-Aldrich. Ethanol (200 proof) was obtained from Pharmco Products. Throughout the experiments, I used DI water with a resistivity of 18.2 MΩ·cm at room temperature.

Synthesis of 12-nm Pd Icosahedral Seeds. The seeds were prepared using a protocol from our previous work [26]. Typically, 80 mg of PVP was dissolved in 2 mL of DEG hosted in a 20-mL vial and the solution was heated at 130 °C in an oil bath under magnetic stirring for 10 min. Afterwards, 1 mL of DEG containing 15.5 mg of Na_2PdCl_4 was injected in one shot with a pipette. The vial was then capped and continued with heating at 130 °C for 3 h. The solid product was collected by centrifugation at a speed of 26,500 x g, washed once with acetone and twice with water to remove DEG and excess PVP. The Pd icosahedra were finally dispersed in water at a concentration of 1.1 $mg \cdot mL^{-1}$ for use as seeds in the synthesis of Pd-Cu nanocrystals.

Synthesis of Pd-Cu Janus Nanocrystals. In a standard synthesis of Pd-Cu pentagonal bipyramids, 50 μL of the suspension of Pd icosahedral seeds was added into a 5-mL aqueous solution containing 45 mg of HDA, 25 mg of glucose, and 1.05 mg of $CuCl_2 \cdot 2H_2O$. The mixture was magnetically stirred overnight at room temperature. To remove the oxygen trapped in the vial, Ar was blown over the solution for 5 min before the vial was tightly capped, transferred into an oil bath set to 100 °C, and heated for 3 h under magnetic stirring. The solid product was collected by centrifugation at a speed of 13,300 x g, washed once with water and twice with ethanol to remove the excess HDA, and finally re-dispersed in ethanol for further characterization. For Pd-Cu decahedra and

truncated bitetrahedra, similar protocols were used except that the amount of $CuCl_2 \cdot 2H_2O$ was increased by five and ten times to 5.25 and 10.5 mg, respectively.

Structural and Compositional Analysis. TEM images were taken using a Hitachi HT7700 microscope. A small drop of the particle suspension was placed on a carbon-coated Cu grid, followed by drying under ambient conditions. STEM images were taken using an aberration-corrected FEI Titan 80–300 kV TEM/STEM microscope at an accelerating voltage of 300 kV, with a probe convergence angle of 30 mrad and a large inner collection angle of 65 mrad to provide a nominal image resolution of 0.7 Å. A portion of the aberration-corrected STEM imaging was performed on a JEM-ARM200F microscope with a spatial resolution of 0.08 nm. EDX mapping was obtained using a Hitachi HD2700 STEM microscope at an acceleration voltage of 200 kV.

UV-vis extinction spectra were recorded on a Cary 60 spectrometer (Agilent Technologies, Santa Clara, CA). The samples were washed twice with water and then dispersed in water for UV-vis characterization. The Cu and Pd contents in the samples were determined using an ICP-MS (NexION 300Q, Perkin-Elmer). XRD patterns were recorded using an X'Pert PRO Alpha-1 diffractometer equipped with a 1.8 kW ceramic copper tube source (PANalytical, Almelo, Netherlands). XPS data were obtained on a Thermo K-Alpha spectrometer with an Al Kα source ($h\nu$ = 1486.6 eV). For XRD and XPS measurements, the samples were washed twice with water, twice with ethanol, and then dropped onto glass slides and dried under ambient conditions.

Preparation of Working Electrode. The as-prepared Pd-Cu nanocrystals were loaded onto a carbon support (Vulcan XC72) at a Cu loading ratio of 20% w/w *via* ultrasonication in an ice bath for 30 min, followed by washing with ethanol twice. The

concentrations of Cu and Pd in all three samples, together with the molar ratio of Cu to Pd, were listed in Table 4.11 (measured by ICP-MS). The catalysts were then re-dispersed in 0.95 mL of ethanol and 50 μL of 5% Nafion with a Cu concentration of 1 mg/mL. For each measurement, 40 μg of the catalyst (based on the mass of Cu) was dropped onto a pre-cleaned glassy carbon electrode (10 mm in diameter) and dried under ambient conditions. For the Pd icosahedra and Cu twinned nanoparticles, the same procedure was applied except for the loading of 40 μg of Pd or Cu onto the electrode.

Table 4.11. Concentrations of Cu and Pd in the inks prepared for the electrochemical measurements.

Samples	Conc. of Cu (mg/mL)	Conc. of Pd (mg/mL)	Ratio of Cu to Pd
pentagonal bipyramids	0.19	0.021	15.2
decahedra	0.24	0.0087	46.2
truncated bitetrahedra	0.20	0.0040	83.7

Electrochemical Measurements and Sample Analysis. A gastight H-type cell separated by a Nafion 117 membrane (Sigma Aldrich) was used for analyzing the electrochemical reduction of CO_2. Each compartment was filled with 40 mL of 0.5 M $KHCO_3$ solution saturated with CO_2 (pH = 7.3). An Ag/AgCl electrode (BASi) was used as the reference electrode while a Pt mesh served as the counter electrode. The potentials were later converted to values with a reference to RHE using the equation of E (*vs.* RHE) = E (*vs.* Ag/AgCl) + $E_{Ag/AgCl}$ + 0.0591 × (7.3 – 1.1), where $E_{Ag/AgCl}$ is the potential of the

Ag/AgCl electrode measured in the 0.1 M $HClO_4$ solution (pH = 1.1) with reference to RHE. Before carrying out the electrochemical measurement, CO_2 (99.999%, Scientific Gas Engineering Co., LTD) was purged into the $KHCO_3$ solution for 1 h. During the measurement, CO_2 was continuously purged into each compartment through mass flow controllers (Sevenstar, Beijing) with a flow rate of 20 sccm. To release the bubbles trapped on the working electrode, the electrolyte solution was magnetically stirred at a rate of 700 rpm.

The gas products were analyzed using an online gas chromatography (GC2060, Ramiin, Shanghai) equipped with the flame ionization detector (FID) and thermal conductivity detector (TCD). Sampling was conducted sequentially at 15, 28, 41, and 54 min and the total charges collected in the 30 s prior to each sampling were used to calculate the current density. A series of standard gas mixtures were used to establish the calibration curves for H_2, CO, CH_4, and C_2H_4 (balanced with Ar; Shanghai Haizhou Special Gas Co., LTD). After 1 h of electrolysis, the liquid products in the $KHCO_3$ solution were collected and analyzed using a Varian 500 MHz NMR spectrometer. Specifically, 50 μL of 500×10^{-6} M phenol contained D_2O (J&K Chemical) was added into 450 μL of the $KHCO_3$ solution and the mixture was then subjected to NMR characterization. The calibration curves were established from a series of standard solutions (0.5 M $KHCO_3$ solutions containing 10, 20, and 100×10^{-6} M of formate, methanol, ethanol, acetate, and n-propanol). The activity and selectivity of each catalyst were measured at least three times, from which the standard errors were derived.

The ECSA of the Pd-Cu Janus nanocrystals in each catalyst was derived from the amount of charges required for the formation of a Cu_2O monolayer [63]. Cyclic

voltammetries (CVs) were recorded in the electrolysis cell with Ar-purged 0.1 M aqueous KOH serving as the electrolyte. A potential range of -0.233 to 0.766 V_{RHE} was employed and the amount of catalyst used in each measurement was fixed to 40 μg. The ECSA was estimated by dividing the amount of charges associated with the anodic peak at around 0.6 V_{RHE} with 360 $\mu C/cm^2$, a value associated with the formation of a Cu_2O monolayer.

***In Situ* ATR-IR Spectroscopy Measurements.** Setups for *in situ* ATR-IR measurements were conducted using a protocol described previously [54]. Real-time ATR-IR spectra were collected during linearly sweeping the catalyst-loaded Au/Si prism working electrode at potentials from 0.1 to -1.0 V_{RHE} with a scanning rate of 5 mV s^{-1} in a CO_2-saturated 0.5 M $KHCO_3$ solution. Each spectrum was collected with 44 scans (collection duration of 10 s) at a resolution of 8 cm^{-1} and named according to the end potential. The first spectrum was used as the IR background.

Density Functional Theory (DFT) Calculations. Periodic DFT calculations were performed using the Vienna ab initio simulation package (VASP) code [64,65]. The exchange-correlation functional was described by the generalized gradient approximation (GGA-PBE) [66], and the electron-ion interactions were described using the projector augmented-wave (PAW) potentials [67,68]. The D3 method developed by Grimme *et al.* was adopted to account for dispersive interactions [69]. The Kohn−Sham electron wave functions were expanded in plane-wave basis sets with a kinetic-energy cutoff of 400 eV. During each calculation on a metal surface, the bottom two atomic layers of the metal slab were fixed at their truncated bulk lattice positions, while all the remaining metal atoms as well as the adsorbate atom(s) were allowed to fully relax. Adsorption is allowed on only one side of the metal slab, and the electrostatic potential was adjusted

accordingly [70,71]. Any pair of successive slabs in the surface norm direction were separated by a vacuum layer of at least 12 Å in thickness. The calculated bulk lattice constants for Pd and Cu are 3.886 Å and 3.568 Å, respectively, which are in good agreement with the experimental values of 3.890 Å and 3.615 Å, respectively [72]. The calculated bulk lattice constant for PdH in its NaCl crystal structure is 4.079 Å, in close agreement with the experimental value of 4.090 Å [73].

For the study of CO adsorption at different surface coverages on Pd(111) and Cu(111), the two close-packed metal surfaces were each modeled using a four-layer slab periodically repeated in a (3 × 3) surface unit cell, which corresponds to a surface coverage of 1/9 monolayer (ML) when a single adsorbate is present in the unit cell. The PdH(111) and PdH_{comp}(111) surfaces were modeled using (3 × 3) slabs consisting of four PdH bilayers, with the bottom two bilayers being fixed at the truncated bulk lattice positions featuring the lattice constants of PdH and metallic Pd, respectively. The PdH_{xL}/Pd(111) surfaces were constructed by placing x (x = 1–3) layers of PdH bilayers pseudomorphically on top of the four-layer (3 × 3) Pd(111) slab with the bottom two Pd layers fixed. For each PdH slab model, both H and Pd terminations were evaluated. For the PdH_{xL}/Pd(111) slabs, all possible PdH bilayer stacking sequences were examined and the lowest-energy one was identified and used for subsequent adsorption studies. The first Brillouin zone of the (3 × 3) unit cell was sampled with a (4 × 4 × 1) Monkhorst-Pack k-point mesh [74].

The twin boundary regions on the Cu nanocrystals were modeled using a similar slab geometry as adopted in previous studies for icosahedral nanocrystals (Figure 4.29) [75,76], which is consistent with the atomic stacking first reported by Mackay [77]. The

slab consists of two four-layer (111) terrace regions, each consisting of six atomic rows, jointed by a twin-boundary edge (grey atoms in Figure 4.29). The slab is arranged in a (1 × 2) unit cell geometry (dashed lines in Figure 4.29), for which the first Brillouin zone was sampled using a (1 × 6 × 1) Monkhorst-Pack k-point mesh. To compare the adsorption properties of the Cu twin boundaries with those on the (111) terrace of Cu, my collaborators also constructed a four-layer (4 × 2) Cu(111) slab. They previously demonstrated that this (4 × 2) unit cell size offers a reasonable comparison at similar surface coverage with the aforementioned Cu twin-boundary model [75]. The first Brillouin zone of the (4 × 2) unit cell was sampled with a (4 × 6 × 1) Monkhorst-Pack k-point mesh.

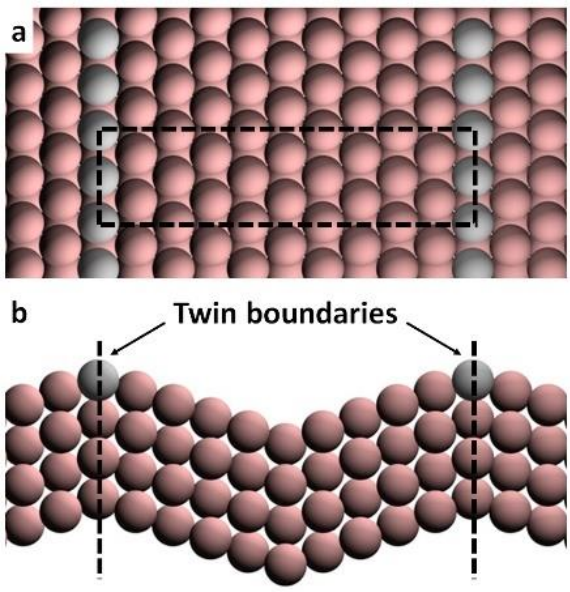

Figure 4.29. (a) Top and (b) side views of the Cu twin boundary slab model. Grey spheres denote the twin boundary Cu atoms. Pink spheres denote the remaining Cu atoms. Dashed lines denote the (1 × 2) surface unit cell.

When a single adsorbate is present in each unit cell, my collaborators define the binding energy of this species as:

$$\mathrm{BE} = E_{\mathrm{slab+species}} - E_{\mathrm{slab}} - E_{\mathrm{species(g)}}$$

where, $E_{\mathrm{slab+species}}$ is the total energy of the slab with the species adsorbed on its surface, E_{slab} is the total energy of the slab in the absence of any adsorbate, and $E_{\mathrm{species(g)}}$ is the total energy of the species itself isolated in the gas phase. For adsorption studies on the PdH slab models, they examined the adsorption on both the H- and Pd-terminated surfaces. E_{slab}, however, is always defined as the total energy of the minimum energy slab geometry (H-terminated). For the high-coverage CO adsorption studies, the $\mathrm{BE_{avg}}$ when n CO molecules are adsorbed in each unit cell is defined as:

$$\mathrm{BE_{avg}} = (E_{\mathrm{slab}+n\mathrm{CO}} - E_{\mathrm{slab}} - nE_{\mathrm{CO(g)}}) / n$$

where $E_{\mathrm{slab}+n\mathrm{CO}}$ is the total energy of the slab with n CO molecules adsorbed on its surface, and $E_{\mathrm{CO(g)}}$ is the total energy of an isolated CO molecule in the gas phase. The dBE of CO is defined as the energy change induced by adding the nth CO molecule to a unit cell where n–1 CO molecules are already adsorbed on the slab, using the following equation:

$$\mathrm{dBE} = E_{\mathrm{slab}+n\mathrm{CO}} - E_{\mathrm{slab}+(n\text{-}1)\mathrm{CO}} - E_{\mathrm{CO(g)}}$$

Procedures for Constructing Pourbaix Phase Diagram. The free energy of a system with n CO molecules adsorbed on Pd(111) is evaluated by assuming the following electrochemical equilibrium (* denotes an empty surface site or an adsorbed species):

$$n\mathrm{CO_2(aq)} + 2n\mathrm{H^+} + 2n\mathrm{e^-} + * \leftrightarrow n\mathrm{CO}* + n\mathrm{H_2O(l)}$$

The free energy (Ω) is then calculated as the Gibbs free energy of reaction for the equilibrium above:

$$\Omega = \mu^0_{nCO*} + n\mu^0_{H_2O(l)} - n\mu^0_{CO_2(aq)} - 2n\mu_{H^+} - 2n\mu_{e^-} - \mu^0_*$$

where μ^0_X denotes the standard chemical potential of Species X.

By the definition of RHE, at 0 V_{RHE}, the Gibbs free energy of reaction for the electrochemical equilibrium $H^+ + e^- \leftrightarrow 0.5\ H_2(g)$ is zero at any pH. Therefore, the chemical potential of a proton-electron pair can be expressed in terms of the applied potential *vs.* RHE (U_{RHE}) as:

$$\mu_{H^+} + \mu_{e^-} = 0.5\mu^0_{H_2(g)} - eU_{RHE}$$

Note that this expression is independent of the pH value.

The chemical potential of CO_2(aq) is estimated using its Henry's constant of 0.034 mol/kg/bar at the standard condition [78].

$$\mu^0_{CO_2(aq)} = \mu^0_{CO_2(g)} + \Delta G^0_{solv} = \mu^0_{CO_2(g)} - \mathrm{RTln}\left(H\frac{p_0}{c_0}\right)$$

where p_0 and c_0 denote the reference state for pressure (1 bar) and concentration (1 mol/kg), respectively.

The standard chemical potential of Species X is computed from its calculated energy using DFT (E_{DFT}) at 0 K using:

$$\mu^0_X(T) = E_{DFT} + ZPE + H^0(T) - H^0(0K) - TS^0$$

where ZPE is the zero-point energy from DFT, and H^0 and S^0 are the standard enthalpy and entropy, respectively.

For gas-phase and liquid-phase species, H^0 and S^0 were obtained from the NIST database [78]. For the surface species (adsorbed CO), the temperature-dependent H^0 and S^0 values were derived from the vibrational frequency values calculated at 1/9 ML CO coverage. The standard chemical potential of the clean Pd(111) slab (μ^0_*) was assumed

constant at the calculated DFT total energy value for the entire four-layer slab in a (3 × 3) surface unit cell.

4.5 Notes to Chapter 4

Part of this Chapter is adapted from "Kinetically-Controlled Synthesis of Pd-Cu Janus Nanocrystals with Enriched Surface Structures and Enhanced Catalytic Activities toward CO_2 Reduction" now under review at *Journal of the American Chemical Society*. We thank Prof. Minhua Shao and Dr. Shangqian Zhu for the electrochemical measurements, Prof. Manos Mavrikakis and Dr. Lang Xu for the DFT calculations.

4.6 References

[1] Gilroy, K. D.; Ruditskiy, A.; Peng, H. C.; Qin, D.; Xia, Y. *Chem. Rev.* **2016**, *116*, 10414–10472.

[2] Gilroy, K. D.; Peng, H. C.; Yang, X.; Ruditskiy, A.; Xia, Y. *Chem. Commun.* **2017**, *53*, 4530–4541.

[3] Zhu, C.; Zeng, J.; Tao, J.; Johnson, M. C.; Schmidt-Krey, I.; Blubaugh, L.; Zhu, Y.; Gu, Z.; Xia, Y. *J. Am. Chem. Soc.* **2012**, *134*, 15822–15831.

[4] Zheng, Z.; Tachikawa, T.; Majima, T. *J. Am. Chem. Soc.* **2014**, *136*, 6870–6873.

[5] Xia, Y.; Xia, X.; Peng, H. C. *J. Am. Chem. Soc.* **2015**, *137*, 7947–7966.

[6] Xia, X.; Xie, S.; Liu, M.; Peng, H. C.; Lu, N.; Wang, J.; Kim, M. J.; Xia, Y. *Proc. Natl. Acad. Sci. U. S. A.* **2013**, *110*, 6669–6673.

[7] Peng, H. C.; Park, J.; Zhang, L.; Xia, Y. *J. Am. Chem. Soc.* **2015**, *137*, 6643–6652.

[8] Yang, Y.; Wang, W.; Li, X.; Chen, W.; Fan, N.; Zou, C.; Chen, X.; Xu, X.; Zhang, L.; Huang, S. *Chem. Mater.* **2013**, *25*, 34–41.

[9] Cathcart, N.; Kitaev, V. *Sci. Rep.* **2016**, *6*, 32561.

[10] Liu, M.; Gilroy, K. D.; Peng, H. C.; Chi, M.; Guo, L.; Xia, Y. *Chem. Commun.* **2016**, *52*, 13159–13162.

[11] Cobley, C. M.; Rycenga, M.; Zhou, F.; Li, Z. Y.; Xia, Y. *Angew. Chem. Int. Ed.* **2009**, *48*, 4824–4827.

[12] Luo, M.; Ruditskiy, A.; Peng, H. C.; Tao, J.; Figueroa-Cosme, L.; He, Z.; Xia, Y. *Adv. Funct. Mater.* **2016**, *26*, 1209–1216.

[13] Gawande, M. B.; Goswami, A.; Felpin, F. X.; Asefa, T.; Huang, X.; Silva, R.; Zou, X.; Zboril, R.; Varma, R. S. *Chem. Rev.* **2016**, *116*, 3722–3811.

[14] Loiudice, A.; Lobaccaro, P.; Kamali, E. A.; Thao, T.; Huang, B. H.; Ager, J. W.; Buonsanti, R. *Angew. Chem. Int. Ed.* **2016**, *55*, 5789–5792.

[15] Nitopi, S.; Bertheussen, E.; Scott, S. B.; Liu, X.; Engstfeld, A. K.; Horch, S.; Seger, B.; Stephens, I. E. L.; Chan, K.; Hahn, C.; Nørskov, J. K.; Jaramillo, T. F.; Chorkendorff, I. *Chem. Rev.* **2019**, *119*, 7610–7672.

[16] Choi, C.; Cheng, T.; Flores Espinosa, M.; Fei, H.; Duan, X.; Goddard, W. A.; Huang, Y. *Adv. Mater.* **2019**, *31*, 1805405.

[17] Ma, S.; Sadakiyo, M.; Heim, M.; Luo, R.; Haasch, R. T.; Gold, J. I.; Yamauchi, M.; Kenis, P. J. A. *J. Am. Chem. Soc.* **2017**, *139*, 47–50.

[18] Huang, J.; Mensi, M.; Oveisi, E.; Mantella, V.; Buonsanti, R. *J. Am. Chem. Soc.* **2019**, *141*, 2490–2499.

[19] Lv, T.; Yang, X.; Zheng, Y.; Huang, H.; Zhang, L.; Tao, J.; Pan, L.; Xia, Y. *J. Phys. Chem. C* **2016**, *120*, 20768–20774.

[20] Jin, M.; Zhang, H.; Wang, J.; Zhong, X.; Lu, N.; Li, Z.; Xie, Z.; Kim, M. J.; Xia, Y. *ACS Nano* **2012**, *6*, 2566–2573.

[21] Zheng, Y.; Vasileff, A.; Zhou, X.; Jiao, Y.; Jaroniec, M.; Qiao, S. Z. *J. Am. Chem. Soc.* **2019**, *141*, 7646–7659.

[22] Kim, J.; Choi, W.; Park, J. W.; Kim, C.; Kim, M.; Song, H. *J. Am. Chem. Soc.* **2019**, *141*, 6986–6994.

[23] Suen, N. T.; Kong, Z. R.; Hsu, C. S.; Chen, H. C.; Tung, C. W.; Lu, Y. R.; Dong, C. L.; Shen, C. C.; Chung, J. C.; Chen, H. M. *ACS Catal.* **2019**, *9*, 5217–5222.

[24] Liu, H.; Xiang, K.; Liu, Y.; Zhu, F.; Zou, M.; Yan, X.; Chai, L. *ChemElectroChem* **2018**, *5*, 3991–3999.

[25] Weng, Z.; Zhang, X.; Wu, Y.; Huo, S.; Jiang, J.; Liu, W.; He, G.; Liang, Y.; Wang, H. *Angew. Chem. Int. Ed.* **2017**, *56*, 13135–13139.

[26] Wang, X.; Choi, S. Il; Roling, L. T.; Luo, M.; Ma, C.; Zhang, L.; Chi, M.; Liu, J.; Xie, Z.; Herron, J. A.; Mavrikakis, M.; Xia, Y. *Nat. Commun.* **2015**, *6*, 7594.

[27] Wang, H.; Zhou, S.; Gilroy, K. D.; Cai, Z.; Xia, Y. *Nano Today* **2017**, *15*, 121–144.

[28] Wang, Z.; Chen, Z.; Zhang, H.; Zhang, Z.; Wu, H.; Jin, M.; Wu, C.; Yang, D.; Yin, Y. *ACS Nano* **2015**, *9*, 3307–3313.

[29] Wu, D.; Cao, M.; Cao, R. *Chem. Commun.* **2014**, *50*, 12970–12972.

[30] Zhang, J.; Langille, M. R.; Mirkin, C. A. *J. Am. Chem. Soc.* **2010**, *132*, 12502–12510.

[31] Biesinger, M. C.; Lau, L. W. M.; Gerson, A. R.; Smart, R. S. C. *Appl. Surf. Sci.* **2010**, *257*, 887–898.

[32] Lyu, Z.; Xie, M.; Gilroy, K. D.; Hood, Z. D.; Zhao, M.; Zhou, S.; Liu, J.; Xia, Y. *Chem. Mater.* **2018**, *30*, 6469–6477.

[33] Pietrobon, B.; Kitaev, V. *Chem. Mater.* **2008**, *20*, 5186–5190.

[34] Pastoriza-Santos, I.; Sánchez-Iglesias, A.; Rodríguez-González, B.; Liz-Marzán, L. M. *Small* **2009**, *5*, 440–443.

[35] Sherry, L. J.; Jin, R.; Mirkin, C. A.; Schatz, G. C.; Van Duyne, R. P. *Nano Lett.* **2006**, *6*, 2060–2065.

[36] Ringe, E.; Zhang, J.; Langille, M. R.; Mirkin, C. A.; Marks, L. D.; Van Duyne, R. P. *Nanotechnology* **2012**, *23*, 444005.

[37] Lyu, Z.; Xie, M.; Aldama, E.; Zhao, M.; Qiu, J.; Zhou, S.; Xia, Y. *ACS Appl. Nano Mater.* **2019**, *2*, 1533–1540.

[38] Dai, Y.; Lu, P.; Cao, Z.; Campbell, C. T.; Xia, Y. *Chem. Soc. Rev.* **2018**, *47*, 4314–4331.

[39] Hung, L. L.; Tsung, C. K.; Huang, W.; Yang, P. *Adv. Mater.* **2010**, *22*, 1910–1914.

[40] Yang, T. H.; Zhou, S.; Gilroy, K. D.; Figueroa-Cosme, L.; Lee, Y. H.; Wu, J. M.; Xia, Y. *Proc. Natl. Acad. Sci. U. S. A.* **2017**, *114*, 13619–13624.

[41] Liu, S. H.; Fichthorn, K. A. *J. Phys. Chem. C* **2017**, *121*, 22531–22541.

[42] Meng, M.; Fang, Z.; Zhang, C.; Su, H.; He, R.; Zhang, R.; Li, H.; Li, Z. Y.; Wu, X.; Ma, C.; Zeng, J. *Nano Lett.* **2016**, *16*, 3036–3041.

[43] Bard, A. J.; Faulkner, L. R. *Electrochemical Methods: Fundamentals and Applications 2nd Ed*, Wiley, New York, **2001**.

[44] Liu, S. H.; Balankura, T.; Fichthorn, K. A. *Phys. Chem. Chem. Phys.* **2016**, *18*, 32753–32761.

[45] Glaria, A.; Cure, J.; Piettre, K.; Coppel, Y.; Turrin, C. O.; Chaudret, B.; Fau, P. *Chem. Eur. J.* **2015**, *21*, 1169–1178.

[46] Kim, M. J.; Alvarez, S.; Chen, Z.; Fichthorn, K. A.; Wiley, B. J. *J. Am. Chem. Soc.* **2018**, *140*, 14740–14746.

[47] Sun, H.; Jiao, X.; Wang, H.; Jiang, Z.; Chen, D. *ACS Appl. Mater. Interfaces* **2011**, *3*, 2425–2430.

[48] Gao, D.; Zhou, H.; Cai, F.; Wang, J.; Wang, G.; Bao, X. *ACS Catal.* **2018**, *8*, 1510–1519.

[49] Huang, H.; Jia, H.; Liu, Z.; Gao, P.; Zhao, J.; Luo, Z.; Yang, J.; Zeng, J. *Angew. Chem. Int. Ed.* **2017**, *56*, 3594–3598.

[50] Reske, R.; Mistry, H.; Behafarid, F.; Roldan Cuenya, B.; Strasser, P. *J. Am. Chem. Soc.* **2014**, *136*, 6978–6986.

[51] Huang, J.; Hörmann, N.; Oveisi, E.; Loiudice, A.; De Gregorio, G. L.; Andreussi, O.; Marzari, N.; Buonsanti, R. *Nat. Commun.* **2018**, *9*, 3117.

[52] Zhu, S.; Li, T.; Cai, W. B.; Shao, M. *ACS Energy Lett.* **2019**, *4*, 682−689.

[53] Hayden, B. E.; Kretzschmar, K.; Bradshaw, A. M. *Surf. Sci.* **1985**, *155*, 553−566.

[54] Zhu, S.; Jiang, B.; Cai, W. B.; Shao, M. *J. Am. Chem. Soc.* **2017**, *139*, 15664–15667.

[55] Rupprechter, G.; Unterhalt, H.; Morkel, M.; Galletto, P.; Dellwig, T.; Freund, H. J. *Vacuum* **2003**, *71*, 83–87.

[56] Hollins, P.; Pritchard, J. *Surf. Sci.* **1979**, *89*, 486–495.

[57] Sheng, W.; Kattel, S.; Yao, S.; Yan, B.; Liang, Z.; Hawxhurst, C. J.; Wu, Q.; Chen, J. G. *Energy Environ. Sci.* **2017**, *10*, 1180–1185.

[58] Gao, D.; Zhou, H.; Cai, F.; Wang, D.; Hu, Y.; Jiang, B.; Cai, W. Bin; Chen, X.; Si, R.; Yang, F.; Miao, S.; Wang, J.; Wang, G.; Bao, X. *Nano Res.* **2017**, *10*, 2181–2191.

[59] Zhu, W.; Kattel, S.; Jiao, F.; Chen, J. G. *Adv. Energy Mater.* **2019**, *9*, 1802840.

[60] Zeng, Z.; Chang, K. C.; Kubal, J.; Markovic, N. M.; Greeley, J. *Nat. Energy* **2017**, *2*, 17070.

[61] Bhandari, S.; Rangarajan, S.; Maravelias, C. T.; Dumesic, J. A.; Mavrikakis, M. *ACS Catal.* **2020**, *10*, 4112–4126.

[62] Ojeda, M.; Nabar, R.; Nilekar, A. U.; Ishikawa, A.; Mavrikakis, M.; Iglesia, E. *J. Catal.* **2010**, *272*, 287–297.

[63] Wang, Y.; Shen, H.; Livi, K. J. T.; Raciti, D.; Zong, H.; Gregg, J.; Onadeko, M.; Wan, Y.; Watson, A.; Wang, C. *Nano Lett.* **2019**, *19*, 8461–8468.

[64] Kresse, G.; Furthmüller, J. *Phys. Rev. B Condens. Matter Mater. Phys.* **1996**, *54*, 11169–11186.

[65] Kresse, G.; Furthmüller, J. *Comput. Mater. Sci.* **1996**, *6*, 15–50.

[66] Perdew, J. P.; Burke, K.; Ernzerhof, M. *Phys. Rev. Lett.* **1996**, *77*, 3865–3868.

[67] Blöchl, P. E. *Phys. Rev. B* **1994**, *50*, 17953–17979.

[68] Joubert, D. *Phys. Rev. B Condens. Matter Mater. Phys.* **1999**, *59*, 1758–1775.

[69] Grimme, S.; Antony, J.; Ehrlich, S.; Krieg, H. *J. Chem. Phys.* **2010**, *132*, 154104.

[70] Neugebauer, J.; Scheffler, M. *Phys. Rev. B* **1992**, *46*, 16067–16080.

[71] Bengtsson, L. *Phys. Rev. B Condens. Matter Mater. Phys.* **1999**, *59*, 12301–12304.

[72] Lide, D. R. *CRC Handbook of Chemistry and Physics, 96th Ed.*, CRC Press, Boca Raton, FL, **2015**.

[73] Schirber, J. E.; Morosin, B. *Phys. Rev. B* **1975**, *12*, 117–118.

[74] Monkhorst, H. J.; Pack, J. D. *Phys. Rev. B* **1976**, *13*, 5188–5192.

[75] Zhao, M.; Xu, L.; Vara, M.; Elnabawy, A. O.; Gilroy, K. D.; Hood, Z. D.; Zhou, S.; Figueroa-Cosme, L.; Chi, M.; Mavrikakis, M.; Xia, Y. *ACS Catal.* **2018**, *8*, 6948–6960.

[76] Gilroy, K. D.; Elnabawy, A. O.; Yang, T. H.; Roling, L. T.; Howe, J.; Mavrikakis, M.; Xia, Y. *Nano Lett.* **2017**, *17*, 3655–3661.

[77] Mackay, A. L. *Acta Crystallogr.* **1962**, *15*, 916–918.

[78] Linstrom, P. J.; Mallard, W. G. *NIST Chemistry WebBook, NIST Standard Reference Database Number 69*, National Institute Of Standards And Technology, Gaithersburg MD, **2017**.

CHAPTER 5

CONTROLLING THE SURFACE OXIDATION OF COPPER NANOWIRES IMPROVES THEIR CATALYTIC SELECTIVITY AND STABILITY TOWARD MULTI-CARBON PRODUCTS IN CARBON DIOXIDE REDUCTION

5.1 Introduction

The large amount of CO_2 produced from transportation and industry has raised increasing concerns in recent years because of the major environmental burdens from this gas and the necessary increase in mitigation investment [1,2]. In addition to photosynthesis, another promising route is to electrochemically convert CO_2 to chemical compounds for use as fuels or feedstock. Typically, a variety of products are generated in this process, with the most common ones being CO and formate. Compared to C_1 species, multi-carbon (C_{2+}) products such as ethylene and ethanol are more desirable considering their higher values, larger energy densities, and broader applications. Despite the remarkable progress, it remains a grand challenge to electrocatalytically promote C-C coupling and thereby achieve high selectivity toward C_{2+} products during the CO_2RR [1–3].

Among all the metals under consideration for CO_2RR, Cu easily stands out for its ability to produce a substantial amount of oxygenates and hydrocarbons. However, for those catalysts based on pure Cu (*e.g.*, Cu foils), they tend to suffer from a number of shortcomings, including low selectivity, poor competition with the HER, high

overpotential, and compromised stability. To address these issues, the Cu nanostructures have been engineered in multiple ways, such as control of their shapes and thus surface structures [4–7], doping with other metals or non-metals [8–10], and complete or partial oxidation of Cu [11–13]. When switching to Cu dendrites with a rough, defective surface, for example, a FE as high as 57% was achieved for ethylene at a potential more negative than -1.4 V_{RHE} in 0.1 M aqueous KBr. The excellent performance was attributed to the presence of high-index facets [5]. In another study, star-shaped Cu decahedra featuring a penta-twinned structure were demonstrated with a good selectivity of 52.4% toward ethylene at -1.0 V_{RHE} in 0.1 M aqueous $KHCO_3$. The tensile surface strain caused by the twin boundaries and the induced surface defects were proposed as a main contribution to the high C_{2+} yields [6].

By partially oxidizing Cu nanostructures or directly using nanostructures made of Cu_xO, improvement in catalytic performance was also achieved, including the observations of lower overpotentials and higher selectivity toward C_{2+} products. The improvement was typically ascribed to an increase in surface roughness and thus a higher density of surface defects, induced changes to the local pH, and the possible existence of residual Cu(I) species that might serve as active sites [1]. In one study, it was reported that when Cu_2O nanoparticles were used as catalysts, a high selectivity approaching 60% was achieved for ethylene after 6 h of electrolysis at -1.1 V_{RHE} in 0.1 M aqueous $KHCO_3$. The 20-nm Cu_2O particles were gradually broken down into 2-4 nm particles under the negative potential, leading to an increase in the selectivity toward ethylene that finally reached 60%. The compact arrangement of small particles and the high density of grain boundaries among them were believed to be responsible for the high yield of C_{2+}

products because the defective structures helped promote C-C coupling [11]. In another report, plasma-activated Cu nanocubes with an oxygen content of 30% (in terms of atomic percentage) showed a higher FE toward ethylene (up to 45% at -1.0 V_{RHE} in 0.1 M aqueous $KHCO_3$) relative to those with lower oxygen contents. The key parameters were believed to be the defects induced by plasma oxidation and the surface/subsurface oxygen species, both capable of enhancing the binding of CO to the Cu surface [13].

In an attempt to leverage the benefits arising from both shape control and surface oxidation, here I synthesize Cu nanowires (CuNWs) and then partially oxidize their surface under two different conditions to generate Cu@Cu_xO core-sheath nanostructures. When the oxide sheath is reduced to elemental Cu, the increase in surface roughness and the penta-twinned structure intrinsic to the nanowires are able to work synergistically in promoting the generation of C_{2+} products during CO_2RR. As a result, FEs as high as 57.7 and 52.0% for ethylene are obtained at -1.0 V_{RHE} in 0.1 M aqueous $KHCO_3$ when the CuNWs oxidized by the O_2 from air (A-CuNWs) and aqueous H_2O_2 (H-CuNWs) serve as catalysts, respectively. The high selectivity toward ethylene, together with C_{2+} yields approaching 78.4 and 71.9%, is among the highest when benchmarked against all the Cu-based nanostructures reported in literature (Table 5.1). In addition to the high selectivity, we also demonstrate that a thick and smooth oxide sheath on the CuNWs can substantially improve their catalytic stability, with H-CuNWs showing a much better stability than A-CuNWs, due to the mitigation of fragmentation and thus preservation of 1-D morphology. This work represents the first attempt to bring a tight control to the oxidation process of CuNWs for the demonstration of its importance in determining the activity, selectivity, and stability of Cu catalysts toward CO_2RR.

Table 5.1. Comparison of Cu-based catalysts used in electrochemical CO_2RR.

Catalyst	Electrolyte	E *vs.* RHE	Faradaic Efficiency (%)				j_{C2H4} (mA cm^{-2})	Stability (h)[(c)]	Ref
			H_2	CH_4	C_2H_4	C_{2+}			
A-CuNWs	0.1 M $KHCO_3$	-1.0	8.5	1.9	57.7	78.4	19.6[(a)]/4.1[(b)]	<22	This work
H-CuNWs	0.1 M $KHCO_3$	-1.0	11.4	6.1	52.0	71.9	12.5[(a)]/3.5[(b)]	22	This work
rGO-wrapped CuNWs/C	0.1 M $KHCO_3$	-1.25	30	55	2	N/A	N/A	5 C[(d)]	[14]
CuNWs/C	0.1 M $KHCO_3$	-0.9	69	<0.5%	20	N/A	N/A	N/A	[15]
Cu_2O NPs/C	0.1 M $KHCO_3$	-1.1	15.0	1.9	57.3	73.9	10[(a)]/0.45[(b)]	10	[11]
Cu@CuO NPs/C	0.1 M $KHCO_3$	-1.1	43.5	7.6	33.2	44.5	N/A	N/A	[11]
Branched CuO/C	0.1 M $KHCO_3$	-1.0	30	~0	68	68	13.5[(a)]/2.0[(b)]	11.7	[12]
Cu_2O cubes/C	0.1 M $KHCO_3$	-1.0	50	~0	32	N/A	5.3[(a)]/1.4[(b)]	~1	[12]
Cu star decahedra	0.1 M $KHCO_3$	-1.0	33.5	6.6	52.4	52.9	8.9[(a)]/ ~15.7[(b)]	12	[6]
Commercial CuNPs	0.1 M $KHCO_3$	-1.0	39.1	7.0	37.1	45.76	~5.8[(a)]/3.0[(b)]	N/A	[6]
Cu cubes	0.1 M $KHCO_3$	-1.15	40.5	7	34	44	2.38[(a)]	N/A	[16]
Cu octahedra	0.1 M $KHCO_3$	-1.15	40	0	19	27	3.78[(a)]	N/A	[16]
Cu_3N@Cu	0.1 M $KHCO_3$	-0.95	17.0	2.5	39.3	63.7	8.5[(a)]/0.9[(b)]	30	[9]
B-doped Cu	0.1 M $KHCO_3$	-1.1	20	0.08	52	79	36.4[(a)]/ 38.2[(b)]	38	[10]
Cu nanoparticles, flow cell	1 M KOH	-0.79	7.0	1.2	45.6	70.0	140[(a)]	4	[17]
Abrupt Cu interface, flow cell	10 M KOH	-0.54	5	0.2	66	83	218.7[(a)]	150	[18]

(a) The current density was normalized by geometric area.
(b) The current density was normalized by ECSA.

(c) The time representing the stability of catalysts is selected based on two factors: the time reported in literature, or the time point when no obvious decrease in ethylene selectivity was observed.
(d) The stability of the catalyst was evaluated by the total electric charge passing through the catalyst.

5.2 Results and Discussion

The preparation of a catalyst typically involved two major steps: synthesis of CuNWs in the presence of hexadecylamine and glucose, followed by surface oxidation at room temperature under different conditions. Figure 5.1 shows TEM images of the as-prepared CuNWs with an average diameter of 22.4 ± 4.2 nm and length up to several micrometers. Based on our previous report, the nanowires had a penta-twinned structure and their side surface was covered by {100} facets [19].

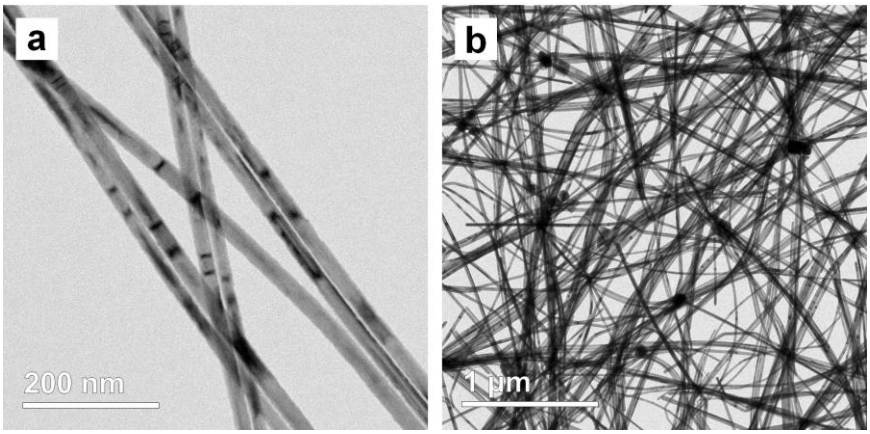

Figure 5.1. TEM images at different magnifications of the pristine CuNWs.

After oxidization with the O_2 from air, the 1-D morphology was retained while the surface was roughened due to the formation of an oxide sheath (Figure 5.2, a and b). As shown in Figure 5.2b, lattice fringes with a spacing of 0.21 nm, corresponding to {111} planes of Cu, could be observed at the central region of the nanowire, indicating

the presence of metallic Cu in the core. The fringes could hardly be observed when moving toward the surface of the nanowire, along with a decrease in contrast, suggesting the formation of oxides on the surface.

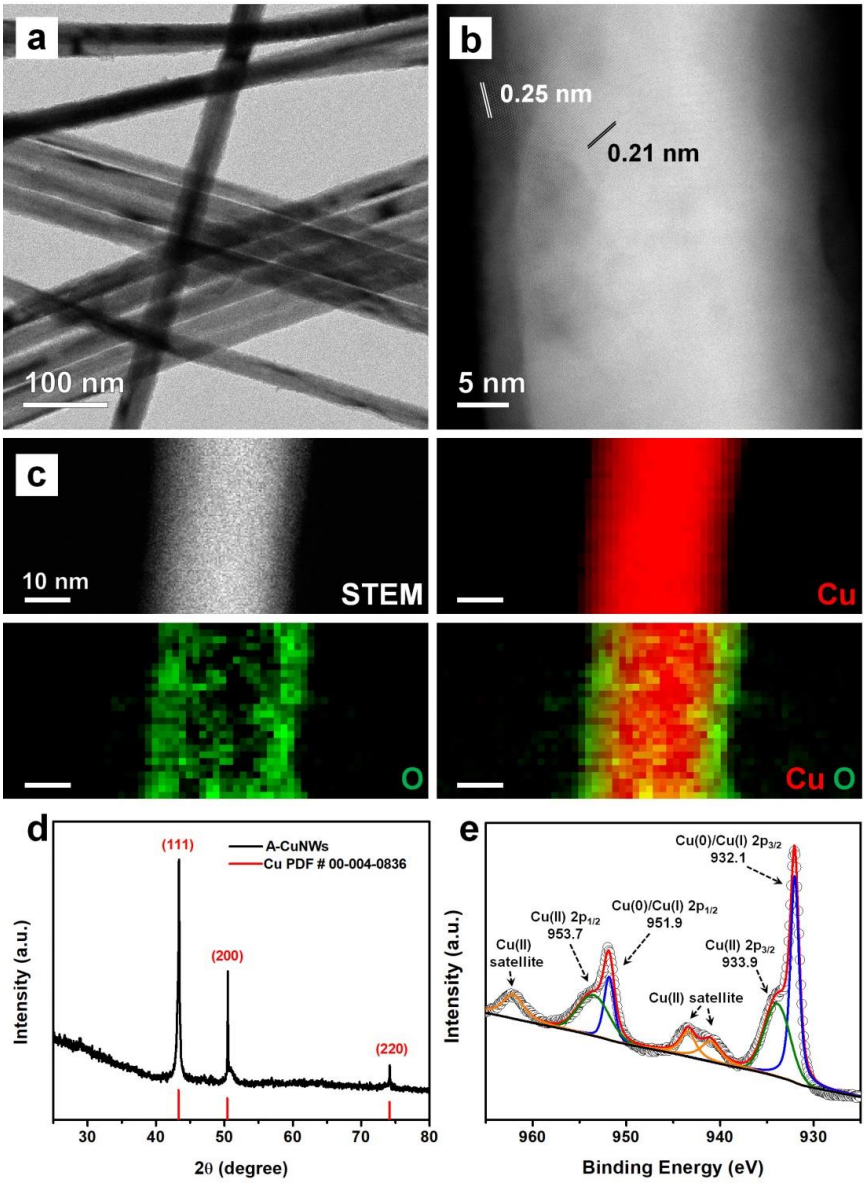

Figure 5.2. (a) TEM and (b) DF-STEM images of CuNWs covered by a thin, non-uniform sheath of Cu_xO formed through oxidation by the O_2 from air (denoted A-CuNWs). (c) EELS mapping, (d) XRD pattern, and (e) XPS spectrum recorded from the same oxidized sample.

At a few spots where lattice fringes could be resolved, the spacing was measured to be 0.25 nm, corresponding to the {111} planes of Cu_2O. Taken together, it can be concluded that the oxide sheath was comprised of a mixture of both amorphous and crystalline copper oxides. The presence of surface oxides was also supported by the electron energy loss spectroscopy (EELS) mapping data shown in Figure 5.2c, where a thin layer containing oxygen could be resolved on the core made of metallic Cu. Interestingly, in the DF-STEM image, I observed the formation of an oxide sheath with varying thickness at different locations. Based on previous reports, it was demonstrated that the formation of copper oxides on Cu(100) facets followed an island-growth mode and it was found to be more obvious under a slow oxidation kinetics [20,21]. Taken together, the non-uniform oxidation occurring on the surface of a CuNW was believed to be responsible for the formation of a Cu_xO sheath with uneven thickness.

In the XPS spectrum recorded from A-CuNWs (Figure 5.2e), two peaks were resolved at 932.1 and 951.9 eV, which could be assigned to Cu(0) or Cu(I) 2p peaks. Additionally, I observed two peaks at 933.9 and 953.7 eV, together with satellite peaks around 941, 943, and 962 eV, and all of them could be assigned to Cu(II) 2p peaks [22]. These results indicate that the oxide sheath was made of a mix of Cu_2O and CuO. In the XRD pattern, however, no peaks of copper oxides were observed (Figure 5.2d). I only resolved three peaks at 43.4°, 50.5°, and 74.2°, corresponding to the diffraction from Cu(111), (200), and (220) planes. The absence of Cu_xO peaks in the XRD pattern confirmed the dominance of amorphous phase, in agreement with our conclusion drawn from STEM imaging.

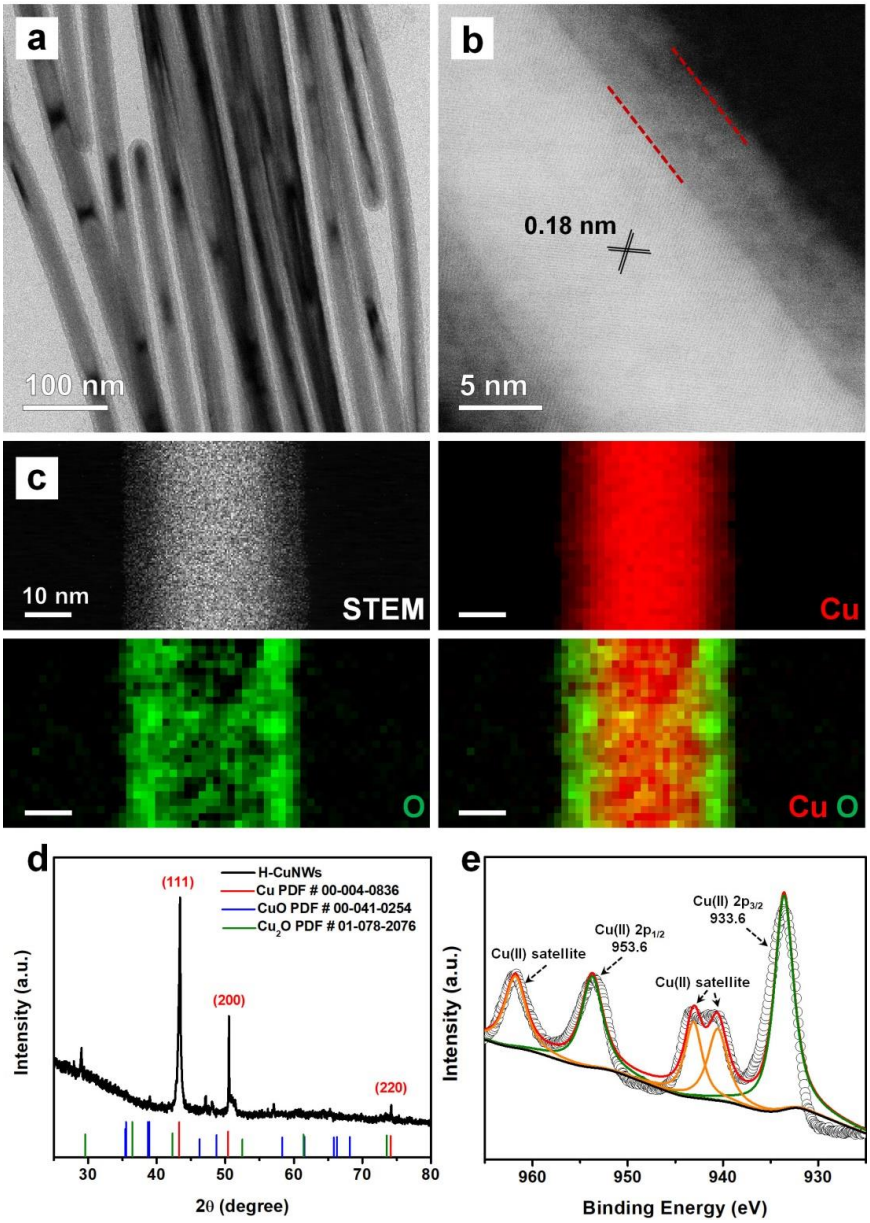

Figure 5.3. (a) TEM and (b) DF-STEM images of CuNWs covered by a smooth, relatively thick (*ca.* 6 nm) sheath of Cu_xO formed through oxidation by aqueous H_2O_2 (denoted H-CuNWs). (c) EELS mapping, (d) XRD pattern, and (e) XPS spectrum recorded from the same oxidized sample.

Different from the slow oxidation by the O_2 from air, CuNWs covered by a relatively thicker Cu_xO sheath (H-CuNWs) were obtained when the sample was subjected to oxidation by aqueous H_2O_2 (Figure 5.3a). The H-CuNWs had a metallic Cu core with

an average diameter of 18.5 ± 3.4 nm and an oxide sheath of 6.9 ± 0.7 nm in thickness. As shown by the DF-STEM image in Figure 5.3b, both the oxide layer and the Cu core had smooth surfaces and this outcome can be attributed to the fast oxidation kinetics. Multiple nucleation sites for copper oxides were generated at the same time across the surface of a nanowire, leading to the formation of an oxide sheath uniform in thickness [20]. The existence of Cu_xO layer was also verified by EELS mapping (Figure 5.3c). A higher intensity of oxygen was observed relative to that of A-CuNWs, consistent with the fact that H-CuNWs had a thicker layer of oxides. In the DF-STEM image, the clearly resolved lattice fringes in the core confirmed its composition as metallic Cu, while nearly no fringes were observed in the sheath.

From the XRD pattern (Figure 5.3d), the intensity of Cu(0) was also the strongest, with three peaks positioned at 43.4°, 50.5°, and 74.2°. In contrast, the peaks of both Cu_2O and CuO were very weak, with that at 28.9° corresponding to Cu_2O and those at 39.0°, 47.0°, and 48.0° to CuO. A plausible reason for the weak intensity of copper oxides in the XRD pattern can be ascribed to the dominance of amorphous structure, which was further proven by nano-beam electron diffraction (NBED). As shown in Figure 5.4, rings along with irregularly distributed diffraction spots were observed in the NBED patterns recorded from selected areas of the Cu_xO sheath, revealing the amorphous phase containing randomly oriented nanocrystallites. In contrast, discrete spots located at nearly the same positions could be clearly observed in the NBED patterns taken from the Cu core, with no accompanied rings, demonstrating the continuity and crystalline structure of the metallic core [23].

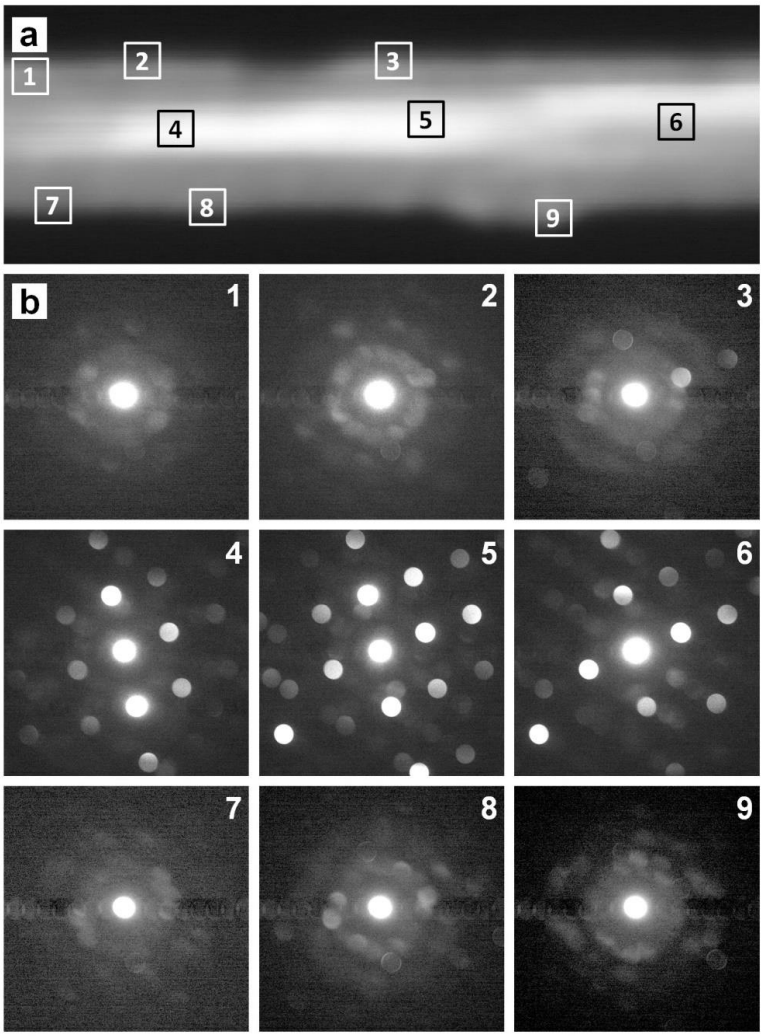

Figure 5.4. The mixture of amorphous and crystalline structure of the Cu_xO sheath and the crystalline structure of the metallic Cu core determined by NBED. (a) DF-STEM image of a H-CuNW. (b) The NBED patterns taken from the areas marked by numbers in (a). The patterns labeled 4–6 were taken from the Cu core, and the others labeled 1-3 and 7-9 were taken from the Cu_xO sheath.

The composition of the surface oxides was also analyzed using XPS (Figure 5.3e). Different from A-CuNWs, the intensity of Cu(II) accounted for the vast majority and the peaks of Cu(0) or Cu(I) were barely detected, suggesting that the surface of H-CuNWs was covered by a relatively thick sheath made of CuO. In a typical process of Cu oxidation, the metallic Cu was first oxidized to Cu_2O, which could be further converted

to CuO in the presence of adequate oxidants. The relatively high concentration of H_2O_2 and its fast oxidation kinetics enabled the fully oxidation of Cu, leading to the formation of a CuO-based sheath [24,25].

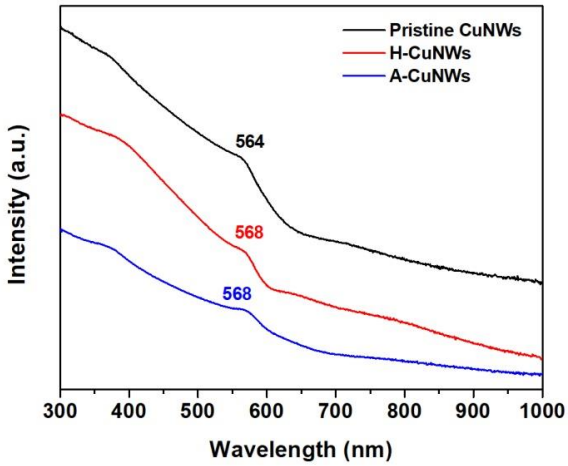

Figure 5.5. UV-vis spectra of pristine CuNWs, H-CuNWs, and A-CuNWs. A red shift in peaks was observed for the two types of CuNWs covered by oxide sheath.

In addition to microscopy evidence, the presence of oxide layer also agreed with the UV-vis spectra (Figure 5.5). Due to the LSPR property, Cu nanostructures exhibit absorption in the visible region, and the peak position is highly sensitive to the oxidation state of Cu on the surface because of the change in dielectric constant [26]. For the freshly prepared CuNWs, A-CuNWs, and H-CuNWs, I obtained peaks located at 564, 568, and 568 nm, respectively. Compared to the as-obtained CuNWs, the peaks of both A-CuNWs and H-CuNWs were slightly red-shifted and the shift can be attributed to the surface oxidation of Cu nanostructures [27,28].

My collaborators and I then measured and compared the selectivity and activity of the CuNWs with different surface oxidation toward CO_2RR in the potential range of -0.8

to -1.2 V_{RHE} in 0.1 M aqueous $KHCO_3$ (Figure 5.6, Table 5.2 and Table 5.3). Multiple products were detected, including CO, CH_4, ethylene, and ethanol, and we paid special attention to the C_{2+} species, in particular, ethylene. For A-CuNWs, a FE approaching 57.7% was obtained at -1.03 V_{RHE} for ethylene, together with a total efficiency reaching 78.4% for C_{2+} products. These values were among the highest selectivity for CO_2RR in a $KHCO_3$ solution, even compelling when compared to the performance measured in a flow cell containing a strong alkaline electrolyte (Figure 5.6a and Table 5.1).

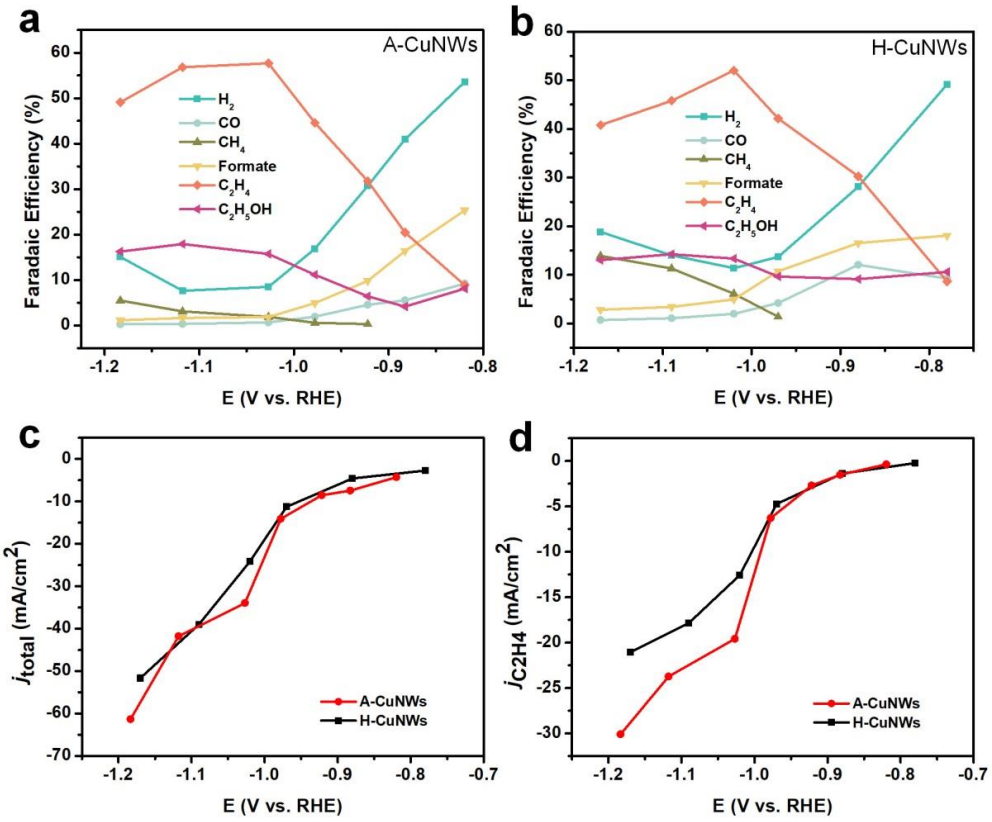

Figure 5.6. (a, b) Faradaic efficiencies of the catalysts based on A-CuNWs and H-CuNWs, respectively. (c) Total and (d) partial current densities toward ethylene for the same types of catalysts in 0.1 M $KHCO_3$. The current densities were normalized to the geometric area.

Table 5.2. Details of the selectivity and geometric current density in CO_2RR using A-CuNWs as the catalyst.

E (V vs RHE)	CO (%)	H_2 (%)	CH_4 (%)	C_2H_4 (%)	Formate (%)	Acetate (%)	Ethanol (%)	1-Propanol (%)	Total (%)	*j* ($mA \cdot cm^{-2}$)
-0.82	9.20	53.58	--	8.84	25.32	0.00	8.13	0.00	105.08	4.3
-0.88	5.53	40.94	--	20.45	16.39	0.00	4.14	2.12	89.57	7.4
-0.92	4.55	30.70	0.32	31.77	9.80	0.00	6.43	2.41	85.99	8.5
-0.98	1.93	16.87	0.58	44.59	4.90	0.00	11.17	5.37	85.42	14.1
-1.03	**0.65**	**8.50**	**1.89**	**57.67**	**1.86**	**0.00**	**15.72**	**5.02**	**91.31**	**34.0**
-1.12	0.35	7.61	3.09	56.83	1.64	0.00	17.92	3.35	90.80	41.8
-1.18	0.25	15.08	5.50	49.10	1.16	0.00	16.25	2.36	89.70	61.3

Table 5.3. Details of the selectivity and geometric current density in CO_2RR using H-CuNWs as the catalyst.

E (V vs RHE)	CO (%)	H_2 (%)	CH_4 (%)	C_2H_4 (%)	Formate (%)	Acetate (%)	Ethanol (%)	1-Propanol (%)	Total (%)	*j* ($mA \cdot cm^{-2}$)
-0.78	9.23	49.18	--	8.63	18.07	--	10.60	--	95.71	2.70
-0.88	12.08	28.13	--	30.28	16.54	1.51	9.12	4.37	102.02	4.60
-0.97	4.20	13.69	1.39	42.13	10.75	1.12	9.66	8.51	91.44	11.3
-1.02	**1.98**	**11.40**	**6.13**	**52.02**	**4.98**	**1.05**	**13.34**	**5.49**	**96.39**	**24.1**
-1.09	1.10	14.01	11.32	45.80	3.44	1.27	14.24	2.95	94.11	39.0
-1.17	0.72	18.82	13.91	40.78	2.83	1.27	13.06	1.59	92.97	51.7

Compared with the high yield of C_{2+} products at -1.03 V_{RHE}, the production of CO and CH_4 only accounted for 0.65 and 1.9%, respectively. The FE of H_2 was as low as 8.5%, indicating the effective suppression of HER. Normalized by geometric area, a total

current density of 34.0 $mA \cdot cm^{-2}$ was achieved along with the high selectivity toward ethylene, whose partial current density reached 19.6 $mA \cdot cm^{-2}$ (Figure 5.6, c and d). When normalized to the mass of catalyst, we obtained a mass activity of 384.1 $mA \cdot mg^{-1}$ for the selective production of ethylene (Figure 5.7). The high current density and mass activity of A-CuNWs clearly demonstrate their prominent performance in electrochemical CO_2RR [11].

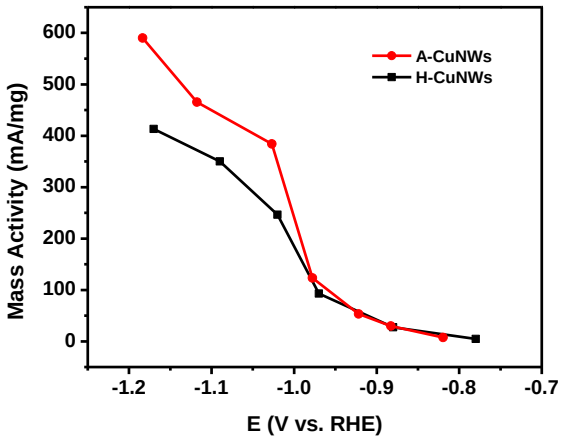

Figure 5.7. Mass activities for ethylene production when A-CuNWs and H-CuNWs were used as catalysts.

In comparison with A-CuNWs, H-CuNWs with a thicker oxide sheath and smoother surface showed a slightly lower FE toward ethylene: 52.0% at -1.02 V_{RHE} (Figure 5.6b). The total yield for C_{2+} products reached 71.9% while the proportion of H_2 was at 11.4%, together with low yields for both CO and CH_4 (2.0 and 6.1%, respectively). At -1.02 V_{RHE}, a geometric current density of 24.1 $mA \cdot cm^{-2}$ was achieved for all the products, with a partial current density of 12.5 $mA \cdot cm^{-2}$ for ethylene (Figure 5.6, c and d). Although slightly lower than A-CuNWs, a mass activity approaching 246.2

$mA \cdot mg^{-1}$ was obtained for ethylene production when H-CuNWs served as the catalyst (Figure 5.7). When normalized to the ECSA, we obtained partial current densities as high as 4.1 and 3.5 $mA \cdot cm^{-2}$ toward ethylene for A-CuNWs and H-CuNWs, respectively, demonstrating their outstanding performance in CO_2RR (Figure 5.8, the current densities of comparable catalysts can be found in Table 5.1). It should be noted that the high (approaching 30 $mA \cdot cm^{-2}$) geometric current densities achieved by CuNWs could be attributed to the involvement of 3-D mass transport, which raised the limitation of current density [31].

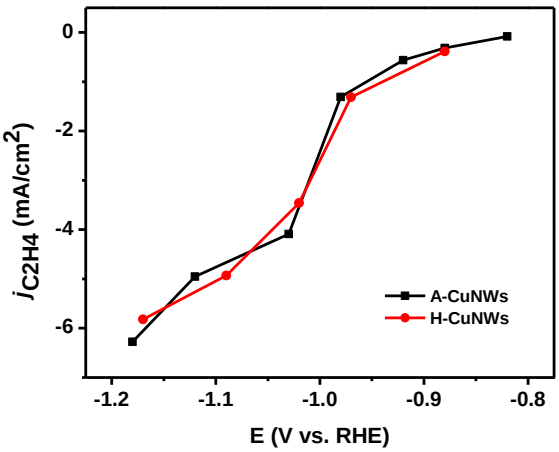

Figure 5.8. ECSA-normalized partial current densities toward ethylene for two types of CuNWs in 0.1 M $KHCO_3$.

To look into the mechanism underlying the high selectivity and activity of CuNW-based catalysts and the reason why they behaved differently, I characterized the structures of both catalysts after 1 h of electrolysis at -1.02 V_{RHE}. As shown in Figure 5.9a, fragmentation was observed for A-CuNWs, where small pseudo-spherical nanoparticles and nanorods resulted from disintegration of nanowires could be found in

the TEM image. For the nanowires whose 1-D structure was preserved, their surface became fairly rough. A close examination of the nanowire illustrated the existence of large holes and cavities on the surface, which could be attributed to the reduction of surface oxides (Figure 5.9b). As shown by the BF-STEM image in Figure 5.9c, the lattice spacing of 0.21 and 0.18 nm could be assigned to the {111} and {200} planes of Cu, respectively, confirming that the majority of surface Cu_xO was reduced to metallic Cu.

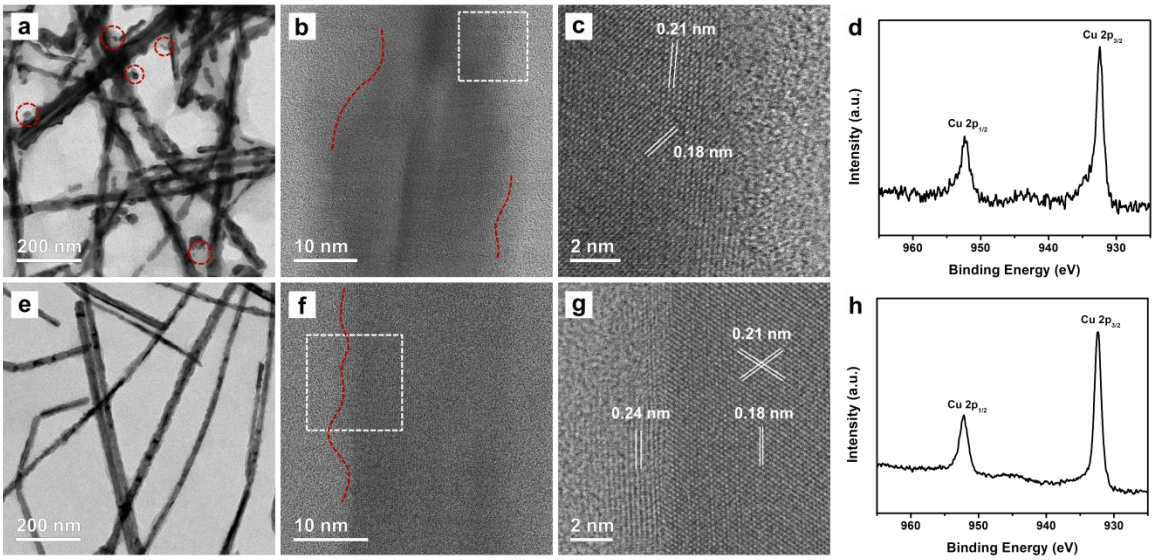

Figure 5.9. (a) TEM, (b, c) BF-STEM images, and (d) XPS spectrum of A-CuNWs after 1 h of electrolysis. (e) TEM, (f, g) BF-STEM images, and (h) XPS spectrum of H-CuNWs after 1 h of electrolysis. A potential of -1.02 V_{RHE} was applied for all measurements. The images in (c) and (g) were taken from the regions marked by boxes in (b) and (f), respectively. The clusters formed during electrolysis are marked by red circles in (a).

The conversion of oxide sheath was also revealed by XPS. Compared to the relatively strong peaks of copper oxides in the as-prepared A-CuNWs (Figure 5.2e), no satellite peaks were observed for the same sample after 1 h of electrolysis (Figure 5.9d),

confirming the reduction of Cu(II) to Cu(0) or Cu(I). Considering the larger lattice spacing of copper oxides and possible surface reconstruction, voids would be generated for the formation of cavities on the surface when Cu_xO was reduced to metallic Cu [32]. The non-uniform thickness of oxide layer caused by the slow oxidation kinetics of O_2 from air resulted in the formation of voids with different sizes and thus the presence of deep cavities, increasing the chance of breaking up the nanowires. In addition to the reduction of copper oxides, detachment of small nanoparticles from the CuNWs during electrolysis might also facilitate their fragmentation [33]. It was reported that the adsorption of either H or CO, intermediates in HER and CO_2RR, on the surface of Cu nanocubes would lead to degradation to the shapes when a low potential was applied. An increased number of pinholes on the surface and a decrease in the size of Cu nanocubes were observed, along with an increased number of nanoparticles emerging around the cubes [34]. This was similar to what I observed on A-CuNWs.

In contrast to the A-CuNWs, the 1-D morphology of the H-CuNWs was largely retained during electrolysis. As shown in Figure 5.9e, I found nearly no fragment around the nanowires, let alone their disintegration. Compared with the smooth surface of H-CuNWs before electrolysis (Figure 5.3a), the surface roughness was increased after being held at -1.02 V_{RHE} for 1 h. As shown by the BF-STEM image in Figure 5.9f, small, shallow voids were formed on the surface. The magnified, atomic-resolution image revealed the presence of metallic Cu on the surface, where the lattice spacing of 0.21 and 0.18 nm could be indexed to the Cu {111} and {100} planes (Figure 5.9g). Some copper oxides were also observed outside the metallic Cu core, but they are highly possible to be generated during the preparation of sample for STEM imaging. Similar to the A-CuNWs,

the XPS peaks of CuO disappeared after electrolysis, confirming the reduction of Cu(II) to Cu(0) or Cu(I) (Figure 5.9h).

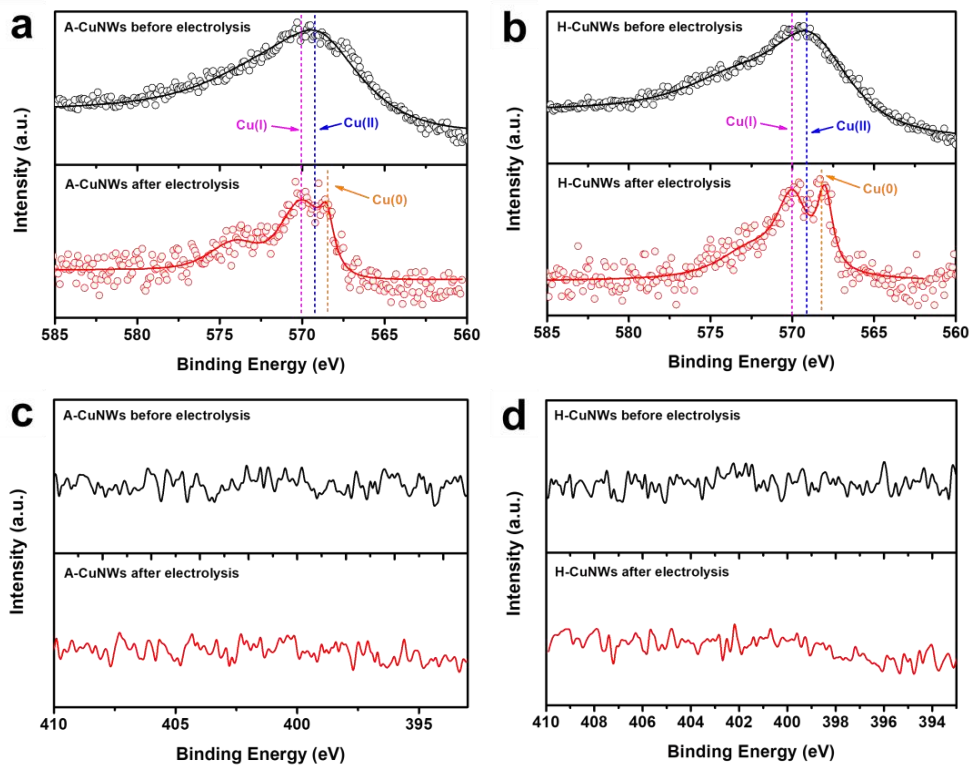

Figure 5.10. XPS spectra of (a, c) A-CuNWs and (b, d) H-CuNWs before and after 1 h of electrolysis in the region of (a, b) Auger Cu LMM and (c, d) N 1s. The orange, pink, and blue dotted lines represent the binding energies of Cu(0), Cu(I), and Cu(II) species, respectively [12].

To further verify the oxidation state of Cu on the surface, I measured the Auger Cu LMM spectra of the nanowires before and after electrolysis. (Figure 5.10) The samples were protected by Ar throughout the transfer process. Before electrolysis, the surface oxides of both types of nanowires were mainly composed of CuO, as revealed by the peaks located at 568.9 eV. After 1 h of electrolysis, I observed both Cu(0) and Cu(I) peaks in the CuNWs, located at 568.0 and 569.8 eV, respectively, suggesting the

presence of Cu(I) ions in the catalysts. It is worth pointing out that the retention of Cu(I) species during electrolysis was also observed in recent studies involving both *ex situ* and *in situ* techniques [10,12,13,34–36].

Based on TEM and STEM imaging, the high yields of C_{2+} products for CuNWs covered with an oxide sheath can be mainly attributed to their increased surface roughness [5,32,37,38]. As previously reported, roughening the surface of Cu catalysts would lead to the generation of a greater density of defective sites, which can enhance the adsorption of C_1 intermediates and thus improve the catalyst's selectivity toward C_{2+} products [37]. In addition to surface roughness, several other factors, including the presence of twin defects and 1-D morphology of the nanowires, may also be involved [6,15]. Based on simulations from previous reports, the twin boundaries and tensile surface strain, together with stacking faults arising from a stress release mechanism, could enhance the adsorption of CO on Cu surface and increase CO coverage density, which in turn facilitated the C-C coupling and formation of C_{2+} products [6]. As such, the high yields of C_{2+} species may also benefit from the penta-twinned structure of the CuNWs. Moreover, the small diameter of the nanowires and their 1-D morphology also enlarged the specific surface area and improved the mass transport in electrocatalysis, contributing to a higher mass activity [39,40]. As a comparison, when H_2O_2-oxidized Cu nanoparticles were used as the catalyst, a FE of 41.8% toward ethylene was obtained at -1.05 V_{RHE}, together with a geometric partial current density of 6.8 mA cm^{-2} (Figure 5.11). The inferior selectivity and lower current density of the nanoparticles further demonstrate the importance of both the 1-D morphology and twinned structure of the nanowires in improving mass transport and facilitating C-C coupling [40].

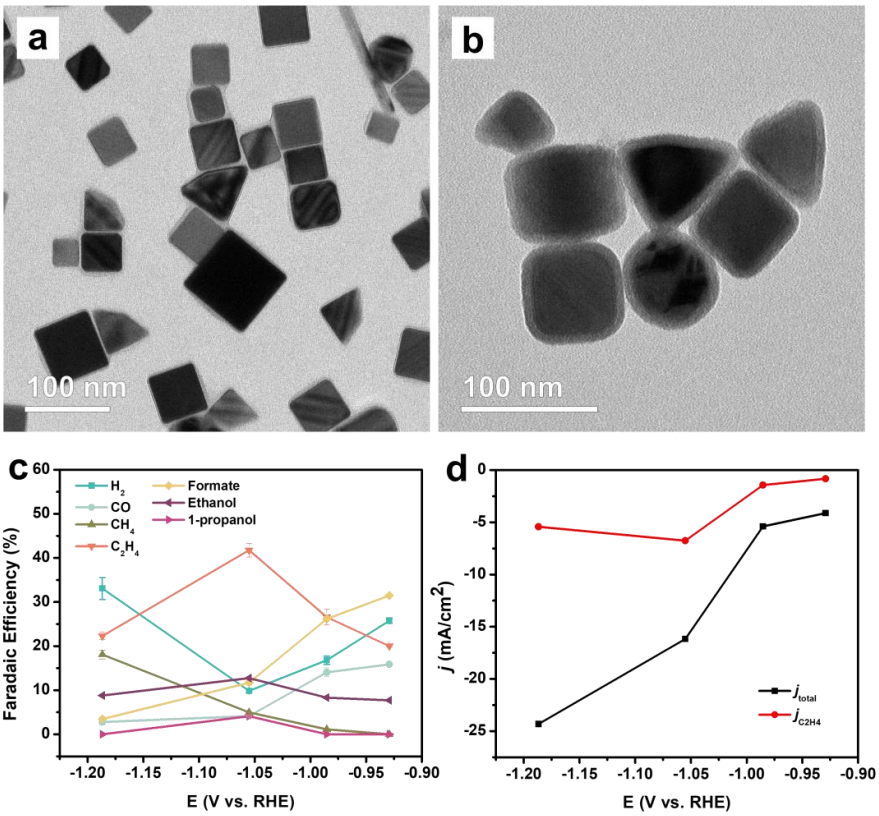

Figure 5.11. (a, b) TEM images of Cu nanoparticles (a) before and (b) after oxidizing by H_2O_2. (c) Faradaic efficiencies of the catalyst based on Cu nanoparticles. (d) Total and partial current densities (toward ethylene) for the Cu nanoparticles in 0.1 M $KHCO_3$. The current densities were normalized to the geometric area.

Comparing the shape evolution of two types of CuNWs during CO_2RR, I proposed that the higher C_{2+} selectivity of A-CuNWs relative to that of H-CuNWs could be ascribed to their even greater surface roughness. As confirmed by the TEM and STEM images in Figure 5.9, b and f, deeper cavities were observed on A-CuNWs, and they were reported to help trap the C_1 and even C_2 intermediates and thus facilitate C-C coupling [41,42]. Besides, the greater extent of roughness also revealed the potential existence of a higher abundance of high-index facets and defective sites on the surface of A-CuNWs, which had been proven to promote the formation of C_{2+} products [7,32].

Table 5.4. Capacitance values, surface roughness factors, and ECSAs measured using CV. The surface roughness factor of electropolished Cu is defined to be 1 [9,29,30].

Sample	Capacitance ($\mu F/cm^2$)	Surface Roughness Factor	ECSA (cm^2)
Electropolished Cu	29	1	0.20
Pristine CuNWs	47	1.6	0.32
H-CuNWs[(a)]	105	3.6	0.71
A-CuNWs[(a)]	140	4.8	0.95

(a) the capacitance was measured after the surface oxides were reduced (-1.02 V_{RHE}, 1 h).

In addition to selectivity, the greater surface roughness also contributed to a larger specific surface area and thus higher mass activity of A-CuNWs compared to H-CuNWs. As shown in Table 5.4, double-layer capacitances of different types of nanowires were measured, correlating their activities with surface areas. A capacitance of 140 $\mu F \cdot cm^{-2}$ was obtained for A-CuNWs, which was 40% greater than that of H-CuNWs, consistent with the higher mass activity of A-CuNWs. When using pristine CuNWs as a reference, both A-CuNWs and H-CuNWs exhibited larger capacitances (with a factor of 3.0 and 2.2, respectively), revealing their increase in surface roughness arising from the presence and subsequent reduction of surface oxides. We also tried to measure the CO_2RR performance of pristine CuNWs as soon as they were prepared, with an effort to avoid significant oxidation like in the case of A-CuNWs. Compared with the surface-oxidized nanowires, pristine CuNWs showed a relatively lower C_{2+} selectivity (66.0%) at -1.07 V_{RHE} owing to the absence of extensive surface oxidation and thus the lower surface roughness (Figure 5.12).

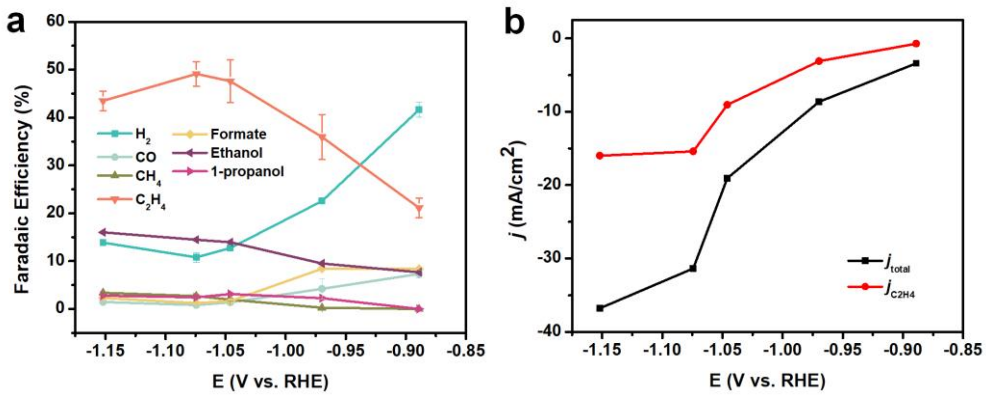

Figure 5.12. (a) Faradaic efficiencies of the catalyst based on pristine CuNWs. (b) Total and partial current densities (toward ethylene) for the pristine CuNWs in 0.1 M $KHCO_3$. The current densities were normalized to the geometric area. It should be noted that it is hard to avoid oxidation during the working electrode preparation process, and the catalytic performance of pristine CuNWs were measured once prepared, with an effort to avoid large extent of oxidation like A-CuNWs.

The stability of the CuNW-based catalysts was then measured at -1.02 V_{RHE}, corresponding to the highest ethylene selectivity. For A-CuNWs, the FE of ethylene gradually decreased as the reaction time was extended, along with an increase in the yields of H_2 and CH_4 (Figure 5.13a), which could be mainly attributed to the severe fragmentation of A-CuNWs during the measurement. It has been suggested by many reports that the selectivity of Cu catalysts is highly related to the particle size [43,44]. When the particle size of Cu decreased, below 5 nm in particular, a dramatic increase in activity and selectivity toward HER was observed, which can be ascribed to the increased proportion of atoms located at edges and corners. Those atoms have relatively low coordination numbers and can serve as strong binding sites for H and CO, limiting their diffusion on surface and further reaction to generate C_{2+} products. Under this circumstance, HER was greatly facilitated due to the improved adsorption of protons on Cu surface while the production of C_{2+} species was suppressed [44]. Along with the

decrease in selectivity toward ethylene, an increase in the total current density by about 40% was also observed after 22 h (Figure 5.13b), confirming the fragmentation of A-CuNWs and further enlargement in specific surface area.

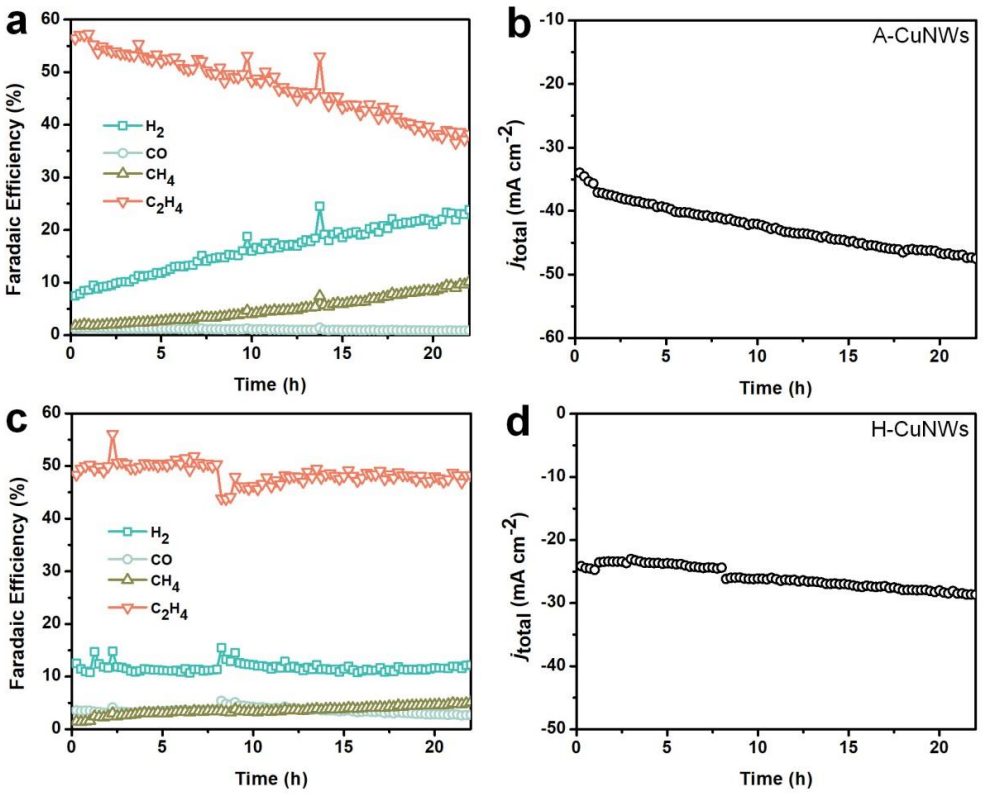

Figure 5.13. Stability tests for the catalysts based on (a, b) A-CuNWs and (c, d) H-CuNWs, respectively, at -1.02 V_{RHE} for 22 h: (a, c) Faradaic efficiencies of gaseous products and (b, d) current densities normalized to the geometric area.

When H-CuNWs served as the catalyst, the selectivity toward ethylene showed nearly no decay after 22 h, indicating its superb stability (Figure 5.13c). In the meantime, the current density of H-CuNWs also stayed relatively constant during the measurement, with an increase less than 5 $mA \cdot cm^{-2}$ (or 20%) (Figure 5.13d). To understand the enhanced stability, TEM imaging was conducted on both types of CuNWs after 5 h of

electrolysis and the results are shown in Figure 5.14. In the case of A-CuNWs, broken nanowires and Cu nanoparticles, either separated from or attached to the nanowires, were observed (Figure 5.14, a–c). As for H-CuNWs, very few of them were fragmented (Figure 5.14, d–f).

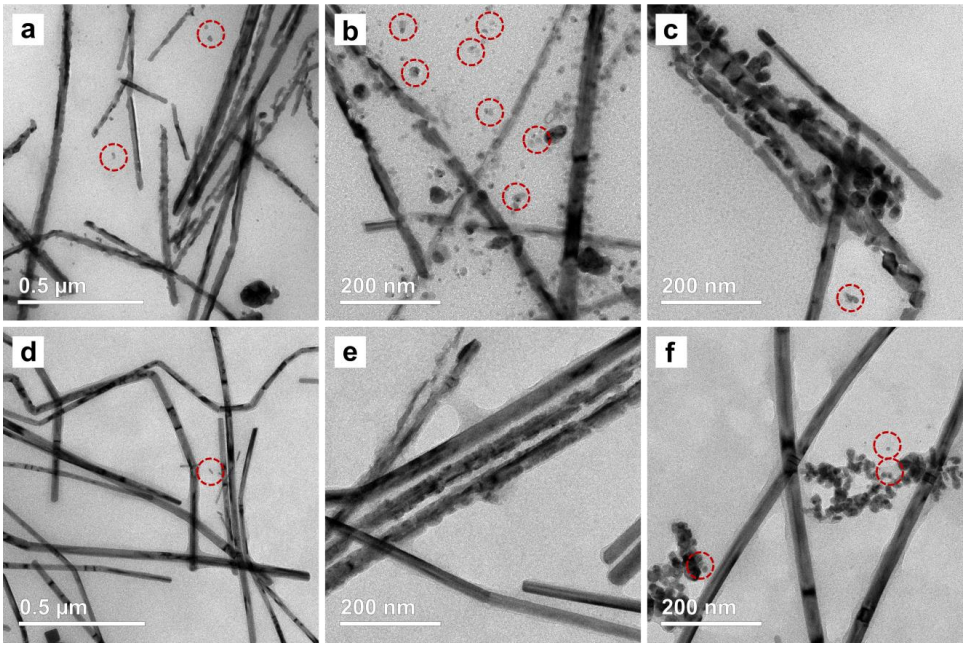

Figure 5.14. TEM images of (a–c) A-CuNWs and (d–f) H-CuNWs after 5 h of electrolysis at -1.02 V_{RHE}. The clusters generated during electrolysis are marked by red circles.

Regarding the difference in morphology, I proposed that the different oxidation pathways and the resultant structures of oxide layers were responsible for the difference in stability. The non-uniform oxidation and the resultant deep cavities led to easier disintegration of nanowires, as mentioned previously, resulting in the poor stability of A-CuNWs. In contrast, for H-CuNWs covered by a thicker and smoother Cu_xO layer, the metallic Cu core was well protected during the CO_2RR. Though the surface oxides were

reduced during catalysis, no large voids were developed on surface and the continuity of the nanowires was well preserved. The preservation of 1-D morphology and suppression of fragmentation by introducing a thick, smooth oxide sheath contributed to an improved stability for H-CuNWs [30]. However, it should be pointed out that although higher durability was achieved for H-CuNWs, they suffered slightly in terms of selectivity and activity when compared to A-CuNWs. Besides, the increase in current density as a function of time also revealed that the fragmentation could be effectively retarded for H-CuNWs, but not completely eliminated. At the moment, it remains a major challenge to design catalysts with both good stability and high selectivity and activity. Addition of supports to stabilize catalysts or covering the surface of a catalyst with proper ligands to prevent surface reconstruction might be promising directions in further research [45].

5.3 Conclusion

In summary, I have demonstrated two effective CO_2RR catalysts based on CuNWs with their surface being partially oxidized through different pathways. The A-CuNWs obtained *via* oxidation by the O_2 from air possessed a rough surface and a thin oxide layer with non-uniform thickness, while the H-CuNWs obtained by oxidation with aqueous H_2O_2 were covered with a relatively thicker and smoother oxide sheath. When applied to electrochemical CO_2RR, both of them exhibited high selectivity and activity toward C_{2+} species, ethylene in particular. The greater extent of surface roughness, the presence of more defective sites and deeper cavities after reduction of non-uniform oxide sheath contributed to a higher C_{2+} selectivity for A-CuNWs relative to H-CuNWs. However, these features were also detrimental to the stability of A-CuNWs due to their increased susceptibility to disintegration during electrolysis. Protected by a thicker and

smoother Cu_xO layer, the fragmentation of nanowires was effectively suppressed for H-CuNWs and nearly no decay in ethylene selectivity was observed after 22 h, demonstrating the improved catalytic stability. Taken together, this work demonstrates that controlling surface oxidation offers an effective strategy for improving both the C_{2+} selectivity and stability of Cu-based catalysts. We believe the same strategy should be extendible to other types of Cu nanostructures for the rational development of effective catalysts toward CO_2RR.

5.4 Experimental Section

Chemicals and Materials. Copper chloride dihydrate ($CuCl_2{\cdot}2H_2O$, 99.0%), D-(+)-glucose ($C_6H_{12}O_6$, 99.5%), hexadecylamine (HDA, 98%), aqueous hydrogen peroxide (H_2O_2, 30% w/w in H_2O), potassium hydrogen carbonate ($KHCO_3$, 99.7%), and 5% Nafion solution were all purchased from Sigma-Aldrich. Ethanol (200 proof) was obtained from Pharmco Products. I used DI water with a resistivity of 18.2 MΩ·cm at room temperature for all the experiments.

Synthesis of CuNWs. The pristine CuNWs were prepared by following a protocol previously reported by our group [19]. In a typical synthesis, 10 mL of an aqueous solution containing 21 mg of $CuCl_2{\cdot}2H_2O$, 180 mg of HDA, and 50 mg of glucose was magnetically stirred overnight to obtain a light-blue mixture, followed by sonication for 5 min. The solution was purged with Ar for 15 min to remove the trapped O_2 and the vial was then transferred into an oil bath set to 120 °C. The reaction was continued for 3 h under magnetic stirring. After completion, the solid products were collected by centrifugation, washed twice with ethanol, and stored in 10 mL of Ar-saturated ethanol solution.

Oxidation of CuNWs. For the preparation of A-CuNW catalyst, the freshly prepared CuNWs were first washed with hexane and ethanol to remove the excess HDA on the surface, and then re-dispersed in ethanol. Argon was blown over the solution for 5 min to remove most of the O_2 trapped in the vial and the solution was capped and left undisturbed for 10 days to oxidize the surface of CuNWs at a slow rate. To obtain H-CuNWs, 2 mL of the freshly prepared nanowires (0.27 mg/mL) was mixed with 2 mL of aqueous H_2O_2, and the mixture was capped in a 5-mL vial and left undisturbed under ambient conditions for 5 h. Both the solid products were collected by centrifugation, washed with ethanol, and then dispersed in Ar-saturated ethanol for further characterization.

Characterization. TEM imaging was performed on a Hitachi HT7700 microscope (Tokyo, Japan). The CuNW suspension was drop-casted onto carbon-coated Cu grids and dried at room temperature. STEM imaging was performed using an HT2700 aberration-corrected STEM (Hitachi, Tokyo, Japan) operated at 200 kV. Part of the STEM and EELS analysis was carried out on an aberration-corrected FEI Titan S 80-300 STEM/TEM microscope equipped with a Gatan OneView camera at 300 kV at Oak Ridge National Laboratory (ORNL). EELS data were collected in STEM mode using a spectrometer collection angle of 40 mrad. The NBED patterns were taken using a FEI Tecnai G2 F30 TEM operated at 300 kV with a convergent angle around 0.1 ~ 0.2 mrad. UV-vis extinction spectra were recorded on a Cary 60 spectrometer (Agilent Technologies, Santa Clara, CA). ICP-MS (NexION 300Q, Perkin-Elmer) was used to determine the concentration of Cu in the final products. XRD pattern was recorded using an X'Pert PRO Alpha-1 diffractometer (PANalytical, Almelo, Netherlands) with a 1.8

kW ceramic copper tube source. XPS data were recorded using a Thermo K-Alpha spectrometer with an Al Kα source (hν = 1486.6 eV). To measure the Auger Cu LMM spectra, the catalysts were loaded onto carbon paper and, after 1 h of electrolysis, transferred rapidly into a vial filled with Ar. The samples sealed in the vial were then transferred to the XPS chamber under the protection of Ar, ensuring the minimization of oxidation before XPS measurements.

Preparation of Working Electrode. The as-prepared A-CuNW and H-CuNW samples were washed with ethanol for several times and dispersed in 0.95 mL of ethanol and 50 μL of 5% Nafion with a Cu concentration of 2 $mg \cdot mL^{-1}$ (measured by ICP-MS). Then 5 μL of the catalyst suspension was dropped onto a pre-cleaned glassy carbon electrode with a diameter of 5 mm (catalyst loading of 51 $\mu g \cdot cm^{-2}$) and dried in air. It should be noted that only a small amount of Nafion was added, and its influence on the potential oxidation or dissolution of CuNWs can be neglected.

Electrochemical Measurements. The CO_2 reduction experiments were conducted in a gas-tight two-compartment H-type cell separated by a Nafion 117 membrane (Aldrich). Each compartment was filled with 40 mL of $KHCO_3$ solution, with a concentration of 0.1 M for catholyte and 0.5 M for anolyte. An Ag/AgCl electrode (BASi) regularly calibrated by a RHE was used as the reference electrode and a Pt mesh was used as the counter electrode. The Pt crossover was effectively prevented through the leverage of a thick Nafion 117 membrane and a Pt mesh with a large surface area (20 x 20 mm^2), which minimized the polarization and dissolution of Pt [46]. Before the electrolysis, CO_2 (99.999%, Asia Pacific Gas Enterprise Co., LTD) was purged into the $KHCO_3$ solution for 1 h to remove the air remaining in the cell, and the pH of the

catholyte was measured to be 6.8. IR compensation was conducted automatically by the potentiostat with a compensation level of 85%. The remaining 15% of IR drop was manually compensated after the reaction. During the measurement, CO_2 was continuously purged through mass flow controllers (Sevenstar, Beijing) into each compartment with a flow rate of 30 sccm. To better release the bubbles trapped on the electrode, the electrolyte solution was magnetically stirred at a rate of 1500 rpm. The potentials were converted to the RHE reference scale by E (*vs.* RHE) = E (*vs.* Ag/AgCl) + $E_{Ag/AgCl}$ + 0.0591 × (6.8 - 1.1), where $E_{Ag/AgCl}$ is the potential of the Ag/AgCl electrode measured against the RHE in 0.1 M $HClO_4$ solution (pH = 1.1). ECSAs were measured in the electrolysis cell with Ar-purged 0.1 M $KHCO_3$ as electrolyte at various scan rates. A potential range of -0.05 ~ 0.15 V_{RHE} was employed and the amount of catalyst used in each measurement was fixed to 10 μg.

The gas products were analyzed using an online gas chromatography (GC2060, Ramiin, Shanghai) equipped with the FID and TCD. Sampling was conducted sequentially at 15, 28, 41, and 54 min and the total charge collected in the 30 s prior to each sampling was used to calculate the current density. A series of standard gas mixtures (H_2, CO, CH_4, and C_2H_4 balanced in Ar, Shanghai Haizhou Special Gas Co., LTD) were used to establish the calibration curves. The faradaic efficiencies (FEs) of gas products for each sample were measured for more than three times. After 1 h of electrolysis, the liquid products were collected and analyzed using a Varian 500 MHz NMR spectrometer. Specifically, 450 μL of post-electrolysis solution was mixed with 50 μL of 500 × 10^{-6} M phenol (Aldrich) and 100 × 10^{-6} M dimethyl sulfoxide (Aldrich) contained D_2O (J&K Chemical), and the mixture was used for measurement. The calibration curves were

established from a series of standard solutions (0.1 M $KHCO_3$ solutions containing 0, 50, and 100 μM of formate, methanol, ethanol, acetate, and n-propanol).

5.5 Notes to Chapter 5

Part of this Chapter is adapted from "Controlling the Surface Oxidation of Cu Nanowires Improves Their Catalytic Selectivity and Stability toward C_{2+} Products in CO_2 Reduction" published in *Angewandte Chemie International Edition* [47]. We thank Prof. Minhua Shao and Dr. Shangqian Zhu for the electrochemical measurements.

5.6 References

[1] Gao, D.; Arán-Ais, R. M.; Jeon, H. S.; Roldan Cuenya, B. *Nat. Catal.* **2019**, *2*, 198–210.

[2] Nitopi, S.; Bertheussen, E.; Scott, S. B.; Liu, X.; Engstfeld, A. K.; Horch, S.; Seger, B.; Stephens, I. E. L.; Chan, K.; Hahn, C.; Nørskov, J. K.; Jaramillo, T. F.; Chorkendorff, I. *Chem. Rev.* **2019**, *119*, 7610–7672.

[3] Arán-Ais, R. M.; Gao, D.; Roldan Cuenya, B. *Acc. Chem. Res.* **2018**, *51*, 2906–2917.

[4] Hori, Y.; Takahashi, I.; Koga, O.; Hoshi, N. *J. Mol. Catal. A Chem.* **2003**, *199*, 39–47.

[5] Reller, C.; Krause, R.; Volkova, E.; Schmid, B.; Neubauer, S.; Rucki, A.; Schuster, M.; Schmid, G. *Adv. Energy Mater.* **2017**, *7*, 1–8.

[6] Choi, C.; Cheng, T.; Flores Espinosa, M.; Fei, H.; Duan, X.; Goddard, W. A.; Huang, Y. *Adv. Mater.* **2019**, *31*, 1805405.

[7] Jeon, H. S.; Kunze, S.; Scholten, F.; Roldan Cuenya, B. *ACS Catal.* **2018**, *8*, 531–535.

[8] Kim, D.; Resasco, J.; Yu, Y.; Asiri, A. M.; Yang, P. *Nat. Commun.* **2014**, *5*, 1–8.

[9] Liang, Z. Q.; Zhuang, T. T.; Seifitokaldani, A.; Li, J.; Huang, C. W.; Tan, C. S.;

Li, Y.; De Luna, P.; Dinh, C. T.; Hu, Y.; Xiao, Q.; Hsieh, P. L.; Wang, Y.; Li, F.; Quintero-Bermudez, R.; Zhou, Y.; Chen, P.; Pang, Y.; Lo, S. C.; Chen, L. J.; Tan, H.; Xu, Z.; Zhao, S.; Sinton, D.; Sargent, E. H. *Nat. Commun.* **2018**, *9*, 3828.

[10] Zhou, Y.; Che, F.; Liu, M.; Zou, C.; Liang, Z.; De Luna, P.; Yuan, H.; Li, J.; Wang, Z.; Xie, H.; Li, H.; Chen, P.; Bladt, E.; Quintero-Bermudez, R.; Sham, T. K.; Bals, S.; Hofkens, J.; Sinton, D.; Chen, G.; Sargent, E. H. *Nat. Chem.* **2018**, *10*, 974–980.

[11] Jung, H.; Lee, S. Y.; Lee, C. W.; Cho, M. K.; Won, D. H.; Kim, C.; Oh, H. S.; Min, B. K.; Hwang, Y. J. *J. Am. Chem. Soc.* **2019**, *141*, 4624–4633.

[12] Kim, J.; Choi, W.; Park, J. W.; Kim, C.; Kim, M.; Song, H. *J. Am. Chem. Soc.* **2019**, *141*, 6986–6994.

[13] Gao, D.; Zegkinoglou, I.; Divins, N. J.; Scholten, F.; Sinev, I.; Grosse, P.; Roldan Cuenya, B. *ACS Nano* **2017**, *11*, 4825–4831.

[14] Li, Y.; Cui, F.; Ross, M. B.; Kim, D.; Sun, Y.; Yang, P. *Nano Lett.* **2017**, *17*, 1312–1317.

[15] Zhang, H.; Zhang, Y.; Li, Y.; Ahn, S.; Palmore, G. T. R.; Fu, J.; Peterson, A. A.; Sun, S. *Nanoscale* **2019**, *11*, 12075–12079.

[16] Suen, N. T.; Kong, Z. R.; Hsu, C. S.; Chen, H. C.; Tung, C. W.; Lu, Y. R.; Dong, C. L.; Shen, C. C.; Chung, J. C.; Chen, H. M. *ACS Catal.* **2019**, *9*, 5217–5222.

[17] Ma, S.; Sadakiyo, M.; Luo, R.; Heima, M.; Yamauchi, M.; Kenis, P. J. A. *J. Power Sources* **2016**, *301*, 219–228.

[18] Dinh, C. T.; Burdyny, T.; Kibria, G.; Seifitokaldani, A.; Gabardo, C. M.; Pelayo García De Arquer, F.; Kiani, A.; Edwards, J. P.; De Luna, P.; Bushuyev, O. S.; Zou, C.; Quintero-Bermudez, R.; Pang, Y.; Sinton, D.; Sargent, E. H. *Science* **2018**, *360*, 783–787.

[19] Luo, M.; Zhou, M.; Da Silva, R. R.; Tao, J.; Figueroa-Cosme, L.; Gilroy, K. D.; Peng, H. C.; He, Z.; Xia, Y. *ChemNanoMat* **2017**, *3*, 190–195.

[20] Yang, J. C.; Kolasa, B.; Gibson, J. M.; Yeadon, M. *Appl. Phys. Lett.* **1998**, *73*, 2841–2843.

[21] Eastman, J. A.; Fuoss, P. H.; Rehn, L. E.; Baldo, P. M.; Zhou, G. W.; Fong, D. D.; Thompson, L. J. *Appl. Phys. Lett.* **2005**, *87*, 1–4.

[22] Lyu, Z.; Xie, M.; Aldama, E.; Zhao, M.; Qiu, J.; Zhou, S.; Xia, Y. *ACS Appl. Nano Mater.* **2019**, *2*, 1533–1540.

[23] Han, H.; Choi, H.; Mhin, S.; Hong, Y. R.; Kim, K. M.; Kwon, J.; Ali, G.; Chung, K. Y.; Je, M.; Umh, H. N.; Lim, D. H.; Davey, K.; Qiao, S. Z.; Paik, U.; Song, T. *Energy Environ. Sci.* **2019**, *12*, 2443–2454.

[24] DeNardis, D.; Rosales-Yeomans, D.; Borucki, L.; Philipossian, A. *Thin Solid Films* **2006**, *513*, 311–318.

[25] Yin, M.; Wu, C. K.; Lou, Y.; Burda, C.; Koberstein, J. T.; Zhu, Y.; O'Brien, S. *J. Am. Chem. Soc.* **2005**, *127*, 9506–9511.

[26] Lyu, Z.; Xie, M.; Gilroy, K. D.; Hood, Z. D.; Zhao, M.; Zhou, S.; Liu, J.; Xia, Y. *Chem. Mater.* **2018**, *30*, 6469–6477.

[27] Guo, H.; Lin, N.; Chen, Y.; Wang, Z.; Xie, Q.; Zheng, T.; Gao, N.; Li, S.; Kang, J.; Cai, D.; Peng, D. L. *Sci. Rep.* **2013**, *3*, 2323.

[28] Hung, L. L.; Tsung, C. K.; Huang, W.; Yang, P. *Adv. Mater.* **2010**, *22*, 1910–1914.

[29] Ren, D.; Wong, N. T.; Handoko, A. D.; Huang, Y.; Yeo, B. S. *J. Phys. Chem. Lett.* **2016**, *7*, 20–24.

[30] Li, C. W.; Kanan, M. W. *J. Am. Chem. Soc.* **2012**, *134*, 7231–7234.

[31] Raciti, D.; Mao, M.; Wang, C. *Nanotechnology* **2018**, *29*, 044001.

[32] Handoko, A. D.; Ong, C. W.; Huang, Y.; Lee, Z. G.; Lin, L.; Panetti, G. B.; Yeo, B. S. *J. Phys. Chem. C* **2016**, *120*, 20058–20067.

[33] Huang, J.; Hörmann, N.; Oveisi, E.; Loiudice, A.; De Gregorio, G. L.; Andreussi, O.; Marzari, N.; Buonsanti, R. *Nat. Commun.* **2018**, *9*, 1–9.

[34] Mistry, H.; Varela, A. S.; Bonifacio, C. S.; Zegkinoglou, I.; Sinev, I.; Choi, Y. W.; Kisslinger, K.; Stach, E. A.; Yang, J. C.; Strasser, P.; Cuenya, B. R. *Nat. Commun.* **2016**, *7*, 12123.

[35] Cavalca, F.; Ferragut, R.; Aghion, S.; Eilert, A.; Diaz-Morales, O.; Liu, C.; Koh, A. L.; Hansen, T. W.; Pettersson, L. G. M.; Nilsson, A. *J. Phys. Chem. C* **2017**, *121*, 25003–25009.

[36] Zhao, Y.; Chang, X.; Malkani, A. S.; Yang, X.; Thompson, L.; Jiao, F.; Xu, B. *J. Am. Chem. Soc.* **2020**, *142*, 9735–9743.

[37] Tang, W.; Peterson, A. A.; Varela, A. S.; Jovanov, Z. P.; Bech, L.; Durand, W. J.; Dahl, S.; Nørskov, J. K.; Chorkendorff, I. *Phys. Chem. Chem. Phys.* **2012**, *14*, 76–81.

[38] Feng, X.; Jiang, K.; Fan, S.; Kanan, M. W. *ACS Cent. Sci.* **2016**, *2*, 169–174.

[39] Chen, Z.; Waje, M.; Li, W.; Yan, Y. *Angew. Chem. Int. Ed.* **2007**, *46*, 4060–4063.

[40] Huo, D.; Kim, M. J.; Lyu, Z.; Shi, Y.; Wiley, B. J.; Xia, Y. *Chem. Rev.* **2019**, *119*, 8972–9073.

[41] Zhuang, T. T.; Pang, Y.; Liang, Z. Q.; Wang, Z.; Li, Y.; Tan, C. S.; Li, J.; Dinh, C. T.; De Luna, P.; Hsieh, P. L.; Burdyny, T.; Li, H. H.; Liu, M.; Wang, Y.; Li, F.; Proppe, A.; Johnston, A.; Nam, D. H.; Wu, Z. Y.; Zheng, Y. R.; Ip, A. H.; Tan, H.; Chen, L. J.; Yu, S. H.; Kelley, S. O.; Sinton, D.; Sargent, E. H. *Nat. Catal.* **2018**, *1*, 946–951.

[42] Yang, K. D.; Ko, W. R.; Lee, J. H.; Kim, S. J.; Lee, H.; Lee, M. H.; Nam, K. T. *Angew. Chem. Int. Ed.* **2017**, *56*, 796–800.

[43] Loiudice, A.; Lobaccaro, P.; Kamali, E. A.; Thao, T.; Huang, B. H.; Ager, J. W.; Buonsanti, R. *Angew. Chem. Int. Ed.* **2016**, *55*, 5789–5792.

[44] Reske, R.; Mistry, H.; Behafarid, F.; Roldan Cuenya, B.; Strasser, P. *J. Am. Chem. Soc.* **2014**, *136*, 6978–6986.

[45] Fu, J.; Zhu, W.; Chen, Y.; Yin, Z.; Li, Y.; Liu, J.; Zhang, H.; Zhu, J. J.; Sun, S. *Angew. Chem. Int. Ed.* **2019**, *58*, 14100–14103.

[46] Clark, E. L.; Resasco, J.; Landers, A.; Lin, J.; Chung, L. T.; Walton, A.; Hahn, C.; Jaramillo, T. F.; Bell, A. T. *ACS Catal.* **2018**, *8*, 6560–6570.

[47] Lyu, Z.; Zhu, S.; Xie, M.; Zhang, Y.; Chen, Z.; Chen, R.; Tian, M.; Chi, M.; Shao, M.; Xia, Y. *Angew. Chem. Int. Ed.* **2020**, DOI:10.1002/anie.202011956.

CHAPTER 6

CONCLUSIONS AND FUTURE DIRECTIONS

6.1 Conclusions

This dissertation focused on the rational synthesis of Cu-based nanocrystals with well-defined shapes and structures, together with exploration of their utilization as effective catalysts toward electrochemical CO_2RR. The first two projects placed more emphasis on the development of synthetic methodology, whereas the other two paid more attention to the design of new catalysts toward CO_2RR.

I first demonstrated a facile synthesis of Cu RBPs with edge lengths controlled in the range of 38−67 nm. The one-pot protocol involved the sequential reduction of Pd(II) and Cu(II) precursors, mixed at a molar ratio of 1:200, by glucose in the presence of HDA. Due to the large difference in standard reduction potential between Pd(II)/Pd and Cu(II)/Cu pairs, the Pd(II) precursor was reduced first for the generation of Pd seeds lined with parallel planar defects, followed by the slow deposition of Cu atoms for the formation of RBPs. Since Pd(II) was used at a trace amount relative to Cu(II), the Pd had essentially no impact on the elemental composition and optical properties of the RBPs. For Cu RBPs with edge lengths greater than 56 nm, two LSPR peaks at 586 and 621 nm were observed, and their positions were both red-shifted as the edge length was increased.

In addition to the one-pot protocol, I also developed a seed-mediated approach to the synthesis of Au@Cu core-shell nanocubes with small sizes. The large (12%) lattice mismatch between Cu and Au led to the localized epitaxial growth of Cu shells on the Au

seeds and the formation of nanocubes with randomly distributed Au cores. Compared to the same synthesis in the absence of Au seeds, the reduction of Cu(II) ions was greatly accelerated in the presence of Au seeds because of the autocatalytic surface reduction. By varying the reaction time and/or the amount of Au seeds, the size of the Au@Cu nanocubes could be tuned in the range of 20–30 nm. The as-synthesized core-shell nanocubes exhibited a strong LSPR peak at 581 nm and the resonance was found to be dominated by absorption rather than scattering.

Compared to the core-shell structure where the core metal is fully covered by the shell, a Janus structure where both metals are exposed on the surface have attracted more attention as a tandem catalyst. To this end, I developed a facile synthesis of Pd-Cu Janus nanocrystals with novel and controllable shapes by controlling the site-selected growth of Cu on Pd icosahedral seeds. Specifically, at a slow reduction rate, the Cu atoms nucleated and grew from one vertex of the icosahedral seed for the formation of a penta-twinned Janus nanocrystal in the shape of pentagonal bipyramid or decahedron. At a fast reduction rate, in contrast, the Cu atoms could directly nucleate from or diffuse to the edge of the icosahedral seed for the generation of a singly-twinned Janus nanocrystal in the shape of truncated bitetrahedron. The segregation of the two elements and presence of twin boundaries on the surface made the Pd-Cu Janus nanocrystals effective catalysts toward CO_2RR. DFT and Pourbaix phase diagram studies demonstrated that the high CO coverage on the Pd site during electrolysis enabled the migration of CO to the Cu site for subsequent C-C coupling, promoting the formation of C_{2+} species.

In addition to the introduction of a CO-producing metal such as Pd, surface oxidation provides another route to enhancing the C_{2+} selectivity of Cu catalysts. My last

project demonstrated this concept by controlling the surface oxidation of CuNWs to greatly improve their C_{2+} selectivity and stability toward CO_2RR. Specifically, high FEs were achieved for ethylene when the CuNWs were oxidized by the O_2 from air or aqueous H_2O_2, and both catalysts showed suppressed HER and low hydrogen selectivity. The high yields of C_{2+} products could be mainly attributed to the increase in surface roughness and the generation of defects and cavities during the electrochemical reduction of oxide layer. This project also indicated that the formation of a relatively thick, smooth oxide sheath by exposure to H_2O_2 could improve the catalytic stability by mitigating the fragmentation issue.

In summary, my research introduced several strategies for shape-controlled synthesis of Cu nanocrystals, which has been a challenging task considering the low reduction potential of Cu and its vulnerability to oxidation. Benefiting from the advanced characterization methods, the growth mechanism involved in each synthesis was also elucidated. Due to the LSPR effect, Cu-based nanocrystals showed absorbance in the visible light region with high sensitivity to size, shape, and composition, making them potential materials for plasmonic applications. Considering the unique capability of Cu in producing C_{2+} species from CO_2, the rationally designed Cu-based nanocrystals were further subjected to test for CO_2RR. The introduction of a CO-producing metal such as Pd, the presence of twin boundaries, and the increase in surface roughness through reduction of surface oxides could all enhance the C_{2+} selectivity. These studies not only offered facile and effective methods for synthesizing Cu nanocrystals with well-defined shapes, but also unveiled the mechanisms underlying the high selectivity toward C_{2+}

species in CO_2RR, providing insightful guideline for designing Cu-based catalysts with superior catalytic performance.

6.2 Future Directions

Though cost-effective in price and promising in various applications, up till now, the research on Cu nanocrystals is still rather limited, and more efforts are desired on the investigation of their synthetic methods, shape control, storage, and reaction mechanisms when applied as catalysts. Below I list some of the issues with great importance or interest related to Cu nanocrystals and CO_2RR that need to be addressed in the future.

1. The vulnerability of Cu to oxidation and corrosion greatly restricts their applications considering the difficulty in terms of not only storage but also mechanistic investigation and maintenance of performance. Thus, there is a pressing need to develop effective methods for stabilizing Cu nanocrystals. One potential method is to introduce effective capping agents, such as formate and HDA, which can protect the nanocrystals from being oxidized. For example, it was reported that Cu nanosheets covered by formate could be stabilized for more than 90 days without any observation of oxides in both XRD pattern and XPS spectra [1]. Another strategy is to coat the Cu nanocrystals with an inert material such as carbon [2,3]. In one example, CuNWs coated with reduced graphene oxides (rGO) have been reported to show high methane selectivity (50%) and superior stability in electrochemical CO_2RR. No change to morphology was observed after 5 C of electrolysis for the rGO-coated CuNWs, while the pure CuNWs had corroded and broken into pieces under the same condition [2]. Besides, alloying/doping with other metals may also be effective in improving the stability of Cu nanocrystals. For example, considering the lower reduction potential of Al and the compact structure of Al_2O_3, doping or coating

Cu nanocrystals with Al or Al_2O_3 may help protect the Cu core from oxidation during long-term storage. The Al_2O_3 shell could later be removed by exposing to an acid or base. It was also reported that Ag-Cu bimetallic nanoparticles showed an enhanced resistance toward oxidation. The electron transfer from Cu to Ag led to a positive valence and the lower electron density of Cu, making it less active in bonding to oxygen [4]. Elevating the valence of Cu seems to offer a great opportunity to improve its stability and the concept deserves further evalution. It should be mentioned that all the strategies proposed above may also change the surface structure or composition, which should be taken into consideration when optimizing the catalysts.

2. More advanced characterization methods are desired for unveiling the growth pathways of Cu nanocrystals and the reaction mechanisms underlying their unique selectivity toward CO_2RR, including the intermediates, surface reconstruction, and composition change during electrolysis. For example, when synthesizing Cu nanocrystals with well-defined shapes, the role of "capping agents" such as amines and halide ions is still ambiguous. Their potential ligand exchange with the precursors and selective binding to certain facets of Cu still need confirmation, and techniques such as mass spectrometry (MS), infrared (IR) spectroscopy, SERS, X-ray absorption near edge structure (XANES), and extended X-Ray absorption fine structure (EXAFS) may provide useful information. Additionally, combining with DFT calculations, the reduction pathway of CO_2 on Cu catalysts could be better understood with the help of advanced characterization methods such as *in situ* ATR-IR [5]. As mentioned in previous chapters, surface reconstruction is commonly observed for Cu catalysts during electrolysis, increasing the difficulty in understanding the active sites for CO_2RR. The potential existence of positive-valence Cu

ions and their influence on enhancing C_{2+} selectivity is still under debate. *In situ* electron microscopes including liquid phase TEM [6] and SEM [7], together with *in situ* X-ray spectroscopy, may significantly help advance our understanding on catalytically active surface structures of Cu during CO_2RR.

3. Considering the LSPR effect and unique catalytic properties of Cu, it would be interesting if combining electrochemical CO_2RR with photocatalysis by employing Cu nanocrystals as catalysts or co-catalysts. Typically, three steps are involved in the photocatalytic CO_2 reduction: *i*) absorption of photons and the generation of electron-hole pairs; *ii*) independent migration of electrons and holes to the surface of the photoelectrode; *iii*) reduction of CO_2 by electrons and oxidation of H_2O by holes [8]. Loading Cu nanocrystals onto photoelectrodes (such as those made of Co_3O_4 and TiO_2) may help manipulate the adsorption strength of certain intermediates such as H and CO, leading to the formation of hydrocarbon products in high yields [9]. As a plasmonic metal, the introduction of Cu could also enhance light absorption, improving the solar-to-chemical conversion efficiency of the photocatalyst [9,10].

4. More endeavors are still needed in improving the activity and selectivity of catalysts for CO_2RR. Concerning the environmental issues, safety regulation, and depletion of fossil fuels, electrochemical reduction of CO_2 shows great promise in chemical production and carbon utilization as a substitute for conventional petrochemical processes. However, in terms of economic feasibility, CO_2RR is still far from profitable considering the low energy conversion efficiency, high electricity cost, high expense of separating products, and disadvantage of pairing with oxygen evolution reaction (OER), among others [11]. For example, a recent technoeconomic analysis suggested that when

electricity costs fall below 4 cents/kWh and electrical-to-chemical conversion efficiency reaches at least 60%, the products from electrochemical CO_2RR will be competitive in market prices with those derived from fossil fuels. However, the best systems today only demonstrate an energy efficiency of approximately 30 to 50% for products such as CO and ethylene. The electricity cost also hovers around 6-10 cents/kWh, with limited regions reaching a cost below 4 cents/kWh [12]. Thus, developing catalysts with high selectivity and current density, long-term stability, as well as low onset potential (to lower the cell potential and reduce electric utility costs) is of critical importance in making CO_2RR economically compelling. It is also believed that the greater competition and advances in manufacturing may eventually realize a low cost of electricity and profitability of electro-synthesized chemicals.

In addition to effective catalysts and reduced electricity costs, the improvement on device is also pivotal in facilitating the commercialization of CO_2RR. For example, compared with H-cell, flow cell with reactants and products circulating in the cell shows greater promise due to its capability of overcoming the mass-transport limitations. The flow cells could also be arranged in larger stacks, benefiting the development of commercial-scale electrochemical reactors [13]. Connecting with a separation device or material to remove by-products and concentrate desired products would further boost CO_2 conversion and yields of certain products, promoting the commercialization of CO_2RR [14]. Combining CO_2RR with other electrochemical devices such as a flow cell further oxidizing ethylene to ethylene oxide, CO_2 could serve as a precursor to generate more value-added species [15]. Instead of using OER as the conventional anode reaction, CO_2RR can be coupled with various organic oxidation reactions to produce more

profitable chemicals rather than oxygen [11]. Moreover, mixing CO_2 with other gases such as CO may contribute to an improved selectivity toward certain products, providing opportunities for more interesting discoveries [16].

6.3 Notes to Chapter 6

Part of this Chapter is adapted from "A Rationally Designed Route to the One-Pot Synthesis of Right Bipyramidal Nanocrystals of Copper" published in *Chemistry of Materials* [17], "Au@Cu Core−Shell Nanocubes with Controllable Sizes in the Range of 20−30 nm for Applications in Catalysis and Plasmonics" published in *ACS Applied Nano Materials* [18], "Kinetically-Controlled Synthesis of Pd-Cu Janus Nanocrystals with Enriched Surface Structures and Enhanced Catalytic Activities toward CO_2 Reduction" now under review at *Journal of the American Chemical Society*, and "Controlling the Surface Oxidation of Cu Nanowires Improves Their Catalytic Selectivity and Stability toward C_{2+} Products in CO_2 Reduction" published in *Angewandte Chemie International Edition* [19].

6.4 References

[1] Dai, L.; Qin, Q.; Wang, P.; Zhao, X.; Hu, C.; Liu, P.; Qin, R.; Chen, M.; Ou, D.; Xu, C.; Mo, S.; Wu, B.; Fu, G.; Zhang, P.; Zheng, N. *Sci. Adv.* **2017**, *3*, 1–10.

[2] Li, Y.; Cui, F.; Ross, M. B.; Kim, D.; Sun, Y.; Yang, P. *Nano Lett.* **2017**, *17*, 1312–1317.

[3] Wang, X.; Wang, Z.; García de Arquer, F. P.; Dinh, C. T.; Ozden, A.; Li, Y. C.; Nam, D. H.; Li, J.; Liu, Y. S.; Wicks, J.; Chen, Z.; Chi, M.; Chen, B.; Wang, Y.; Tam, J.; Howe, J. Y.; Proppe, A.; Todorović, P.; Li, F.; Zhuang, T. T.; Gabardo, C. M.; Kirmani, A. R.; McCallum, C.; Hung, S. F.; Lum, Y.; Luo, M.; Min, Y.; Xu, A.; O'Brien, C. P.; Stephen, B.; Sun, B.; Ip, A. H.; Richter, L. J.; Kelley, S. O.; Sinton, D.; Sargent, E. H. *Nat. Energy* **2020**, *5*, 478–486.

[4] Kim, N. R.; Shin, K.; Jung, I.; Shim, M.; Lee, H. M. *J. Phys. Chem. C* **2014**, *118*, 26324–26331.

[5] Zhu, S.; Li, T.; Cai, W. Bin; Shao, M. *ACS Energy Lett.* **2019**, *4*, 682–689.

[6] Li, Y.; Kim, D.; Louisia, S.; Xie, C.; Kong, Q.; Yu, S.; Lin, T.; Aloni, S.; Fakra, S. C.; Yang, P. *Proc. Natl. Acad. Sci. U. S. A.* **2020**, *117*, 9194–9201.

[7] Velasco-Velez, J. J.; Velasco-Velez, J. J.; Mom, R. V.; Sandoval-Diaz, L. E.; Falling, L. J.; Chuang, C. H.; Gao, D.; Gao, D.; Jones, T. E.; Zhu, Q.; Zhu, Q.; Arrigo, R.; Roldan Cuenya, B.; Knop-Gericke, A.; Knop-Gericke, A.; Lunkenbein, T.; Schlögl, R.; Schlögl, R. *ACS Energy Lett.* **2020**, *5*, 2106–2111.

[8] Chang, X.; Wang, T.; Yang, P.; Zhang, G.; Gong, J. *Adv. Mater.* **2019**, *31*, 1–13.

[9] Shen, Q.; Chen, Z.; Huang, X.; Liu, M.; Zhao, G. *Environ. Sci. Technol.* **2015**, *49*, 5828–5835.

[10] Duchene, J. S.; Tagliabue, G.; Welch, A. J.; Cheng, W. H.; Atwater, H. A. *Nano Lett.* **2018**, *18*, 2545–2550.

[11] Na, J.; Seo, B.; Kim, J.; Lee, C. W.; Lee, H.; Hwang, Y. J.; Min, B. K.; Lee, D. K.; Oh, H. S.; Lee, U. *Nat. Commun.* **2019**, *10*, 5193.

[12] De Luna, P.; Hahn, C.; Higgins, D.; Jaffer, S. A.; Jaramillo, T. F.; Sargent, E. H. *Science* **2019**, *364*, eaav3506.

[13] Weekes, D. M.; Salvatore, D. A.; Reyes, A.; Huang, A.; Berlinguette, C. P. *Acc. Chem. Res.* **2018**, *51*, 910–918.

[14] Li, H.; Qiu, C.; Ren, S.; Dong, Q.; Zhang, S.; Zhou, F.; Liang, X.; Wang, J.; Li, S.; Yu, M. *Science* **2020**, *367*, 667–671.

[15] Leow, W. R.; Lum, Y.; Ozden, A.; Wang, Y.; Nam, D. H.; Chen, B.; Wicks, J.; Zhuang, T. T.; Li, F.; Sinton, D.; Sargent, E. H. *Science* **2020**, *368*, 1228–1233.

[16] Wang, X.; de Araújo, J. F.; Ju, W.; Bagger, A.; Schmies, H.; Kühl, S.; Rossmeisl, J.; Strasser, P. *Nat. Nanotechnol.* **2019**, *14*, 1063–1070.

[17] Lyu, Z.; Xie, M.; Gilroy, K. D.; Hood, Z. D.; Zhao, M.; Zhou, S.; Liu, J.; Xia, Y. *Chem. Mater.* **2018**, *30*, 6469–6477.

[18] Lyu, Z.; Xie, M.; Aldama, E.; Zhao, M.; Qiu, J.; Zhou, S.; Xia, Y. *ACS Appl. Nano Mater.* **2019**, *2*, 1533–1540.

[19] Lyu, Z.; Zhu, S.; Xie, M.; Zhang, Y.; Chen, Z.; Chen, R.; Tian, M.; Chi, M.; Shao, M.; Xia, Y. *Angew. Chem. Int. Ed.* **2020**, DOI:10.1002/anie.202011956.